AN ABSTRACT OF THE THESIS OF

James J. Walters for the degree of Master of Science in Civil Engineering presented on August 14, 2013.

Title: Characterization of Reinforced Fill Soil, Soil-Reinforcement Interaction, and Internal Stability of Very Tall MSE Walls

Abstract approved:

Armin W. Stuedlein

In many geotechnical design situations involving tight right-of-way constraints, Mechanically Stabilized Earth (MSE) walls are often the most cost-effective and reliable earth retention technology among available alternatives. However, few well-documented case histories with detailed material testing, instrumentation programs and construction observation of performance are available in the literature. Despite the small number of case histories, empirical design methods are used in place of more theoretically-based methods. As a result, current design methods for MSE walls result in a large amount of inaccuracy, especially when their empirical calibration limits are exceeded.

This study characterizes the constitutive behavior of a sandy gravel backfill soil and ribbed steel strip reinforcement material used in the construction of two very tall MSE walls constructed during the 3rd Runway Expansion Project at the Seattle-Tacoma International Airport (SeaTac). Tension testing was performed on coupons cut from the reinforcement material in order to measure its Young's modulus and yield strength. Consolidated drained triaxial strength testing was performed to measure the stress-strain behavior of the loose, medium dense, and densely-compacted backfill materials. Then the

frictional interaction between the reinforcement and densely-compacted backfill soil was evaluated by performing twenty full-scale single-strip laboratory pullout tests.

Using the results from the material testing and in-situ reinforcement strain measurements taken at the SeaTac MSE walls, the accuracy of four reinforcement load prediction methods was evaluated. The pullout test results were used to develop a backfill-specific design model, as well as being combined with other pullout test results for gravels reported in the literature to develop a global gravel design model for predicting peak reinforcement pullout resistances. These newly developed pullout design models were compared to the current AASHTO design model and found to produce much more accurate predictions of peak reinforcement pullout resistance. Walls designed and constructed with the kinds of backfill evaluated herein and with the new models generated will be more cost-effective than typically accepted design models.

Characterization of Reinforced Fill Soil, Soil-Reinforcement Interaction, and Internal Stability of Very Tall MSE Walls

by

James J. Walters

A THESIS

submitted to

Oregon State University

in partial fulfillment of
the requirements for the
degree of

Master of Science

Presented August 14, 2013
Commencement June 2014

Master of Science thesis of James J. Walters presented on August 14, 2013.

APPROVED:

Major Professor, representing Civil Engineering

Head of the School of Civil and Construction Engineering

Dean of the Graduate School

I understand that my thesis will become part of the permanent collection of Oregon State University libraries. My signature below authorizes release of my thesis to any reader upon request.

James J. Walters, Author

ACKNOWLEDGEMENTS

Many individuals and organizations made the completion of this research possible. I would like to take this opportunity to thank all who contributed.

First and foremost, I would like to acknowledge my advising Professor Armin W. Stuedlein who provided me with the opportunity, and encouraged me to perform this research. The guidance and feedback Dr. Stuedlein provided both in the laboratory and while writing was vital to the successful completion and this thesis. I am grateful to Dr. Stuedlein for the knowledge he has provided me and for always holding me to the highest ethical, professional, and intellectual standards.

Furthermore, I would like to thank my committee members Dr. Matt Evans, Dr. Ben Leshchinsky, and Dr. Wade Marcum (GCR) for their support. Their insightful comments and ideas have provided much perspective and were greatly appreciated.

I would like to acknowledge the Pacific North West Transportation Consortium (PacTrans) and the National Science Foundation (NSF) for providing the funds necessary to conduct this research, as well as FEI Testing and Inspection Inc. for donating time and resources in performing both Proctor tests and nuclear density tests.

I would also like to thank Dr. Christopher Higgins and Dr. Scott Ashford for lending laboratory equipment and materials which were used during pullout testing. I am most grateful to Michel Dyson and James Batti for their help in assembling laboratory testing equipment, measurement sensors, and data acquisition software.

I would like to extend a much deserved thanks to Daniel Simpson, Spencer Ambuen, Jose Bañuelos, Kyle Fortner, Chris Newton, Therese Pflaum, Seth Reddy, Andrew Strahler, Robert Leaf, and Stephan Stys for their help in preparing pullout test samples. I would also like to extend a special thanks to Stephan Stys for his help in carefully performing many of the consolidated drained triaxial shear strength tests reported in this thesis, as well Colin McCormick and Andrew Strahler for their help in developing the triaxial testing procedure found in Appendix A. I owe a great deal of gratitude to Seth Reddy, Andrew Strahler, and Tadesse Meskele for their intellectual council and assistance in the analysis of data presented in this thesis.

My father and mother Eric and Sabrina Walters and especially my wife Amy Walters have continually provided me with love and support though out my time at OSU. I would not have completed this research without them.

TABLE OF CONTENTS

TABLE OF CONTENTS (Continued)

Page

TABLE OF CONTENTS (Continued)

Page

LIST OF FIGURES

LIST OF FIGURES (Continued)

Figure Page

LIST OF FIGURES (Continued)

Figure Page

LIST OF FIGURES (Continued)

Figure Page

LIST OF FIGURES (Continued)

Figure Page

LIST OF FIGURES (Continued)

Figure Page

LIST OF FIGURES (Continued)

Figure Page

LIST OF FIGURES (Continued)

Figure Page

LIST OF FIGURES (Continued)

Figure Page

LIST OF TABLES

LIST OF TABLES (Continued)

Table Page

LIST OF APENDICES

LIST OF APPENDIX FIGURES

Figure Page

LIST OF APPENDIX FIGURES (Continued)

Figure Page

LIST OF APPENDIX FIGURES (Continued)

Figure Page

LIST OF APPENDIX FIGURES (Continued)

Figure Page

LIST OF APPENDIX FIGURES (Continued)

Figure Page

NOTATION

Acronyms

AASHTO	American Association of State Highway and Transportation Office
ANOVA	Analysis of variance
ASTM	American Society for Testing and Materials
BDA	Balloon Density Apparatus
CD	Consolidated-Drained
CMFE	Curved Mohr-Coulomb Failure Envelope
COV	Coefficient of variation
DAQ	Data acquisition system
FEI	FEI Testing & Inspection
FHWA	Federal Highway Administration
LSSE	Least sum of squared errors
MLR	Multi Linear Regression
MSE	Mechanically Stabilized Earth
NDG	Nuclear Density Gauge
SeaTac	Seattle-Tacoma International Airport

NOTATION (Continued)

Symbols

a	Fitting coefficient used for calculating Φ_{local}
A_r	Area of reinforcement per unit width of wall
A_s	Contact surface area
A_t	Wall facing tributary area
b	Width of reinforcing element
c	Cohesion intercept
c'	Effective cohesion intercept
C_u	Coefficient of uniformity
d	Constant coefficient used for calculating Φ_{fb}
$D_{t\max}$	Load distribution factor
e	Eccentricity
E_i	Initial tangent modulus
E_r	Modulus of reinforcement material
E_t	Tangent modulus
f_y	Yield stress
f^*	Apparent friction coefficient
FS_{PO}	Factor of safety with respect to reinforcement pullout
F_T	Resultant of the lateral earth pressure on the back of the reinforced soil mass
H	Height of wall from bearing pad to top of wall facing
H_1	Height of wall from bearing pad to top of active zone
k	Modulus number for loading
k_{ur}	Modulus number for unloading
K	Modulus number

NOTATION (Continued)

K_a	Coefficient of active lateral earth pressure
K_B	Bulk modulus number
K_{aa}	Equivalent active earth pressure coefficient
K_{abh}	Active lateral earth pressure coefficient considering facing batter
K_{avh}	Active lateral earth pressure coefficient assuming vertical face batter
K_c	lateral earth pressure coefficient considering compaction
K_o	Coefficient of at-rest lateral earth pressure
K_p	Coefficient of passive lateral earth pressure
K_r	Coefficient of lateral earth pressure at depth of the interest
$K_{\Delta 2}$	Decremental lateral earth pressure coefficient
L	Length of roller used for compaction
L_a	Length of reinforcement within the active zone
L_e	Embedded length of reinforcement
$L_{e,req'd}$	Required embedded length for pullout
L_r	Total length of reinforcement
m	Bulk modulus exponent
n	Modulus exponent
n_r	Number of reinforcement layers
N_γ	Bearing capacity factor for Rankine wedge theory
OCR	Overconsolidation ratio
P_a	Atmospheric pressure
$P_{\max}$	Maximum load observed during a pullout test
P_r	Pullout resistance per unit width of reinforcement
q	Vertical traffic surcharge stress

NOTATION (Continued)

Q	Maximum compaction force produced during compaction
R	Resultant force due to eccentric loading on the reinforced mass
R_c	Reinforcement coverage ratio
R_f	Failure ratio
s	Shear strength
S	Equivalent height of uniform surcharge pressure
S_h	Horizontal reinforcement spacing
S_i	Reinforcement-soil stiffness index
S_{local}	Local reinforcement stiffness
S_r	Global reinforcement stiffness
S_v	Vertical reinforcement spacing
t_{90}	Time to 90 percent consolidation
T_a	Allowable reinforcement tension
$T_{\max}$	Maximum predicted tensile load
V_1	Resultant force produced by the reinforced soil mass
V_2	Resultant force produced by the back slope mass
z	Vertical distance from the reinforcement to the intersection of back slope and the plane defined by the back of the reinforced soil mass
Z	Vertical distance from the reinforcement to the top of the wall

NOTATION (Continued)

α	Unloading coefficient
α_{ks}	Fitting coefficient used for calculating Φ_g
β	Back slope angle
β_{ks}	Fitting coefficient used for calculating Φ_g
γ_d	Dry unit weight
γ_f	Unit weight of fill unreinforced fill material
γ_r	Unit weight of fill reinforced fill material
δ	Reinforcement displacement during pullout
ε_1	Axial Strain
ε_v	Volumetric strain
ν_o	Poisson's ratio corresponding to K_o loading
ν_{nu}	Poisson's ratio for unloading
ρ	Interface friction angle
σ_1	Major principal stress
σ_3	Minor principal stress
σ_e	Portion of deviator stress required for sample expansion
σ_h	Horizontal stress acting on back of wall facing
σ_n	Normal stress
σ_v	Vertical stress
σ'_z	Overburden stress
σ'_{zc}	Peak vertical stress during compaction
$\tau_{\max}$	Maximum shear stress
ϕ	Friction angle
ϕ_B	Bishop's Linearly reduced friction angle

NOTATION (Continued)

ϕ_d	Peak drained friction angle
ϕ_{DS}	Friction angle as measured by direct shear
ϕ_f	Rowe's hyperbolically reduced friction angle
ϕ_{PS}	Plane strain friction angle
ϕ_r	Residual or critical state friction angle
ϕ_R	Resistance factor for LRFD
ϕ_{TX}	Friction angle as measured in triaxial compression
ϕ_μ	Friction angle of sliding between two particles
Φ	Influence factor
Φ_{fb}	Facing batter factor
Φ_{fs}	Facing stiffness factor
Φ_g	Global stiffness factor
Φ_{local}	Local stiffness factor
$\psi_{\max}$	Maximum dilation angle
Ω_1	Reinforcement type coefficient
Ω_2	Global reinforcement stiffness Coefficient

DEDICATION

For Amy, my lovely and supportive wife.

1.0 INTRODUCTION

1.1 Statement of Problem

As densely populated metropolitan areas continue to grow, right-of-way available for public infrastructure development becomes constricted. These pressures from urban expansion have resulted in a dramatic increase in the number of retaining walls being constructed around the world. Of the various types of retaining wall technologies currently used, Mechanically Stabilized Earth (MSE) walls are often the most cost-effective and reliable option, with thousands of walls being built since their introduction over 40 years ago (Christopher et al. 1990a). Surprisingly, few well-documented case histories with detailed material testing, instrumentation programs, and construction observation of performance are available in the literature. Despite the small number of case histories, empirical design methods are used in place of more theoretically-based methods. As a result, current design methods for MSE walls result in a large amount of inaccuracy, especially when their empirical calibration limits are exceeded.

1.2 Purpose and Scope

This study focuses on the internal stability of ribbed steel strip MSE walls used with gravels and sand-gravel mixtures by assessing: (1) the stiffness, strength, and volumetric response of a sandy gravel fill, (2) the reinforcement-backfill interaction developed during reinforcement strip pullout, and (3) the accuracy of reinforcement load and pullout resistance prediction methods assuming various soil failure envelopes and pullout resistance models.

An extensive laboratory testing program was performed on sandy gravel backfill and steel reinforcement strips used in the construction of two very tall MSE Walls. The purpose of the laboratory testing program was to understand the constitutive behavior of the soil backfill and the soil-reinforcement interaction. Once measured, the constitutive parameters of the reinforcements were used, in conjunction with the measured reinforcement strain measurements in two very tall MSE walls, to estimate the actual

reinforcement loads being generated within the walls. These inferred reinforcement loads were then compared to the estimates of load from reinforcement load prediction models in order to assess the accuracy of these methods.

The pullout resistance of single reinforcement strips was evaluated using a newly constructed pullout test apparatus. Twenty pullout tests were performed on ribbed steel reinforcement strips embedded within sandy gravel to characterize the soil-reinforcement interaction behavior. The effect of the relative compaction and vertical effective stress acting on the reinforcement strip was assessed using multiple linear regression modeling. A backfill-specific pullout resistance design model was generated for use in predicting pullout capacities of ribbed steel reinforcement strips in the backfill evaluated. The pullout test results were then combined with data from other pullout tests results on gravels and sand-gravel mixtures found in the literature in order to create a global gravel pullout resistance model. The backfill-specific, global gravel, and standard pullout resistance models were used to assess the effect of model on pullout length calculations.

Following a literature review on granular soil mechanics and internal stability of MSE walls (Chapter 2), and description of the research objectives and program (Chapter 3), the laboratory evaluation of the backfill and reinforcement (Chapter 4), the pullout testing (Chapter 5), and the application of the experimental work towards the evaluation of internal stability is presented (Chapter 6). This thesis concludes with a summary of work performed, findings, and suggestions for future study (Chapter 7).

2.0 LITERATURE REVIEW

The concept of modern Mechanically Stabilized Earth (MSE) walls with was first developed by Vidal (1969) and used steel reinforcements. Since Vidal's initial work, which began over 50 years ago, the understanding of the behavior and design of MSE walls has grown extensively. As with many geotechnical design procedures, MSE wall design is based on empirical performance observations in consideration of soil mechanics principles.

An understanding of the history and development of design procedures for MSE walls is necessary to identify those areas where improvements can be made. However, to gain a deeper understanding of the basic mechanics governing the behavior of MSE walls, a firm understanding of the soil mechanics principles at work is needed. MSE walls built with steel strip reinforcements rely significantly on frictional resistance and therefore are almost always designed using granular reinforced backfill. Therefore soil mechanics principles relevant to granular soil-reinforcement interaction will be reviewed in Section 2.1, and general MSE wall design procedures will be covered in Section 2.2.

2.1 Behavior of Drained Granular Materials

The response of drained granular soils varies based on factors that include relative density, confining stress, gradation, angularity, surface roughness and boundary conditions, among others (Rowe 1962; Lee and Seed 1967; Cornforth 1973; Verdugo and Hoz 2007; Bareither et al. 2008; Hashash et al. 2009). The effects of relative density and confining stress are particularly important in the development of reinforcement loads and resistance, and therefore will be the focus of this Section.

2.1.1 Mohr-Coulomb Failure Criterion

The stresses on any plane within an element can be represented by a Mohr circle in stress-stress space as shown in Figure 2.1. The points at which the Mohr circle crosses the normal stress axis represent planes of zero shear stress and are termed principal stresses. For the purpose of discussion it is convenient, and common convention, to refer to these stresses as the major principal stress, σ_1, the intermediate principal stress, σ_2, and

the minor principal stress, σ_3, where $\sigma_1 \geq \sigma_2 \geq \sigma_3$. MSE walls are most typically constructed in long, linear geometries such that plane strain conditions exist and where $\sigma_2 > \sigma_3$, as shown in Figure 2.1.

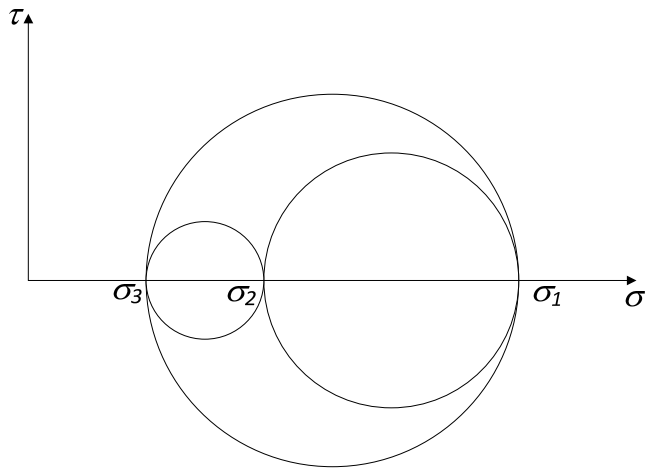

Figure 2.1. Mohr circle diagram in three dimensions.

The shear strength, s, of a soil mass can be defined by the Mohr-Coulomb failure criterion (Rowe 1962):

$$s = c + \sigma \tan \phi \qquad (2.1)$$

where σ_{ff} is the normal stress on the failure plane at failure, ϕ is the friction angle, and c is the apparent cohesion intercept associated with capillarity, and is typically neglected for granular materials because strength associated with seasonal moisture variations cannot be relied upon.

Assuming equal shear resistance on any plane within a soil mass, the Mohr-Coulomb failure criterion can be defined as the shear stress where the Mohr circle becomes tangent to the failure envelope defined by Equation 2.1. Figure 2.2 depicts the failure criterion for the triaxial condition where $\sigma_2 = \sigma_3$.

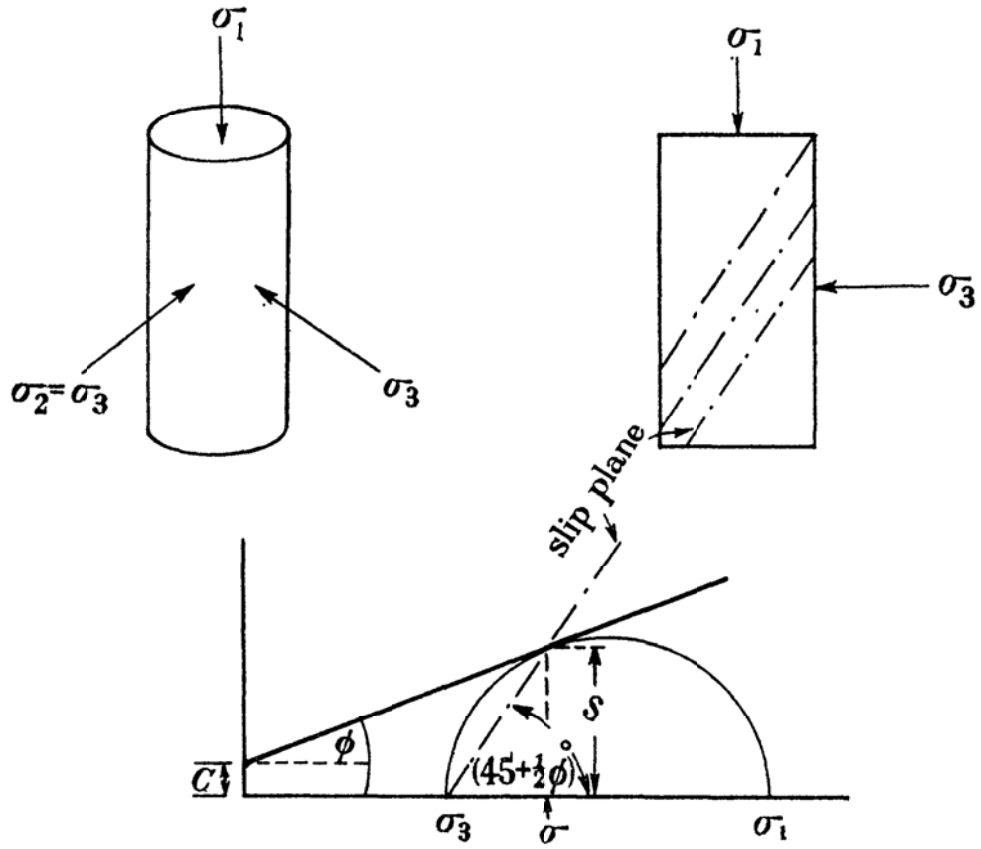

Figure 2.2. Mohr-Coulomb failure criterion for the triaxial condition (after Rowe 1962).

Since granular soils are assumed to have no apparent cohesion the strength is strictly defined by the friction angle, ϕ. The consequences of this definition will be explored further in the proceeding sections.

2.1.2 Effect of Relative Density on Response of Granular Materials

Early studies of the shear behavior of granular soils indicated that denser sands tended to increase in volume and looser sands tended to decrease in volume during shearing (Reynolds 1885; Casagrande 1938, 1940). Casagrande (1938) postulated the idea of a critical state void ratio, developed further by Casagrande (1940), where the influence of relative density on the peak friction angle was demonstrated. Casagrande (1940) described the observed response of the sand (Figure 2.3) as follows:

- Samples with initial void ratios less than the critical state void ratio tended to dilate during shearing, a peak friction angle, ϕ_d, was reached, then the shear strength reduced to a residual value where a critical state friction angle, ϕ_r, was observed.
- Samples with initial void ratios larger than the critical state void ratio (looser specimens) tended to contract, and the shear strength would slowly increase, without reaching a peak, to a residual or critical state value of ϕ_r, similar to dense specimens.
- Samples with initial void ratios equal to the critical state void ratio did not change in volume during shearing.

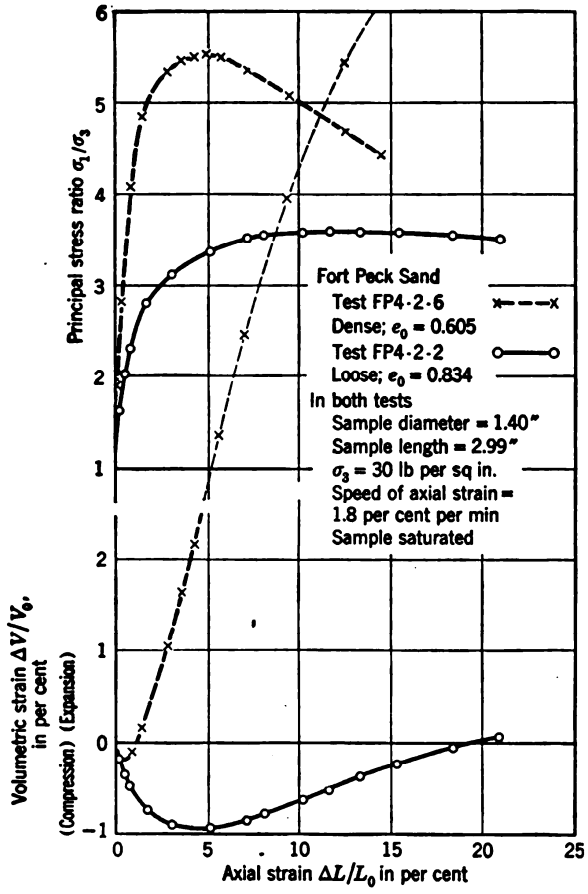

Figure 2.3. Stress-strain and volumetric response for both loose and dense sand in triaxial compression (after Taylor 1948).

Taylor (1948) and Bishop (1954) attempted to explain the observations of Casagrande (1940) by suggesting that the observed shearing resistance was not entirely due to inter-granular sliding friction, but included a volume change component. The volume change component, as described by Bishop (1954), was quantified as the energy needed to overcome the confining pressure during expansion. Bishop proposed that the portion of the deviator stress required to produce the energy for sample expansion, σ_e, could be calculated as:

$$\sigma_e = \sigma_3 \frac{d\varepsilon_v}{d\varepsilon_1} \tag{2.2}$$

where $d\varepsilon_v$ is the incremental change in volumetric strain, and $d\varepsilon_1$ is the incremental increase in axial strain. Bishop (1954) derived the following expression for the friction angle with the dilation-induced portion removed, ϕ_B:

$$\phi_B = \sin^{-1}\left[\frac{(\sigma_1 - \sigma_e) - \sigma_3}{(\sigma_1 - \sigma_e) + \sigma_3}\right] \tag{2.3}$$

which implies that the difference between ϕ_B and the peak friction angle, ϕ_d, is equivalent to equivalent to the dilation angle.

Rowe (1962) performed direct shear tests, shown in Figure 2.4, on quartz soil particles with the bottom half of the shear box replaced with a quartz block. This enabled Rowe (1962) to approximate the sliding friction between two particles, ϕ_μ. Rowe observed that the friction angle calculated using Bishop's expression to correct for dilation effects (Equation 2.3) was greater than the sliding friction, ϕ_μ, measured. This led Rowe to the conclusion that the peak friction angle, ϕ_d, is comprised of three components; the particle-to-particle sliding friction, a dilatant component, and a component related to the work performed by the soil particles as they rearrange and

reorient. Rowe (1962) developed the following expression to determine the friction angle with the dilation effects removed, ϕ_f:

$$\phi_f = 2\left(\tan^{-1}\sqrt{\frac{\sigma_1}{\sigma_3\left(1+\frac{d\varepsilon_v}{d\varepsilon_1}\right)}} - 45 \right) \qquad (2.4)$$

As implied by Rowe (1962), the difference between ϕ_d and ϕ_f is the dilation angle, ψ, as illustrated in Figure 2.5.

The difference between ϕ_f and ϕ_μ is attributed to reorientation effects, and is described graphically in Figure 2.6. At high void ratios (i.e., high initial porosities), the peak friction angle, ϕ_d, consists of sliding and particle re-orientation effects, as the void ratio decreases, the dilation component increases at a rate greater than the decrease in re-orientation, resulting in a net increase in total or peak friction angle.

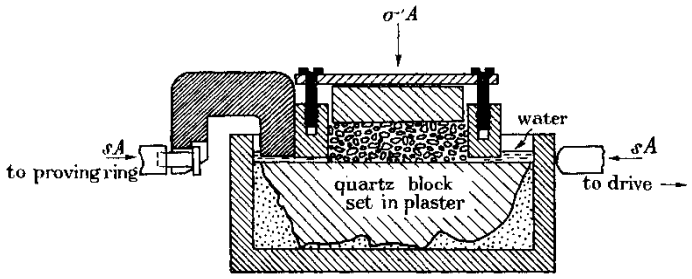

Figure 2.4. Standard shear box modified to record particle friction (after Rowe 1962).

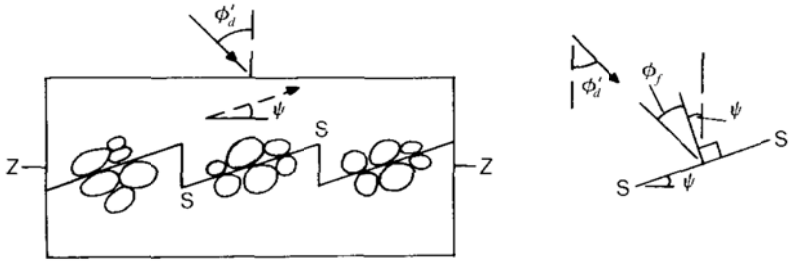

Figure 2.5. Saw tooth model for dilatancy (adapted from Bolton 1986).

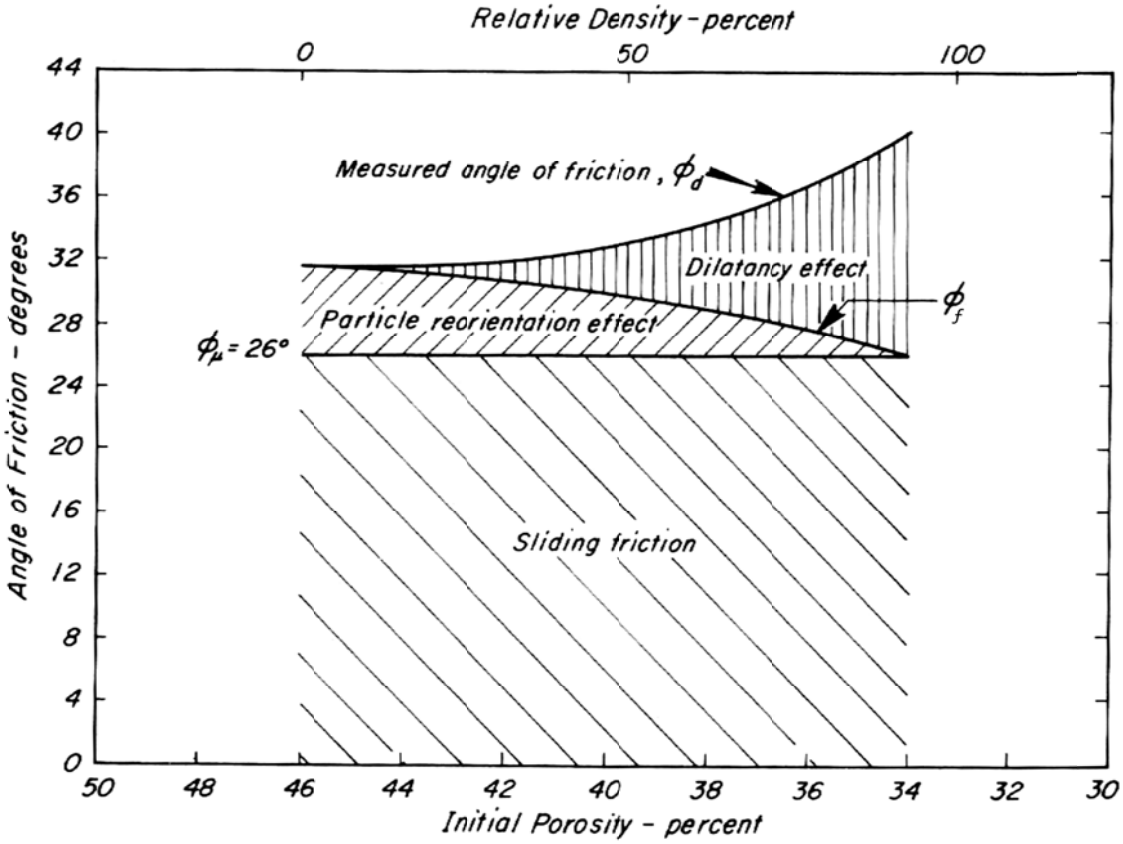

Figure 2.6. Components of friction angle at different relative densities as hypothesized by Rowe (1962) (adapted from (Lee and Seed 1967).

2.1.3 Effects of Confining Pressure on Shear Strength

The work discussed to this point was performed at relatively low confining pressures. In the mid-1950's through the 1960's there was increased interest in the measurement of the response of granular soils at high confining pressures (Golder and Akroyd 1954; Hall and Gordon 1963; Hirschfeld and Poulos 1963; Vesiĉ and Barksdale 1963; Lee and Seed 1967; Vesiĉ and Clough 1968). These studies produced similar findings: at low confining pressures the Mohr-Coulomb failure envelope was steepest, then, with relatively small increases in confining pressure, peak friction angles reduced to a relatively constant value. Figure 2.7 presents strength test results by Hirschfeld and Poulos (1963) that shows the failure envelope curved at confining pressures exceeding approximately 20 kg/cm^2 (1.96 MPa); note that this figure does not show tests conducted at lower confining

pressures and therefore the initial curvature of the Mohr-Coulomb envelope cannot be seen.

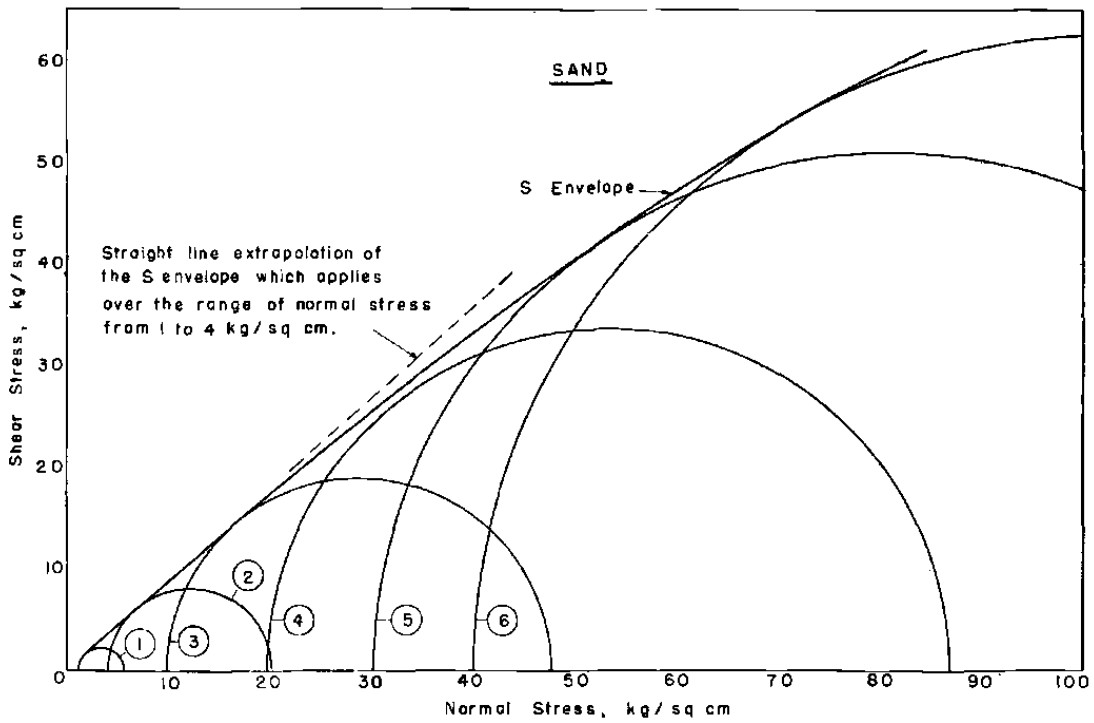

Figure 2.7. Mohr circles at failure showing the curvature of the failure envelope at high pressures (Hirschfeld and Poulos 1963). Note: 1 kg / sq cm = 98 kPa.

The reduction in friction angle at moderate confining pressures was mainly attributed to the suppression of dilation; as the confining pressure increased, soil particles tended to reorient and contract rather than dilate. At extremely large confining pressures, the stresses induced in the soil particles exceed their compressive strength, and particles tended to break apart and fill voids. This crushing behavior resulted in densification and changes in particle characteristics such as surface roughness and angularity which can have complex effects on the Mohr-Coulomb failure envelope. These crushing effects are not discussed herein, because, even at the base of the tallest MSE walls, the compressive strengths of most reinforced backfill particles are not reached.

Figure 2.8, exaggerated for clarity, presents the theoretical influence of dilation, sliding friction, particle crushing, and particle rearrangement on the drained shear

strength of sand (Lee and Seed 1967). The consequence of extrapolation of test data from low confining pressures is apparent; using low confining stresses to estimate ϕ_d for high confining stresses results in non-conservative estimates of ϕ.

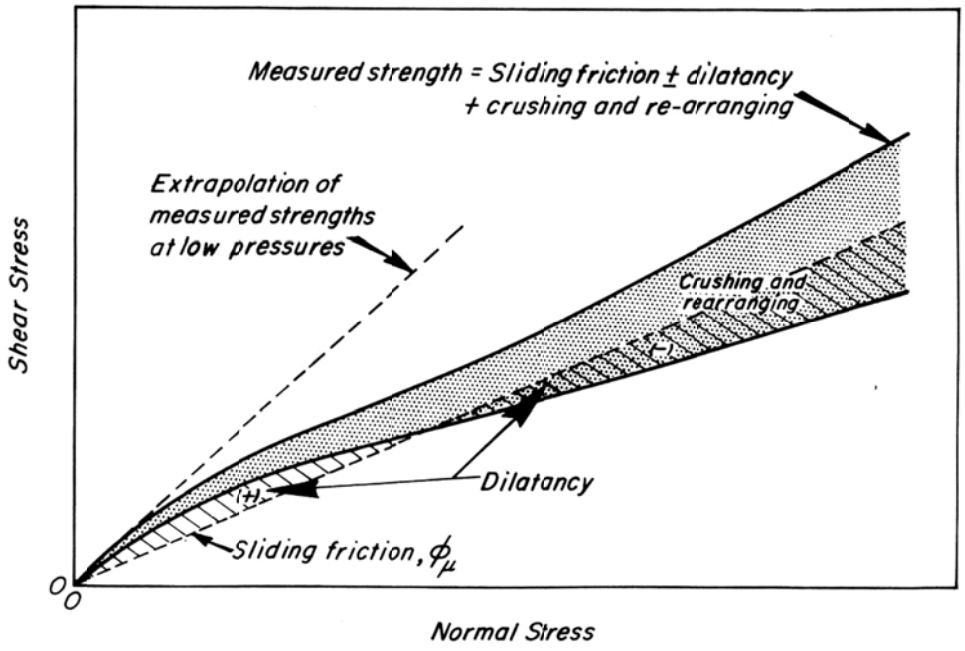

Figure 2.8. Effects of sliding friction, dilatancy and particle crushing on the measured failure envelope for drained sands as theorized by Lee and Seed (1967).

2.1.4 Stiffness of Granular Materials

For accurate predictions of deformation in geotechnical engineering applications, it is necessary to consider the nonlinear and stress-dependent response exhibited by soils. For simplicity, a soil is often assumed to follow a linear elastic-perfectly plastic stress-strain curve with a single elastic modulus and Poisson's ratio. Figure 2.3 shows that granular materials are neither linear, nor elastic; in other words, none of the above assumptions hold for a given soil over any significant range of strains.

For soils, the equivalent Young's modulus changes continuously with strain. The modulus at any strain can be determined using incremental stress analysis to determine the tangent modulus, E_t, as (Duncan and Chang 1970):

$$E_t = \frac{\partial(\sigma_1 - \sigma_3)}{\partial \varepsilon_1} \tag{2.5}$$

A typical measure of soil stiffness is the initial tangent modulus, E_i. As shown in Figure 2.9 E_i increases both with relative density, and confining pressure.

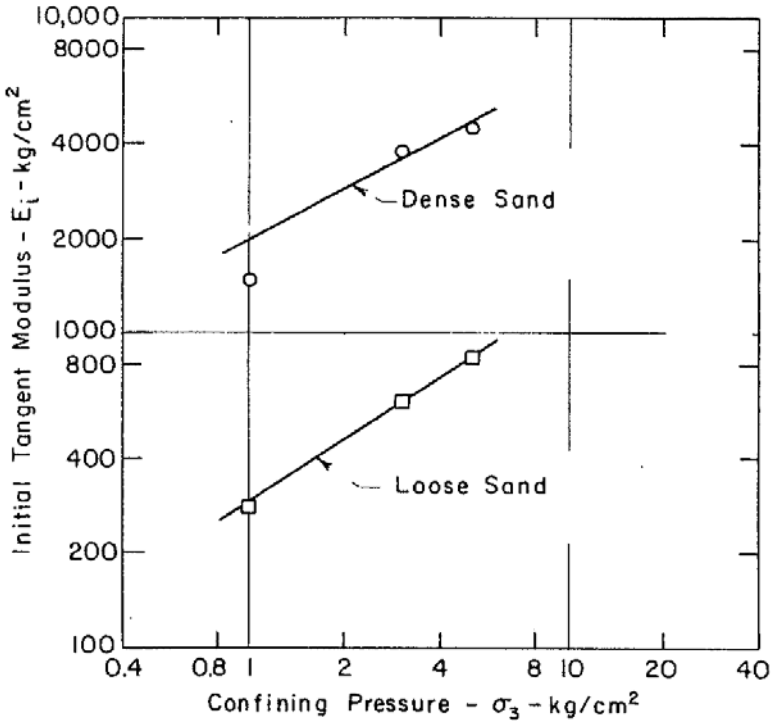

Figure 2.9. Variations of initial tangent modulus with confining pressure and initial relative density for drained triaxial tests on silica sand (after Duncan and Chang 1970).

2.1.5 Constitutive Modeling of Stress–Strain and Volumetric Response of Granular Materials

One of the most widely used nonlinear constitutive models for soils was developed by Duncan and Chang (1970). Some of the advantages of the Duncan and Chang (1970) model over other nonlinear models includes the ability to measure parameters using the ordinary triaxial test, the ability to model the contractive response of soils incorporated

by Wong and Duncan (1974), and the availability of the database of parameters for over 150 types of soils including index properties provided in Duncan et al. (1980). The following is a summary of the Duncan et al. (1980) calibration procedure:

For a given drained triaxial test at a confining pressure of σ_3, the volumetric strain at any point, $\varepsilon_{v,B}$, is determined, as well as the coinciding principal stress difference, $(\sigma_1 - \sigma_3)_B$ (i.e., at the same axial strain). From the principal stress difference-axial strain data, the following are determined: the principal stress difference at failure, $(\sigma_1 - \sigma_3)_f$ and the axial strains corresponding to 70 and 95 percent of the principal stress difference at failure, $\varepsilon_{1,70}$, and $\varepsilon_{1,95}$, respectively. The initial tangent modulus, E_i, is determined by:

$$E_i = \frac{2}{\frac{\varepsilon_{1,70}}{(\sigma_1 - \sigma_3)_{70}} + \frac{\varepsilon_{1,95}}{(\sigma_1 - \sigma_3)_{95}} - \left(\frac{1}{(\sigma_1 - \sigma_3)_{\text{ult}}}\right)(\varepsilon_{1,70} + \varepsilon_{1,95})} \qquad (2.6)$$

where $(\sigma_1 - \sigma_3)_{70}$ and $(\sigma_1 - \sigma_3)_{95}$ are 70 and 95 percent of the principal stress difference at failure, and $(\sigma_1 - \sigma_3)_{ult}$ is the ultimate principal stress difference defined by:

$$(\sigma_1 - \sigma_3)_{\text{ult}} = \frac{\varepsilon_{1,95} - \varepsilon_{1,70}}{\frac{\varepsilon_{1,95}}{(\sigma_1 - \sigma_3)_{95}} - \frac{\varepsilon_{1,70}}{(\sigma_1 - \sigma_3)_{70}}} \qquad (2.7)$$

The stiffness of soil when considering only volumetric strains (i.e., bulk modulus), B, is determined by:

$$B = \frac{(\sigma_1 - \sigma_3)_B}{3\varepsilon_{v,B}} \qquad (2.8)$$

Once the initial tangent and bulk moduli are determined for several confining pressures, the modulus number, K, and the modulus exponent, n, can be determined by fitting a curve to the initial tangent modulus-confining pressure data using the functional form of a power law:

$$E_i = K \cdot \sigma_3^{\,n} \tag{2.9}$$

The bulk modulus number K_B, and the bulk modulus exponent, m, can also be determined by fitting a power law curve to the bulk modulus-confining pressure data using:

$$B = K_B \cdot \sigma_3^{\,m} \tag{2.10}$$

Refer to Duncan et al. (1980) for a more comprehensive discussion of the model calibration procedure.

The main disadvantage of the Duncan and Chang (1970) model is that the volume change behavior of dilative soils cannot be adequately simulated. Figure 2.10 shows that the fitted hyperbolic model can simulate the initial contractive behavior of Monterey Sand, but does not model the reversal in volumetric response and subsequent dilation. Additionally, the Duncan and Chang model cannot capture the strain softening behavior of dense sands at low to medium confining pressures. However, in many design situations this strain softening behavior occurs well outside the expected working stress range (i.e., at large stresses) and therefore, may not need to be modeled.

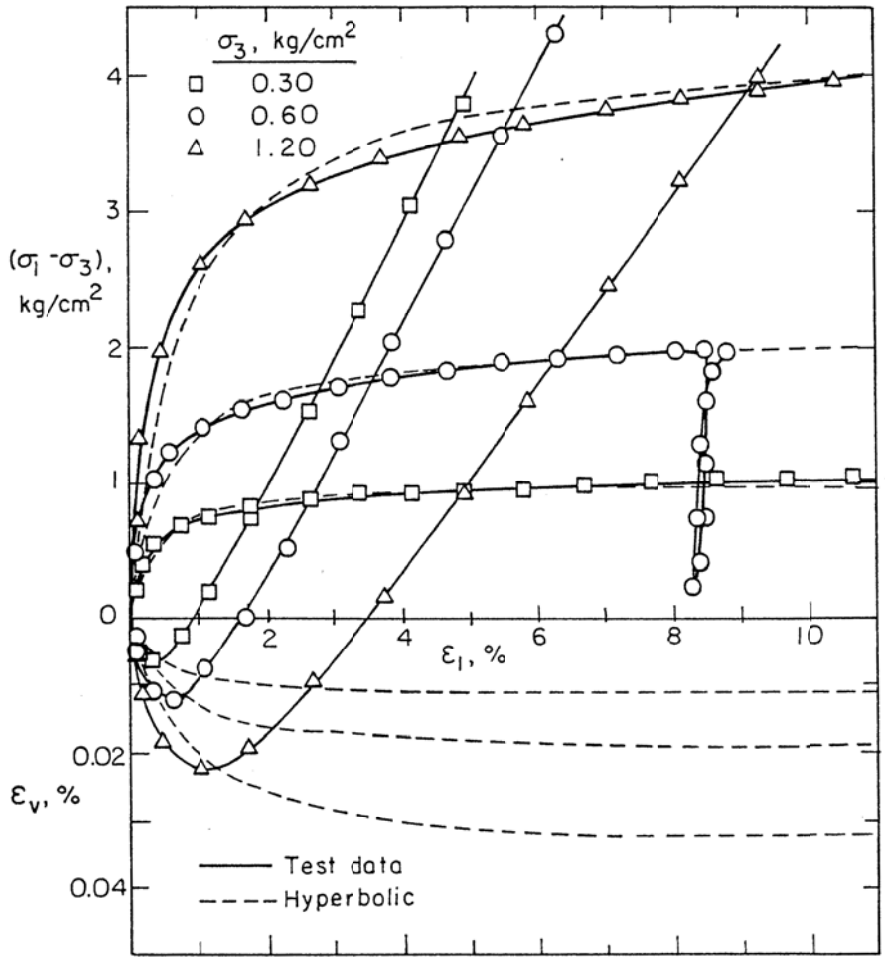

Figure 2.10. Comparison of hyperbolic fit for stress- strain and volume change data for Monterey No. 0 sand (Duncan et al. 1980).

More advanced nonlinear models exist such as the cap-yield (C-y) soil model developed for use in the computer software FLAC. Models such the Cysoil model address some of the problems with using the Duncan-Chang (1970) model. For example, the Cysoil model allows for strain softening, strain hardening, and dilation to be modeled. More sophisticated constitutive models will not be described herein as numerical models are not directly employed within this thesis.

2.2 Design of Mechanically Stabilized Earth Walls

In general, the reinforced soil mass within a MSE wall is subdivided into an active zone and resistant zone. The active zone is the zone closest to the wall facing and tends to move outward and downward away from the resistive zone. However, this movement is resisted by shear forces developed between the reinforcement and soil in the resistive zone as shown in Figure 2.11.

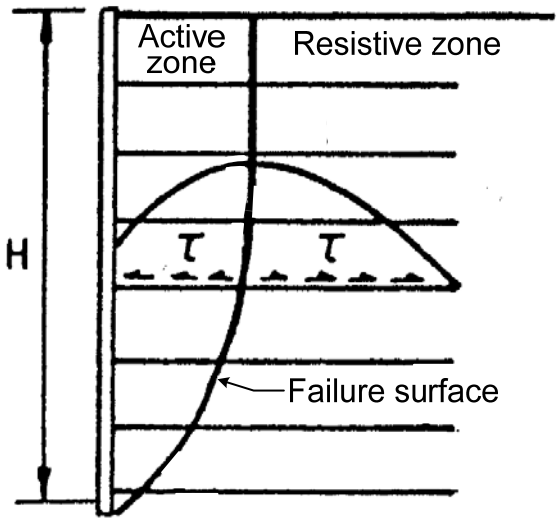

Figure 2.11. Development of shear forces between the backfill and reinforcement within an MSE wall (adapted from Schlosser 1990)

The main design goals for MSE walls include checks for external and internal stability. This section mainly focuses on internal stability as it is the main focus of this study. A complete overview of MSE wall design may be found in Christopher et al. (1990a), Elias et al. (2001), and Berg et al. (2009).

2.2.1 Design Methodology for Internal Stability

Internal instabilities may arise from three possible mechanisms: the shear resistance of the panel-reinforcement connection may be locally exceeded, the tensile stress in the reinforcement strip can exceed the yield stress, resulting in large plastic strains (and associated wall movement) and leading to the eventual rupture of the strip, or the tensile reinforcement forces will exceed the frictional pullout resistance provided to the

reinforcement by the soil, resulting in movement relative to the surrounding soil. The three mechanisms of internal instability can result in large deformations and/or collapse of the wall depending on the degree of wall redundancy.

Stability is determined by comparing the maximum predicted tensile load, T_{max}, to the allowable reinforcement tension, T_a, and the maximum pullout resistance of the reinforcement, P_r, at each reinforcement level. The following criteria must be met for the wall to be considered stable:

$$T_{\max} = \sigma_h A_t \tag{2.11}$$

$$T_{\max} \leq T_a \tag{2.12}$$

$$T_{\max} \leq P_r \tag{2.13}$$

where σ_h is the horizontal earth pressure, and A_t is the wall facing tributary area.

2.2.1.1 Internal Loading

Many design methods have been developed for predicting maximum reinforcement loads. The main differences between methods are the way in which the lateral earth pressure coefficient for the reinforced soil mass, K_r, is calculated, and the assumption on where the maximum tension is located behind the retaining wall. These methods include the Coherent Gravity method (Schlosser 1978), the Tieback Wedge method (Lee et al. 1973; Bell et al. 1975, 1983), the FHWA Structure Stiffness method (Christopher et al. 1990a; Christopher 1993), the working stress method by Ehrlich and Mitchell (1994), the American Association of State Highway Transportation Office (AASHTO) Simplified Method (Allen et al. 2001), and the K-Stiffness method (Allen et al. 2004). Stuedlein et al. (2012) provides a detailed discussion on the differences between many of these methods. Each of the design methods are summarized below.

Coherent Gravity Method (Schlosser 1978)

The maximum tensile reinforcement load is typically used to define the failure surface in the reinforced soil mass, though these are not usually coincident. Early methods of determining this failure surface, such as that by Lee et al. (1973), neglected the influence of the reinforcements on the failure surface and assumed a wedge failure surface that started at the toe of the wall that extends upward at an angle of $45 + \phi/2$ from the horizontal plane. Juran (1977) outlines the theoretical shortcoming of this Rankine-type failure plane. Using laboratory and full-scale testing, Juran and Schlosser (1978) concluded that the presence of inextensible reinforcements in an earth mass affects the failure surface, and that a log spiral-shaped failure surface starting at the toe of the wall and becoming vertical at ground surface would be more appropriate. Schlosser and Elias (1978) modified the work by Juran and Schlosser (1978) by approximating the log spiral surface as a bi-linear curve as shown in Figure 2.12.

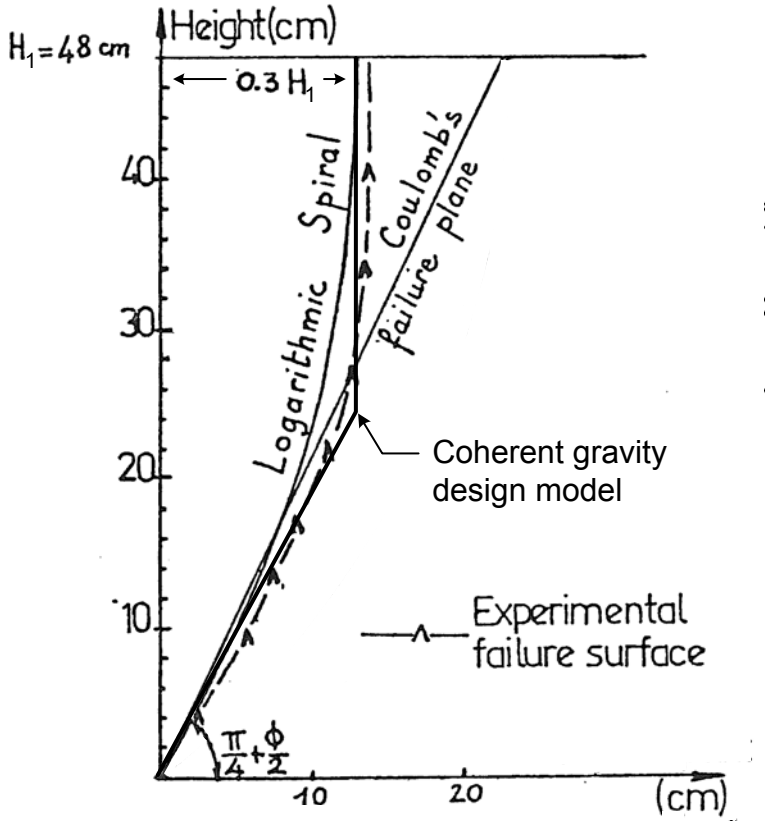

Figure 2.12. Results from scale model tests with theoretical logarithmic spiral failure surface, Coulomb's failure plane, and the coherent gravity design model (adapted from Juran and Schlosser 1978).

Loading in MSE walls is controlled by the earth pressures from the retained soil mass acting on the back of the wall and the influence of wall stiffness, described below. Baquelin (1978) suggested that the at-rest lateral earth pressure would dominate near the top of the wall, and then decrease with depth until the active state was reached at 6 meters below the top of the wall; this was referred to as the coherent gravity distribution. Figure 2.13 shows the design distribution for reinforced fill material with $\phi = 45$ deg. The lateral earth pressure coefficient decreased from an at-rest value, K_o, as defined by Jaky (1948), at the top of the wall:

$$K_o = 1 - \sin\phi \qquad (2.14)$$

then linearly decreased to an active value, K_a, as defined by Rankine (1857) at a depth of 6 ft:

$$K_a = \tan^2\left(45 - \frac{\phi}{2}\right) \qquad (2.15)$$

Note that as the friction angle increases, the value of K_0/K_a increases.

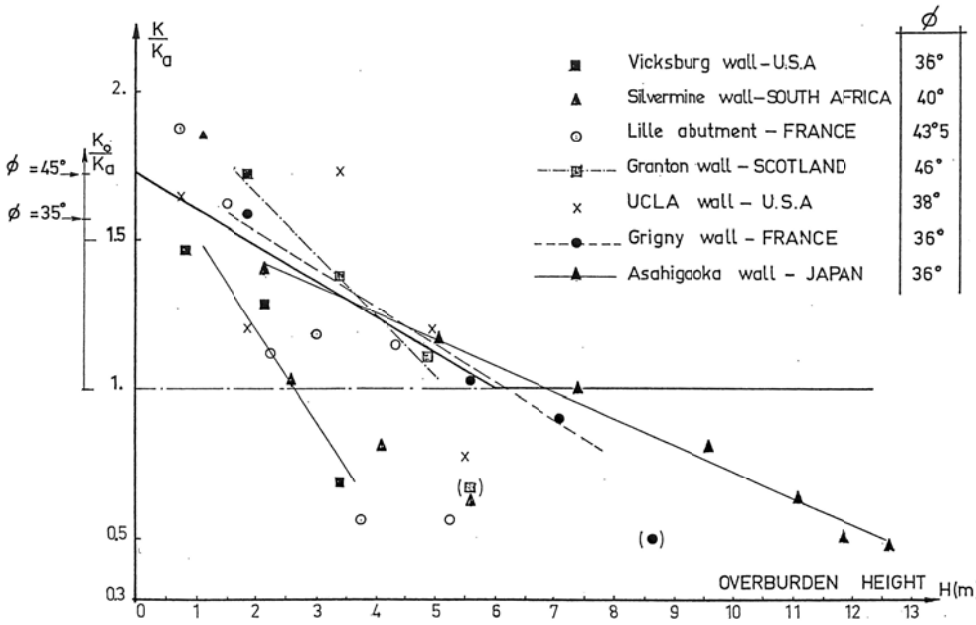

Figure 2.13. Depth below top of wall versus normalized lateral stress coefficient for the seven case studies used to calibrate the coherent gravity method and design distribution for ϕ = 45° (Baquelin 1978).

The use of the earth pressures calculated from Baquelin (1978) and the failure surface proposed by Schlosser and Elias (1978), is generally referred to as the Coherent Gravity method. Though Juran and Schlosser (1978) used limit equilibrium analysis to argue its validity, the Coherent Gravity method was originally calibrated empirically with the use of seven wall case histories as shown above in Figure 2.13. These case histories included both smooth and ribbed steel strip reinforcements but did not include extensible

reinforcements (e.g. geo-synthetic), or bar mat type in-extensible reinforcements (Schlosser 1978).

Schlosser and Segrestin (1979) summarized the Coherent Gravity method with assumed location of maximum tension (i.e., the bilinear failure surface) and the distribution of earth pressure coefficients. The maximum reinforcement load for a given reinforcement layer, T_{max}, was determined as:

$$T_{\max} = K_r \sigma_v S_v R_c \tag{2.16}$$

where σ_v is the vertical effective stress at the level of the reinforcement, S_v is the vertical reinforcement spacing and R_c is the reinforcement coverage ratio defined as:

$$R_c = \frac{b}{S_h} \tag{2.17}$$

where b is the width of the strip, and S_h is the horizontal reinforcement spacing as shown in Figure 2.14.

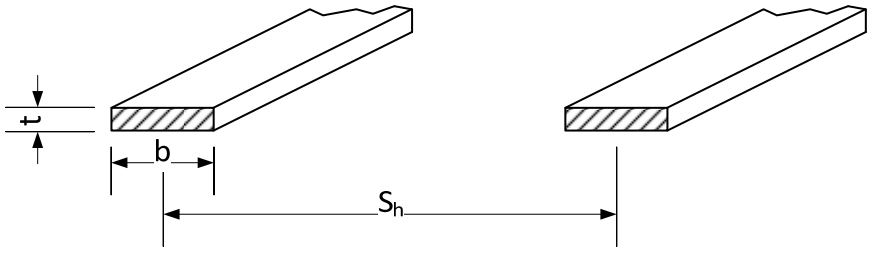

Figure 2.14. Parameters for coverage ratio, R_c, calculation with steel strip reinforcements.

The vertical effective stress at the level of the reinforcement of interest, σ_v, was determined by assuming the reinforced fill to be a rigid block (Schlosser and Segrestin 1979); then, the equations of static equilibrium were used to calculate vertical stresses.

For the case of level backfill (i.e. a slope angle, β, equal to zero), the vertical effective stress is calculated as:

$$\sigma_v = \gamma_r Z \tag{2.18}$$

where γ_r is the unit weight of the reinforced fill, and Z is the vertical distance from the top of the wall to the reinforcement layer of interest. However, when the back slope angle is greater than zero, as shown in Figure 2.15, the resultant of the reaction stress distribution (i.e., R in Figure 2.15) is assumed to become eccentrically located a distance e from the center of the reinforcement towards the wall. This assumed eccentricity can be determined algebraically by setting the sum of the moments about the center of bottom of the "rigid block" (i.e. point c in Figure 2.15) equal to zero. Solving for the moment arm of the reaction force, e, produces the following expression:

$$e = \frac{F_T(\cos\beta)z/3 - F_T(\sin\beta)L_r/2 - V_2(L_r/6)}{V_1 + V_2 + F_T\sin(\beta)} \tag{2.19}$$

where F_T is the resultant force of the lateral earth pressure acting on the back of the reinforced soil mass, z is the vertical distance from the reinforcement layer of interest to the intersection of the back slope and the plane defined by the back of the reinforced soil mass, L_r is the total length of the reinforcement, V_1 is the resultant of the pressure from the reinforced soil mass acting on the reinforcement layer of interest, V_2 is the resultant force produced by the weight of the slope mass acting vertically at the top of the reinforced soil mass. The vertical stress acting on the reinforcement is then calculated as the sum of the vertical forces acting over the reinforcement length less two times the eccentricity:

$$\sigma_v = \frac{V_1 + V_2 + F_T\sin(\beta)}{L_r - 2e} \tag{2.20}$$

where e is the eccentricity of the reaction force, and K_r is the lateral earth pressure coefficient of the reinforced soil at the depth of the reinforcement of interest as described in Figure 2.16.

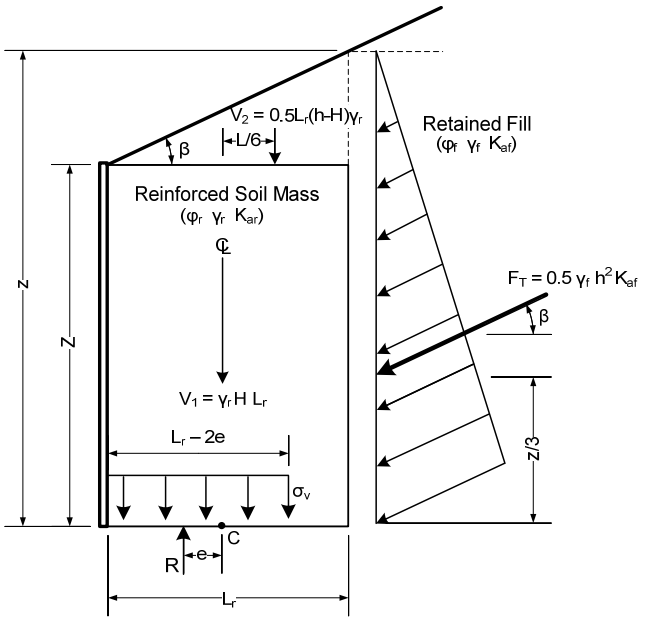

Figure 2.15. Meyerhof vertical stress distribution in MSE walls (adapted from Allen et al. 2001 and AASHTO 1999).

The Coherent Gravity method assumes a bi-linear failure surface, as shown in Figure 2.16. The failure surface, and thus the active zone, was defined by the vertical distance from the toe of the wall to the point where the failure surface exists the back slope, H', calculated as:

$$H' = H + \frac{0.3H \tan\beta}{1 - 0.3\tan\beta} \qquad (2.21)$$

where H is the vertical distance from the toe of the wall to the top of the wall face. The horizontal distance from the wall face to the point where the failure surface exists the back slope is assumed to be 0.3 H'. For the top half of the length H' the failure surface is

vertical, then, as shown in Figure 2.16, the failure surface exits the reinforced soil mass at the toe of the wall.

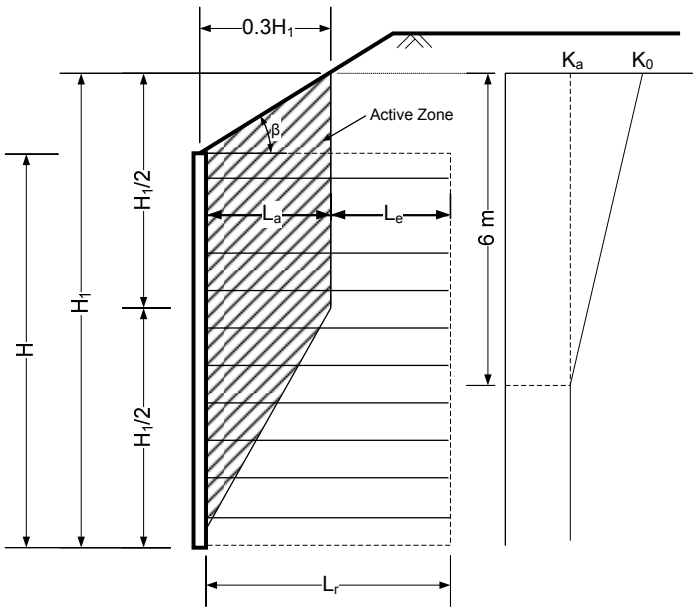

Figure 2.16. Graphic summary of the geometry assumed for use with the Coherent Gravity Method (adapted from Allen et al. 2001 and AASHTO 1996).

Bathurst et al. (2008) evaluated the accuracy of the Coherent Gravity method by comparing the ratio of measured to predicted maximum reinforcement load for walls with different backfill friction angles. For backfill soils with friction angles larger than 45 degrees, the Coherent Gravity method consistently under predicted the maximum reinforcement load as shown in Figure 2.17. This raises concern as it is common practice in design to reduce the friction angle in order to increase the reliability of the structure. However, reducing the friction angle can have non-conservative effect due to "locking-in" of compaction stresses near the top of the wall tending to be larger for soils with higher friction angles (Bathurst et al. 2008).

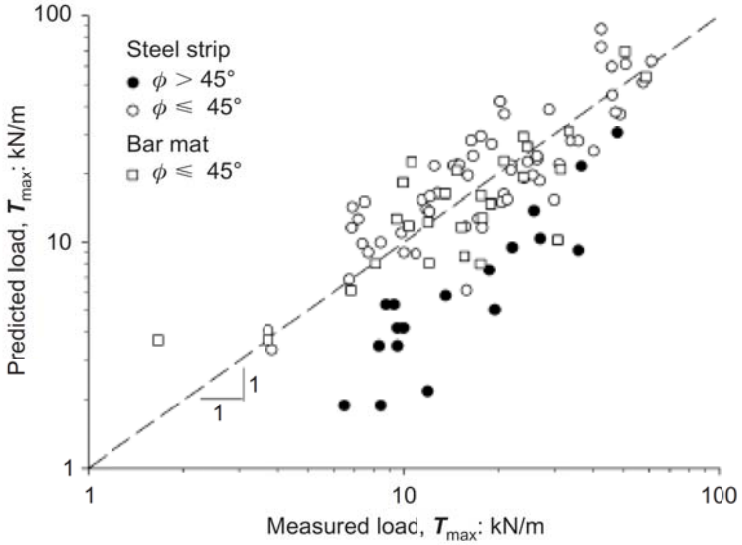

Figure 2.17. Predicted versus measured maximum reinforcement loads for the Coherent Gravity method and steel reinforced MSE walls showing the influence of friction angle (after Bathurst et al. 2008).

Since the Coherent Gravity method is empirically based, it is limited by the database of case histories to which it has been calibrated. The maximum wall height in the database used to calibrate the Coherent Gravity method was 13 m; therefore the use of the method should be limited to wall heights of 13 m or less (Stuedlein et al. 2012).

Tieback Wedge Method (Bell et al. 1983)

Originally developed by Bell et al. (1975) and Steward et al. (1977), the Tieback Wedge method was intended for use with geotextile and other extensible type reinforcing inclusions. The method was later adapted for use with welded wire reinforcements (Allen et al. 2001).

The primary difference between the Tieback and the Coherent Gravity methods is the assumed distribution of lateral earth pressure. For the Tieback Wedge method, the use of K_a was permitted along the entire back face of the wall due to the flexibility of the reinforced soil mass; this flexibility allowed minimum active pressure to be mobilized and a failure plane to develop. Walls reinforced with inextensible reinforcements are

significantly stiffer, and it was proven that the displacements were minimized and the full development of an active wedge was not realized (Bell et al. 1983).

The maximum reinforcement tensile load for the Tieback Wedge method is determined using Equation 2.16, where $K_r = K_a$ for all values of Z, and the vertical overburden stress calculated as:

$$\sigma_v = \left(\gamma_r Z + S + \mathrm{q}\right) \tag{2.22}$$

where S is the average surcharge from the soil above the wall (if any), q is the vertical traffic surcharge stress, and all other variables have been defined (Allen et al. 2001).

FHWA Structure Stiffness Method (Christopher et al. 1990a; Christopher 1993)

The Federal Highway Administration (FHWA) Structure Stiffness method was developed from an extensive effort by the FHWA to research and standardize the design of reinforced earth. The Structure Stiffness method was the first method to directly consider the combined effect of reinforcement spacing (i.e., reinforcement density) and the reinforcement stiffness referred to as the global reinforcement stiffness, S_r, and its effect on reinforcement stresses:

$$S_r = \frac{E_r A_r}{\left(H / n_r\right)} \tag{2.23}$$

where E_r and A_r is the reinforcement modulus and the reinforcement area per unit width of wall, respectively, and n_r is the number of reinforcement layers. Christopher et al. (1990a) studied the behavior of eight 6 m tall instrumented walls with different facings, reinforcements, fill material, and geometries. The study of wall behavior lead to a design method that is applicable for both extensible and inextensible reinforcements.

The location of the failure plane is determined using Figure 2.16, similar to the Coherent Gravity method. The maximum reinforcement tension, T_{max}, is determined

using Equation 2.16, with the vertical overburden stress, σ_v, calculated using Equation 2.22, and K_r calculated as:

$$K_r = \begin{cases} K_a\left(\Omega_1\left(1+0.4\dfrac{S_r}{47880}\right)\left(1-\dfrac{Z}{6}\right)+\Omega_2\dfrac{Z}{6}\right) & \text{if } Z \le 6 \text{ m} \\ K_a\Omega_2 & \text{if } Z > 6 \text{ m} \end{cases} \qquad (2.24)$$

where S_r is in units of kPa and Ω_1 is an empirical fitting coefficient related to the reinforcement type defined as:

$$\Omega_1 = \begin{cases} 1.0 & \text{for strip and sheet reinforcements} \\ 1.5 & \text{for grids and welded wire mats} \end{cases} \qquad (2.25)$$

and Ω_2 is an empirical fitting coefficient related to the global reinforcement stiffness and defined as:

$$\Omega_2 = \begin{cases} 1.0 & \text{if } S_r \le 47.88 \text{ MPa} \\ \Omega_1 & \text{if } S_r > 47.88 \text{ MPa} \end{cases} \qquad (2.26)$$

Ehrlich and Mitchell (1994)

Compaction-induced stresses should always be considered in fill-type walls. Compaction-induced stresses are especially important for the design of MSE walls as facing panels and reinforcement connections are extremely stiff, and develop stress concentrations at the connections. The method developed by Ehrlich and Mitchell (1994) is the only method developed to-date that addressed both compaction-induced reinforcement stresses and global reinforcement stiffness directly. The maximum reinforcement load for the Ehrlich and Mitchell (1994) method was calculated using plane strain soil properties as:

$$T_{max} = S_v S_h K_r \sigma'_z \tag{2.27}$$

where σ'_z is the overburden stress corrected for eccentric loading and for case of no surcharge loading is defined as:

$$\sigma'_z = \frac{\gamma' Z}{1-\left(K_a/3\right)\left(Z/L_r\right)^2} \tag{2.28}$$

where L_r is the length of the reinforcement. When comparing the overburden stresses for level ground calculated using Equation 2.28 to those using the Coherent Gravity method, the overburden stresses calculated using the Coherent Gravity method are slightly larger (7 percent greater at Z = 25 m), but appears suitable for substitution due to the relatively small difference in stresses. Ehrlich and Mitchell (1994) do not provide guidance on overburden stress calculations for the case of a back slope or surcharge. However, Equation 2.20 from the Coherent Gravity method can be used in calculating the overburden stress for these cases as it also considers overturning moment.

The lateral earth pressure coefficient, K_r, is determined for each reinforcing layer iteratively using:

$$\frac{1}{S_i}\left(\frac{\sigma'_z}{P_{atm}}\right)^n = \frac{\left(1-\nu_{un}^2\right)\left[\left(K_r - K_{\Delta 2}\right) - \left(K_c - K_{\Delta 2}\right)\mathrm{OCR}\right]}{\left(k_{ur}/K\right)\left(K_c \mathrm{OCR} - K_r\right)K_r^n} \tag{2.29}$$

where P_{atm} is atmospheric pressure, OCR = the overconsolidation ratio, k_{ur} is the modulus number for unloading, K is the modulus number for loading, and n is the modulus exponent, described previously in regard to the Duncan Chang (1970) hyperbolic model. The variables k_{ur}, K, and n can be found in Duncan et al. (1980) for various soils if soil-specific test information is unavalible. The relative reinforcement-soil stiffness index, S_i, was defined as:

$$S_i = \frac{\left(E_r A_r\right)}{kP_{atm} S_v S_h} \tag{2.30}$$

where the peak vertical stress during compaction, σ'_{ZC}, was defined as:

$$\sigma'_{zc} = \frac{\nu_o \left(1 - K_a\right) \sqrt{\frac{\gamma' Q N_\gamma}{2L}}}{K_o} \tag{2.31}$$

where Q is the maximum compaction force produced during compaction, L is the length of the roller used to compact the back fill, and N_γ is the bearing capacity factor for Rankine wedge theory. The Poisson's ratio corresponding to K_0 loading, ν_0, was defined as:

$$\nu_o = \frac{K_o}{1 + K_o} \tag{2.32}$$

Poisson's ratio for unloading, ν_{un}, was given as:

$$\nu_{un} = \frac{K_{\Delta 2}}{1 + K_{\Delta 2}} \tag{2.33}$$

where $K_{\Delta 2}$ is the "decremental lateral earth pressure coefficient" and defined as:

$$K_{\Delta 2} = \frac{K_o \left(OCR - OCR^{\alpha}\right)}{OCR - 1} \tag{2.34}$$

and the unloading coefficient, $\alpha = 0.7\ sin(\phi'_{PS})$.

The lateral earth pressure coefficient considering compaction, K_c, must be determined iteratively using:

$$\frac{1}{S_i}\left(\frac{\sigma'_{zc}}{P_{atm}}\right)^n = \frac{\left(1-\nu_o^2\right)\left(1-K_{aa}\right)^2\left(K_o-K_c\right)\mathrm{K}_o}{\left(K_c-K_{aa}\right)\left(K_o-K_{aa}\right)K_c^n} \tag{2.35}$$

where the "equivalent active earth pressure coefficient", K_{aa} was defined as:

$$K_{aa} = \frac{K_a}{\dfrac{\left(1-K_a\right)\left(\dfrac{c'}{\left(\sigma'_{zc}K_c\tan\phi'\right)}+1\right)}{R_f}+K_a} \tag{2.36}$$

where c' is the effective cohesion intercept, and R_f is the failure ratio as defined by Duncan et al. (1980).

The main advantage of the Ehrlich and Mitchell (1994) method is its ability to predict maximum reinforcement tension during construction. The Coherent Gravity method typical does fairly well estimating the reinforcement tension for the case of end of construction; however, for intermediate construction stages the measured tension loads are typically larger than those at the end of construction (Stuedlein et al. 2012). Figure 2.18 compares measured maximum tension to those predicted using the Coherent Gravity, and Ehrlich and Mitchell (1994) methods.

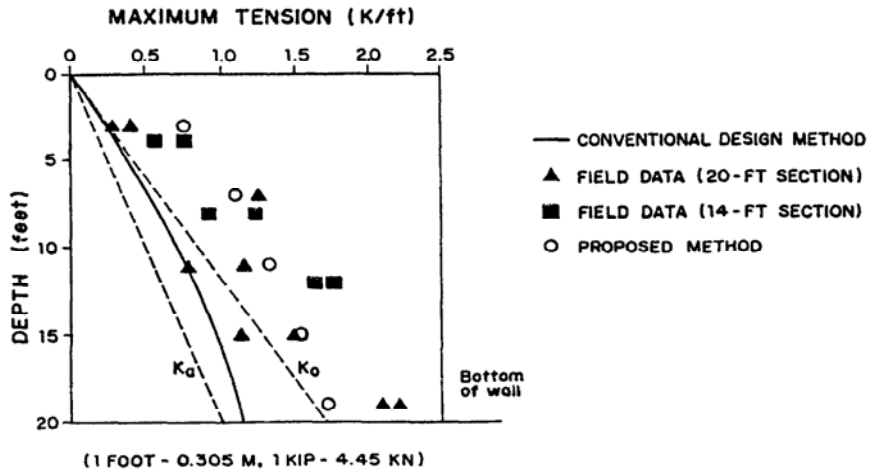

Figure 2.18. Comparison of the Ehrlich and Mitchell (1994) method (proposed method) to the Coherent Gravity method (conventional design method) and field measurements at the VSL wall at Hayward (after Neely 1995).

Because the Ehrlich and Mitchel (1994) method requires that the compaction equipment to be used during construction be known or estimated with some degree of certitude, it may be impractical to use this method in typical design situations. However, the Ehrlich and Mitchell (1994) method it is an extremely valuable tool for the analysis of wall behavior due its theoretical robustness and accuracy (Stuedlein et al. 2012).

AASHTO Simplified method(Allen et al. 2001)

The most common method for estimating reinforcement loads in the U.S. is the AASHTO Simplified method (Bathurst et al. 2009). The Simplified method was developed with the goal of replacing the Coherent Gravity method, the Tieback Wedge method, and the FHWA Structure Stiffness method; however, the Coherent Gravity method is still widely used for design of walls with steel strip reinforcements and has recently been admitted back into AASHTO specifications. The three main goals for developing the Simplified method were (Allen et al. 2001):

- to develop a K_r/K_a curve for each general type of reinforcement as shown in Figure 2.19,
- to simplify calculations by excluding the rigid body assumption and associated overturning-induced stresses for internal stability calculations, and
- To calibrate the method using a large dataset of full scale wall case histories.

The use of K_r/K_a curves unique to the reinforcement type indirectly allows for the consideration of the stiffness of the reinforced soil mass and some compaction stress history effects. However, the density of reinforcements is not taken into consideration, that is, as S_v and S_h change, the K_r/K_a curves remain constant, despite the potential for an increase or decrease in the "locking-in" of compaction stresses due to the increase or decrease in spacing, respectively. Research performed by Stuedlein et al. (2010) showed that the local reinforcement stiffness, S_{local}, accounted for up to 81 percent of the measured reinforcement strains in two tall MSE walls. The rigid body assumption results in the application of an overturning moment to be assumed to be transmitted through the reinforced soil mass thus increasing vertical stresses. Removing this assumption greatly reduces computational effort and is arguably more accurate (Allen et al. 2001). Neither the Tieback Wedge method, FHWA Structure Stiffness method, nor the K-Stiffness method (discussed subsequently) assumes a rigid body. On the other hand, the Coherent Gravity and the Ehrlich and Mitchell (1994) methods do assume a rigid reinforced mass (Stuedlein et al. 2012).

Prior to the development of the Simplified method there was confusion in industry regarding which design method (mainly Coherent Gravity or Tieback method) was appropriate for different types of reinforcement material (e.g. inextensible or extensible). Typically, overly conservative designs resulted from the use of the Coherent Gravity method for extensible reinforcements.

Similar to the Coherent Gravity method the Simplified method is empirically based and is therefore limited by the database to which it has been calibrated. The data base used to calibrate the Simplified method is limited to wall heights less than 18 m (Allen et al. 2001).

The maximum reinforcement tension, T_{max}, for the AASHTO Simplified Method is determined using Equation 2.16, with σ_v determined using Equation 2.22, K_r is determined depending on reinforcement type using Figure 2.19. The active lateral earth pressure coefficient for use with Figure 2.19 is determined using a friction angle as measured in triaxial compression or direct shear test, but limited to 40 degrees.

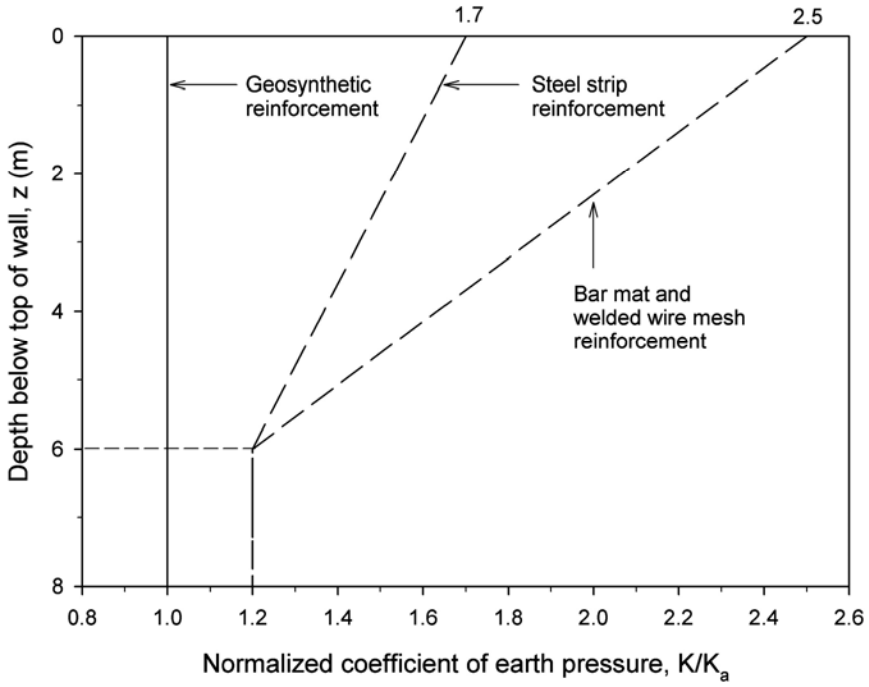

Figure 2.19. Normalized lateral earth-pressure distributions for use with the AASHTO simplified method (after Bathurst et al. 2009)

Bathurst et al. (2009) evaluated the accuracy of the Simplified method by comparing the ratio of measured to predicted maximum reinforcement load for walls with different backfill friction angles. For backfill soils with friction angles larger than 45 degrees, the Simplified method consistently under predicts the maximum reinforcement load as shown in Figure 2.20 and is similar to the Coherent Gravity method.

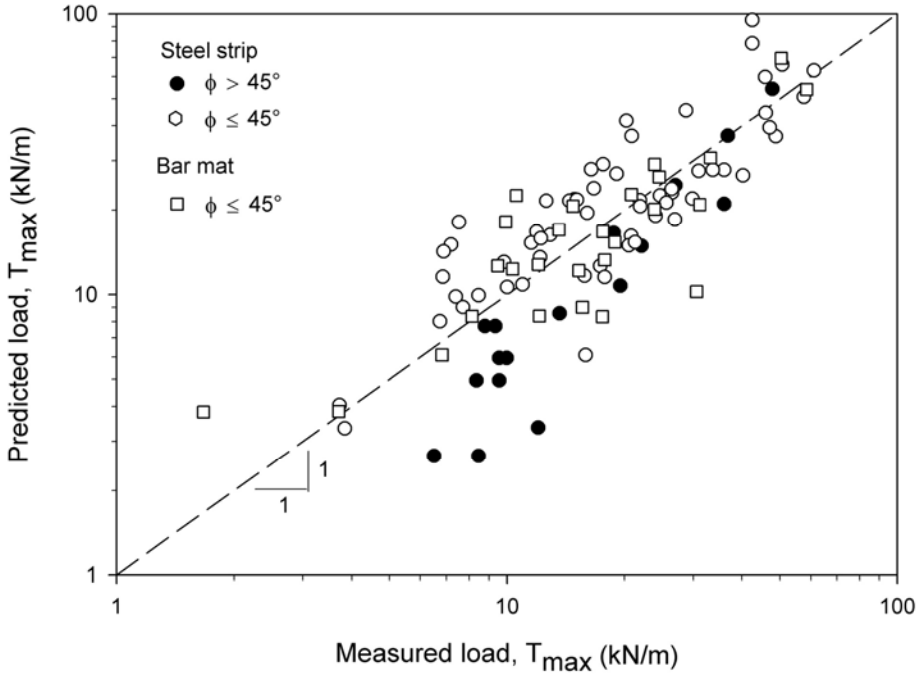

Figure 2.20. Predicted versus measured maximum reinforcement loads for the AASHTO Simplified method and steel reinforced MSE walls showing the influence of friction angle (after Bathurst et al. 2009).

K-Stiffness Method (Allen et al. 2003, 2004)

The K-Stiffness method for steel reinforced walls developed by Allen et al. (2004) was intended to update the FHWA Structure Stiffness method by considering facing stiffness, wall batter, and local reinforcement stiffness. The method was also calibrated using an extensive dataset which included 19 full scale instrumented steel reinforced walls. Similar to the Coherent Gravity and Simplified methods, the K-Stiffness method is empirically based and is therefore limited by the database to which it has been calibrated. The same data base used to calibrate the Simplified method was used to calibrate the K-Stiffness method; therefore the use of the method is also limited to wall heights of 18 m or less. Additionally, the K-Stiffness method utilizes plane strain soil properties; this is in contrast to the Coherent Gravity and Simplified methods which use shear strength parameters determined by triaxial or direct shear tests.

The maximum reinforcement tension for the K-Stiffness Method is calculated as:

$$T_{\max} = \frac{1}{2} K_r \gamma_r \left(H + S\right) S_v D_{t\max} \Phi \qquad (2.37)$$

where $D_{t\max}$ is a factor that adjusts the load depending on the location of the reinforcement in relation to the top of the wall facing which varies from 0.1 at the top of the wall to one at 60 percent of the wall depth, as shown in Figure 2.21.

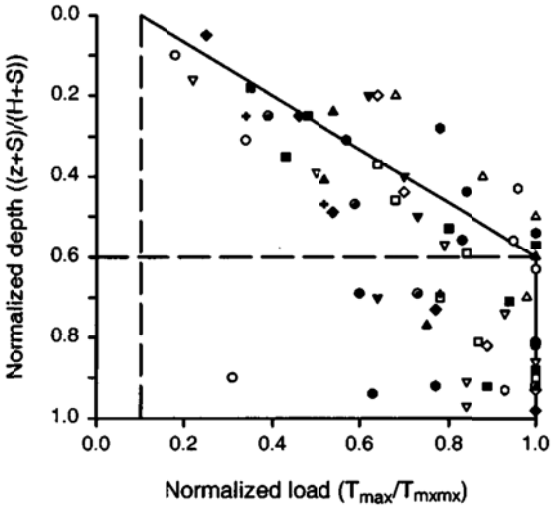

Figure 2.21. Distribution of $D_{t,\max}$ recommended by Allen et al. (2004) for steel strip reinforced walls (after Alen et al. 2004).

The factor Φ attempts to capture the influence of different wall components on the magnitude of reinforcement load and is defined as follows:

$$\Phi = \Phi_{\text{local}} \times \Phi_{\text{fs}} \times \Phi_{\text{g}} \times \Phi_{\text{fb}} \qquad (2.38)$$

where Φ_{local} and Φ_{fs} are the local reinforcement stiffness and facing stiffness factors, respectively, both taken as 1 for steel reinforcements ($\Phi_{\text{local}} = \Phi_{\text{fs}} = 1$). The global stiffness factor, Φ_{g}, is calculated as:

$$\Phi_{\mathrm{g}} = \alpha_{\mathrm{ks}} \left(\frac{S_r}{P_a} \right)^{\beta_{\mathrm{ks}}} \tag{2.39}$$

where α_{ks} and β_{ks} are dimensionless fitting parameters. The value of $\alpha_{ks} = \beta_{ks} = 0.25$ was used by Allen et al. (2004), though no further guidance was provided. The facing batter factor, Φ_{fb}, is calculated as:

$$\Phi_{\mathrm{fb}} = \left(\frac{K_{abh}}{K_{avh}} \right)^{d} \tag{2.40}$$

where K_{abh} is the active lateral earth pressure coefficient considering the facing batter, K_{avh} is the active lateral earth pressure coefficient assuming the face batter is vertical, and d is a dimensionless fitting parameter. A value of $d = 0.25$ is suggested by Allen et al. (2004).

The improved accuracy of the K-Stiffness method, as shown in Figure 2.22, is not surprising since the method was developed to incorporate both primary and secondary factors (e.g., batter and facing stiffness) that influence the development of reinforcement load to improve its predictive ability. Because the K-Stiffness method is highly empirical in nature it should only be applied to those types of walls for which it was calibrated.

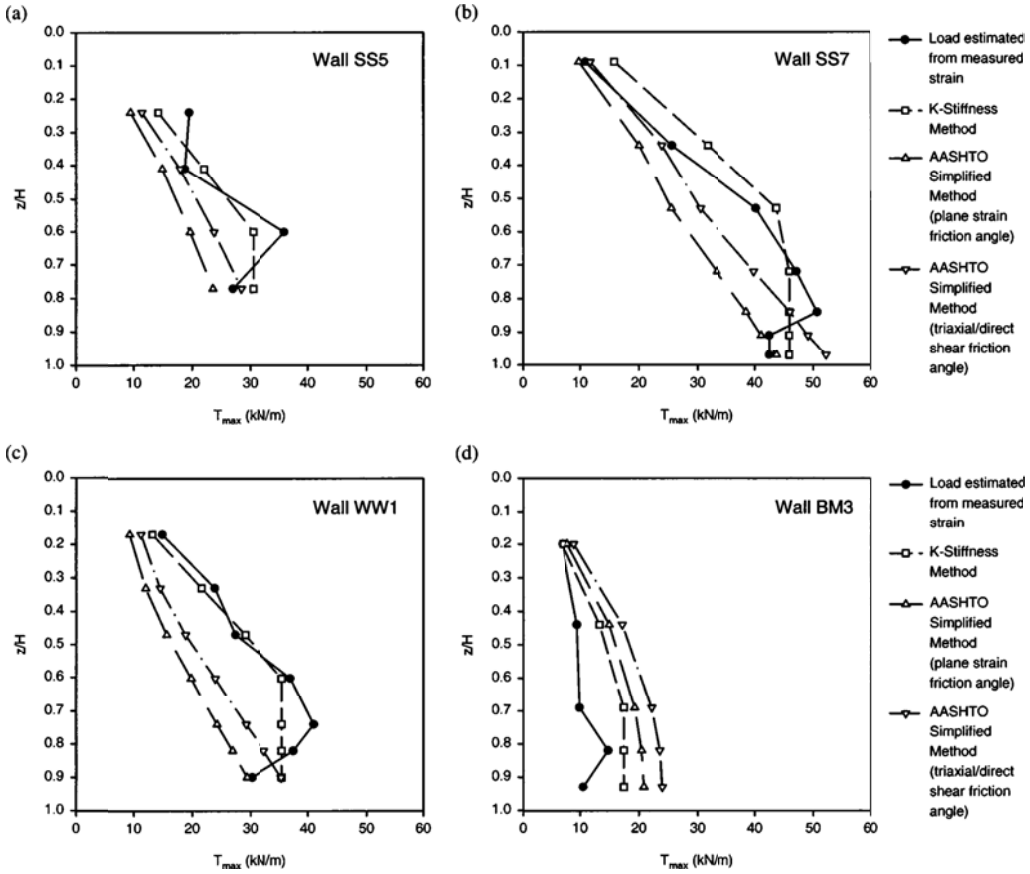

Figure 2.22. Comparison of maximum reinforcement tension as estimated by the AASHTO Simplified and K-Stiffness methods to those measured in the field: (a) steel strip reinforced wall, (b) steel strip reinforced wall, (c) welded wire reinforced wall, and (d) bar mat reinforced wall (after Allen et al. 2004).

Comparison of Design Methods for Use with Tall MSE Walls

Stuedlein et al. (2012) compared the reinforcement loads as predicted by the Coherent Gravity, Simplified, K-Stiffness, and the Ehrlich and Mitchell (1994) methods to those measured during and after the construction of two very tall MSE walls at Seattle-Tacoma International Airport (SeaTac). The soil properties used in the study were developed from direct shear test measurements required for contractor submittals. Since the K-Stiffness and Ehrlich and Mitchell (1994) methods require plane strain friction angles, the friction angle measured in direct shear of 43 degrees was converted to plane strain friction angles, ϕ'_{PS}, of 48 degrees considering the empirical correlations presented by Bolton (1986) and Jewell and Wroth (1987):

$$\phi'_{PS} = \tan^{-1}\left(1.2\tan\phi_{DS}\right) \qquad (2.41)$$

However, a triaxial and direct shear friction angle, $\phi'_{DS,\ TX}$ = 40 degrees and a plane strain friction angle ϕ'_{PS} = 44 degrees were used in load calculations to conform to AASHTO specifications.

Bias values, defined as the ratio of measured to predicted reinforcement loads, were determined for each of the reinforcement load prediction methods. It was observed that both the Simplified and Coherent Gravity methods tended to under-predict reinforcement loads during construction. The K-Stiffness method conservatively provided the best prediction of peak reinforcement stresses at intermediate construction stages where the backfill height was less than 20 m. The Ehrlich and Mitchell (1994) method provided the best overall prediction of reinforcement loads for both the North and West MSE wall as depicted in Table 2.1 by the bias values closest to one and low coefficients of variation (COV). Figure 2.23 compares the predicted distribution of reinforcement loads to those measured approximately 4 years after construction of the west wall was complete.

Table 2.1. Summary statistics of the bias in reinforcement loads for the SeaTac North and West MSE walls taken in August 2009 with capped constant friction angles ($\phi'_{DS,TX}$ = 40 deg., ϕ'_{PS} = 44 deg.) (Stuedlein et al. 2012).

	Mean bias	Range in bias		COV (%)
North MSE wall (n = 6)				
Coherent Gravity method	1.47	1.19	2.04	23
AASHTO Simplified method	1.27	1.03	1.72	21
Ehrlich & Mitchell (1994)	0.93	0.80	1.05	11
K-Stiffness method	0.73	0.58	0.85	15
West MSE wall (n = 14)				
Coherent Gravity method	1.40	1.04	2.06	21
AASHTO Simplified method	1.30	0.95	1.96	23
Ehrlich & Mitchell (1994)	0.87	0.69	1.19	17
K-Stiffness method	0.65	0.42	1.27	39

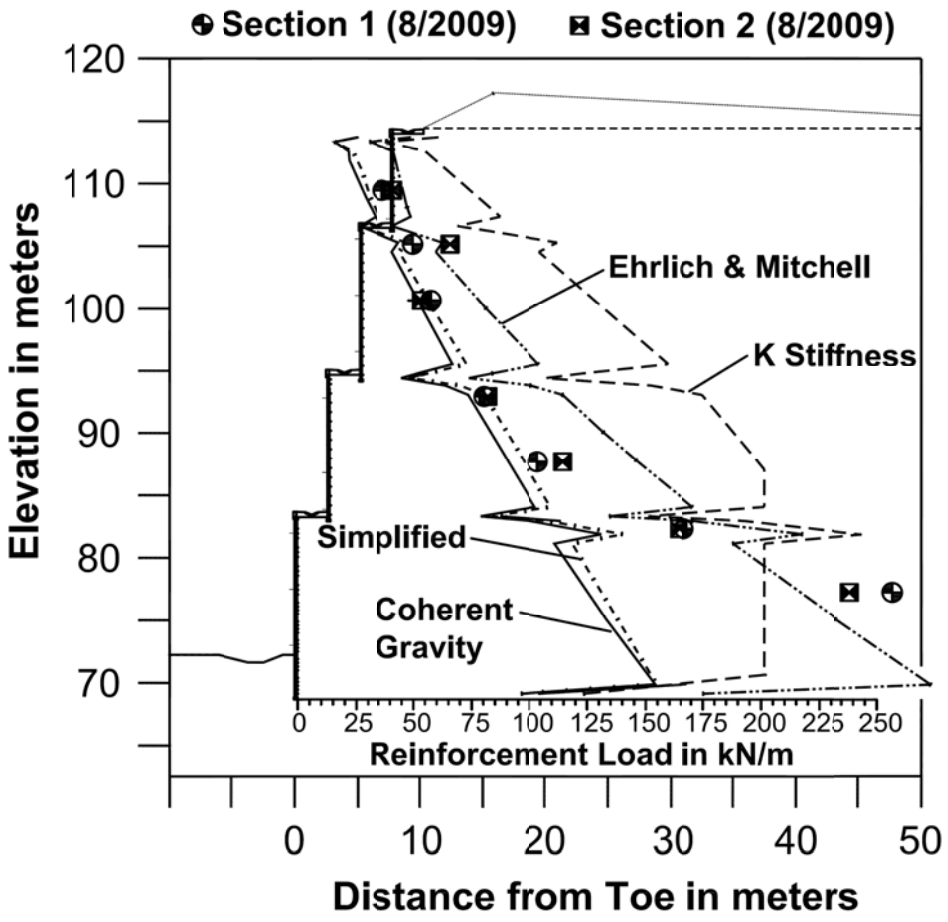

Figure 2.23. Comparison between measured and predicted peak reinforcement loads for the SeaTac West MSE wall after construction (after Stuedlein et al. 2012).

2.2.1.2 Pullout Resistance and Apparent Friction Coefficient

The earliest wall design methods involved smooth steel strips. When smooth strips are used, resistance is developed strictly through interface friction between the soil and reinforcement surface (Lee 1978). Examples of the application of this method can be found in Chang and Forsyth (1977), Lee et al. (1973), and Vidal (1969). The interface friction angle, ρ, used in early applications were those largely measured by Potyondy (1961) with the direct shear test. Potyondy (1961) conducted direct shear interface tests by replacing the bottom half of a standard direct shear box with different construction materials (e.g. wood, concrete, and steel). Direct shear tests were popular due to the availability of testing equipment, and produced fairly reasonable yet conservative results

for smooth planar reinforcements where interface friction was responsible for a majority of the resistance (Schlosser 1990). Figure 2.24(a) describes the stress transfer mechanism for smooth planer reinforcements.

Ribbed reinforcements were developed by the Reinforced Earth Company to increase the amount of pullout resistance of steel reinforcements. In addition to generating friction along the reinforcement, ribbed reinforcements generate passive failure zones due to bearing in front of the ribs (Christopher et al. 1990b) as shown in Figure 2.24(b). Since performing direct shear interface friction tests on ribbed strips could not capture the complex soil reinforcement interaction, measuring the pullout resistance directly with pullout tests became the standard of practice (Schlosser 1990).

Schlosser and Elias (1978) conducted a parametric study on soil-reinforcement interaction and load transfer. Figure 2.25 presents the load- displacement data for pullout tests on a smooth and a ribbed strip at the same overburden pressure, each with the same plan dimensions. The following was concluded in light of the experimental data:

- At most working stress levels, displacement sufficient to mobilize passive resistance was not developed and resulted in similar behavior between smooth and ribbed strips.
- Once the ribbed strip displaced relative to the soil, passive resistance began to dominate the load displacement response, with significant gain in resistance as compared to the force-displacement curves for smooth strips.

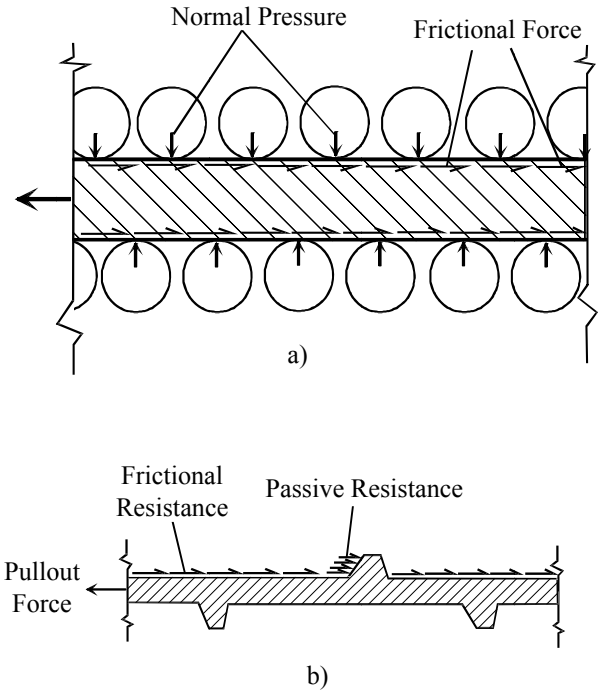

Figure 2.24. Stress transfer mechanisms for soil reinforcement: (a) frictional stress transfer between soil and reinforcement; and (b) soil passive resistance on reinforcement surface, reproduced from (Mitchell and Christopher 1990).

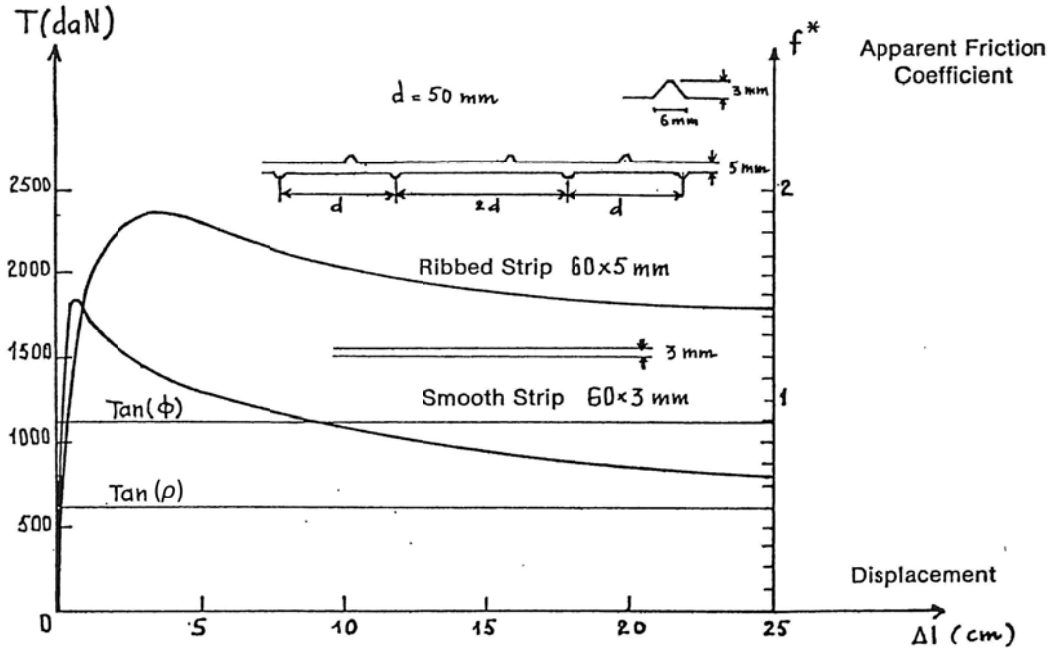

Figure 2.25. Smooth and ribbed steel strip reinforcement pullout load versus displacement curves (adapted from Schlosser and Elias 1978).

The soil-reinforcement interaction shown by the ribbed strips prompted Alimi et al. (1978) and Schlosser and Elias (1978) to develop an empirical design parameter referred to as the apparent friction coefficient (or friction bearing interaction factor), f^*. The apparent friction coefficient is determined using load-displacement pullout test data by:

$$f^* = \frac{P_{max}}{\sigma_v A_s} \tag{2.42}$$

where P_{max} is the maximum load observed during the pullout test.

Schlosser and Elias (1978) tested several factors hypothesized to affect pullout resistance, which included:

- strip width and height,
- surface characteristics (ribbed or smooth),
- relative density,
- embedment length, and
- effective overburden pressure.

Of these factors, overburden stress, σ'_v, relative density, and reinforcement surface characteristics had the largest effects on the apparent friction coefficient. It was observed that f^* decreases as σ_v increases, this was mainly attributed to dilation effects; that is, as the overburden pressure increases, dilation is suppressed and thus the excess normal pressures provided by the dilation decreases. This accounts for the increased apparent friction coefficients typically observed at lower confining pressures as shown in Figure 2.26. Unfortunately, researchers rarely provide basic classification information (e.g., gradation and angularity) with f^* data and therefore the effects of these variables usually cannot be aggregated and quantified. Additionally, the development and peak magnitude of f^* can also be influenced by the testing conditions, as described subsequently.

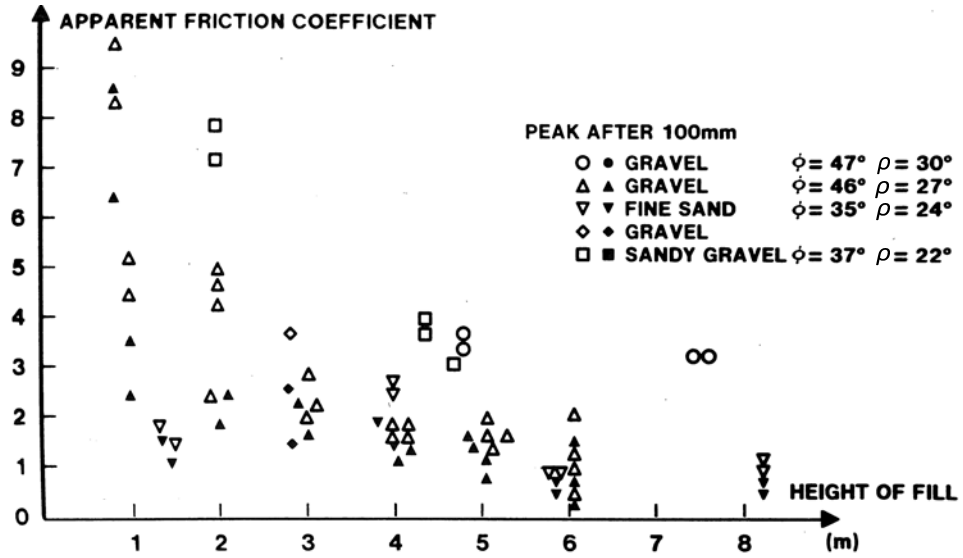

Figure 2.26. Apparent friction coefficient verses height of fill data used to originally calibrate the pullout design procedure (after McKittrick 1978).

2.2.1.3 Pullout Test Design Considerations

Pullout tests are typically performed in the laboratory using a large box with the overburden stress applied through an air or water bladder or full-scale tests where a sacrificial strip is placed during construction and pulled out using a hydraulic jack. The overburden pressure is not typically measured; rather, it is assumed that the full vertical overburden stress (e.g. the bladder pressure for the laboratory or γz for the full-scale method) acts on the surface of the reinforcement. For these tests, it is required that the reinforcement length or the overburden pressure be limited to prevent yielding at the connection to the reinforcement.

Palmeira and Milligan (1989) describe the design of different pullout tests and the effects of boundary conditions on the resulting behavior. The three aspects considered by Palmeira and Milligan (1989) were:

- the uniformity of load application or top boundary condition;
- the manner in which the strip exits the soil mass during the test; and,
- the reinforcement embedment length.

The top boundary condition was found to have some effect on the load-displacement response for steel grid reinforcements as shown in Figure 2.27. For the rigid boundary

condition, a rough rigid plate attached to a hydraulic actuator was used to apply the overburden pressure. For the flexible condition, a water filled bladder was used to apply the overburden pressure. As shown in Figure 2.27, the top loading boundary condition didn't affect the initial response, but a rigid boundary condition, which deviates significantly from the field condition, resulted in approximately 10 percent larger peak pullout resistance.

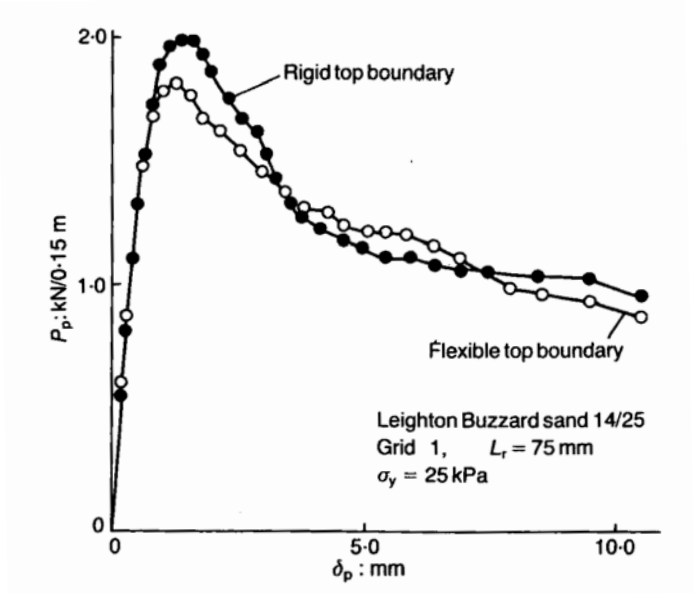

Figure 2.27. Effect of top boundary condition on pullout test results with steel grid reinforcements (after Palmeira and Milligan 1989).

Palmeira and Milligan (1989) concluded that neither the strip length nor the load application (rough rigid plate or pressure bladder) had a significant effect on the measured pullout force, but the boundary condition where the strip exits the soil mass did have a large effect on measured pullout resistance. It was found that large passive-type resisting stresses built up at the front of steel grid reinforcements, and locally increased the normal stress on the reinforcements, resulting in artificially high pullout resistance. These stresses were reduced when the front wall was lubricated. Figure 2.28 shows a large increase in peak bond strength for grid reinforcements when the front wall was not lubricated. However, the use of longer strips causes the front wall friction effects to be

reduced since the ratio of the front wall friction load contribution to the load contribution of the soil-reinforcement interaction is smaller. No comparative study of the effect of front wall friction on the pullout load measured using ribbed steel strip reinforcements has been conducted. Some studies have chosen to have the strip exit the soil away from the cell wall using an intruded slot or pipe (e.g. Schlosser and Elias, 1978) as shown in Figure 2.29, however, it is unclear as to what the effect of the pipe interacting with the strip and soil would have on the magnitude of measured pullout resistance.

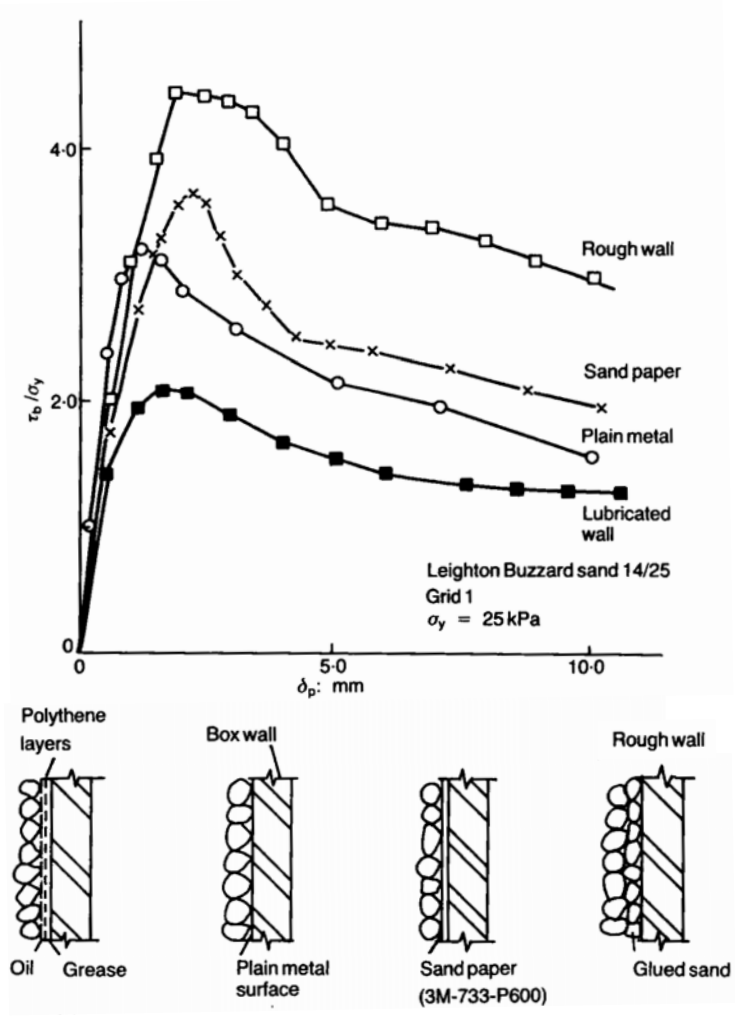

Figure 2.28. Bond strength versus displacement of a steel grid for different front wall friction conditions (after Palmeira and Milligan 1989).

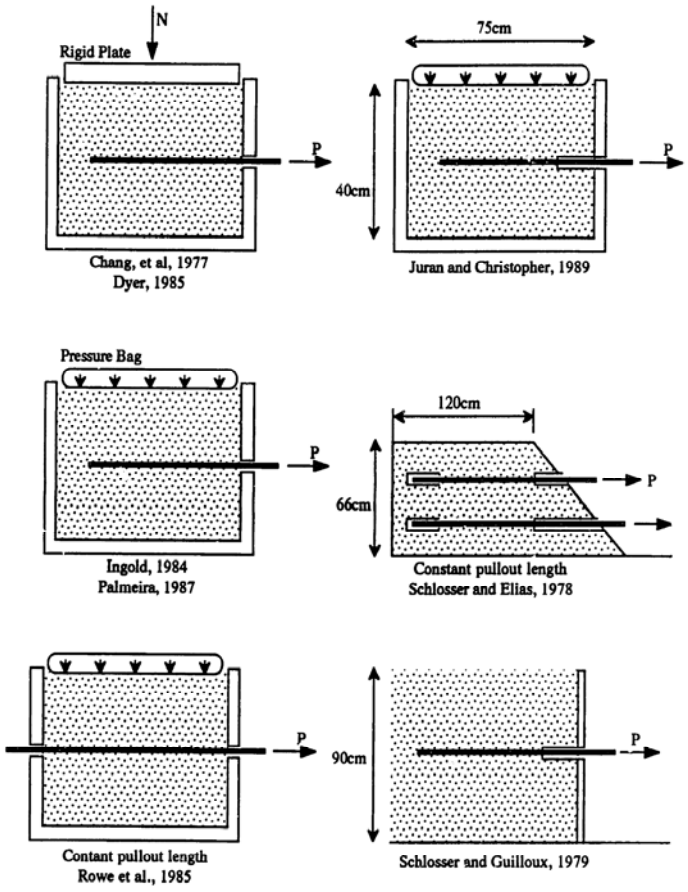

Figure 2.29. Boundary conditions for different pullout test presented in literature (after Larson 1992).

2.2.1.4 Development of Design Procedures for Pullout Resistance

For a given soil-reinforcement combination, most pullout studies observed that a constant value of f^* is obtained approximately 6 m below the top of the wall. This is the basis of the Allowable Stress Design (ASD) method outlined in Christopher et al. (1990) and which remains the standard of practice for steel ribbed strips (Berg et al. 2009). The pullout data used in calibrating this design procedure is presented in Figure 2.26.

As stated in Christopher et al. (1990a), the distribution of f^* can be obtained in two ways: either by performing pullout tests with the backfill and reinforcement to be used in construction, or by calculating f^* at the top of the wall using the coefficient of uniformity, C_u, of the retained fill as:

$$f^* = 1.2 + \log C_u \tag{2.43}$$

and reducing linearly to:

$$f^* = \tan \phi \tag{2.44}$$

at a depth of 6 m with the qualifier that $f^* \leq 2$ for all depths. This procedure results in a bilinear or tri-linear design curve, depending on the backfill characteristics, intended to follow a 95% confidence limit. However, this design model was calibrated using data from a variety of soil types and thus the model tends to underestimate f^* when dilative backfill soils such as dense gravels are used.

Other design procedures that have been proposed include those by Huang et al. (2012) and Miyata and Bathurst (2012). Using the same database as used to calibrate the current design model Huang et al. (2012) reported a Load and Resistance Factors Design (LRFD)-calibrated method for the internal stability of steel strip reinforced MSE walls. The intent of LRFD is to separate the uncertainty in the load from that of the resistance and use partial reduction or increasing factors to accommodate differences in uncertainty. LRFD-based procedures require that a model that accurately represents the statistical distribution of a sample population, and thus the design model presented in Figure 2.30 is not appropriate for use with current ASD design procedures.

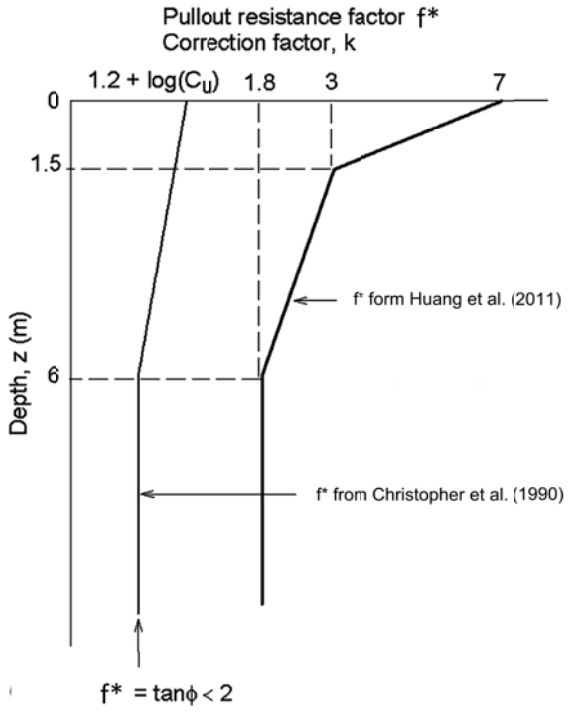

Figure 2.30. LRFD calibration model for apparent friction coefficient and example design distribution (adapted from Huang et al. 2012).

Miyata and Bathurst (2012) developed a new database of Japanese pullout test results and developed a three parameter exponential model. The previous Japanese design model was overly conservative at low confining pressures and exhibited a large bias when used with LRFD procedures (Miyata and Bathurst 2012). As shown in Figure 2.31, two models are proposed for use with steel ribbed reinforcements: the "fit" model which is intended for use with LRFD, and the "lower bound" model intended to replace the Japanese bilinear model currently for use with allowable stress design. Note that because LRFD procedures directly accounts for the uncertainty in an empirical model, a best-fit line (i.e., an unbiased model) is typically preferred.

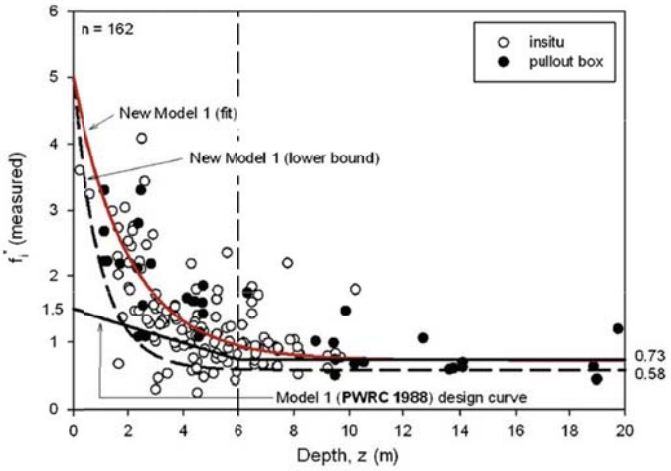

Figure 2.31. Apparent friction coefficient versus depth for Japanese pullout test database for ribbed steel strips with current Japanese design model and proposed model by Miyata and Bathurst (2012).

2.2.1.5 Factor of Safety and Resistance Factors with Respect to Pullout

For linear ribbed reinforcements, the Factor of Safety with respect to reinforcement pullout, FS_{PO}, at a given reinforcement layer, can be calculated as:

$$FS_{PO} = \frac{P_r R_c}{T_{\max}} \tag{2.45}$$

where P_r, the pullout resistance per reinforcement, is determined by:

$$P_r = \sigma'_v \; 2L_e b f^* \tag{2.46}$$

where L_e is the embedded length of reinforcement as depicted in Figure 2.16. Typically a factor of safety of 1.5 is used for ASD (Elias et al. 2001).

The FHWA has mandated the use of LRFD for bridges designed by state transportation departments. Because MSE walls are commonly used for bridge abutments and approaches, MSE wall design procedures are transitioning to LRFD. In order to be consistent with current design standards, the symbol ϕ_R was taken to represent the

resistance factor; however, this should not be confused with friction angle. For LRFD pullout design, the following must be satisfied (Berg et al. 2009):

$$\phi_R L_e \geq \frac{T_{\max}}{f^* \sigma_v 2R_c} \tag{2.47}$$

The resistance factors of for the static and seismic conditions are typically $\phi = 0.40$ to 0.75 and $\phi = 1.0$, respectively (Bathurst et al. 2008a; AASHTO 2010)

.

2.2.2 Design Methodology for External Stability

The reinforced soil mass is treated similar to a gravity wall for purposes of determining the external stability of MSE walls. As with gravity walls, four external, or global, failure mechanisms are typically considered (Christopher et al. 1990a). These mechanisms include sliding, limiting eccentricity (overturning), bearing failure, and deep seated instability and are summarized in Figure 2.32. Christopher et al. (1990a) provides an in-depth discussion on design procedures for each mechanism listed above; the most current design standards incorporate LRFD procedures and can be found in Berg et al. (2009). Because the focus of this research is on internal stability of MSE walls, interested readers are referred to Christopher et al. (1990a) and Berg et al. (2009).

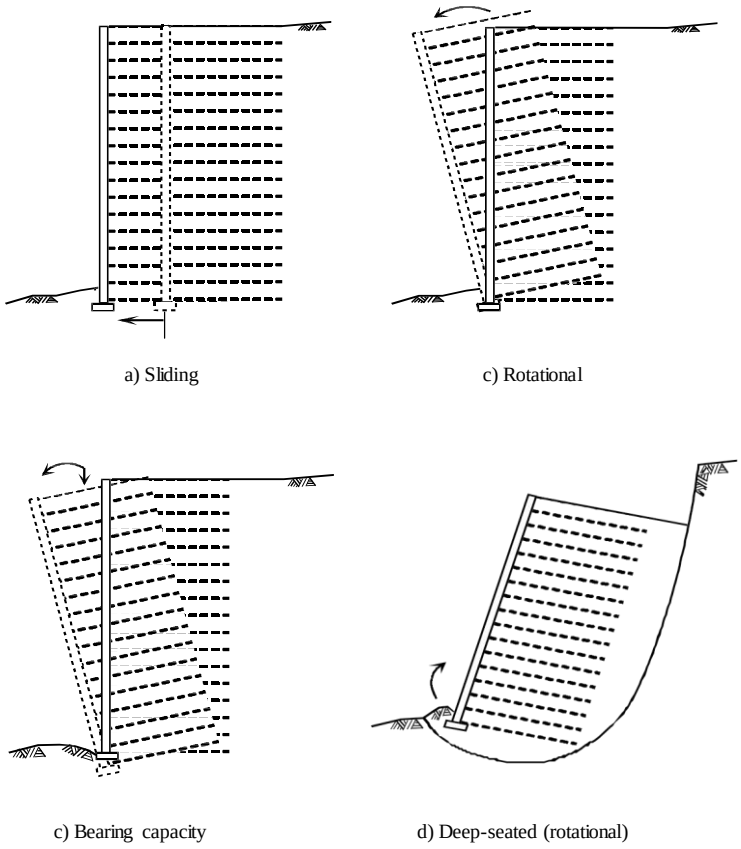

Figure 2.32. Global stability failure mechanisms for MSE walls (after Liang 2004).

2.3 Summary of the Literature Review

The state of practice for determining internal stability of MSE walls uses semi-empirical and empirical design procedures, some of which were developed over 30 years ago. This chapter reviewed the soil mechanics principles necessary to understand soil-reinforcement interaction with particular focus on the behavior of dilative soils, such as the response anticipated for compacted granular fill which is the focus of this study. The development of design procedures for internal stability has been discussed with regard to the development of reinforcement loads as well as the resistance. Six methods for determining reinforcement loads have been historically used in North America. Of these, two are commonly used in the design of ribbed steel strip reinforcements: the Coherent Gravity and Simplified methods. A disadvantage of these two methods is that they do not directly account for global reinforcement stiffness in determining reinforcement loads or

compaction induced loads during construction. Additionally, both of these design methods are empirically based and therefore limited in their use by the conditions in the database of case histories by which they were calibrated, such as their height or reinforcement density. An alternative method for determining reinforcement loads is the method developed by Ehrlich and Mitchell (1994). The Ehrlich and Mitchell (1994) method is theory-based and is therefore not bound by a case history database; also, this method explicitly accounts for compaction-induced stresses as well global reinforcement stiffness. Nonetheless, all of the models suffer from the requirement that a single friction angle be used in the computation of internal stresses; this presents a limitation that may be responsible for some inaccuracy in reinforcement load predictions, particularly for tall MSE walls that exhibit large stress gradients.

In contrast to load prediction methods, resistance prediction methods, particularly pullout resistance, have remained relatively unchanged over the history of modern MSE wall design. The pullout resistance is calculated using a frictional model, however, due to dilation effects and accumulation of passive resistance, a constant friction coefficient cannot be used with varying vertical effective stresses. This forces the designer to have to choose between using empirically based models or performing pullout tests on the specific reinforcement-backfill combination to be used in construction. It is not usually practical to perform pullout tests since the specific backfill to be used is not typically known prior to construction. However, the empirical model currently in use does not take into account soil type and consequently the apparent friction coefficient is often under-predicted when high strength-dilative soils are used. This apparent conservatism has not been evaluated for tall walls, and therefore this gap in the literature should be investigated.

3.0 RESEARCH OBJECTIVES AND PROGRAM

3.1 Research Objectives

The main objective of this study is to develop an improved understanding of the interaction between soil and ribbed steel reinforcements in MSE walls constructed using well-graded sandy gravel backfill and its role in providing internal stability to the reinforced soil system. Much of this research is performed using materials and data from two very tall MSE walls built during the SeaTac 3rd Runway Expansion Project. However, the intent of this study is not to focus on any specific wall, but add to the general knowledge of MSE wall design and performance. The specific objectives of this study include:

1. Characterization of the stress-strain behavior of the reinforcement material;
2. Characterization of the stress-strain response of the reinforced soil (i.e., backfill) material;
3. Determination of the soil-reinforcement interaction and pullout resistance of the reinforcement at varying normal stress magnitudes;
4. Development of a pullout resistance design model for well graded sand-gravel mixtures; and
5. Application of the backfill soil-specific and general models to the prediction of reinforcement loads and pullout resistance for two very tall MSE walls considering curvature of the backfill soil failure envelope.

3.2 Research Program

The research program undertaken to achieve the objectives includes:

1. Perform tension tests on coupons cut from steel ribbed strips in order to measure its constitutive properties (Chapter 4);
2. Perform consolidated-drained axisymmetric triaxial strength tests at various effective confining pressures and relative densities on the reinforced backfill (Chapter 4);

3. Compare the results of the triaxial testing to results from similar soils reported in the literature (Chapter 4);
4. Determine the curvature of the Mohr Failure Envelope for the backfill soil (Chapter 4);
5. Design and construct a pullout test apparatus for single reinforcement strips (Chapter 5);
6. Perform a series laboratory pullout tests at various normal effective stresses on the reinforced backfill and steel ribbed strip reinforcements (Chapter 5);
7. Develop a load-displacement model to estimate the pullout behavior of the reinforcements (Chapter 5);
8. Develop a new backfill-specific and global ultimate pullout resistance model for predicting the variation in apparent friction coefficient with normal effective stress for gravel backfills and steel ribbed strip reinforcements (Chapter 5);
9. Using the measured constitutive properties of the reinforcement material and the strain measurements from the SeaTac 3rd runway project, calculate the maximum reinforcement loads and stresses, and compare them to those calculated using the constitutive properties assumed during design (Chapter 6).
10. Compare the reinforcement load distributions that were determined using a constant friction angle assumed during design to those computed using the backfill specific Mohr Failure Envelope (Chapter 6); and,
11. Compare the measured pullout resistances to those computed using the accepted AASHTO design model, the global design model, and the backfill-specific design model (Chapter 6).

4.0 MATERIAL CHARACTERIZATION

The characterization of soil-reinforcement interaction requires the measurement of index properties and strength of the soil and the reinforcement materials. This chapter presents the results of strength and index tests conducted on the ribbed steel strip reinforcements and the reinforced backfill materials, and discusses their role in the context of MSE walls.

4.1 Reinforcement Material Property Characterization

Generally speaking, the reinforcement strips manufactured by the Reinforced Earth Co. are 50 mm wide by 4 mm thick (Berg et al. 2009). However, the MSE wall reinforcements used in this study were galvanized ribbed steel strips 50 mm (2 in.) wide by 6 mm (0.24 in.) thick, because these were used in the construction of the SeaTac 3rd Runway Expansion Project (Stuedlein et al. 2010). The dimensions of the ribbed steel strip reinforcements are presented in Figure 4.1. In order to properly evaluate tensile stress-strain behavior of these reinforcement strips, tension testing was performed on the actual steel strips used in the 3rd Runway Project.

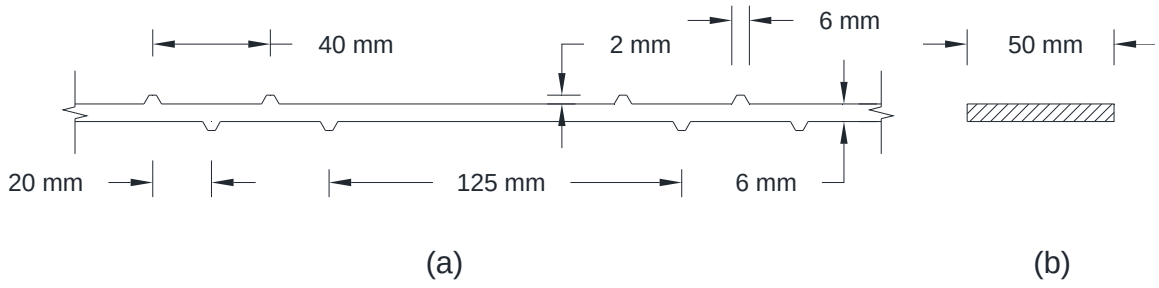

Figure 4.1. Steel ribbed reinforcement dimensions (a) elevation view, and (b) cross-section.

4.1.1 Tension Testing on Reinforcement Material

The constitutive parameters of the steel reinforcements such as the Young's modulus, yield strength, and ultimate strength, were needed to assess the internal stability of the MSE wall (presented in Chapter 6). Another motivation for studying the stress-strain behavior of the reinforcement material is the calibration of numerical models for use in

analyzing the behavior of tall MSE walls. However, detailed numerical model calibration is beyond the scope of this thesis and therefor will not be discussed herein.

To measure the constitutive properties mentioned above, tension tests were conducted on steel coupons. Six dog-bone-shaped steel coupons, with dimensions shown in Figure 4.2, were cut from a MSE wall reinforcement strip. All tests were performed on an Instron universal testing machine in accordance with ASTM standards E8-08 and A370-12a. An extensometer with a gauge length of 50 mm (2 in.) and a 6 mm (2.5 in.) range was used to measure strain through yielding and strain hardening. Due to the limited range of the extensometer the tests were paused at 10 percent strain and the extensometer removed. A computer-controlled camera was used to measure strain for the remainder of the test. The specimens were designated S1 through S6. Samples S1 and S2 are not considered in this study because of software malfunctions that led to an inability to make extensometer measurements.

The cross head (Figure 4.2) speed was set to 3.05 mm per minute for all specimens. Approximately two and a half minutes was required to rupture each specimen. The information obtained from the coupon testing program includes the Young's modulus, the upper and lower yield strength, the yield point elongation, the ultimate tensile strength, the maximum elongation, and the area reduction. The yield strength was determined using the Autographic Diagram Method (ASTM 2008), and the elongation and area reduction were measured after rupture.

The stress-strain behavior of each specimen was similar to one another and produced an average modulus of elasticity of 211 GPa, a mean yield stress of approximately 530 MPa, a average yield point elongation of 0.92 percent, and a mean ultimate tensile strength of 700 MPa, summarized in Table 4.1 and Figure 4.3. The "representative" values listed in Table 4.1 were chosen using judgment in order to reduce the effect of possible outliers and were selected to model the strips in subsequent chapters.

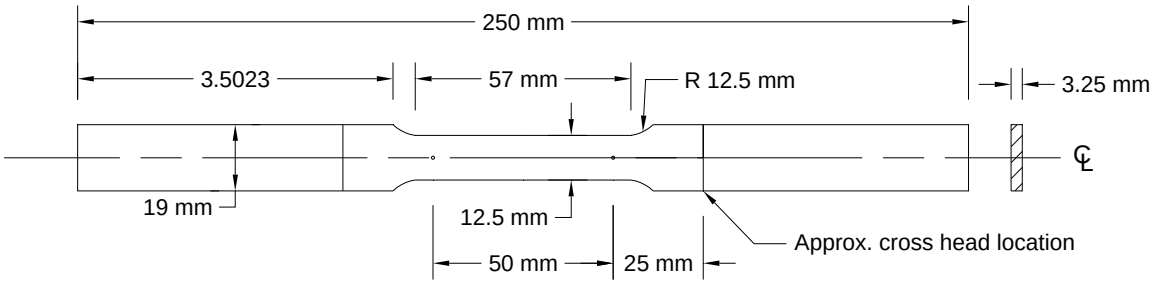

Figure 4.2. Typical coupon dimensions.

Table 4.1. Summary of MSE wall reinforcement material testing.

Specimen ID	Modulus of Elasticity (GPa)	UYS[a] (MPa)	LYS[b] (MPa)	YPE[c] (percent)	Ult. Tensile Strength (MPa)	Max. Elongation (percent)	Area Reduction[d] (percent)
S3	208.1	531	527	0.97	701	23	53
S4	207.2	529	526	0.88	690	22	50
S5	220.4	528	526	0.89	701	21	50
S6	209.0	534	530	0.94	707	23	54
Average	211.2	531	527	0.92	700	22	52
Representative	208.0	530	526	-	700	-	-

[a]Upper Yield Strength, [b]Lower Yield Strength, [c]Yield Point Elongation, [d]area reduction was measured post rupture.

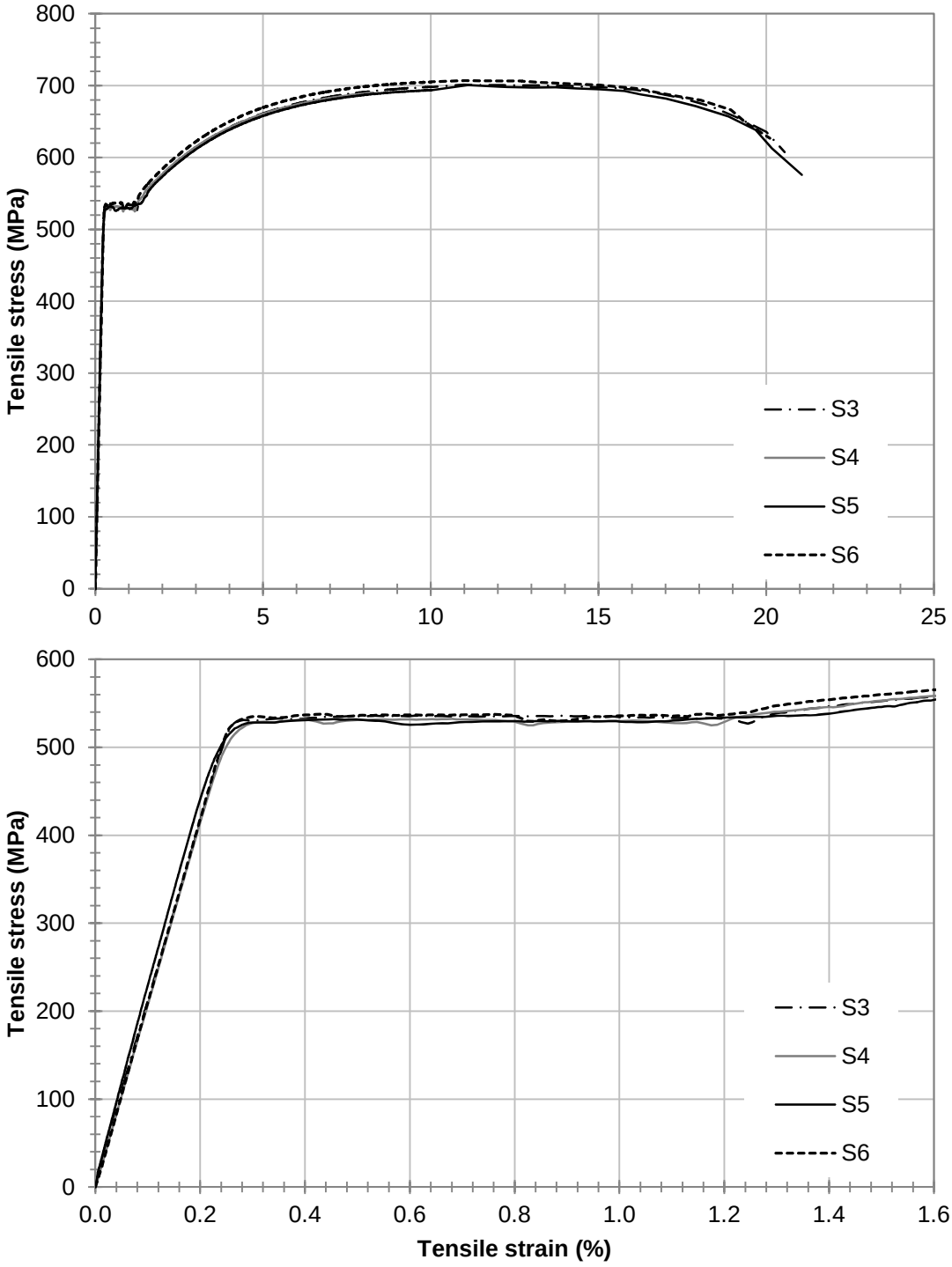

Figure 4.3. Stress - strain behavior of steel coupons.

4.2 Index and Shear Strength Testing of Reinforced Backfill

The reinforced backfill material used in the SeaTac MSE walls was quarried from a glacial outwash deposit located near Kanaskat, Washington at approximately N47°19'09", W121°52'57". The gravel particles ranged from sub-angular to well-rounded, and the sand particles ranged from angular to sub-round as determined by visual inspection. Gradation analysis, modified Proctor, maximum void ratio, and consolidated drained triaxial compression tests were performed on the backfill material. The results from these tests are discussed below.

4.2.1 Gradation Analysis

Approximately five cubic meters of the reinforced backfill material was delivered to the OSU geotechnical research laboratory. Six 32 kg samples were randomly extracted from the backfill material. Gradation analyses were performed on each sample and presented in Figure 4.4. The Quality Assurance (QA) limits in Figure 4.4 and Figure 4.5 plotted as bold solid black lines represent the rejection criteria for the reinforced backfill used in the SeaTac 3rd Runway Project, and indicate that the gradation of the soil used as reinforced backfill could not fall outside these lines.

The maximum and minimum grain sizes for each sample were similar, however, the average grain sizes, D_{50} ranged from 2 mm to 8 mm. The grain size distributions of all samples showed a "gap" with significantly small portions of material having grain sizes between 7 and 1 mm. Due to this "gap" the coefficient of curvature, C_c, was calculated to be less than 1, where C_c is determined using:

$$C_c = \frac{\left(D_{30}\right)^2}{D_{10} \cdot D_{60}} \tag{4.1}$$

where D_{10}, D_{30}, and D_{60} are the grain sizes at which 10, 30, and 60 percent of material (by mass) are smaller, respectively. According to the Unified Soil Classification System, gravels and sands with coefficients of curvature less than one or greater than three

classify as poorly-graded. However, if the ratio of D_{60} to D_{10}, the coefficient of uniformity, C_u, is greater than four, a gravel is considered well-graded. Though the coefficient of uniformity for the average sample gradation was 42, none of the samples classified as well-graded due to the C_c criterion.

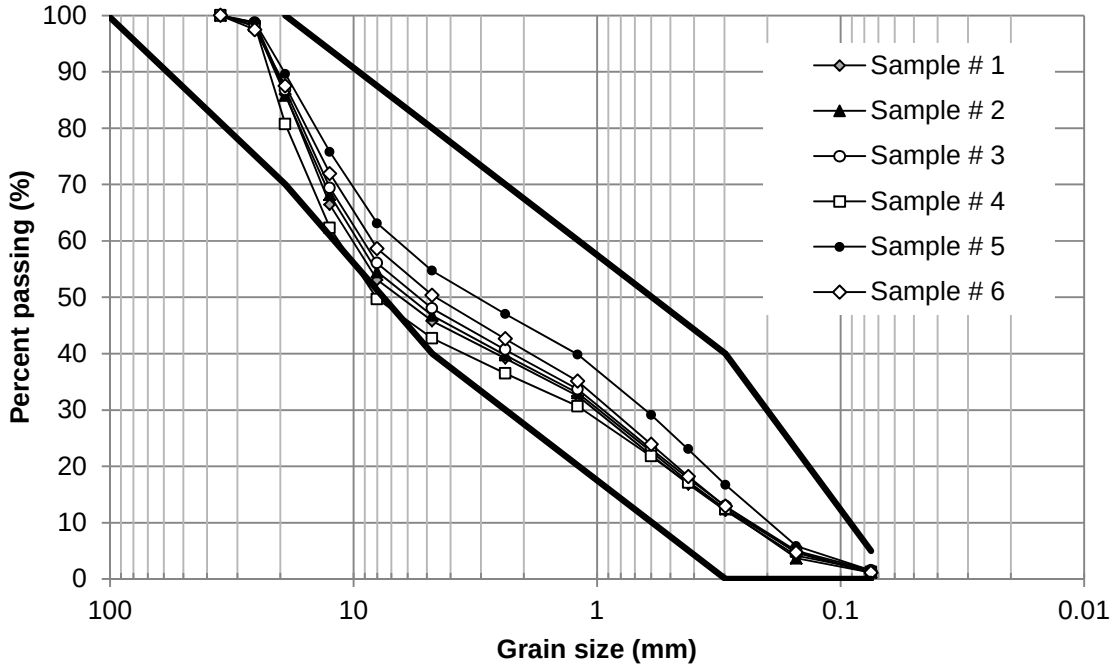

Figure 4.4. Individual gradations of six random samples of reinforced backfill material and the upper and lower bound gradation limits used for quality assurance (QA) during the SeaTac 3rd runway expansion.

The target gradation for the axisymmetric CD triaxial strength tests shown in Figure 4.5 was established in order provide a standard test gradation. The target gradation was developed by limiting the maximum grain size to 25.4 mm (1 in) and averaging the results of the six gradations. The target gradation had a D_{50} = 6 mm, a C_u = 42, and a C_c = 0.46. In order to reproduce the target gradation for subsequent CD triaxial testing, the backfill material was separated into 12 grain size ranges and then carefully recombined to produce the required 17 kg samples as shown in Figure 4.6.

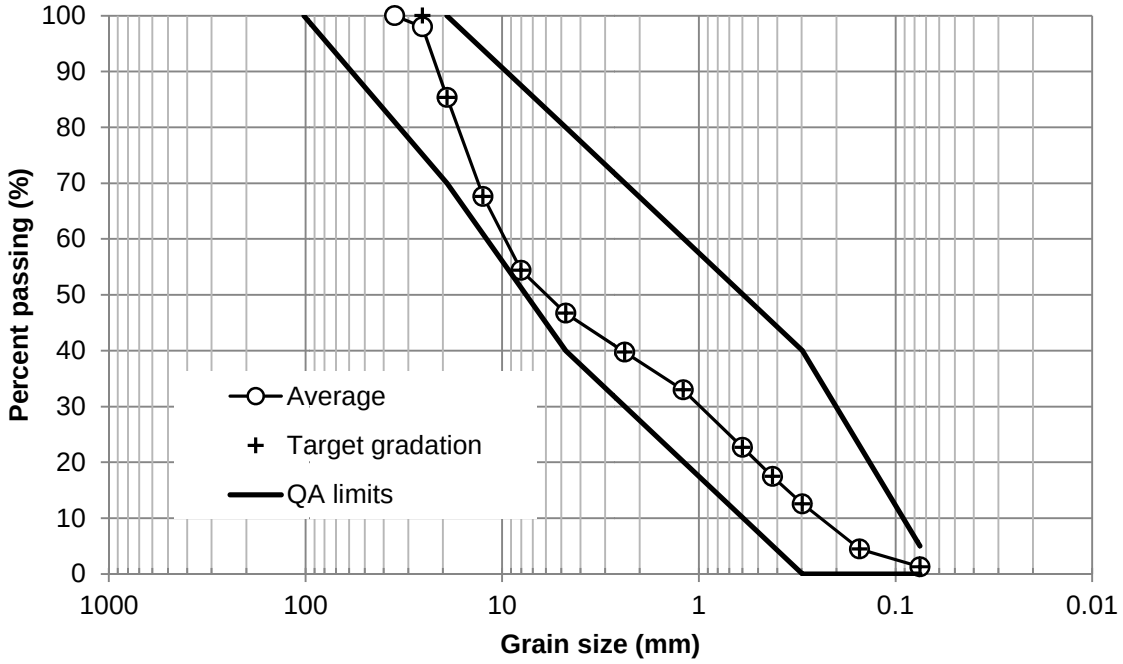

Figure 4.5. Average gradation of the reinforced back fill as measured at OSU and the target gradation for CD triaxial testing.

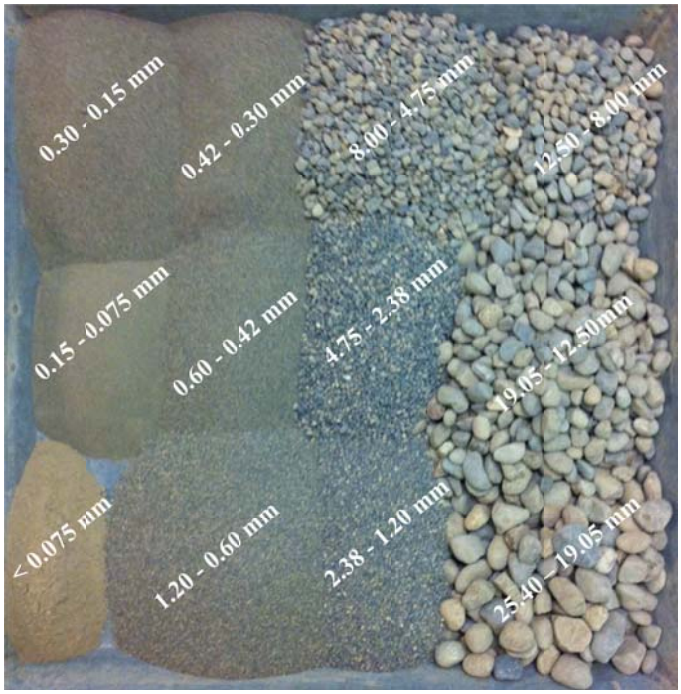

Figure 4.6. Photo of a 17 kg triaxial sample prior to mixing (maximum grain size = 25.4 mm).

4.2.2 Modified Proctor Tests

The specifications for the SeaTac MSE wall required that the reinforced backfill be compacted at ± 2 percent of optimum water content, and to a minimum of 92 percent of the maximum modified Proctor dry density (Stuedlein et al. 2010b). In order to determine the maximum modified Proctor dry density, and thus be able to select a target relative densities for the CD triaxial test specimens, modified Proctor tests were carried out on the target gradation. The modified Proctor tests were performed by FEI Testing & Inspection of Corvallis, OR (FEI 2011), and verified by the OSU geotechnical lab. Method C as defined in ASTM D1557 (ASTM 2009) was used. Method C required oversized particles to be removed and a correction to be applied to the resulting compaction curve. Both the uncorrected and corrected proctor curves, as reported by FEI (2011), are presented in Figure 4.7. The maximum dry unit weight and optimum moisture content was determined equal to 22.4 kN/m^3 and 6.5 percent, respectively.

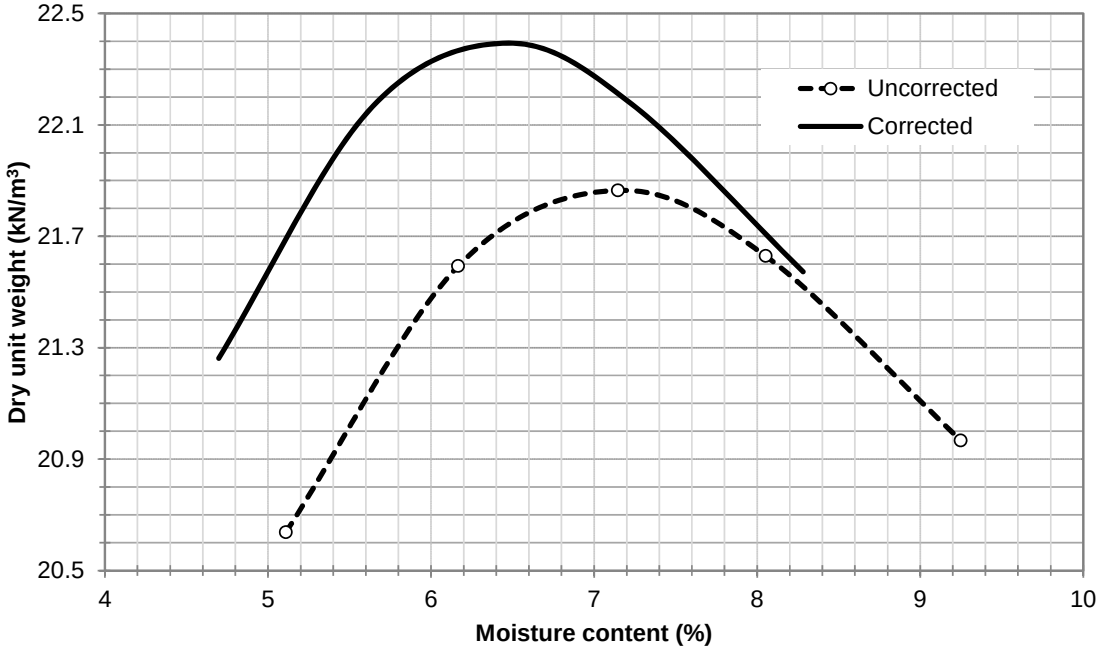

Figure 4.7. Corrected and uncorrected Modified – C Proctor curves as reported by FEI (2011).

4.2.3 Maximum and Minimum Void Ratio and Relative Density

The state of compaction of soils can be described using many metrics such as the dry unit weight, dry density, relative compaction, porosity, and void ratio. However, the state of compaction for granular materials is typically referred to in terms of relative density, D_r, given by:

$$D_r = \frac{e_{\max} - e}{e_{\max} - e_{\min}} \tag{4.2}$$

where e is the void ratio, $e_{\max}$ is the maximum void ratio or the void ratio at the loosest possible state of the soil, and $e_{\min}$ is the minimum void ratio or the void ratio at a soil's densest possible state prior to particle crushing. Relative density, when compared to void ratio alone, typically provides the best correlation for strength (Cornforth 1973), and will therefore be the basis of discussion for this study.

To determine the maximum void ratio of the backfill material, Method A, described in ASTM D4254 (ASTM 2006a) was performed with the following exception: a Modified-C Proctor mold with a volume of 2124 cm^3 (0.075 ft^3) was used instead of the specified 2830 cm^3 (0.10 ft^3) mold due to availability of testing equipment. Seven tests were performed on the backfill design gradation and a mean maximum void ratio, $e_{\max}$, of 0.365 and a standard deviation of 0.003 was determined as shown in Table 4.2.

Table 4.2. Results from maximum void ratio tests on backfill material.

Test No.	Measured Void Ratio, e
1	0.365
2	0.363
3	0.368
4	0.368
5	0.360
6	0.368
7	0.364
Mean	0.365
St. Dev.	0.003

An effort was made to determine the minimum void ratio, e_{min}, using the procedure outlined in ASTM D4253 (ASTM 2006b) in which a surcharge is placed on top of a cylinder filled with dry soil and then placed on a vibrating table. Densities obtained using method D4253 were significantly less than those obtained during the modified Proctor tests and thus did not represent 100 percent relative density. Following the recommendation of Duncan et al. (2007), the maximum dry unit weight was designated as the corrected maximum modified proctor dry unit weight of 22.4 kN/m^3, corresponding to a minimum void ratio of $e_{min} = 0.182$.

4.2.4 Consolidated Drained Triaxial Compression Tests

An extensive series of consolidated drained triaxial compression tests was performed on the target gradation at three different relative densities. A triaxial testing system was developed at the OSU Geotechnical Laboratory in order to perform these tests and in doing so a triaxial testing manual, that complies with ASTM (2011b), was developed for future research. The manual provides a detailed account of the methods used herein and is given in Appendix A. The results from the CD triaxial tests are presented below.

4.2.4.1 Specimen Compaction Protocol and Test Program

In order to measure the effect of relative density on the constitutive behavior of the reinforced backfill, three target relative densities were considered for the CD triaxial testing series. These target relative densities were, 35, 55, and 65 percent, with corresponding target unit weights of 20.3, 20.9, and 21.3 kN/m^3, respectively. Each cylindrical specimen was compacted in eight 3.81 cm (1.5 in.) thick lifts using a Modified Proctor hammer and a 152.4 mm (6 in.) diameter by 304.8 mm (12 in.) tall split compaction mold. The number of blows per lift was adjusted depending on the target relative density. Only specimens with initial relative densities that achieved +/- 2.5 percent of the target relative density were sheared in the test program.

The saturation of each specimen was determined by measuring the B-value as prescribed by ASTM (2011b). Black and Lee (1973) found that for very stiff soil

structures the B-value corresponding to 100 percent saturation can be as low as 0.91. Therefore, a minimum B-value of 0.90 was required for all triaxial shear strength tests.

Each specimen was sheared using the same axial strain rate of $d\varepsilon_1/dt$ = 0.25 percent per minute. This axial strain rate is in accordance ASTM D7181 if a time to 90 percent consolidation, t_{90}, of 1.5 minutes is conservatively assumed.

Each specimen was given a name indicating the effective confining pressure and the overconsolidation ratio (OCR) as well as the "test number" (e.g., σ'_3 in kPa – OCR – test number). For example the third specimen sheared at 100 kPa with and OCR = 1 would be labeled as specimen 100-1-3. Eight tests with varying confining pressures were performed at each target relative density for a total of 24 tests. The target confining pressures included 10, 20, 50, 100, 200, 300, 500, and 1,000 kPa. Table 4.3 summarizes the results from each CD triaxial test.

4.2.4.2 CD Triaxial Results

In this study, the two controlled variables of interest were relative density and confining pressure. Originally the effect of OCR was considered, however after initial testing and further review of the literature, the effect of OCR was found to be insignificant as compared to relative density.

Since relative density affects the behavior of granular materials it is important to note that for a given specimen the relative densities before and after consolidation were typically not the same. It was observed that the magnitude of change in relative density depended on the consolidation confining pressure and the initial relative density. Table 4.3 and Figure 4.8 summarize the change in relative density for all of the strength tests. The increase in relative density due to consolidation is larger for tests with higher confining pressures and lower initial relative densities. In order to replicate field conditions, the initial (i.e., before consolidation) relative density is used as the basis for comparison.

Table 4.3. Summary table of CD triaxial results.

Test designation	Initial void ratio, e_{BC} [a]	Initial relative density, $D_{r,BC}$ [a]	Void ratio after consolidation e_{AC} [b]	Relative density after consolidation $D_{r,AC}$ [b]	Peak friction angle (deg.) ϕ_{peak}
10-1-9	0.301	0.369	0.301	0.368	43.7
20-1-5	0.305	0.346	0.303	0.356	41.3
50-1-6	0.306	0.340	0.300	0.372	39.3
100-1-5	0.305	0.347	0.295	0.399	38.7
200-1-6	0.304	0.353	0.291	0.421	40.0
300-1-4	0.305	0.347	0.285	0.451	38.3
500-1-4	0.304	0.350	0.285	0.454	39.1
1000-1-3	0.303	0.354	0.276	0.500	38.8
10-1-11	0.261	0.581[c]	0.261	0.581	50.1
20-2-3	0.266	0.554	0.265	0.556	48.4
50-1-4	0.269	0.537	0.266	0.552	45.6
100-1-2	0.264	0.566	0.258	0.595	45.9
200-1-1	0.269	0.535	0.260	0.584	44.2
300-1-3	0.267	0.548	0.255	0.610	43.2
500-1-1	0.265	0.559	0.251	0.634	41.6
1000-1-2	0.266	0.553	0.243	0.674	40.9
10-1-5	0.251	0.633	0.251	0.633	54.3
20-1-3	0.251	0.634	0.250	0.641	51.6
20-1-4	0.245	0.663	0.244	0.668	54.1
50-1-3	0.244	0.669	0.242	0.683	51.1
100-1-3	0.246	0.662	0.240	0.692	47.1
200-1-2	0.250	0.639	0.241	0.686	45.2
300-1-1	0.247	0.655	0.237	0.705	44.6
500-1-3	0.244	0.668	0.233	0.730	43.3
1000-1-1	0.246	0.660	0.227	0.760	41.6

[a] Before Consolidation (BC), [b] After Consolidation (AC), [c] Test 10 - 1 - 11 did not meet density criteria by 0.6 percent.

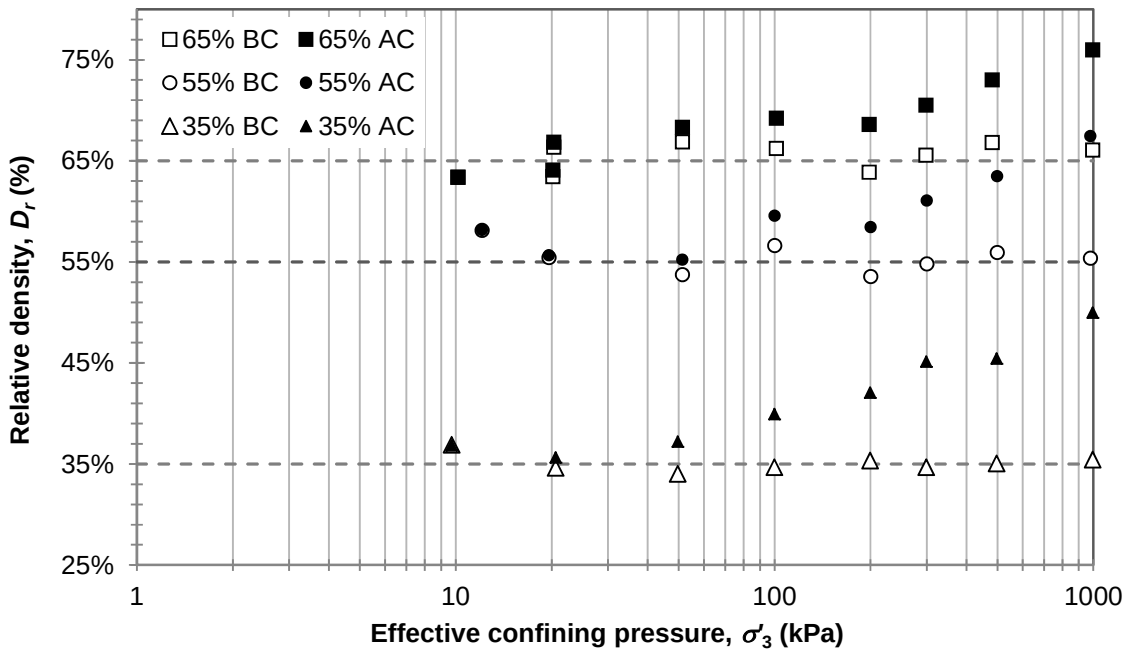

Figure 4.8. Relative density versus confining pressure for all test (BC = before consolidation, AC = after consolidation).

Figure 4.9, Figure 4.10, and Figure 4.11 show the effective principal stress difference-axial strain behavior for tests at 35, 55, and 65 percent relative density, respectively. As shown in Figure 4.11, strain softening occurred at confining pressures up to and including 10 atmospheres (i.e., 1000 kPa) for specimens at a relative density of 65 percent. The amount of strain softening and the initial slopes of the stress-strain curves at 55 percent relative density, shown in Figure 4.10, were smaller than that observed at 65 percent relative density, and was stronger for data at 35 percent relative density, shown in Figure 4.9, as expected from well-known soil mechanics described in chapter 2. See Appendix B for individual stress-strain plots.

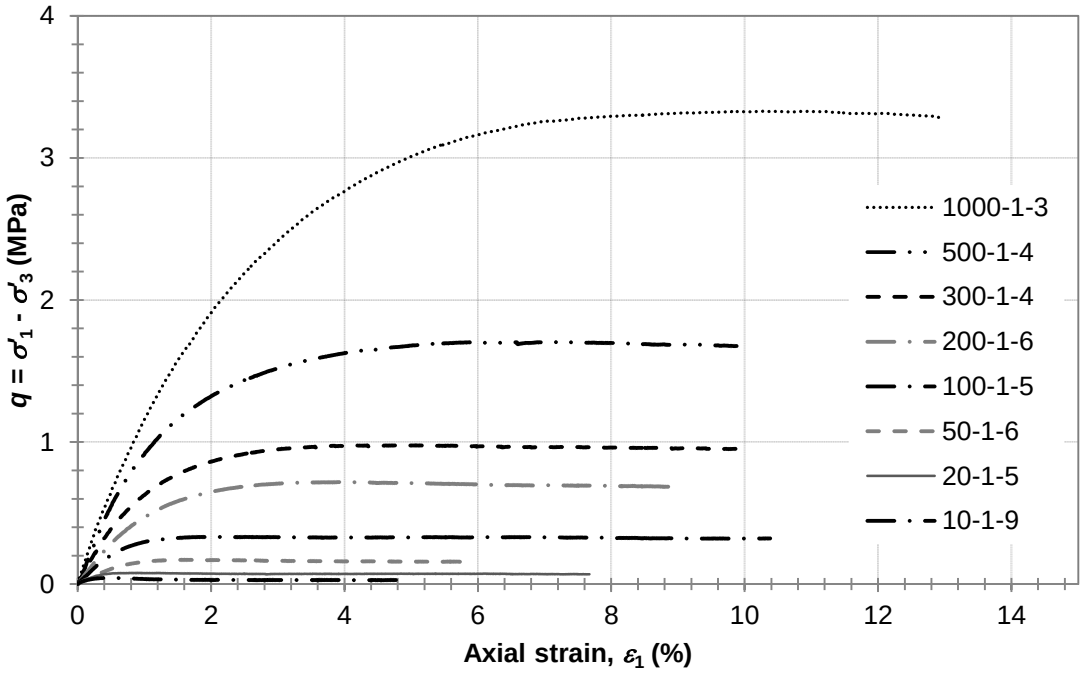

Figure 4.9. Effective principal stress difference versus axial strain for tests at 35 percent relative density.

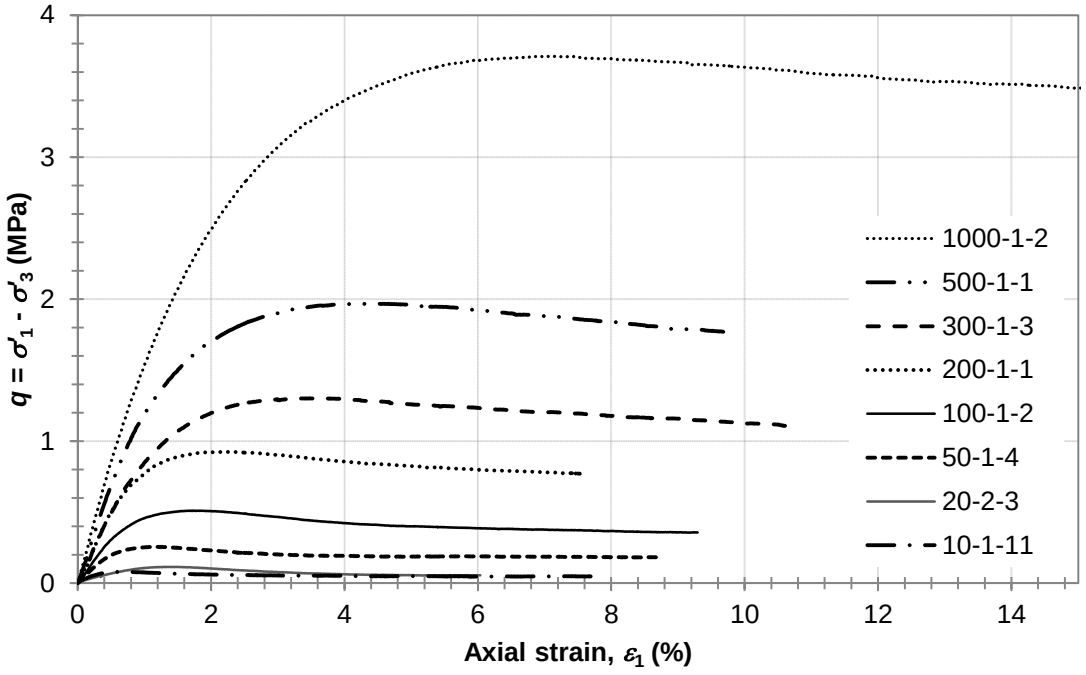

Figure 4.10. Effective principal stress difference versus axial strain for tests at 55 percent relative density.

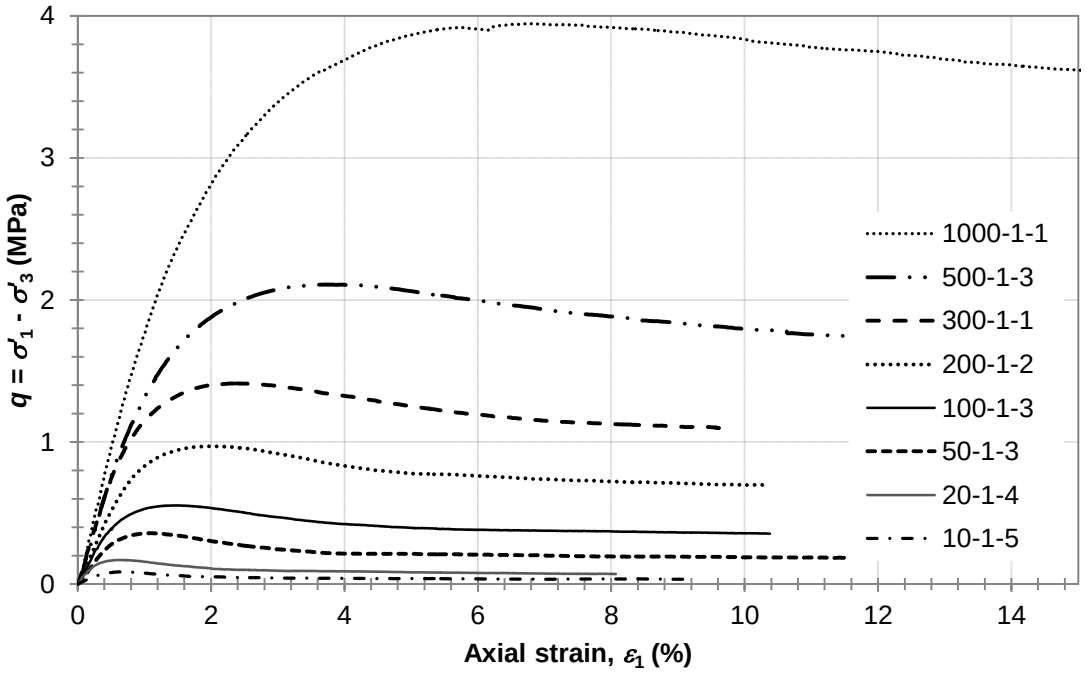

Figure 4.11. Effective principal stress difference versus axial strain for tests at 65 percent relative density.

An important constitutive parameter for soil is the Young's modulus defined as the ratio of the change in principal stress difference to the change in axial strain. Due to the non-linear stress-strain response of soil, Young's modulus is typically reported as an initial tangent modulus, E_i. Figure 4.12(a) presents the variation in initial tangent modulus with effective confining pressure for the 24 specimens evaluated. The initial tangent modulus was computed by dividing the principal stress difference at approximately 0.1 percent axial strain by the corresponding axial strain. In general E_i was found to vary with σ'_3 according to Equation 2.9 (Duncan et al. 1980):

$$\frac{E_i}{P_{atm}} = K\left(\frac{\sigma'_3}{P_{atm}}\right)^n \qquad (2.9)$$

where K is the modulus number, n is the modulus exponent, and P_{atm} is atmospheric pressure.

The initial tangent modulus tended to be larger for specimens sheared at larger effective confining pressures and greater relative densities. Computed values of initial tangent modulus ranged from 18 to 165 MPa. Due to fluctuations in pressure supply, larger variability was observed in E_i for specimens sheared at lower confining pressures, consistent with other mechanical properties as described subsequently. Due to this variability the initial tangent modulus versus confining pressure was plotted again with only those specimens sheared at $\sigma'_3 > 20$ kPa and presented in Figure 4.12(b). With the specimens at lower confining pressure removed two general patterns became apparent: increasing the relative density caused K to increase and the modulus exponent n to decrease.

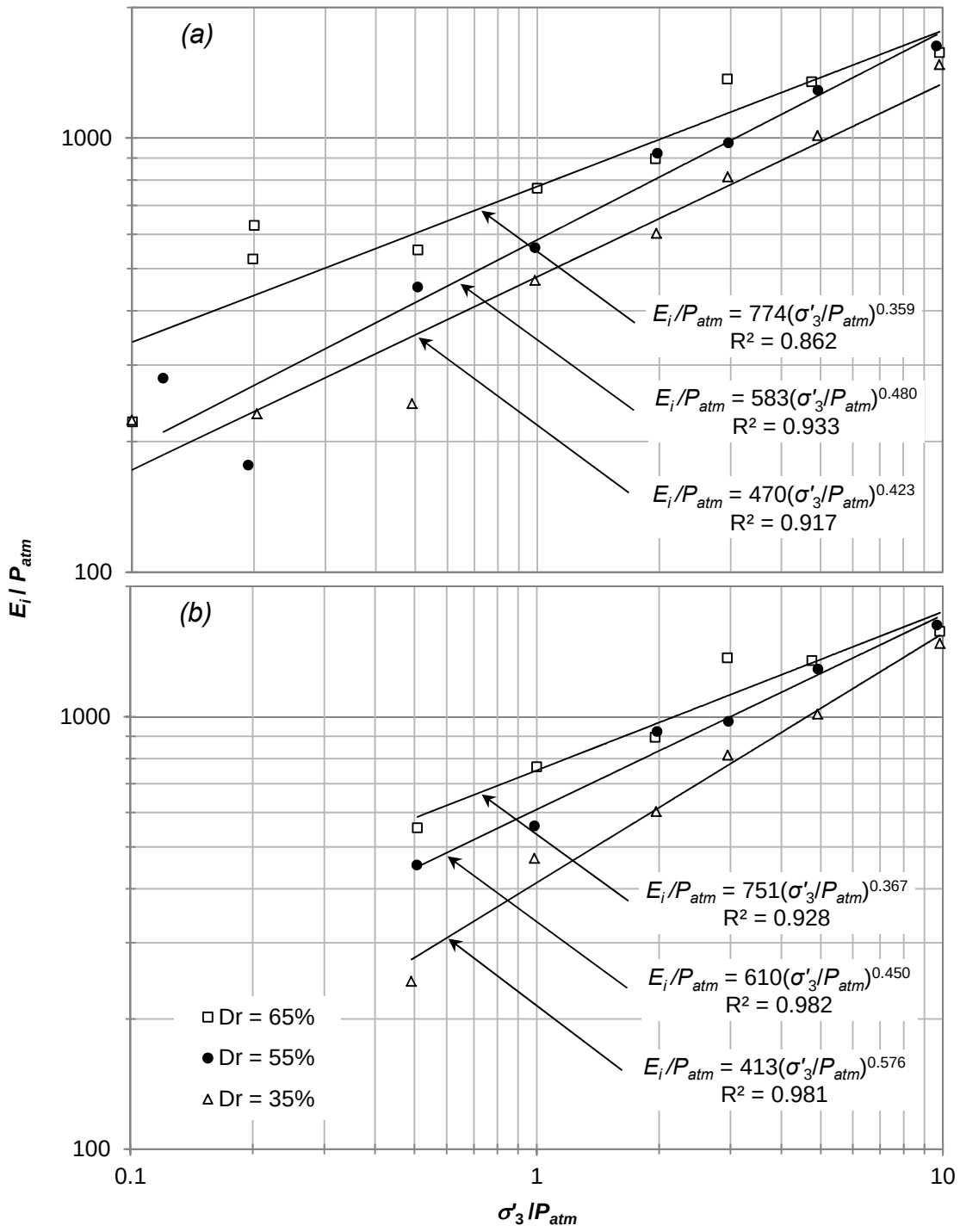

Figure 4.12. Initial tangent modules versus effective confining pressure normalized to atmospheric pressure for (a) all specimens and (b) excluding specimens sheared at $\sigma'_3 \leq 20$ kPa.

For CD triaxial strength tests, failure is typically defined by the maximum principal stress difference $(\sigma'_1-\sigma'_3)_{max}$, the maximum principal stress ratio $(\sigma'_1/\sigma'_3)_{max}$, or at a predetermined amount of shear strain. For the present study, failure was defined as the maximum principal stress ratio as it provides a convenient way to visualize trends in the stress-strain response over a large range in confining pressures. Principal stress ratio versus axial strain for tests at 35, 55, and 65 percent relative density are presented in Figure 4.13, Figure 4.14, and Figure 4.15, respectively. The principal stress ratio increases gradually for tests sheared at σ'_3 = 1000 kPa to a maximum value at axial strains greater than 5 percent. For specimens sheared at σ'_3 < 1000 kPa, the principal stress ratio increases more rapidly, reaching a distinct peak before decreasing to a residual value approximately equal to that of the specimen sheared at σ'_3 = 1000 kPa. The rate of post-peak decay was greater for specimens sheared at lower confining pressures and higher relative densities. This behavior indicates that granular soil exhibits more dilatancy at lower confining pressures and higher relative densities, constant with values reported by Taylor (1948), Bishop (1954), Rowe (1962), Lee and Seed (1967), Rowe (1969), and Bolton (1986). Generally, the peak principal stress ratio tended to be larger at higher relative densities. Furthermore, the peak principal stress occurs at larger axial strains as the effective confining pressure increases, indicating that "failure" occurs at larger strains for specimens sheared at higher effective confining pressures. Figure 4.17 presents the principal stress ratio and axial strain at failure for all test specimens. The previous observation that the peak principal stress ratio tends to be larger for specimens with higher relative densities is reinforced by presenting Figure 4.18 and Figure 4.19.

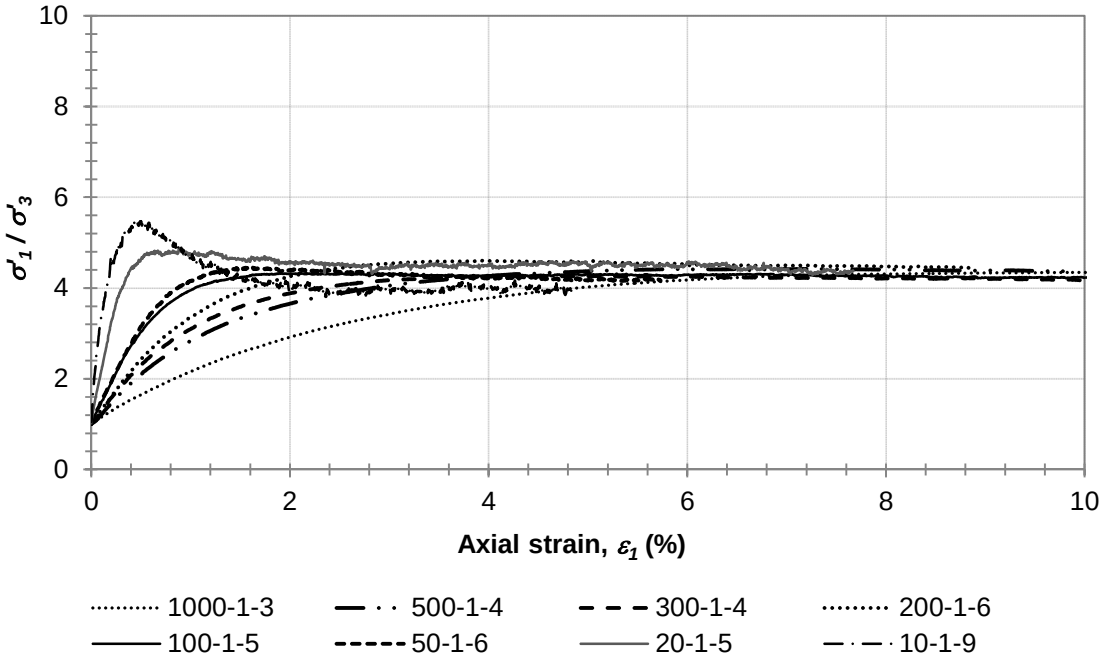

Figure 4.13. Principal stress ratio versus axial strain for tests at 35 percent relative density.

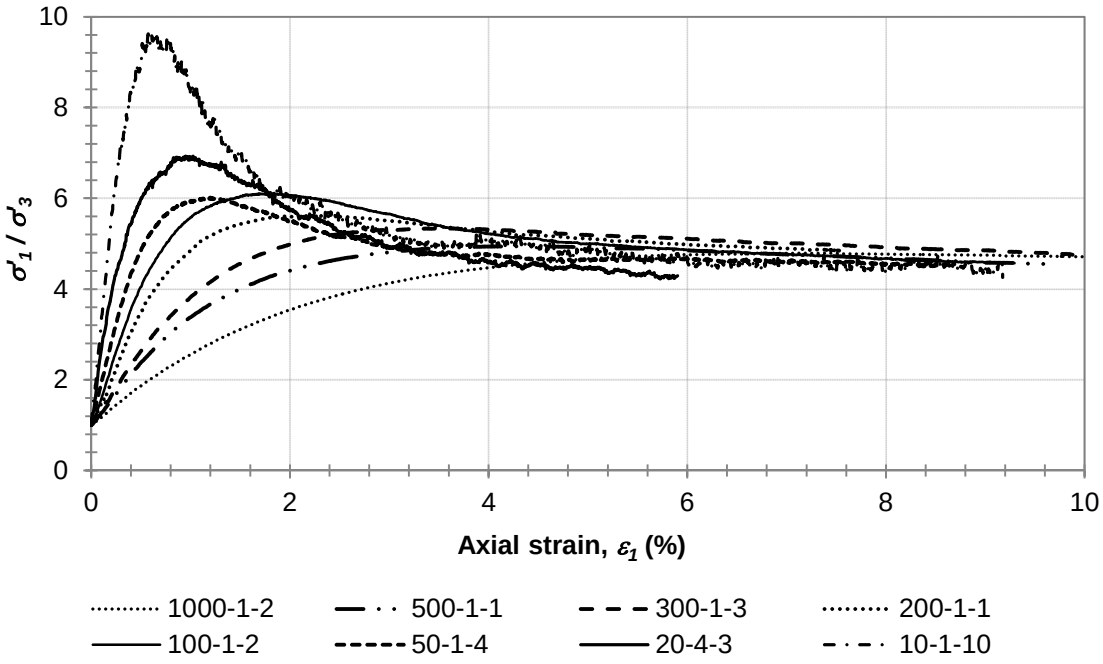

Figure 4.14. Principal stress ratio versus axial strain for tests at 55 percent relative density.

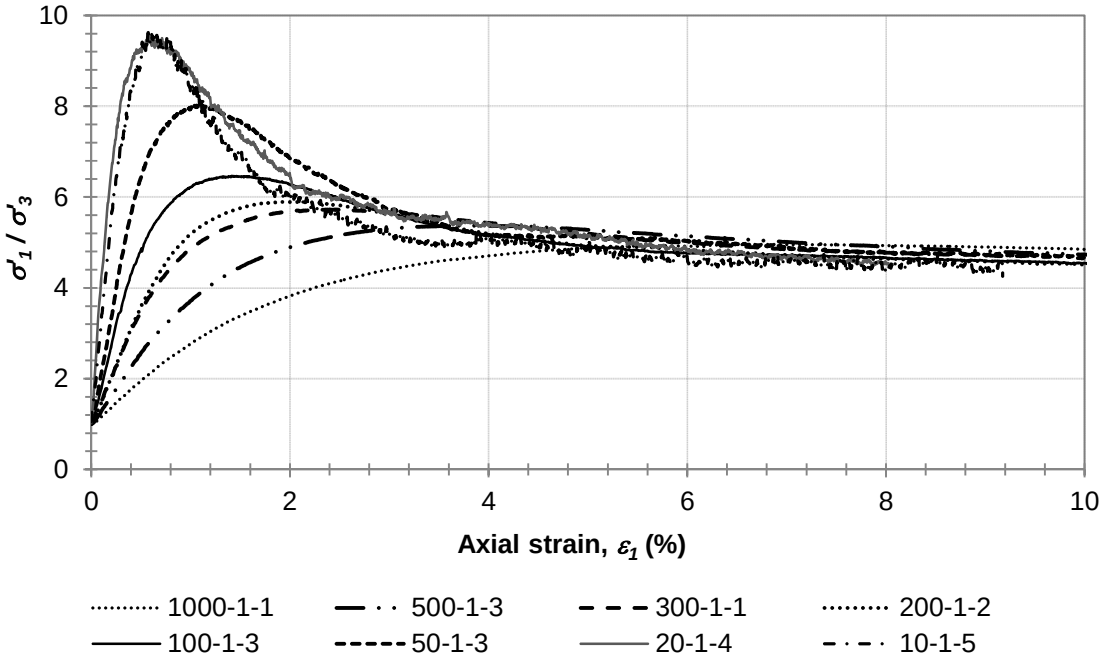

Figure 4.15. Principal stress ratio versus axial strain for tests at 65 percent relative density.

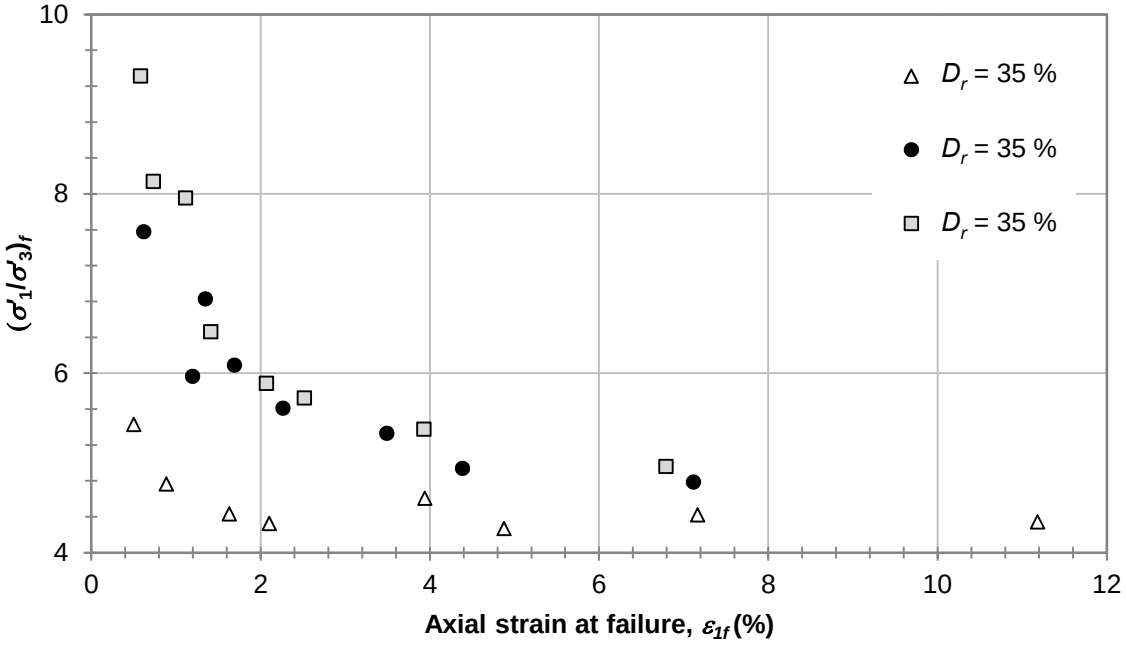

Figure 4.16. Principal stress ratio at failure versus axial strain at failure.

The volumetric behavior of dense granular materials is unique as it tends to increase in volume as it shears. Figure 4.17, Figure 4.18 and Figure 4.19 show the volumetric strain versus axial strain for specimens at 35, 55, and 65 percent relative density, respectively. Initially all specimens displayed contractive behavior (positive volumetric strain; note: expansion is considered negative in this thesis). For denser specimens (i.e. specimens with D_r = 55 or 65 percent) and for loose specimens sheared at lower confining pressures, the slope of the volumetric strain versus axial strain reversed, becoming progressively more negative until failure occurred corresponding to an inflection point on the volumetric strain-axial strain curve. For loose specimens sheared at higher confining pressures (i.e., tests 500-1-4 and 1000-1-3) the volumetric strain increased near-monotonically throughout the range in axial strains experienced. The volumetric strains recorded at large axial strains for relative densities of 55 and 65 percent shows continued linear dilative behavior. This behavior does not agree with evidence that suggests soil in a shear zone will reach a critical state where shearing can occur without volume change (Roscoe 1970). This observed linear dilation may be explained by considering that the deformed shape of the specimen progressively deviates from the assumed deformed shape due to membrane and end restraints (Bishop and Henkel 1962). The difference between the assumed and observed triaxial deformation is shown conceptually in Figure 4.20. Since the volumetric strains recorded at larger axial strains may be inaccurate, the volumetric behavior at these strains was not considered.

As discussed in Chapter 2, the maximum rate of dilation is defined as the ratio of change in volumetric strain and change in axial strain during the dilative portion of shearing, $(\Delta\varepsilon_v/\Delta\varepsilon_1)_{max}$. As shown in Figure 4.17, Figure 4.18, and Figure 4.19 the maximum dilation rate depended on the confining pressure and relative density. Specimens sheared at low confining pressures and higher relative densities tended to have larger dilations rates. Dilation rates ranged from –2.83 for the specimen sheared at 10 kPa with a relative density of 65 percent, to 0.14 for the specimen sheared at 1000 kPa with a relative density of 35 percent.

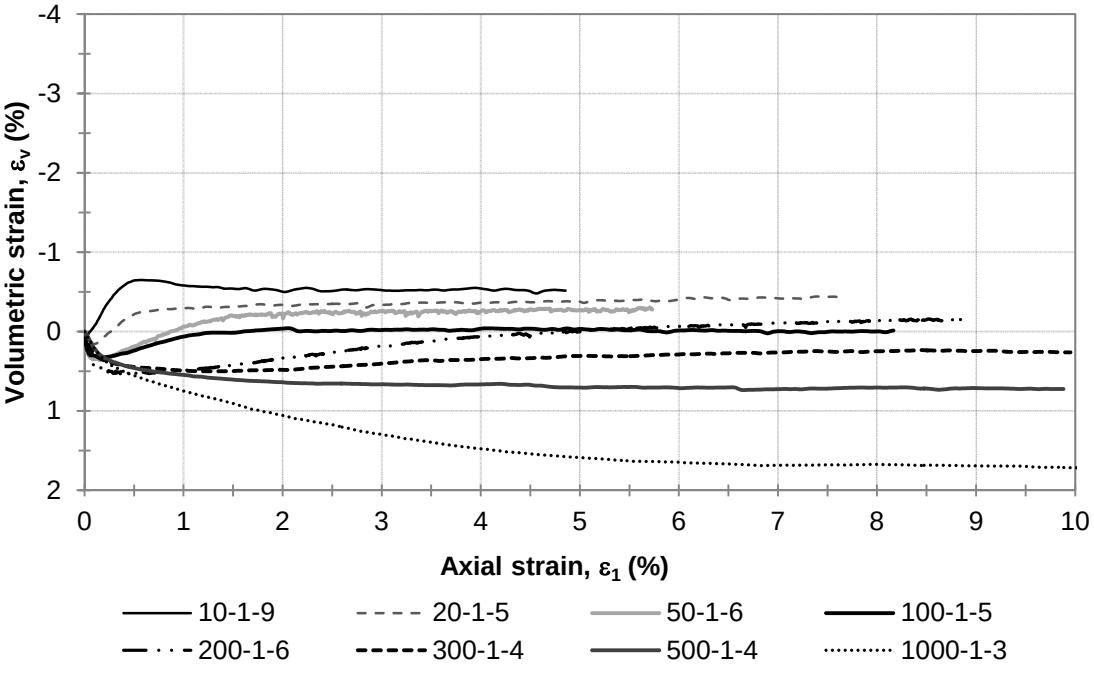

Figure 4.17. Volumetric strain versus axial strain for tests at 35 percent relative density.

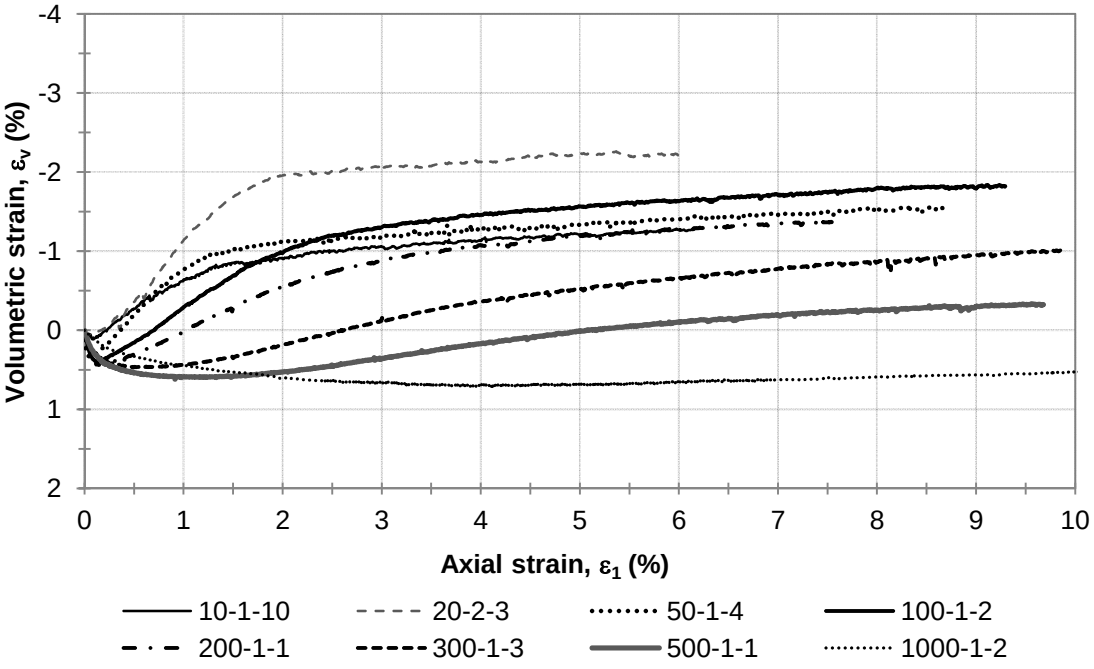

Figure 4.18. Volumetric strain versus axial strain for tests at 55 percent relative density.

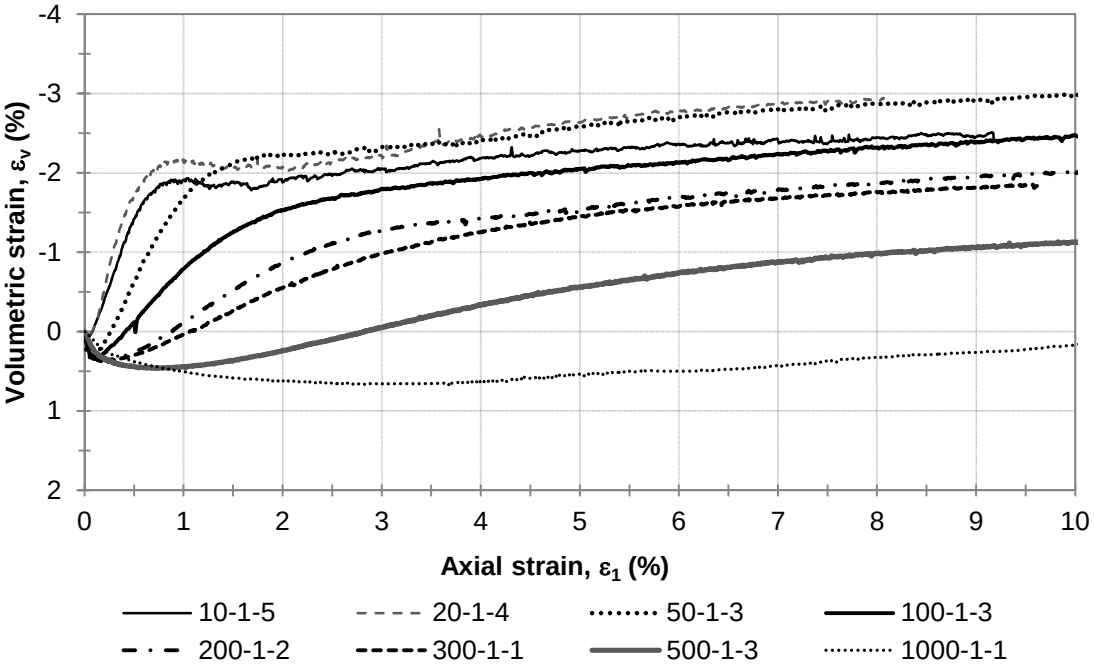

Figure 4.19. Volumetric strain versus axial strain for tests at 65 percent relative density.

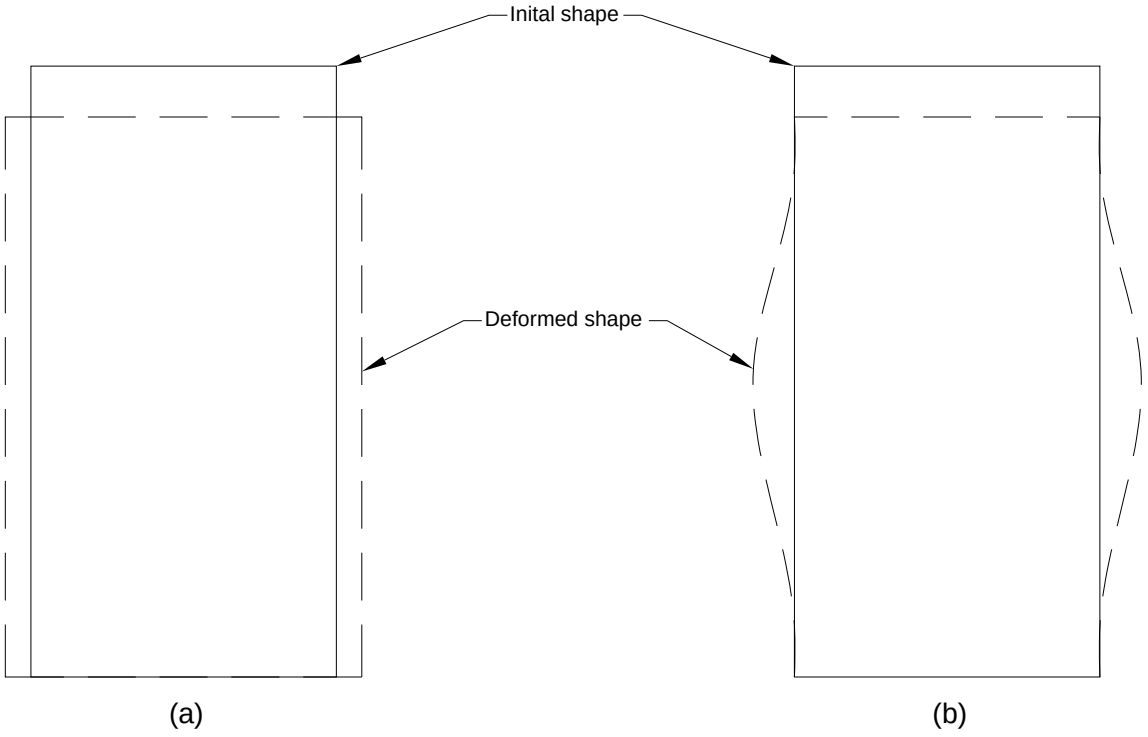

Figure 4.20. Difference between the (a) assumed and (b) observed deformed shape of triaxial specimens.

4.2.4.3 Friction Angles

Chapter 2 describes the basic behavior of granular soils and some typical strength parameters used to calculate the shear strength for different conditions. For each specimen, the friction angle was calculated twice using:

$$\phi' = \sin^{-1}\left(\frac{\sigma'_1 - \sigma'_3}{\sigma'_1 + \sigma'_3}\right) \qquad (4.3)$$

First, the friction angle was calculated using the principal stresses at failure (i.e., at the maximum principal stress ratio), defined as the effective peak friction angle, ϕ'_d, and then using the residual principal stresses to compute what is termed the effective residual friction angle, ϕ'_r.

Figure 4.21 presents the variation in peak friction angle with effective confining pressure and the effective confining pressure normalized to atmospheric pressure (P_{atm} = 101.3 kPa = 14.7 psi). Generally, the peak friction angle decreases linearly with an increase in natural logarithm of effective confining stress as shown by coefficients of determination, R^2, near unity. Peak friction angles ranged from 54° for the specimen sheared at 10 kPa with a relative density of 65 percent, to 39° for the specimen sheared at 1000 kPa with a relative density of 35 percent.

Similar to the dilation rate, it was observed that the peak friction angle was dependent on relative density. The log-linear rate of decrease of peak friction angle was greater for specimens sheared at higher relative densities. For specimens sheared at 65 percent relative density, a reduction of 7° per log cycle was observed, whereas a 2° reduction per log cycle was observed for samples sheared at 35 percent relative density. The smaller reduction in friction angles for specimens sheared at D_r = 35 percent may be due to the significant densification that occurred in specimens consolidated to σ'_3 > 100 kPa. The consolidation-based increase in relative density would tend to result in an increase in friction angle.

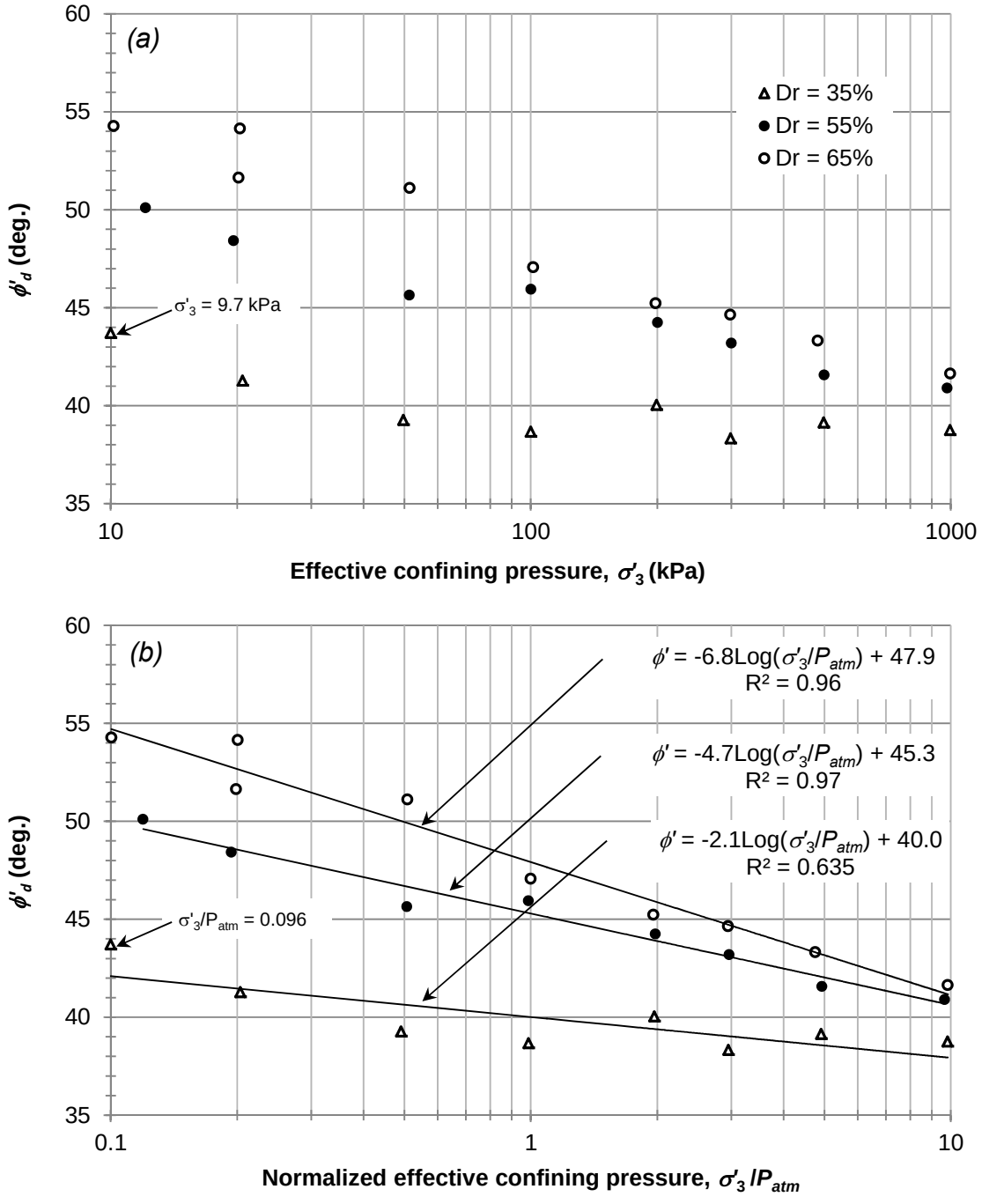

Figure 4.21. Peak friction angles as measured in triaxial compression versus (a) σ'_3 and (b) σ'_3/P_{atm}.

Effective residual friction angles were computed for each test and are presented in Figure 4.22. The "residual" principal stresses were taken at 10 percent axial strain, or at the last recorded principal stresses prior to termination of the tests .

Residual friction angles were fairly constant over the range of confining pressures tested. This behavior may indicate that the sheared region of the specimens reached a pseudo-critical state. When considering all 24 tests, the average residual friction angle was 39.5 degrees. However, based on an analysis of variance (ANOVA) F-test, the mean residual friction angle for specimens sheared at 35 percent relative density was found to be significantly different from those sheared at 55 and 65 percent with a 5 percent significance level (p-value = 0.0003).

The average residual friction angles for specimens tested at relative densities of 35, 55, and 65 percent are presented in Table 4.4. Specimens tested at low confining pressures produced considerably more scatter than those tested at higher pressures. This behavior may be due to small specimen imperfections being amplified by the lack of confinement, as well as the sensitivity to flucuations in supply pressure as discribed previusly. Two specimens in particular, 10-1-5 65 (D_r = 65 percent) and 20-2-3 (D_r = 55 percent), were suspected of being outliers with residual friction angles differing by more than 2 standard deviations from their mean.

Table 4.4. Average and standard deviation of residual friction angles for specimens sheared at 35, 55, and 65 percent relative densities.

D_r (%)	$\phi'_{r,avg}$ (deg)	Standard Deviation (deg)
35	38.2	0.89
55	39.6	2.06
65	40.4	1.64
All	**39.5**	**1.79**

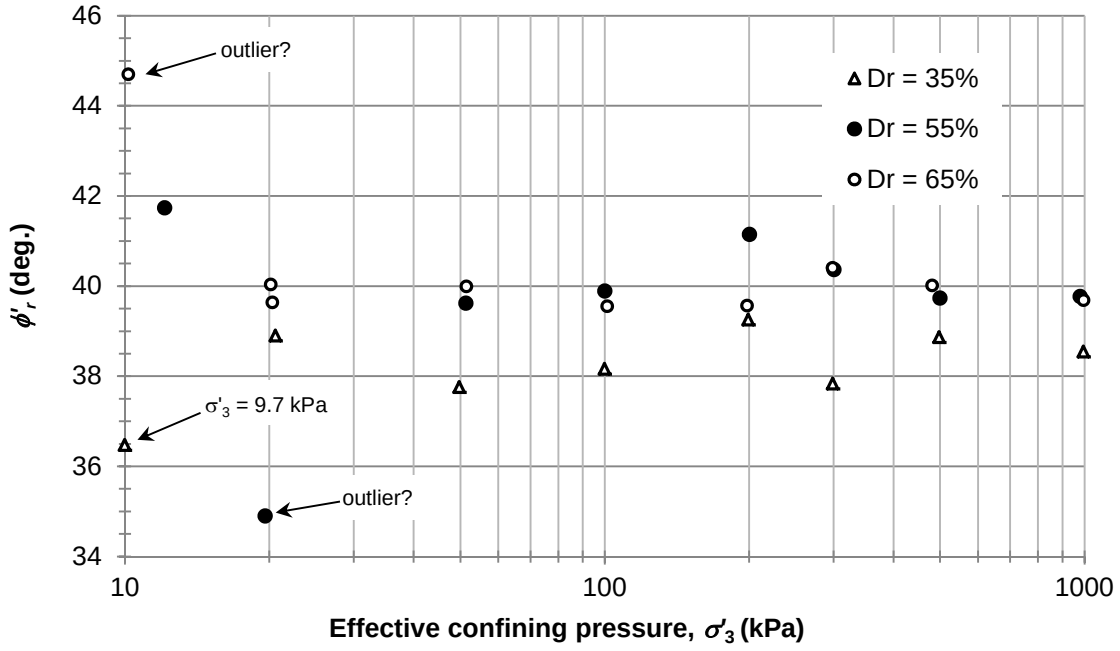

Figure 4.22. Residual friction angles as measured in triaxial compression.

4.2.4.4 Dilation Angles

The dilation angle is an important constitutive parameter used to model volumetric deformations during shearing as discussed in Chapter 2. Dilation angles were determined by measuring the maximum negative slope (maximum dilation rate) of the volumetric strain, ε_v, versus major principal strain, ε_1, curves $(d\varepsilon_v/d\varepsilon_1)_{max}$. This was done by fitting a third order polynomial to the dilative portion of the volumetric strain versus axial strain curve and then determining the maximum calculated incremental change in volumetric strain.

Two definitions of the dilation angle were compared. The friction angle with the contribution of dilation removed, ϕ_f, was first calculated using Equation 2.4 proposed by Rowe (1962). To determine the dilation angle, ϕ_f was subtracted from the peak friction angle. Secondly, the definition of dilation proposed by Tatsuoka (1987) was computed using:

$$\psi_{max} = \sin^{-1}\left(-\frac{\frac{d\varepsilon_v}{d\varepsilon_1}}{2-\frac{d\varepsilon_v}{d\varepsilon_1}}\right)_{max} \quad (4.4)$$

Figure 4.23 presents the dilation angles calculated using the Rowe (1962) approach and the method by Tatsuoka (1987) for all tests with D_r = 65 percent; Table 4.5 presents dilation angles for each of the 24 specimens. The ratio of dilation angles calculated using the approach by Rowe (1962) to those computed using the method by Tatsuoka (1987) varies from 0.75 to 0.92 with mean and median of 0.83 and 0.84, respectively.

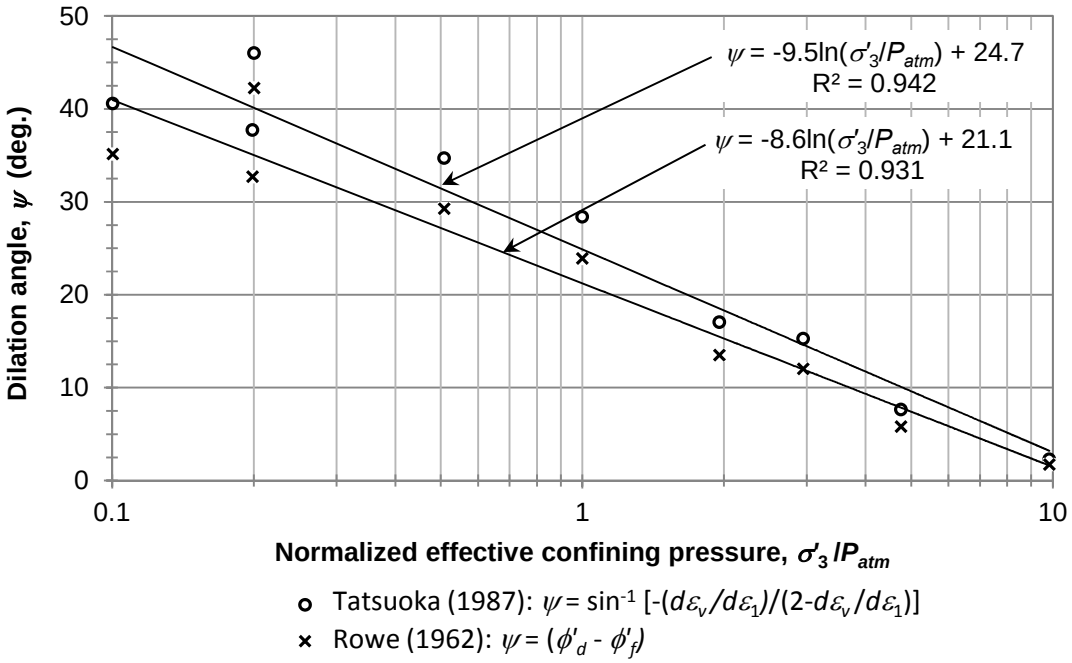

Figure 4.23. Comparison of dilation angles calculated using Tatsuoka (1987) and Rowe (1962) for D_r = 65 percent.

Figure 4.24 presents the variation in peak dilation angle following Tatsuoka (1987) with effective confining pressure normalized to atmospheric pressure. Generally, the peak dilation angle decreases linearly with an increase in the natural logarithm of effective confining stress as shown by coefficients of determination, R^2, near unity. Peak dilation

angles ranged from 40° for the specimen sheared at 10 kPa with a relative density of 65 percent, to -0.2° for the specimen sheared at 1000 kPa with a relative density of 35 percent.

Similar to the peak friction angle, it was observed that the peak dilation angle was dependent on relative density and confining stress. The log-linear rate of decrease of peak dilation angle was greater for specimens sheared at higher relative densities. For specimens sheared at 65 percent relative density, a reduction of 9 degrees per log cycle was observed, whereas only a 6 degrees reduction was observed for samples sheared at 35 percent relative density.

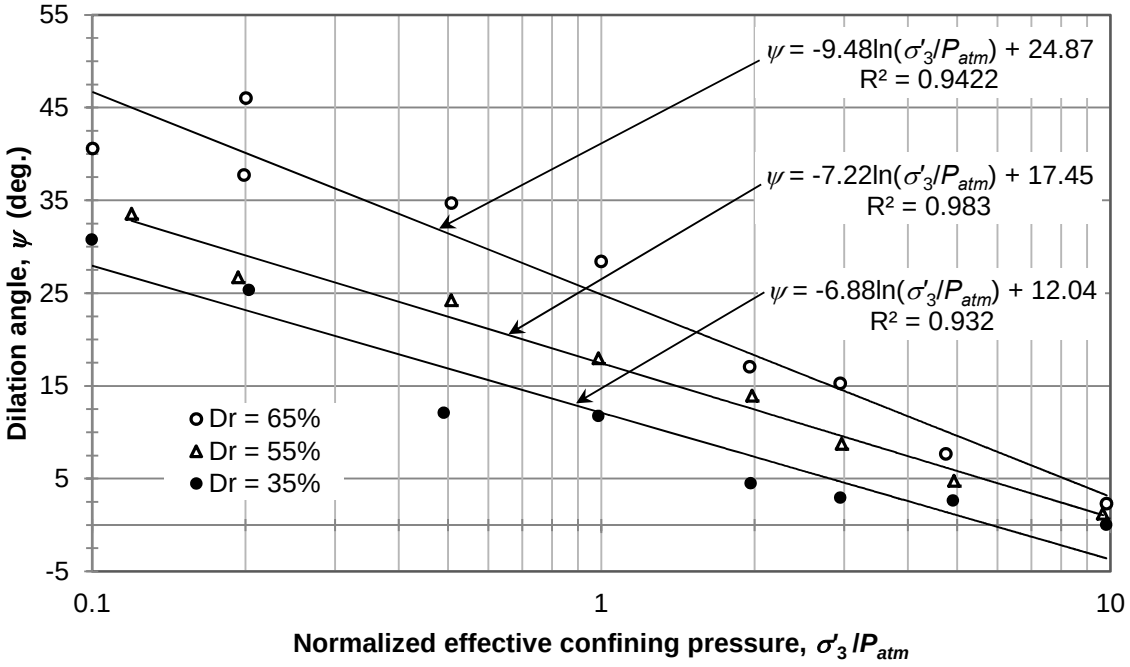

Figure 4.24. Dilation angles calculated using Tatsuoka (1987) versus normalized confining pressure.

Table 4.5. Summary table of dilation angles calculated using Tatsuoka (1987) and Rowe (1962).

Test ID (σ'_3 - OCR - Test #)	D_r BC[a]	σ'_3/P_{atm}	ψ (Tatsuoka 1987) (deg.)	ψ (Rowe 1962) (deg.)
10-1-9	0.369	0.10	30.8	27.0
20-1-5	0.346	0.20	25.3	23.1
50-1-6	0.340	0.49	12.1	10.1
100-1-5	0.347	0.99	11.7	9.8
200-1-6	0.353	1.97	4.5	3.5
300-1-4	0.347	2.95	2.9	2.3
500-1-4	0.350	4.91	2.6	2.1
1000-1-3	0.354	9.82	-0.3	-0.2
10-1-11	0.581[b]	0.12	33.5	28.2
20-2-3	0.554	0.19	26.7	22.1
50-1-4	0.537	0.51	24.2	20.3
100-1-2	0.566	0.99	18.0	14.2
200-1-1	0.535	1.98	14.0	11.0
300-1-3	0.548	2.97	8.7	6.8
500-1-1	0.559	4.93	4.8	3.7
1000-1-2	0.553	9.67	1.2	1.0
10-1-5	0.633	0.10	40.6	35.1
20-1-3	0.634	0.20	37.7	32.7
20-1-4	0.663	0.20	46.0	42.2
50-1-3	0.669	0.51	34.7	29.3
100-1-3	0.662	1.00	28.4	23.9
200-1-2	0.639	1.96	17.0	13.5
300-1-1	0.655	2.95	15.3	12.0
500-1-3	0.668	4.76	7.6	5.8
1000-1-1	0.660	9.84	2.3	1.7

[a] Before Consolidation (BC), [b] Test 10 - 1 - 11 did not meet density criteria by 0.6 percent.

To better visualize the combined effect of relative density and confining pressure on the volumetric response of the backfill soil, the three variables were plotted together to create what is typically referred to as a Peacock diagram (Holtz and Kovacs 1981). In Figure 4.25, a three dimensional surface presented as contour lines was created by plotting the relative density after consolidation on the y-axis, the normalized confining pressure on the x-axis, and the volumetric strains at failure on the z-axis. Because the relative density after consolidation is referenced in Figure 4.25, this diagram may best represent the global shearing response of the granular material investigated from a fundamental standpoint. In general, the most positive volumetric strains, indicating contractive behavior at failure, occur at high effective confining pressures and low relative densities. The most negative volumetric strains, indicating dilative behavior at failure, occur at lower confining pressures and higher relative densities. Additionally, the contour lines become more closely spaced at lower confining pressure indicating that the effect of dilation increases nonlinearly as the confining pressure decreases. This behavior reinforces the trends observed with the dilation angles in Figure 4.24. Using the Peacock diagram, the volumetric strain at failure may be easily estimated for any combination of effective confining pressure and post-consolidation relative density.

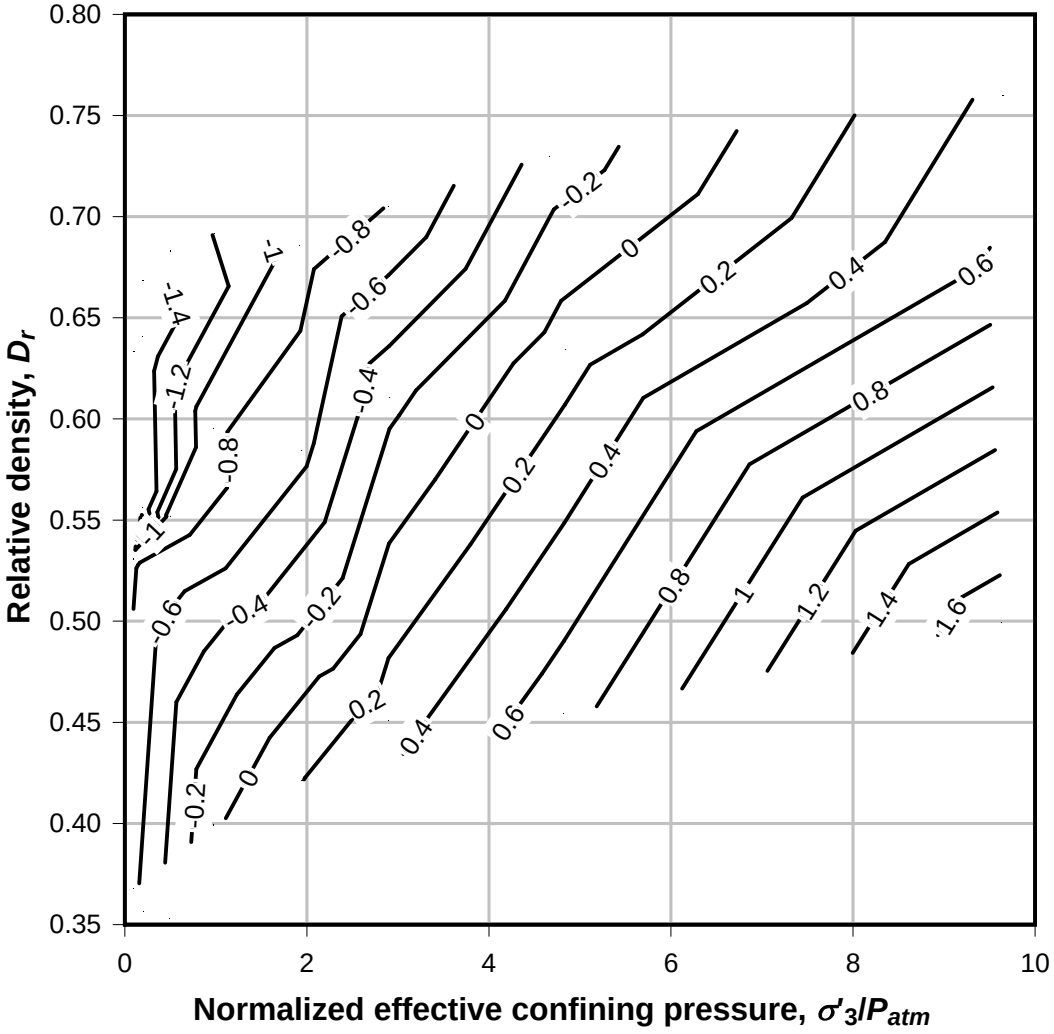

Figure 4.25: Peacock diagram showing the relationship between volumetric strain at failure (shown by the contour lines), relative density and confining pressure.

4.3 Comparison to Previous Triaxial Test Results

In order to evaluate the results of the CD triaxial strength testing program, they were compared to triaxial compression data reported by Verdugo and Hoz (2007). Verdugo and Hoz (2007) tested five different fluvial gravels using 15 cm (6 in.) diameter specimen with non-lubricated ends. The main objective of Verdugo and Hoz (2007) was to study the effect of parallel gradations on stress-strain response. It was concluded that the use of parallel gradations from the same parent soil resulted in little change in the stress-strain

response in triaxial compression. Conclusions regarding the effect of volumetric response were not provided by Verdugo and Hoz (2007). Table 4.6 presents the index properties for the soils considered by Verdugo and Hoz (2007).

Table 4.6. Gradation classification information for five of the soil gradations tested by Verdugo and Hoz (2007) and the present study.

Soil	D_{50} (mm)	D_{60} (mm)	D_{30} (mm)	D_{10} (mm)	C_u	C_c	γ_{min} (kN/m^3)	γ_{max} (kN/m^3)	D_r
A-1	12.7	15.8	6.6	1.9	8.3	1.4	17.6	20.2	0.80
M-1	2.4	3.6	1.1	0.5	6.7	0.7	16.0	19.7	0.80
M-2	3.8	5.4	1.2	0.3	16.1	0.8	17.8	21.3	0.70
M-3	5.7	6.8	2.8	0.3	21.2	3.5	17.5	19.9	0.70
P-1	2.4	3.7	0.7	0.1	28.8	1.1	17.1	21.6	0.80
Present Study	6.0	9.5	1.0	0.2	39.6	0.4	19.4	22.4	0.65

By observing the gradations plotted in Figure 4.26, the soils with gradations most parallel to the target gradation used in the present study appear to be soils A-1 and M-2. The principal effective stress difference-axial strain and volumetric strain-axial strain data for soils A-1 and M-2 are compared to those of the backfill soil in Figure 4.27 and Figure 4.28, respectively.

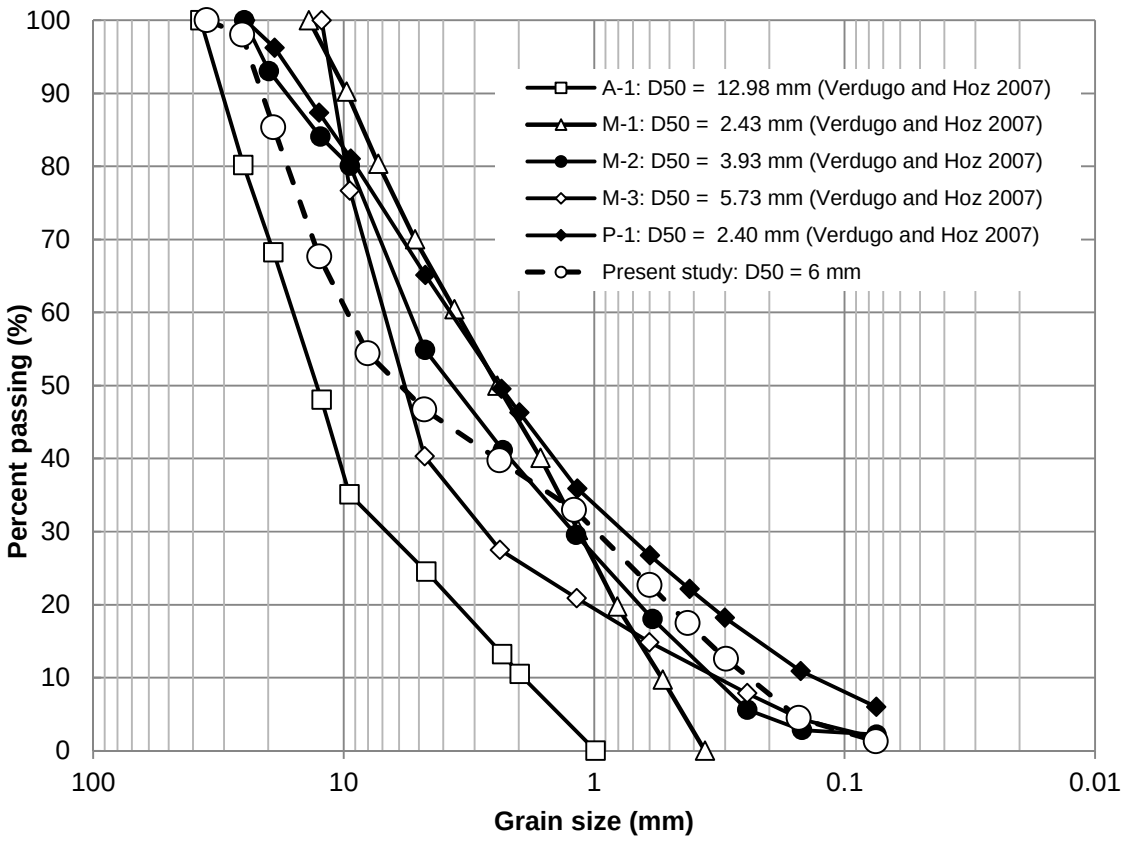

Figure 4.26. Comparison of Grain size distributions from Verdugo and Hoz (2007) and the present study.

As shown in Figure 4.27, the initial stiffness of soil A-1 is similar to that of the backfill soil. The maximum effective principal stress difference was considerably larger for soil A-1, though it is important to note that the relative density and confining pressures were not the same as those in the used in the present study. The relative density of the A1 specimens were 15 percent greater than the specimens considered in the present study as shown in Table 4.6 which may explain the larger principal stress ratios observed for the A1 specimens. Additionally, it should be noted that the A1 specimens tested at confining pressures of 400 and 600 kPa are compared to present study specimens sheared at confining pressures of 300 and 500 kPa, respectively, causing the peak principal stress difference of the A1 specimens to be larger. The maximum negative volumetric strains were also much larger for soil A-1, though the maximum dilation rates appeared to be similar to those of the backfill soil.

For soil M-2, shown in Figure 4.28, the initial stiffness of the specimens were less than those of the backfill soil, though the peak and residual principal stress differences for both soils were very similar. The maximum negative volumetric strains were similar for soil M-2 and the backfill, though the dilation rates appeared to be much lower for soil M-2. Additionally, the longevity of the initial contractive portion of the volumetric strain-axial strain curves was much larger for soil M-2 than for the backfill soil. The discrepancies between these soils regarding the stress-strain and volumetric behavior were mainly attributed to variations in general soil characteristics such as surface roughness and angularity. However, differences in relative densities should be noted as well. The wide range in responses between these relatively similar soils emphasizes the need for soil-specific testing.

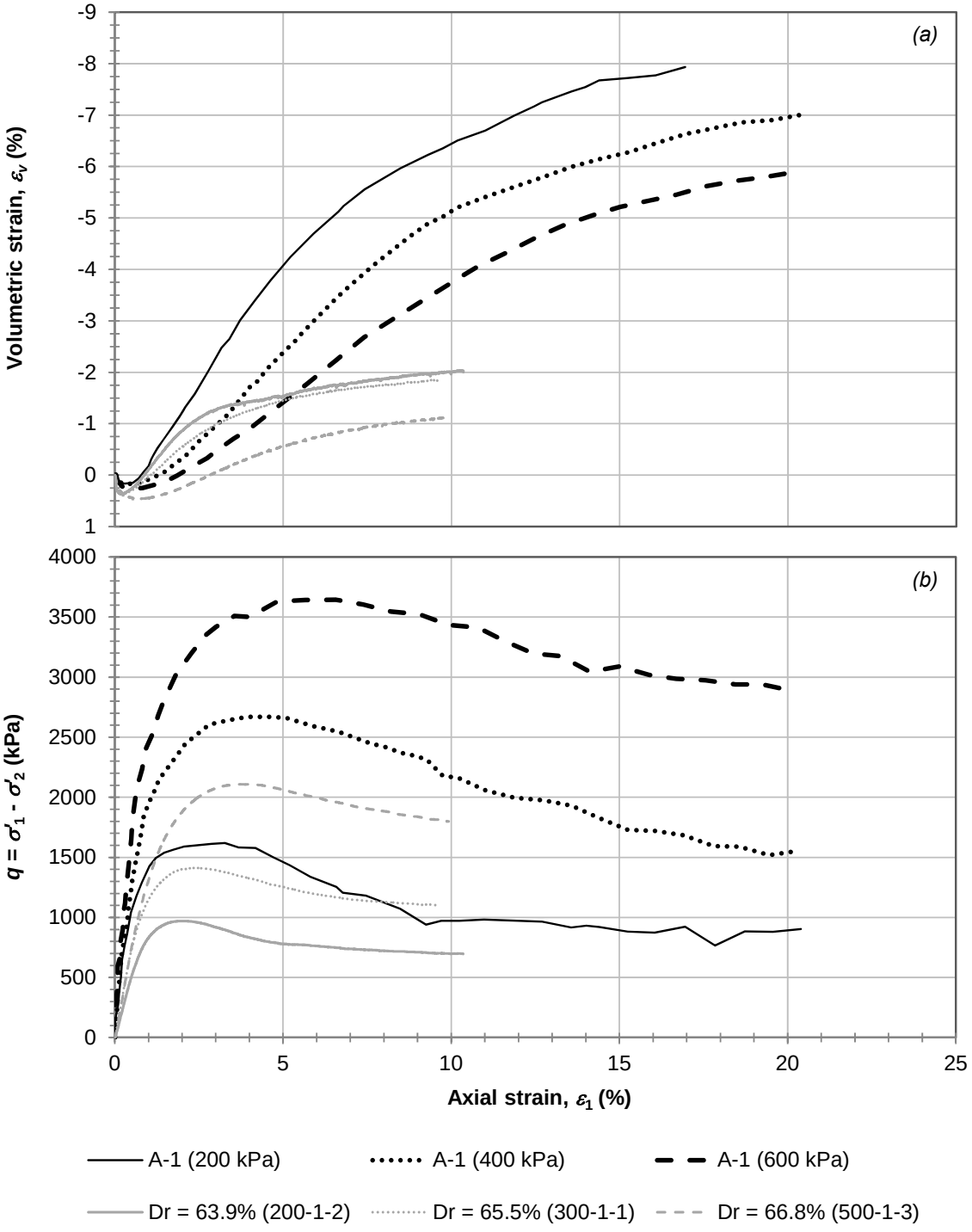

Figure 4.27. Deviatoric stress-axial strain and volumetric strain-axial strain comparison plots for soil A-1 (Verdugo and Hoz 2007) and the present study.

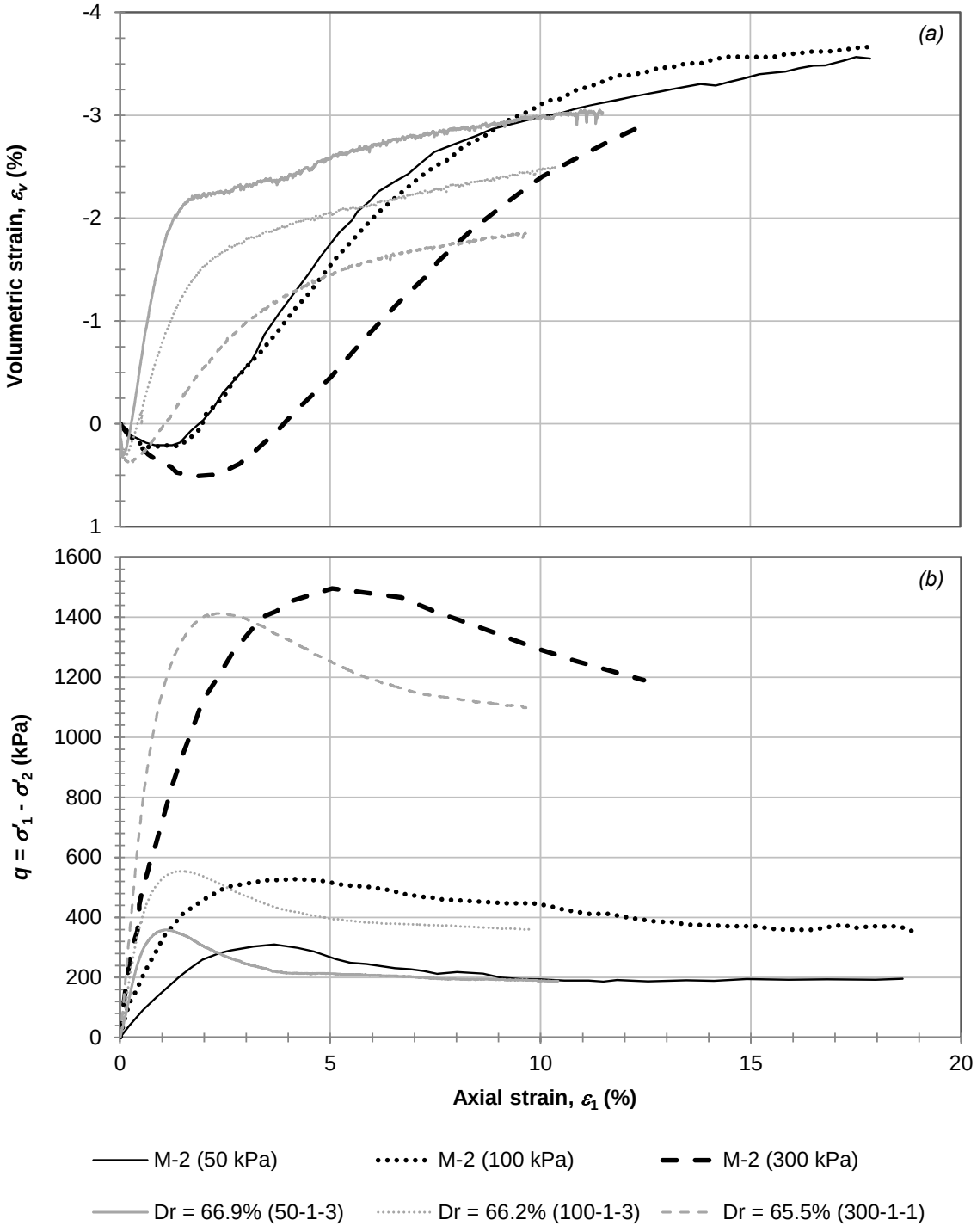

Figure 4.28. Deviatoric stress-axial strain and volumetric strain-axial strain comparison plots for soil M-2 (Verdugo and Hoz 2007) and the present study.

In order to compare the volumetric response of each soil type, the maximum dilation angles were calculated for each test using the Tasuoka (1987) method. The computed dilation angles are presented in Figure 4.29 along with the maximum dilation angles computed for the backfill soil at 65 percent relative density. For confining stresses of 200 kPa and greater, the dilation angles for the present study are within the range presented by Verdugo and Hoz (2007). However, there were no data to confirm the higher dilation angles computed for confining pressures of 100 kPa and less.

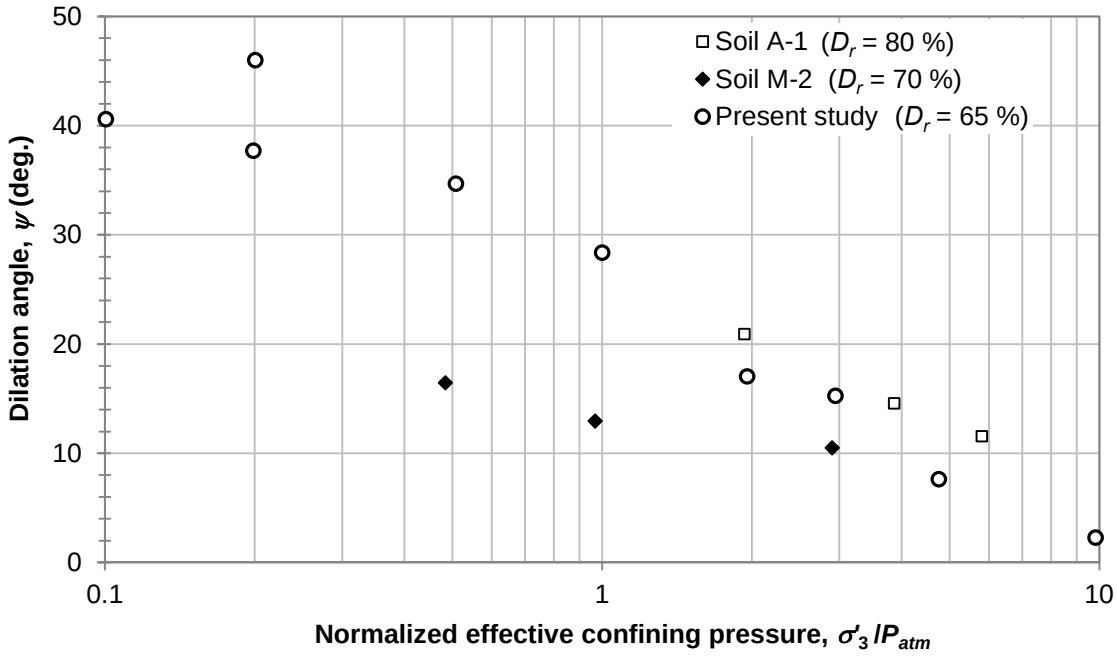

Figure 4.29. Comparison of dilation angle versus normalized confining pressure for Verdugo and Hoz (2007) and the present study with D_r = 65 percent (dilation angles calculated using Equation 4.4).

4.4 Hyperbolic Constitutive Model Calibration

The stress-strain response of soil is non-linear and therefore should not be modeled with a constant modulus. In many cases, a hyperbolic constitutive model can be used to estimate the stress-strain behavior of soils. Using the methods outlined in Duncan and Chang (1970) and Duncan et al. (1980), a hyperbolic stress-strain model was fit to the

stress strain and volumetric strain versus axial strain data. Section 2.1.5 discusses the procedure used in calibrating this model.

The fitting parameters for relative densities of 35, 55, and 65 percent are presented in Table 4.7. Figure 4.30 presents the initial tangent moduli and bulk moduli calculated for each specimen. Similar to the initial tangent moduli, E_i, presented in Figure 4.12, the initial tangent moduli calculated using Duncan and Chang (1970) have modulus exponents of approximately 0.4. However, the initial tangent moduli calculated using Duncan and Chang (1970) are significantly larger than those measured directly. This discrepancy arises from the hyperbolic relationship not having a theoretical basis, but rather an empirical one. The larger tangent modulus values simply provide a better fit over the full range in the data.

The bulk moduli, B, have exponents of approximately 0.9. Although the bulk moduli are presented here, the hyperbolic model cannot predict the volumetric response of dilative soil beyond initial contraction phases as described in Chapter 2 and Duncan et al. (1980). Figure 4.31 compares the fit of the Duncan and Chang (1970) hyperbolic model to the CD triaxial data for specimens sheared at a relative density of 65 percent. The Duncan and Chang (1970) model fits the general trend of the stress-strain behavior for working stress levels ranging from 0.5 to 3 percent axial strain for σ'_3 ranging from 10 to 1000 kPa, respectively. However, as specimens approach or achieve failure, the predicted stress-strain curve deviates significantly from that observed.

Table 4.7. Hyperbolic fitting parameters determined using the procedures outlined in Duncan and Chang (1970).

Relative density, D_r (percent)	Average failure ratio, $R_{f(average)}$	Bulk Modulus, K_b	Bulk modulus exponent, m	Modulus, K	Modulus exponent, n
65	0.644	114.3	0.980	1200.0	0.475
55	0.673	103.3	0.961	893.1	0.525
35	0.719	104.6	0.861	725.7	0.383

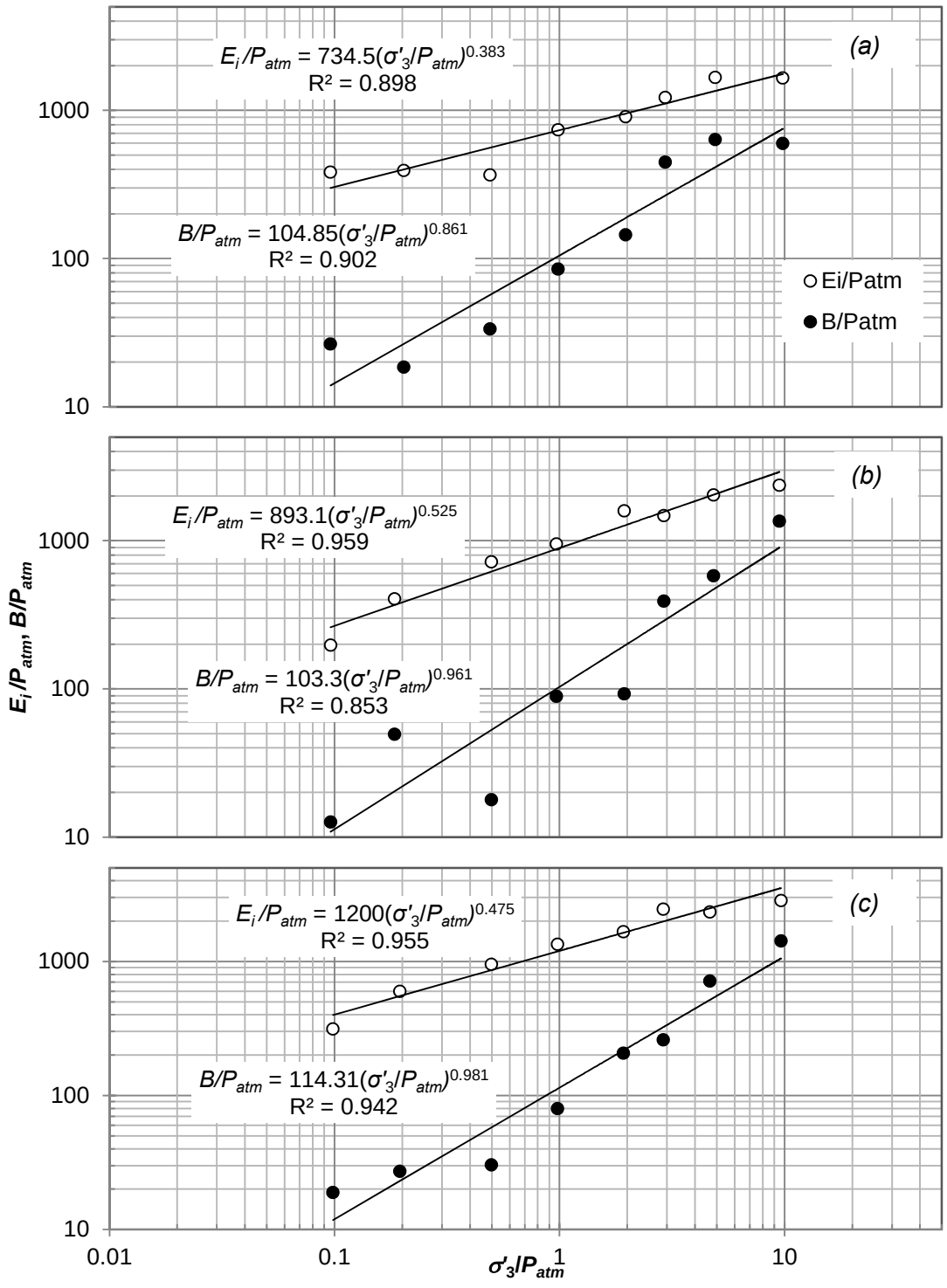

Figure 4.30. Normalized tangent modulus verse normalized confining pressures for relative densities of (a) 35, (b) 55, and (c) 65 percent.

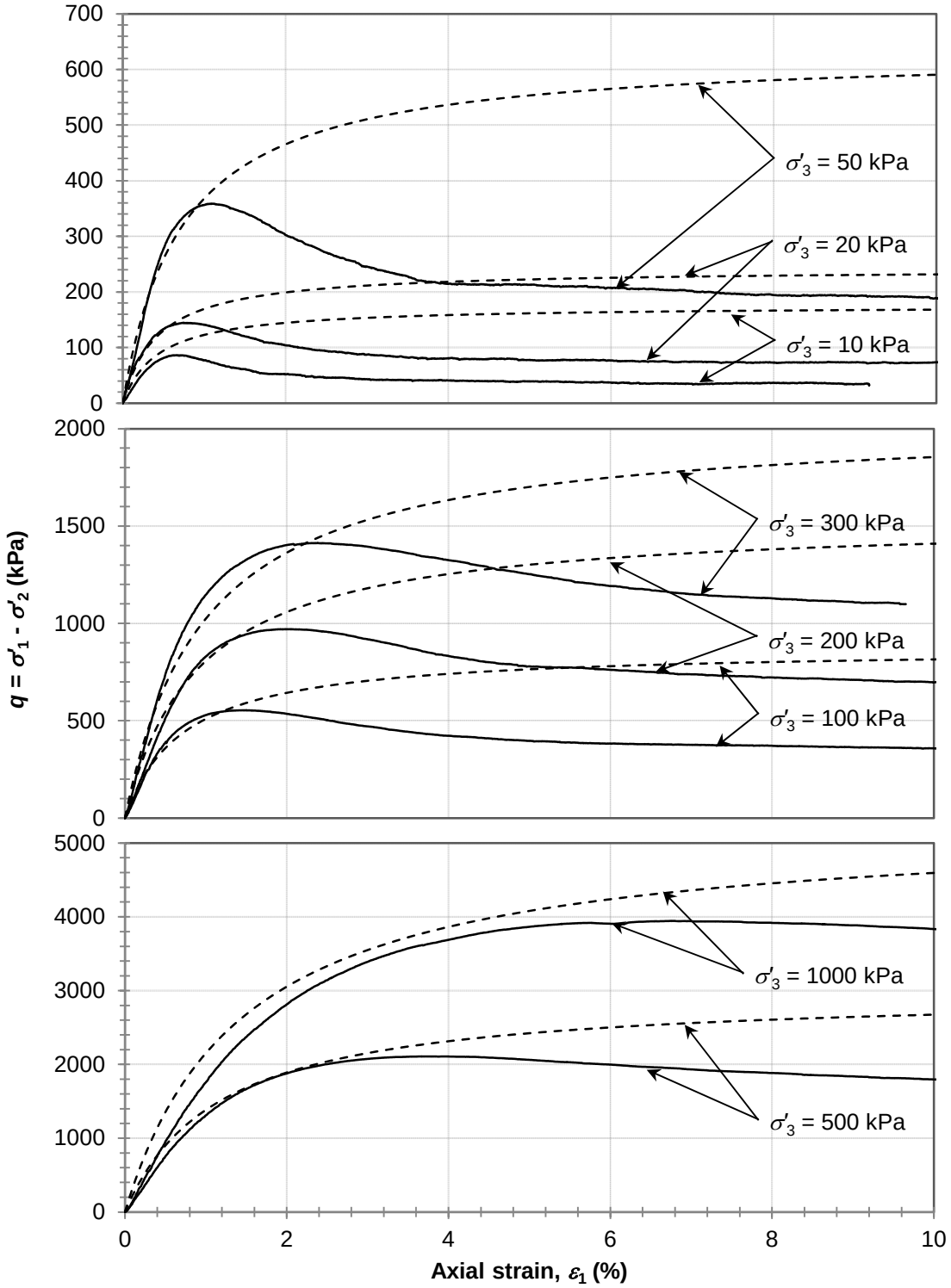

Figure 4.31. Comparison of test data to hyperbolic fit for 65 percent relative density.

The Duncan and Chang (1970) procedure uses only three points per triaxial test in its calibration. In an attempt to improve the hyperbolic fit, a least sum of squared errors (LSSE) procedure was applied to the part of the stress-strain curve prior to the onset of strain-softening. Since these models are only calibrated to working-level stresses, they are only applicable to a limited range of axial strains of approximately one to four percent depending on the confining stress. Figure 4.32 and Figure 4.33 compare the measured deviatoric stress-axial strain response of specimens 200-1-1 and 1000-1-1, respectively, and the fit of their hyperbolic models calibrated using the LSSE and the Duncan and Chang (1970) procedures. For specimen 200-1-1, both calibration procedures produced similar results which closely fit the measured data up to axial strains of approximately 1.5 percent. For the specimen 1000-1-1, the LSSE procedure produced a fit closer to the measured response, though the difference was small. To further compare the two methods, the initial tangent modulus was determined for each of the specimens sheared at 65 percent relative density using the LSSE Procedure and plotted against those calculated using the Duncan and Chang (1970) procedure and presented in Figure 4.34. Though some variation is observed, the modulus number and modulus exponents determined using both methods are similar. Overall, the LSSE procedure did not show a large advantage over the Duncan and Chang (1970) procedure besides being slightly more accurate over small strains.

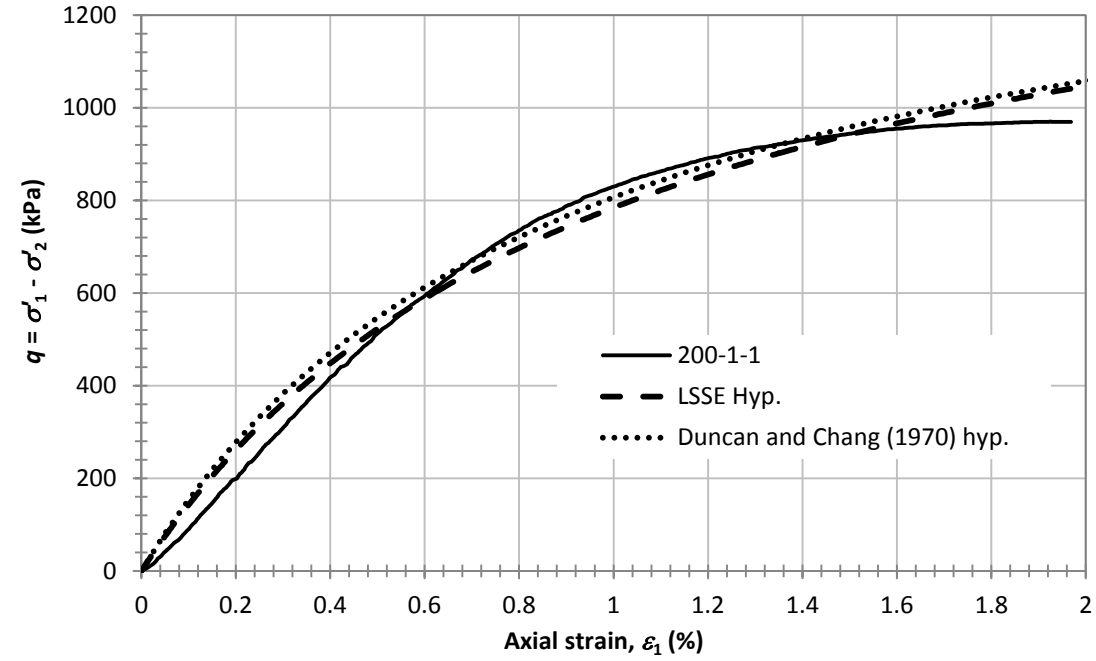

Figure 4.32. Comparison of hyperbolic fit using the LSSE procedure, and the Duncan Chang (1980) procedure to the principal stress difference-axial strain measurements from test 200-1-1.

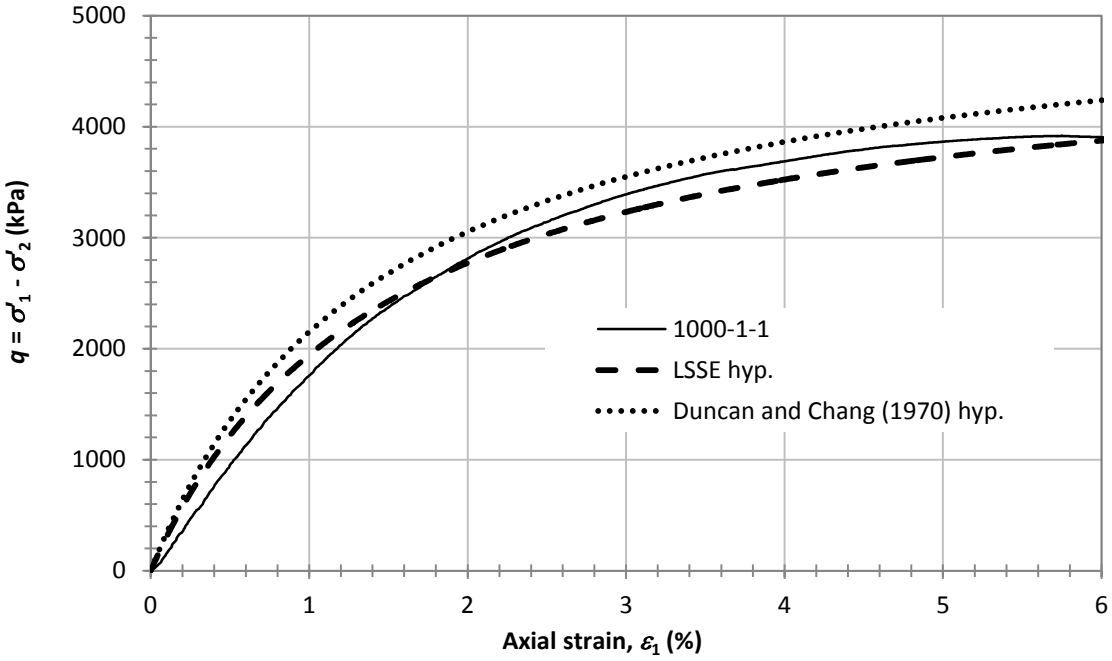

Figure 4.33. Comparison of hyperbolic fit using the LSSE procedure, and the Duncan Chang (1980) procedure to the principal stress difference-axial strain measurements from test 1000-1-1.

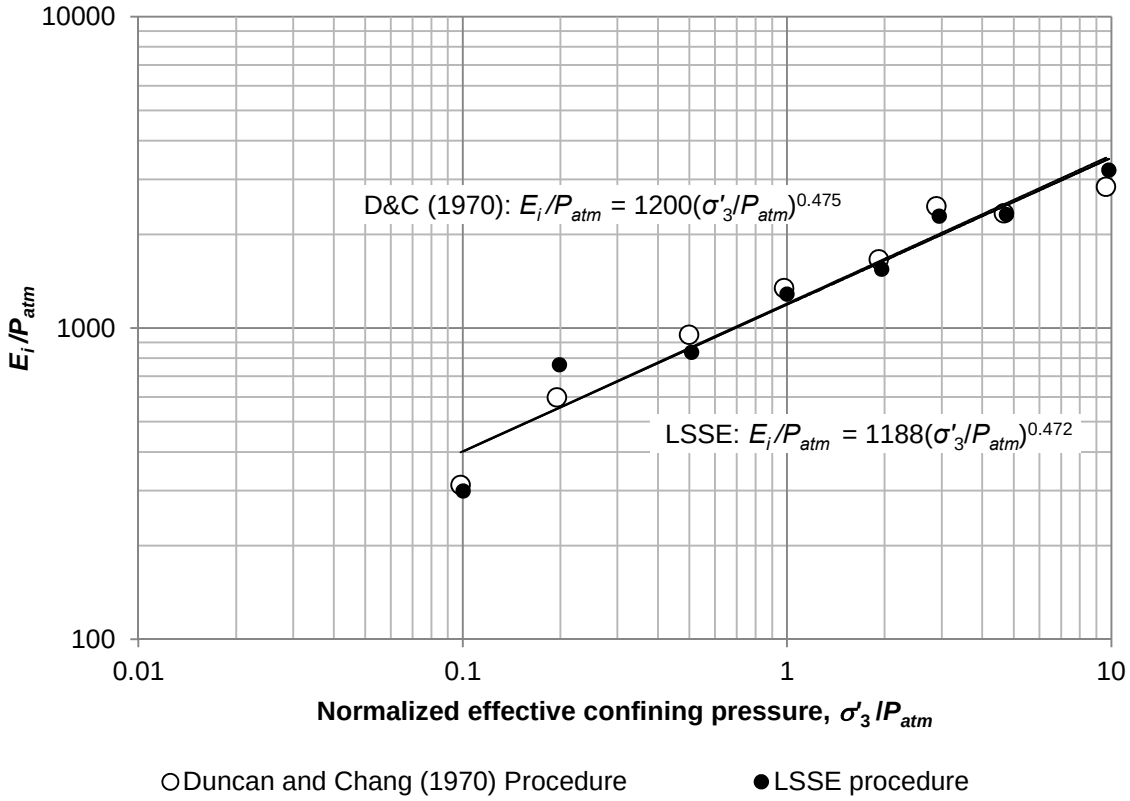

Figure 4.34. Comparison between the LSSE and Duncan and Chang (1970) fitting procedures showing normalized tangent modulus verse normalized confining pressures for tests with D_r = 65percent.

4.5 Summary

In this chapter the material characteristics for the ribbed steel strip reinforcements and reinforced backfill materials were presented along with a discussion on the testing procedures used to measure the material properties. Tension testing was performed on coupons of the reinforcement material to provide the yield strength and modulus of elasticity, which were determined equal to 700 MPa and 208 GPa, respectively. Axial symmetric triaxial compression tests were performed on 15 cm diameter specimens of the reinforced backfill material compacted to relative densities of 35, 55, and 65 percent and tested at effective confining pressures ranging from 10 to 1,000 kPa. Peak friction angles

ranging from 54 to 39 degrees were measured. The dilation angles were calculated using the methods by Rowe (1962), and Tatsuoka (1987) and resulted in dilation angles ranging from 45 to -0.3 degrees with ratios of dilation angles calculated using the method by Rowe (1962) to those computed using the method by Tatsuoka (1987) varied from 0.75 to 0.9.

The stress-strain and volumetric behavior of the reinforced backfill material was compared to the behavior of two soils reported by Verdugo and Haz (2007) and found to behave relatively similar. Finally, the Duncan and Chang (1970) hyperbolic model was calibrated to the stress-strain and volumetric behavior recorded during triaxial testing. Modulus numbers ranging from 726 to 1200, and modulus exponents ranged from 0.385 to 0.525 were observed. The appropriateness of the Duncan and Chang (1970) stress strain model was visually analyzed and determined acceptable at working stress levels from approximately one to four percent depending on the effective confining stress. In the following chapter the interaction between the reinforced backfill material and the ribbed steel strip reinforcements is discussed and data from laboratory pullout tests are presented.

5.0 SOIL-REINFORCEMENT INTERACTION

In-situ and laboratory pullout tests are usually performed to measure the apparent friction coefficient, f^*, between a MSE wall reinforcement strip and the surrounding backfill (as discussed in Section 2.2.1.3). In current MSE wall design, conservative design models for f^* are typically used rather than performing pullout tests on specific backfill-reinforcement combinations as this can make up for poor field quality control on compaction. The f^* design models were calibrated with a wide variety of soils including fine sands with friction angles as low as 35 degrees and therefore under-predict the apparent friction coefficient when high strength sand-gravel mixtures are used as backfill.

Since a major focus of this study is to accurately measure the interaction between a specific backfill and specific reinforcement, it was deemed necessary to perform pullout tests and produce specific f^* design models for the backfill under consideration. This chapter discusses the design of a laboratory pullout test apparatus, the methods used in conducting the pullout tests, and the observed interactions between the backfill soil and the ribbed reinforcement. Additionally, two new f^* design models will be presented: one calibrated to the specific backfill being tested, and a second calibrated using all available data from pullout tests on gravels and sand-gravel mixtures.

5.1 Pullout Test Apparatus for Single Reinforcement Strips

A pullout test apparatus was designed to measure the load-displacement behavior of single reinforcement strips. This system consisted of a pullout box, air bladder, hydraulic actuator, reaction frame, two load cells, string potentiometer, and data acquisition system (DAQ).

The pullout test box was designed to accommodate a 2 m long segment of reinforcement strip within a compacted rectangular prism of backfill soil with dimensions of 0.356 m (14 in.) in height, 0.456 m (17.75 in.) in width, and 2.16 m (84 in.) in length. Refer to Appendix C for a full set of pullout box design schematics. The pullout box was designed to house an air bladder capable of applying 300 kPa (gauge) uniform pressure to the top of the backfill. The structure of the box consists of MC 4 x 13.8 channel sections, 9.5 mm (3/8 in.) thick steel plates and 12.7 mm (1/2 in.) A354 (f_u = 150 ksi) threaded

rods configured as shown in Figure 5.1 and Figure 5.2. The design calculations are presented in Appendix D which were performed using AISC (2010).

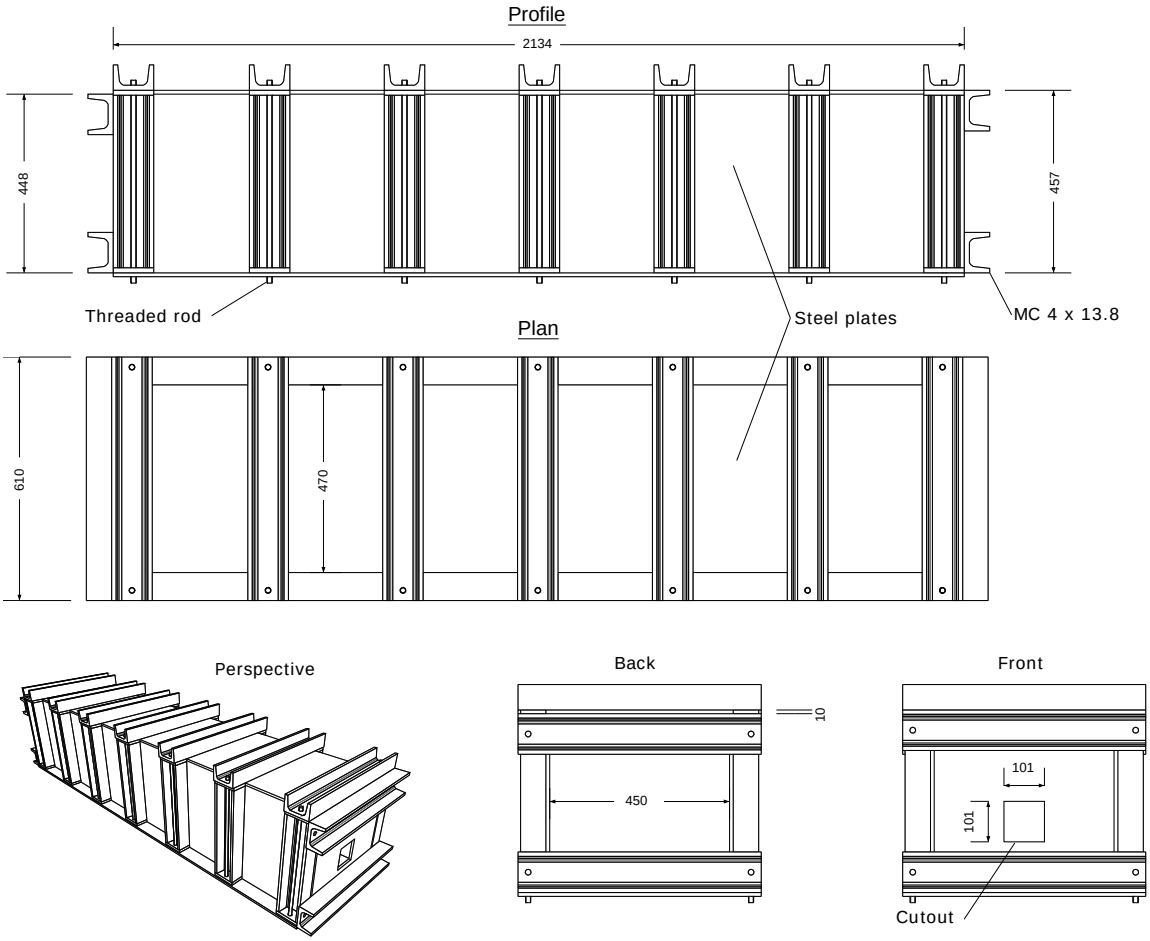

Figure 5.1. Schematic of the pullout box with dimensions in mm.

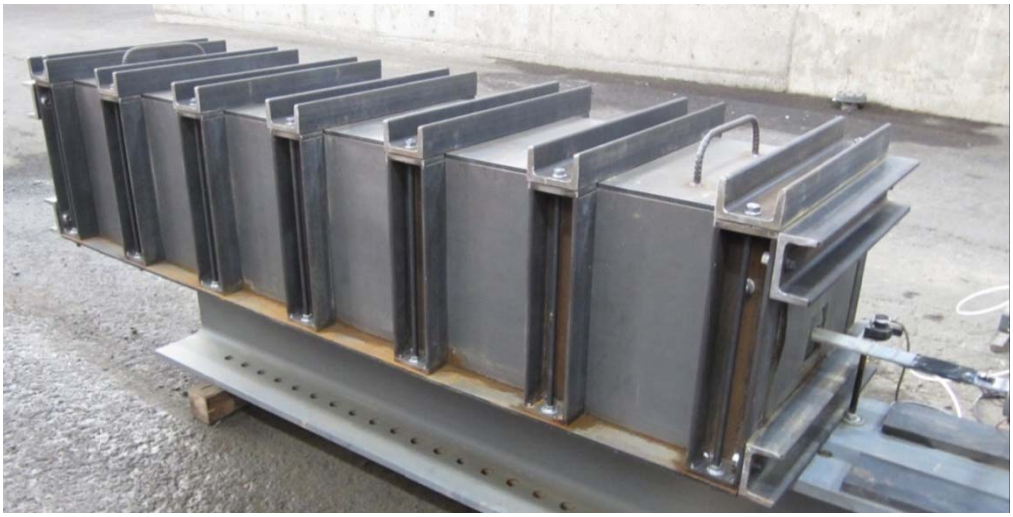

Figure 5.2. Pullout box before loading (looking northeast).

The pullout box was secured to a reaction beam along with a 2200 kN (500 kips) capacity hydraulic actuator as shown in Figure 5.3. The actuator was connected to the pullout strip with a 100 kN (22.5 kip) load cell (Figure 5.4), except when the required pullout load was predicted to exceed the capacity of the load cell. For the tests where the 90 kN load cell was removed, 4 strain gauges attached to the reinforcement strip (2 on each side), were used to measure the load in the reinforcement as shown in Figure 5.5. The loads measured with the strain gauges agreed with the load cells that accompany the actuator.

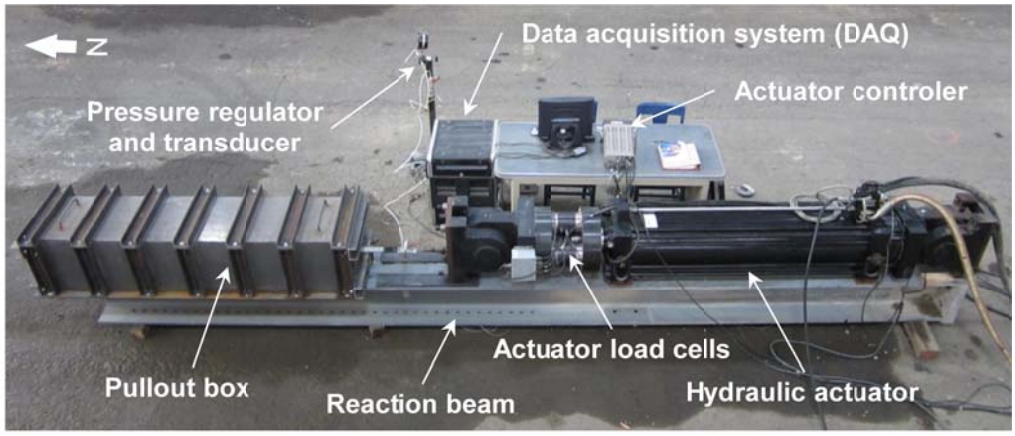

Figure 5.3. Reinforcement pullout testing system.

The air bladder used consisted of a common queen size inflatable mattress with a modified valve capable of being attached to a pneumatic regulator. The integrity of the air bladder was checked periodically throughout each test by momentarily shutting off the air supply while still being able to measure the pressure inside the bladder.

All tests were performed in a displacement controlled manner with a displacement rate of 1 mm (0.04 in) per minute. The displacement of the reinforcement strip was independently measured using a string potentiometer (M/N: LX-PA-15-P10K; S/N: 38120817), shown in Figure 5.5 secured to the reaction beam.

5.2 Test Program

The two main motivations for performing these single strip pullout tests were:

- to expand the current pullout test database for high strength reinforced gravel backfill; and,
- to produce baseline results for comparison with subsequent multi-strip pullout tests (not included in this thesis).

Currently, the number of well documented pullout tests for high strength sand-gravel mixtures using ribbed steel strip reinforcements is small. By combining the results from the present study with those reported in the literature, new f^* design models for use with gravels and sand-gravel mixtures were able to be developed.

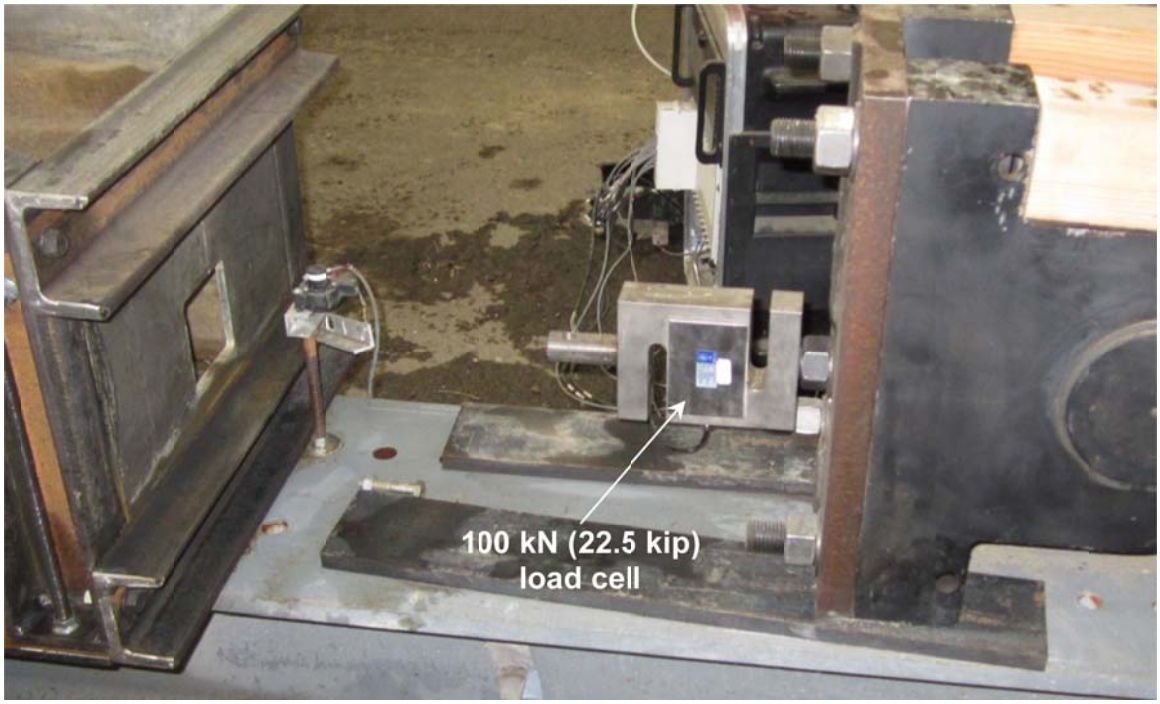

Figure 5.4. Load cell used for the majority testing (looking east).

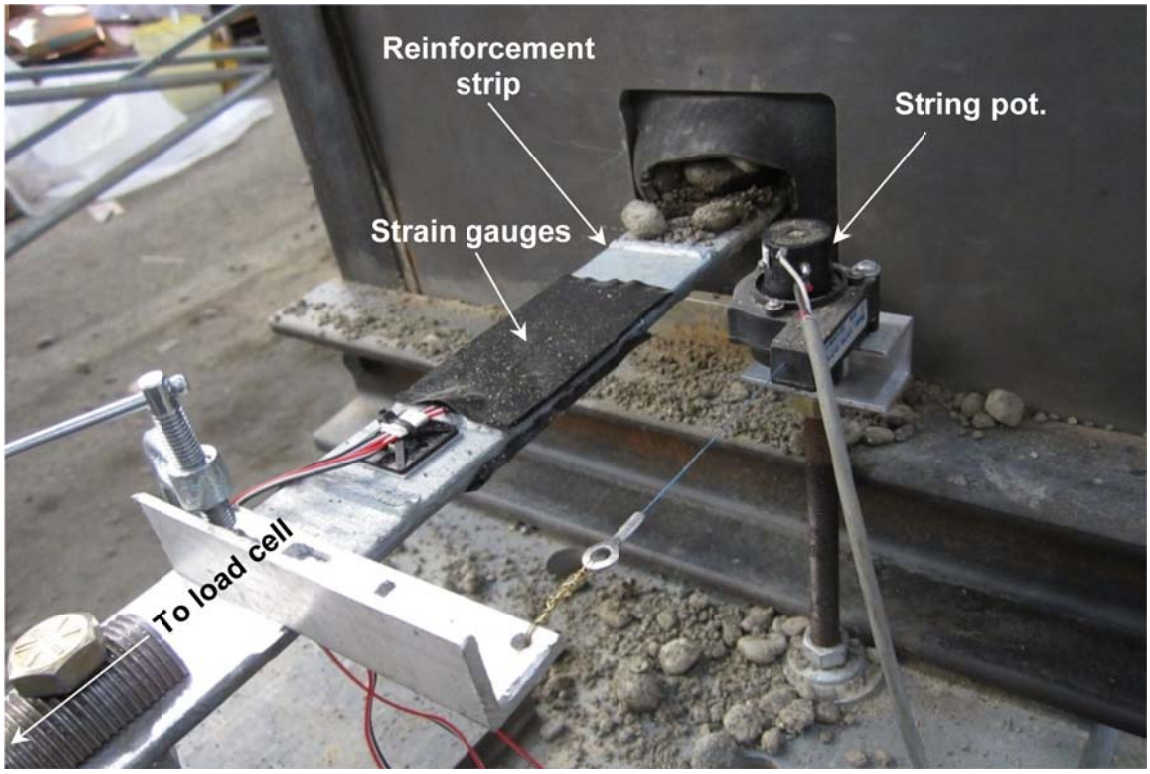

Figure 5.5. Strain gauges and string potentiometer (looking northwest).

The present study is a part of a larger group of research projects aimed at analyzing the behavior of tall MSE walls. Due to the large stresses developed in tall MSE walls, small reinforcement spacing, both vertical and horizontal, is required to develop sufficient resistance. However, the effect of reinforcement spacing on the backfill-reinforcement interaction is not well understood. Research is currently being carried out that employs a larger pullout apparatus used to perform tests with multiple reinforcement strips at varying horizontal and vertical spacing. In subsequent research, the results from the present study will be used as a baseline in the analysis of these multi-strip pullout test results.

The test program for the present study included 20 pullout tests at vertical effective stresses ranging from 10 to 300 kPa. All tests had the same target relative density of 65 percent corresponding to a relative compaction of 95 percent and a dry unit weight of 21.3 kN/m^3 (135.6 pcf). Each of the twenty pullout test specimens were given a unique designation consisting of the vertical effective stress the specimen was subjected to, and a subset chronologic indication number. For example, the fourth test performed at a vertical effective stress of 100 kPa was given the designation of 100-4. Table 5.1 provides the designations of each test considered in the present study.

Table 5.1. Pullout tests considered in the present study.

Single strip pullout test designations	
10-1	100-5
20-1	100-6
50-1	150-1
50-2	150-2
50-3	150-3
75-1	150-4
100-1	200-1
100-2	200-2
100-3	250-1
100-4	300-1

5.3 Compaction of Reinforced Backfill

In contrast to the CD triaxial test specimens discussed in Chapter 4, all pullout test specimens were targeted to achieve the same relative compaction of 95 percent of maximum dry density (ASTM D-1557) (i.e, 65 percent relative density). Specimen compaction was carried out using the vibratory plate compactor shown in Figure 5.6a (Bomag M/N: BVP 18/45) with a mass of 90 kg (6.17 slugs), a vibratory frequency of 90 Hz, a manufacture rated dynamic force of 18 kN (4050 lb), and a total force of 18.9 kN (4140 lb). Each lift had a target compacted thickness of 9 cm (3.5 in.). The soil for each lift was weighed and brought to optimum water content (6.4 percent) before being placed in the box and compacted. The same compactive effort was used for each test. The compactor was passed over the top of the soil five times starting from the south end of the box and ending at the north. Then the compactor was rotated 180 degrees and passed over the soil five more times in the opposite direction. After the second lift was compacted, the surface of the backfill was inspected to make sure it was level, then the reinforcement strip was placed and the final two lifts were compacted.

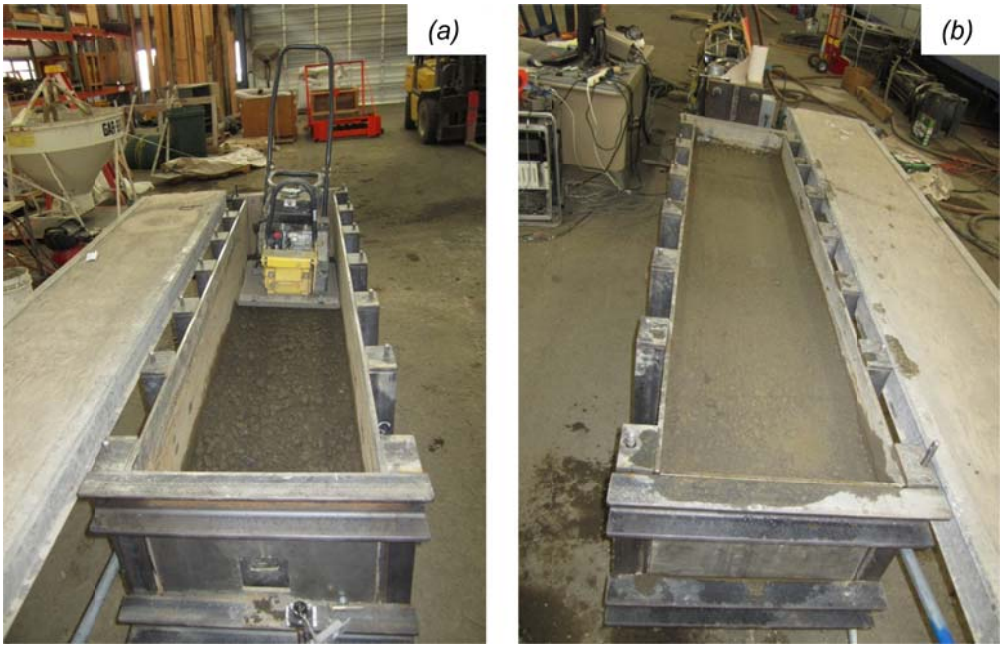

Figure 5.6. Compaction of backfill soil inside pullout box (a) before compaction of second lift (looking north), and (b) after compaction of fourth (final) lift (looking south).

Compaction verification was completed with a Nuclear Density Gauge (NDG) on the first test specimen. The initial NDG testing was performed by FEI (2012a) by taking 3 measurements: one approximately 0.3 m (1 ft.) from the north end of the box, one at approximately the center and one approximately 0.3 m from the south end of the box. The average relative compaction was found to be 94 percent which corresponded to a dry unit weight of 21.03 kN/m^3 (133.9 pcf). After reviewing the initial NDG test results it was decided that no further density verification was needed as long as the same compaction procedure was strictly followed for the remaining tests. However, after observing relatively high variability in the peak pullout load between tests with the same vertical effective stress, as described subsequently, it was suspected that variations in density were possible

In order to frequently measure the dry unit weight of each specimen, a lower cost alternative to the NDG was required. Due to the availability of testing equipment, the Balloon Density Apparatus (BDA) shown in Figure 5.7 was selected. The dry unit weights of two more specimens were measured with both the NDG (FEI 2012b; c) and the BDA. In order to test the same soil mass with each device, the balloon density tests were conducted between where the source rod of NDG was driven and where the photon sensor was located as shown in Figure 5.8.

Figure 5.7. Balloon density apparatus (BDA).

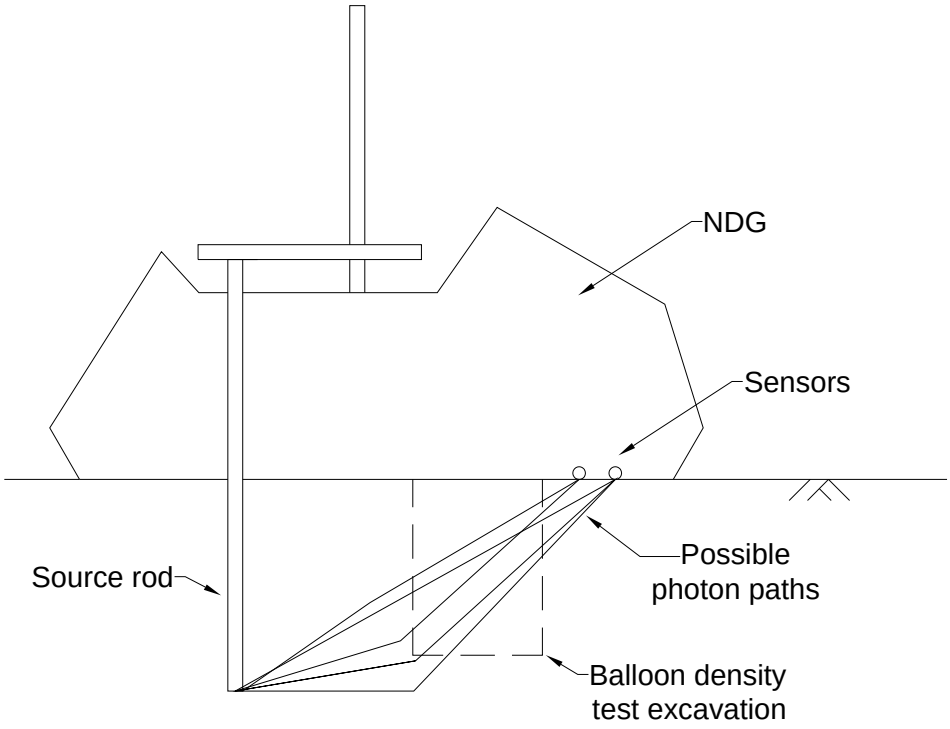

Figure 5.8. Location of balloon density excavation relative to the nuclear density gauge (modified from Holtz et al. (2011) and Troxler Electronic Laboratories Inc.).

On average, the dry unit weight was 0.55 kN/m^3 (3.5 pcf) higher when measured with the BDA. Since the NDG test is the standard test used in industry, the average difference (0.55 kN/m^3) was subtracted from the dry unit weights of subsequent test specimens measured with the BDA. Figure 5.9 shows the variation in the measured relative compaction within and between specimens. The maximum and minimum recorded value was 103 and 88 percent, respectively, with a global median and global mean was 95.5 and 96.1 percent, respectively. The consequences of these variations are discussed in Section 5.4.

5.4 Single Reinforcement Strip Pullout Resistance

As mentioned previously, each pullout test was conducted at a specific vertical effective stress ranging from 10 kPa to 300 kPa. The vertical effective stress was the single controlled variable for the pullout test program.

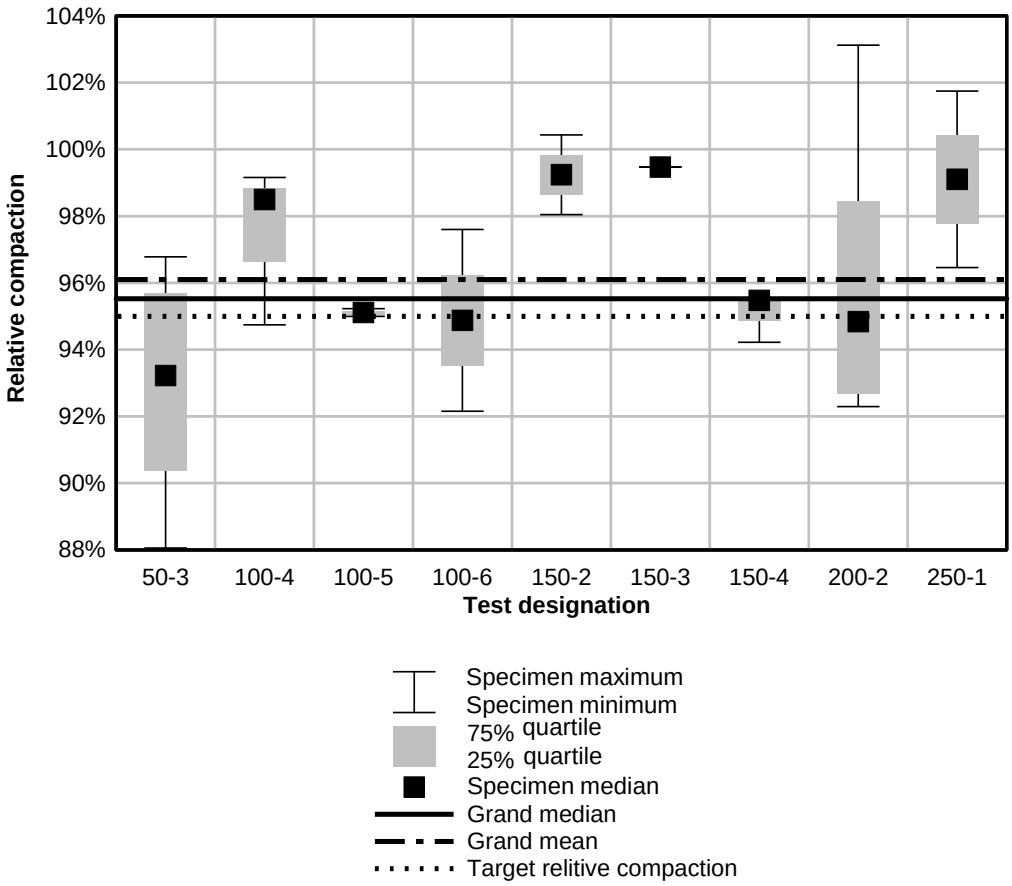

Figure 5.9. Variation in corrected relative compaction for pullout test specimens measured with the BDA.

5.4.1 Interpretation of Pullout Tests

In general, the load-displacement behavior was categorized into three different parts: initial non-slip resistance, monotonic accumulation of resistance, and a transition to the development of reinforcement slip with a reduction in resistance (Figure 5.10). Initially, load accumulated with little to no displacement. The load at which movement of the strip relative to the soil was initiated was referred to as the initial non-slip resistance and is shown in Figure 5.10(b). The initial non-slip resistance develops from the passive rib resistance and the static friction between the reinforcement and backfill. Although, a correlation of the non-slip resistance with effective vertical stress was expected this was not observed as discussed subsequently in Section 5.4.2.

As the reinforcement strips began to displace under the applied loading, the resistance increased monotonically until slippage between the reinforcement and the surrounding soil occurred. The initial of the reinforcement strips evaluated in this study slippage typically occurred between 8 and 16 mm of displacement.

After the initial slippage occurred, the pullout resistance generally continued to increase with small sporadic reductions as slipping continued. Larger cycles of reductions followed by gradual increases in resistance were also observed in many of the tests. These resistance cycles were attributed to larger particles being overridden or crushed by the reinforcement ribs resulting in losses of passive resistance and dilation-induced confining pressures. Figure 5.11 shows a broken gravel particle found near a reinforcement rib subsequent to testing. Pullout resistance typically decreased noticeably with continued local variations at approximately 60 mm of displacement.

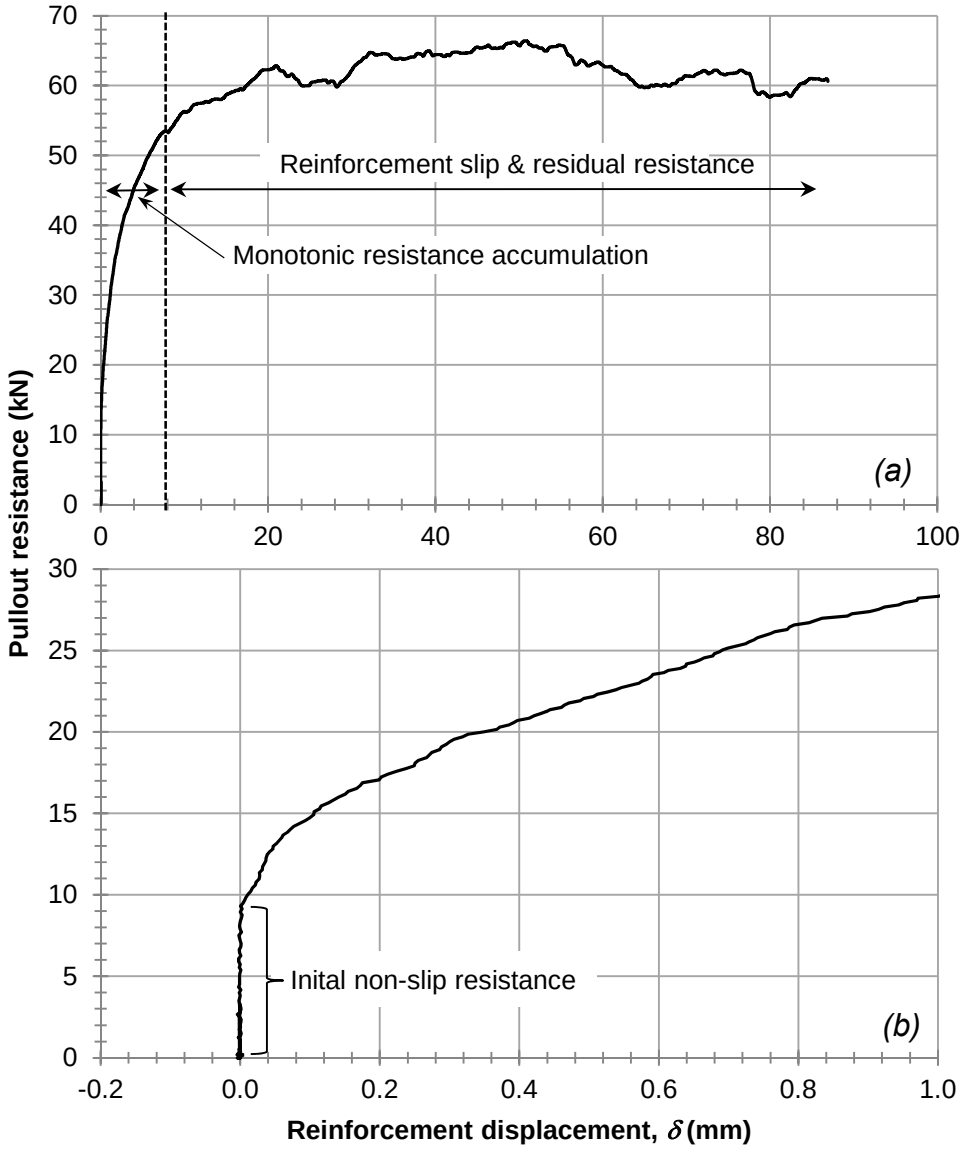

Figure 5.10. Pullout resistance vs. reinforcement strip displacement curve for test 200-2 showing (a) the full range in displacement, and (b) an expanded view of the initial load-displacement and non-slip resistance.

Figure 5.11. Photo of a gravel particle crushed by a reinforcement rib.

5.4.2 Pullout Test Results

Table 5.2 summarizes the results of each pullout test conducted. Some data, such as unit weight, initial non-slip resistance, measured initial stiffness, and maximum pullout resistance for certain specimens were not available. For example, a faulty potentiometer was used to measure displacement for the first seven tests conducted. The initial potentiometer was not a string potentiometer as shown in Figure 5.5, it was a spring-loaded plunger type potentiometer. For these seven tests, the plunger was initially contracted at the beginning of each test, then, as displacement occurred, the plunger would begin to release. However, the faulty potentiometer did not produce a change in resistance (and thus voltage) for the first 5 mm of travel. This non-responsive range was only encountered for four of the seven tests including tests 10-1, 50-1, 75-1, and 200-1. Neither the initial non-slip resistance nor the initial stiffness was measured for those tests. Additionally, the air bladder used for the test 300-1 lost pressure prior to achieving peak resistance at approximately 5 mm of displacement. Consequently, neither the peak resistance nor the apparent friction coefficient could be reported for that test.

Figure 5.12 shows the load-displacement measurements for specimens tested at σ'_v = 10 and 20 kPa. The 10 kPa increase in σ'_v produced an increase of 15 kN in the peak reinforcement pullout resistance. The load-displacement curves for tests conducted at σ'_v = 50 and 75 kPa are shown in Figure 5.13; it should be noted that the vertical effective stress for specimen 50-1 was 57.2 rather than its intended target value of 50 kPa and therefore should not be directly compared to tests 50-2 and 50-3 based on effective vertical stress. Pullout test specimen 50-3 (γ_d = 21.3 kN/m^3) produced the smallest maximum pullout resistance of 38.5 kN, specimen 50-2 initially exhibited significantly stiffer behavior than observed for specimen 50-3 suggests a denser specimen. However, unit weight was not measured for specimens 50-1, 50-2, nor 75-1. Figure 5.14 shows the load displacement measurements for tests performed at σ'_v = 100 kPa. Peak pullout resistance values ranging from 54.6kN for specimen 100-6 (γ_d = 21.3 kN/m^3) to 80.3 kN for specimen 100-4 (γ_d = 22.4 kN/m^3) were observed. The peak reinforcement load for specimen 100-5 was 9.3 kN less than that observed for specimen 100-4 despite having the same measured unit weight of 22.4 kN/m^3. The measured pullout resistances and reinforcement displacements for specimens tested at σ'_v = 150 kPa are shown in Figure 5.15. Specimen 150-4 behaves much stiffer than specimens 150-3 and 150-2 despite having a lesser unit weight. Figure 5.16 presents the load-displacement measurements for specimens tested at σ'_v = 200, 250, and 300 kPa. The peak reinforcement load measured for Specimen 200-1 was 12.2 kN larger than that measured for specimen 250-1 (γ_d = 22.7 kN/m^3), and 28 kN larger than that measured for 200-2 (γ_d = 21.3 kN/m^3) suggesting that over-densification may have occurred during the compaction of specimen 200-1.

The initial non-slip resistance varied between 0.9 and 14.7 kN as shown in Figure 5.17. From basic knowledge of frictional behavior, it was speculated that the initial non-slip resistance would correlate with σ'_v. Using the Spearman-Rank test with the initial non-slip resistance effective confining pressure data, the null hypothesis of non-correlation was rejected at a significance level of five percent (p-value = 0.021) suggesting the presence of a correlation. However, the significant variability of the relationship between initial non-slip resistance and σ'_v can be seen in Figure 5.17. The

cause of this variability was suspected to be local density variations within the soil specimens.

In order to exclude the effect of the initial non-slip resistance, the initial stiffness was determined by measuring the rate of load accumulation between 0.25 mm and 1 mm of displacement. Values of initial stiffness ranged from 4.9 to 23.0 kN/mm.

Generally, peak reinforcement load, P_{max}, increased with increases in σ'_v (Figure 5.18). However, variations in P_{max} of up to 26 kN were observed between tests with equal effective vertical stresses.

Table 5.2. Summary of pullout test results.

Test Designation	γ_d (kN/m^3)	*RC* (%)	σ'_v (kPa)	Initial Non-Slip Resistance (kN)	Meas. Initial Stiffness, (0.25 – 1.0 mm) (kN/mm)	P_{max} (kN)	f^* (-)
10-1	N/A	N/A	10	N/A	N/A	18.6	9.92
20-1	21	94	23.7	4.6	10.7	33.5	7.56
50-1	N/A	N/A	57.2	N/A	N/A	53.1	4.96
50-2	N/A	N/A	50	5.7	12.4	45.7	4.89
50-3	N/A	N/A	50	0.9	12.5	38.5	4.11
75-1	N/A	N/A	75	N/A	N/A	57.3	4.09
100-1	N/A	N/A	100	11.2	12.1	71.2	3.81
100-2	N/A	N/A	100	7.1	12.4	63.3	3.38
100-3	N/A	N/A	100	7.5	13.4	65.1	3.48
100-4	21.85	98	100	6.0	18.0	80.3	4.29
100-5	21.35	95	100	7.4	14.4	71.0	3.80
100-6	20.75	93	100	5.0	16.8	54.6	2.92
150-1	N/A	N/A	150	5.8	17.2	80.1	2.86
150-2	22.25	99	150	7.6	7.5	66.4	2.37
150-3	22.25	99	150	4.1	4.9	61.9	2.21
150-4	21.25	95	150	9.2	15.6	69.4	2.47
200-1	N/A	N/A	200	N/A	N/A	92.8	2.48
200-2	20.75	93	200	14.7	13.7	64.8	1.73
250-1	22.15	99	250	8.2	9.7	80.6	1.72
300-1	N/A	N/A	300	7.5	23.0	N/A	N/A

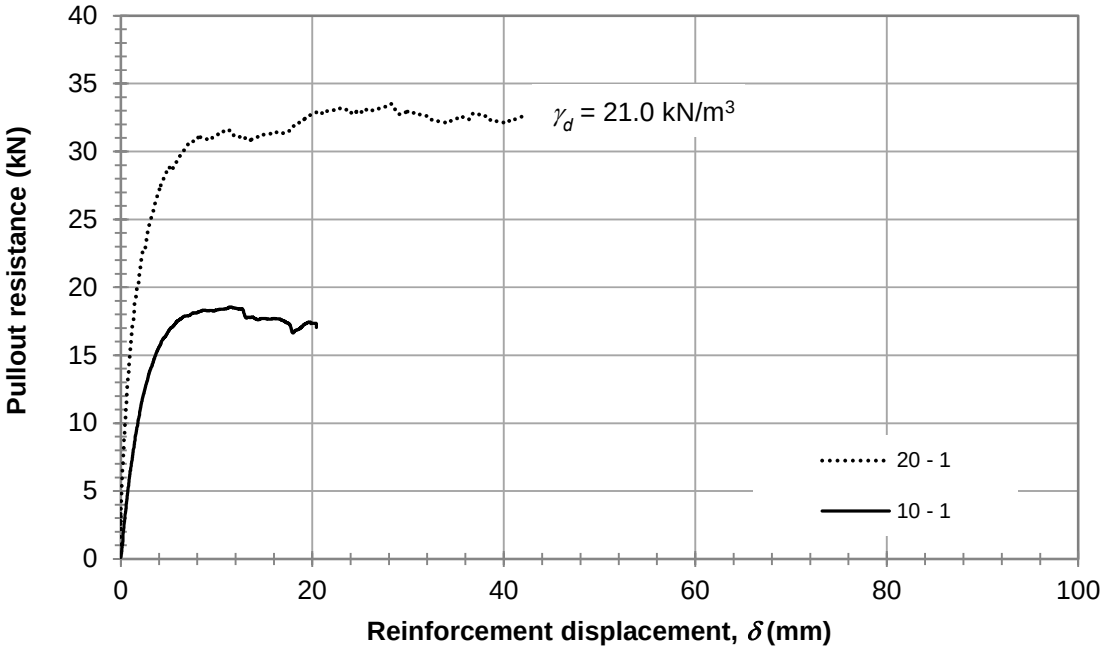

Figure 5.12. Pullout resistance versus reinforcement displacement for tests with vertical effective stresses of 10 and 20 kPa. Note, the unit weight of 10-1 was not measured.

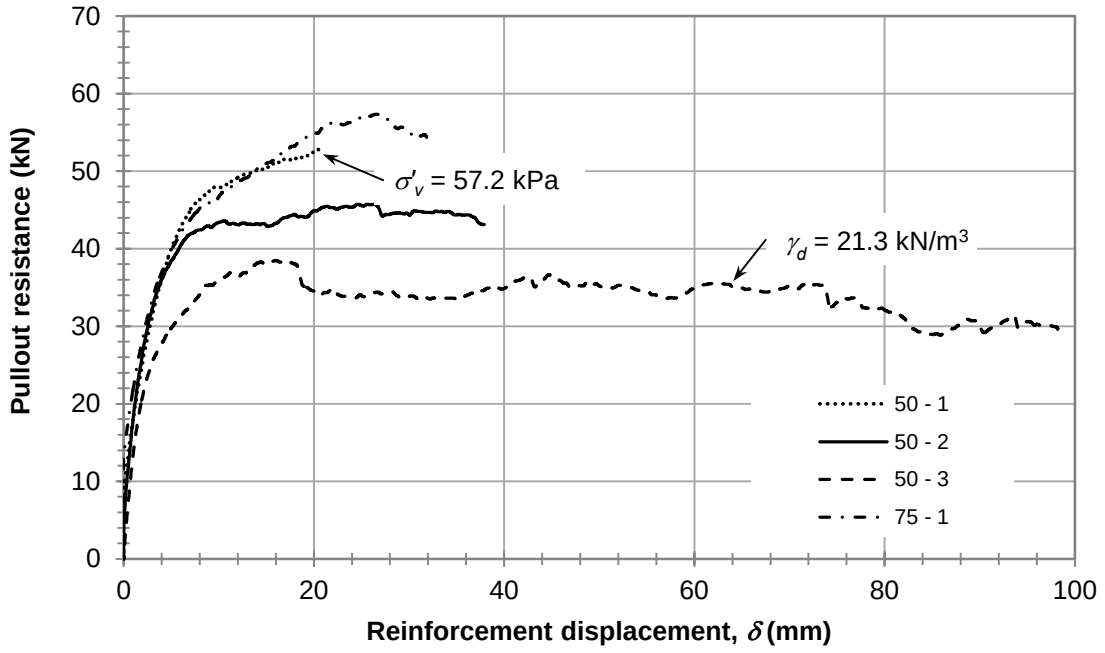

Figure 5.13. Pullout resistance versus reinforcement displacement for tests with vertical effective stresses of 50 and 75 kPa. Note, the unit weight of 50-1, 50-2, and 75-1 was not measured.

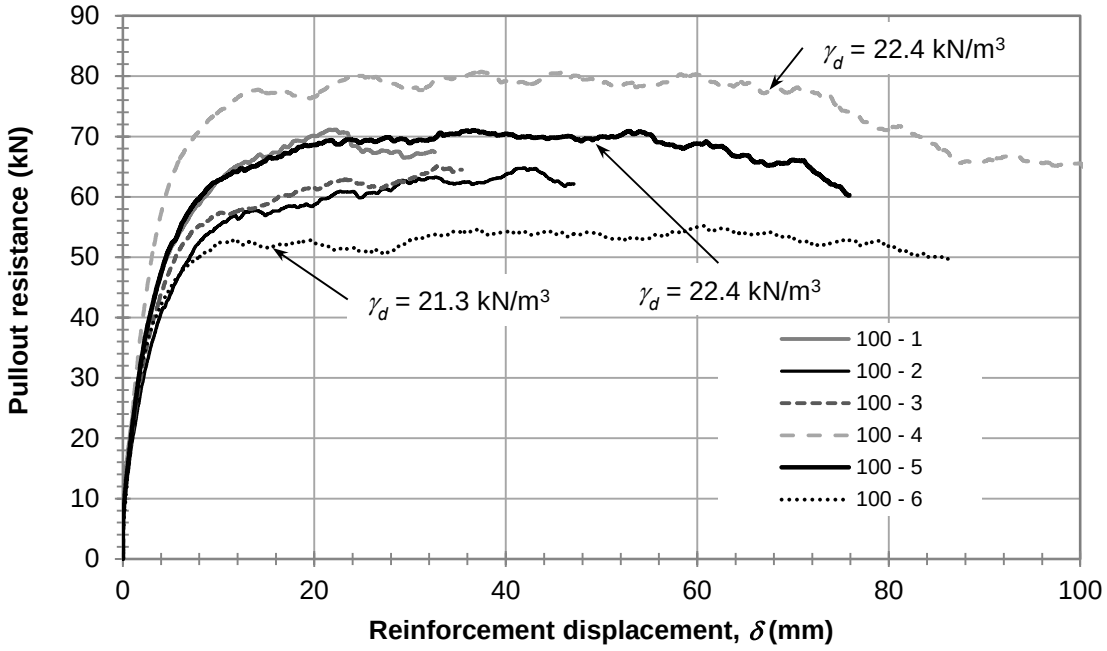

Figure 5.14. Pullout resistance versus reinforcement displacement for tests with vertical effective stresses of 100 kPa. Note, the unit weight of 100-1, 100-2, and 100-3 was not measured.

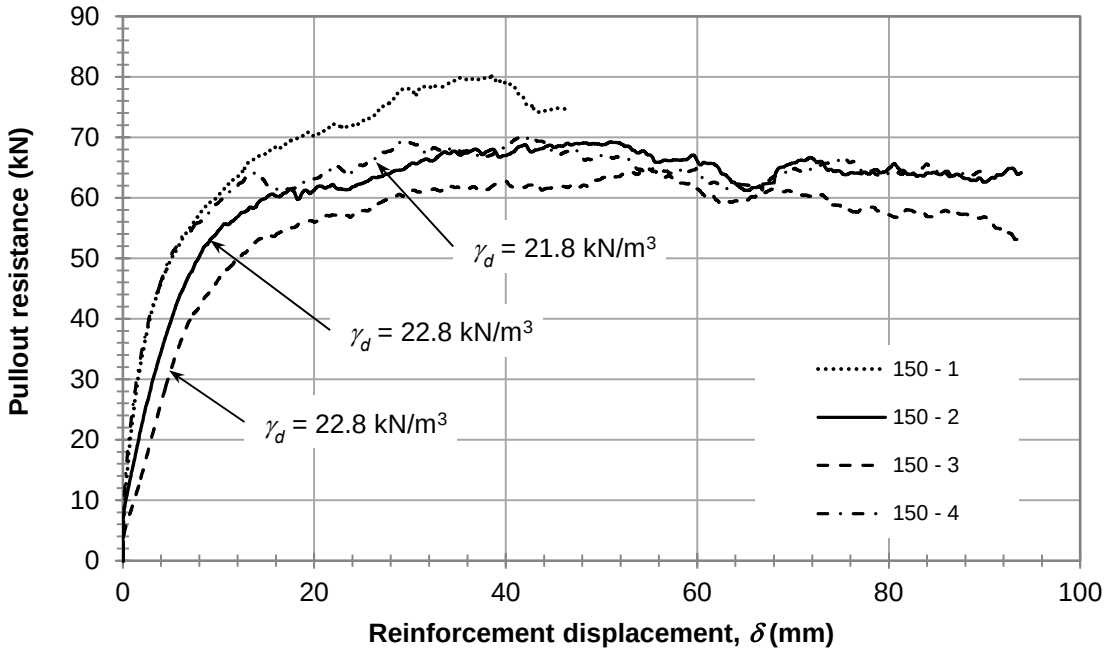

Figure 5.15. Pullout resistance versus reinforcement displacement for tests with a vertical effective stress of 150 kPa. Note, the unit weight of 150-1 was not measured.

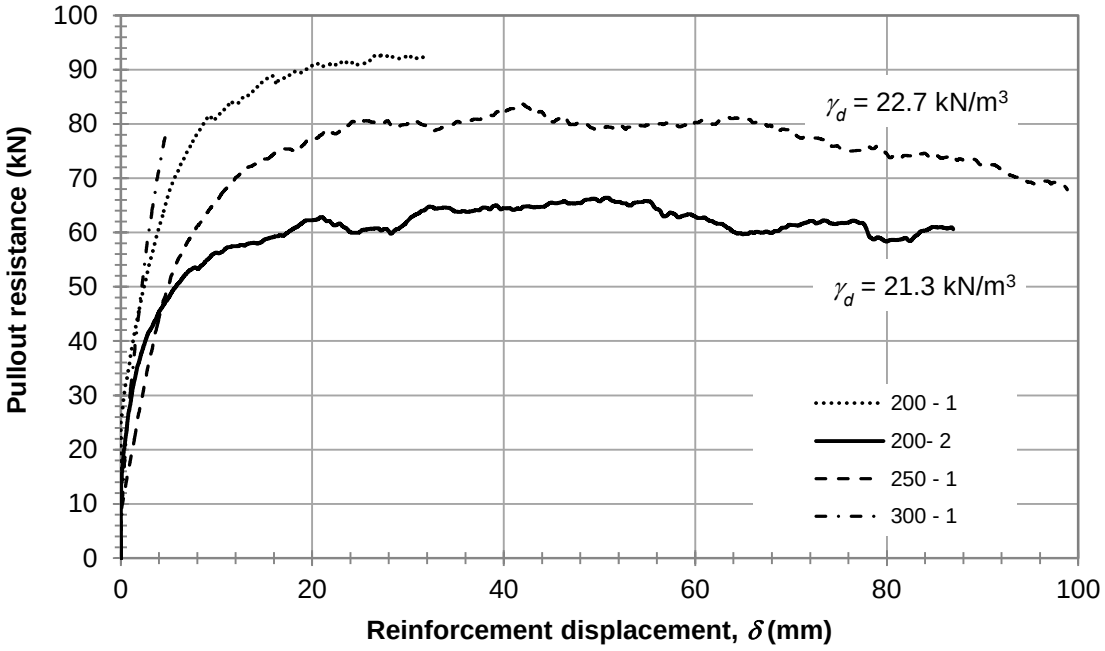

Figure 5.16. Pullout resistance versus reinforcement displacement for tests with vertical effective stresses of 200, 250 and 300 kPa. Note, the unit weight of 200-1, and 300-1 was not measured.

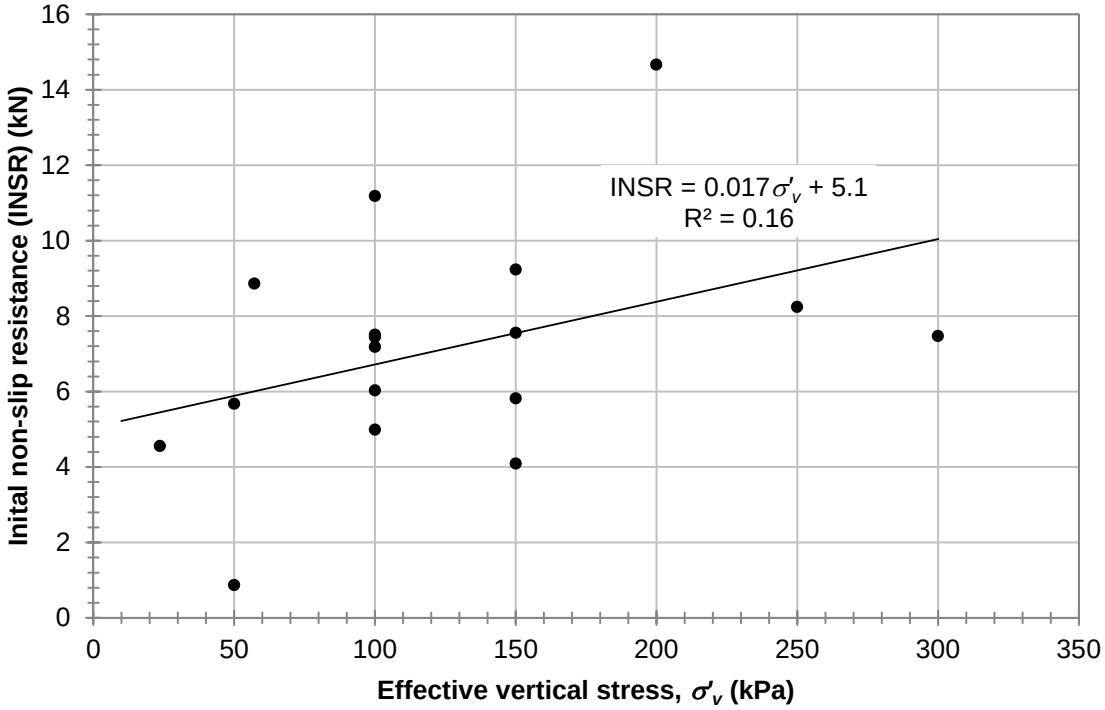

Figure 5.17. Initial non-slip resistance versus effective confining stress.

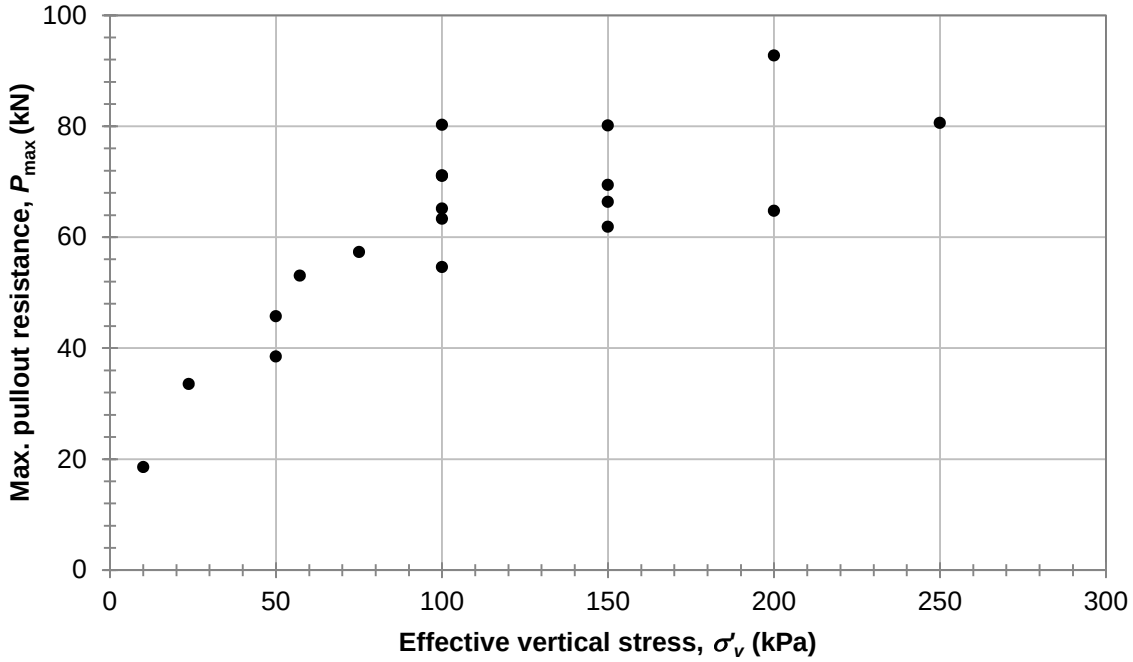

Figure 5.18. Maximum pullout resistance versus effective confining stress.

The uncertainty in the computed apparent friction coefficient, f^*, values reported in Table 5.2 were quantified using the procedure outlined in Kline and McClintock (1953). The 95 percent uncertainty intervals for each f^* input variables ($w_{\sigma'v}$, w_{Pmax}, w_b, and w_L) were estimated and used to compute combined f^* uncertainty intervals, w_{f^*}, for each test using the first order-second moment approach:

$$w_{f^*} = \left[\left(\frac{df^*}{d\sigma'_v} w_{\sigma'_v} \right)^2 + \left(\frac{df^*}{dP_{\max}} w_{P_{\max}} \right)^2 + \left(\frac{df^*}{db} w_b \right)^2 + \left(\frac{df^*}{dL} w_L \right)^2 \right]^{1/2} \quad (5.1)$$

The uncertainty interval for the vertical overburden stress, $w_{\sigma'v}$, was estimated to be ± 0.4 kN/m^2 based on the fluctuation in airbladder pressure recorded by the pressure transducer. The uncertainty interval for the maximum pullout resistance, w_{Pmax}, was estimated to be ± 0.01 kN based on the manufacture's specifications for the 100 kN load cell. The uncertainty intervals for the width and embedded length of the reinforcement,

w_b = ± 0.0005 m and w_L = ± 0.02 m, respectively, were estimated using the author's judgment.

As shown in Figure 5.19, the *f** uncertainty interval is larger for tests conducted at lower effective vertical confining pressures and smaller for tests conducted at larger vertical confining pressures. The computed *f** uncertainty interval values ranged from 0.76 at σ'_v = 10 kPa to 0.05 at σ'_v = 250 kPa with a mean and median values of 0.15 and 0.10, respectively.

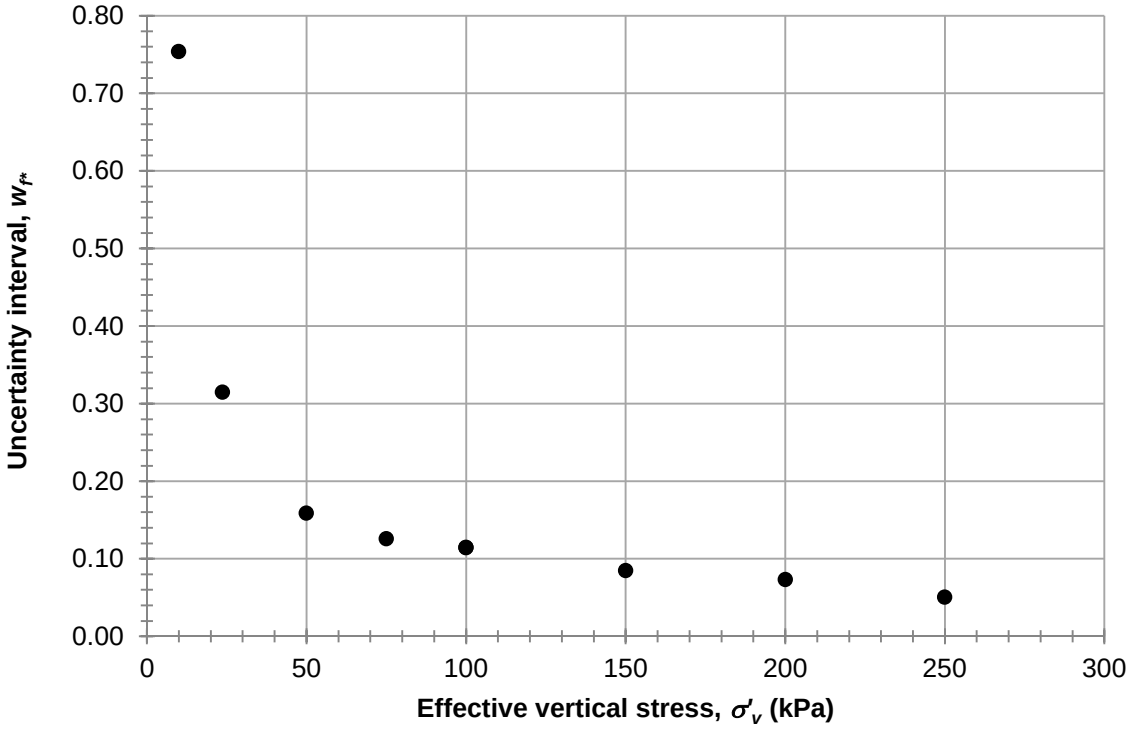

Figure 5.19. Average estimated *f uncertainty intervals for various effective vertical stresses.**

Multi-linear regression (MLR) modeling was performed on the measured pullout resistance data that was associated with a known dry unit weight in order to quantify the combined effect of compaction and vertical effective stress on the maximum pullout resistance. Two models were investigated, including a two-parameter MLR model, which included both the dry unit weight in kN/m3 and the vertical effective stress in kPa, and a one-parameter MLR model, which included just the vertical effective stress. Based

on Figure 5.20, the MLR modeling was performed using the natural logarithm of vertical effective stress. The effect of dry unit weight, a proxy for relative compaction and relative density, should influence the maximum pullout resistance; however, the results of the two-parameter MLR model shows that the dry unit weight is not statistically significant at the significance level of 5 percent, as shown in Table 5.3. This could be due to the lack of data compounded with the small variation in dry unit weight associated with relative compaction values largely greater than 93 percent. If the relative compaction, and therefore relative density, varied over a larger range, it would be likely that the dry unit weight would be a statistically significant parameter. Despite the use of a statistically insignificant prediction variable, the global p-value and adjusted R^2 of the two-parameter model was 0.01 and 0.653, indicating moderately strong predictive power.

Table 5.3 Summary of multiple linear regression (MLR) modeling on maximum pullout resistance.

Model Parameters		Fitted Estimate	Standard Error	*t* statistic	*p*-value
Two-parameter MLR; global p-value = 0.010; global adjusted R^2 = 0.653					
Intercept	[kN]	-155.42	110.47	-1.41	0.2023
Ln(σ'_v)	[kPa]	7.05	5.66	1.24	0.2534
Dry unit weight, γ	[kN/m^3]	13.53	5.39	2.51	0.0404
One-parameter MLR; global p-value = 0.004; global adjusted R^2 = 0.629					
Intercept	[kN]	-20.21	20.64	-0.98	0.3560
Ln(σ'_v)	[kPa]	17.67	4.38	4.03	0.0038

Nonetheless, removal of the dry unit weight to form the one-parameter MLR model appeared warranted, and resulted in a strengthening of the significance of the vertical effective stress variable, as shown in Table 5.3. Figure 5.20 shows that the effective predictive power is essentially the same between the one and two-parameter MLR models as compared to data that represent those pullout tests with and without dry unit weight measurements. However, the one-parameter model clearly shows improved generality with respect to all of the pullout test data (i.e., the model predicts all of the data equally

well), despite the use of training data that were associated with known dry unit weights, only. Figure 5.21 compares the measured maximum pullout resistance and those predicted using the two MLR models; based on this comparison, it appears that the use of the one-parameter MLR model is most appropriate for use with this specific backfill gradation until additional pullout resistance data with a larger variation in dry unit weight can be obtained.

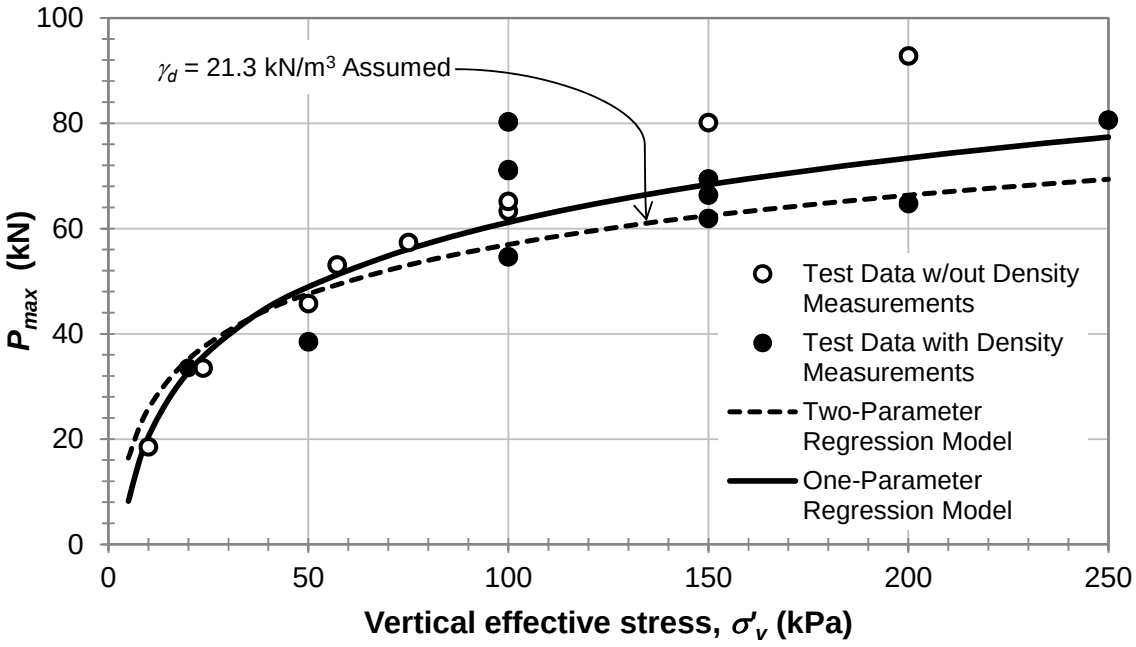

Figure 5.20. Comparison of measured and predicted maximum pullout resistance as a function of vertical effective stress.

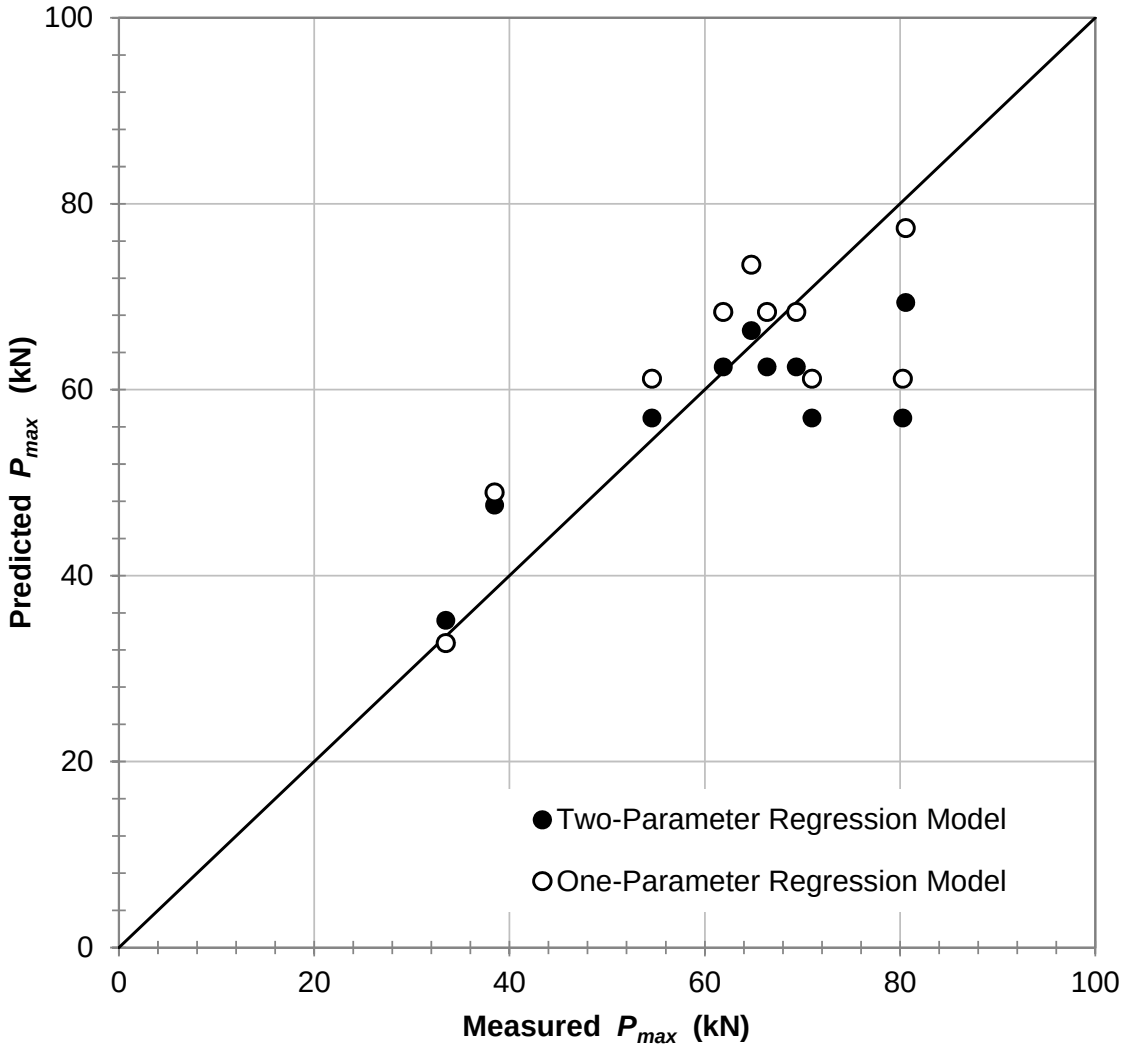

Figure 5.21. Predicted maximum pullout resistance verses measured maximum pullout resistance.

5.4.3 Hyperbolic Modeling of Pullout Resistance-Displacement Behavior

The prediction of the load displacement behavior of MSE wall reinforcement strips at any vertical effective stress is desirable because it allows for the prediction of wall deformation under working loads and it provides a way to predict the response of sacrificial reinforcement strips scheduled to be pulled out at the SeaTac MSE walls in the

near future. Hyperbolic curves were fit to the pullout load-displacement data in order to provide a general working stress displacement estimation method.

To calibrate the model, a least sum of squares regression was used on the general hyperbolic model, given by:

$$P = \frac{\delta}{\frac{1}{a_1} + \frac{\delta}{a_2}} \tag{5.2}$$

where P is the pullout resistance at displacement δ, a_1 is a coefficient related to the initial stiffness of the soil-reinforcement interaction (initial slope of the load-displacement curve), and a_2 is the asymptotic coefficient related to the maximum pullout resistance.

The variation of coefficients a_1 and a_2 with vertical effective confining pressure are shown in Figure 5.22 and Figure 5.23, respectively. The variation of the coefficient a_1 with vertical effective stress appears to be relatively random when considering all data as shown in Figure 5.22(a). However, upon removing those test data for which compaction data was either unavailable or did not meet requirements, a linear relationship was observed and was characterized with a coefficient of determination of 0.47 (Figure 5.22b). The relationship used to correlate the initial stiffness coefficient to vertical effective can be expressed as:

$$a_1 = 0.053\sigma'_v + 30.8 \tag{5.3}$$

As shown in Figure 5.23(a), a much stronger relationship exists between a_2 and vertical effective stress such that a log increase in vertical confining stress results in a 51 kN increase in maximum the maximum resistance coefficient. However, in order to capture the load-displacement behavior at the relative density of interest the same subset of pullout tests used to calibrate the initial stiffness coefficient, a_1, was used to calibrate the maximum resistance coefficient, a_2. Figure 5.23(b) shows the fitted logarithmic relationship along with the reduced dataset of a_2 coefficients. The models produced by

the full dataset and the reduced dataset are fairly similar, though a reduction in logarithmic slope was observed; that is, for every log cycle increase of vertical effective stress resulted in a 44 kN increase in maximum reinforcement coefficient. The calibrated relationship for a_2 can be described using:

$$a_2 = 44.3Log\left(\sigma'_v\right) - 29.2 \qquad (5.4)$$

In order to compare the calibrated model to measured behavior, the measured load-displacement data was compared to the load-displacement predicted using Equations 5.2, 5.3, and 5.4. As shown in Figures 5.23 through 5.26, the model does relatively well at approximating the measured behavior at displacements greater than 2 mm. However, it is difficult for the hyperbolic relationship to capture the initial non-slip portion of the measured load-displacement curve.

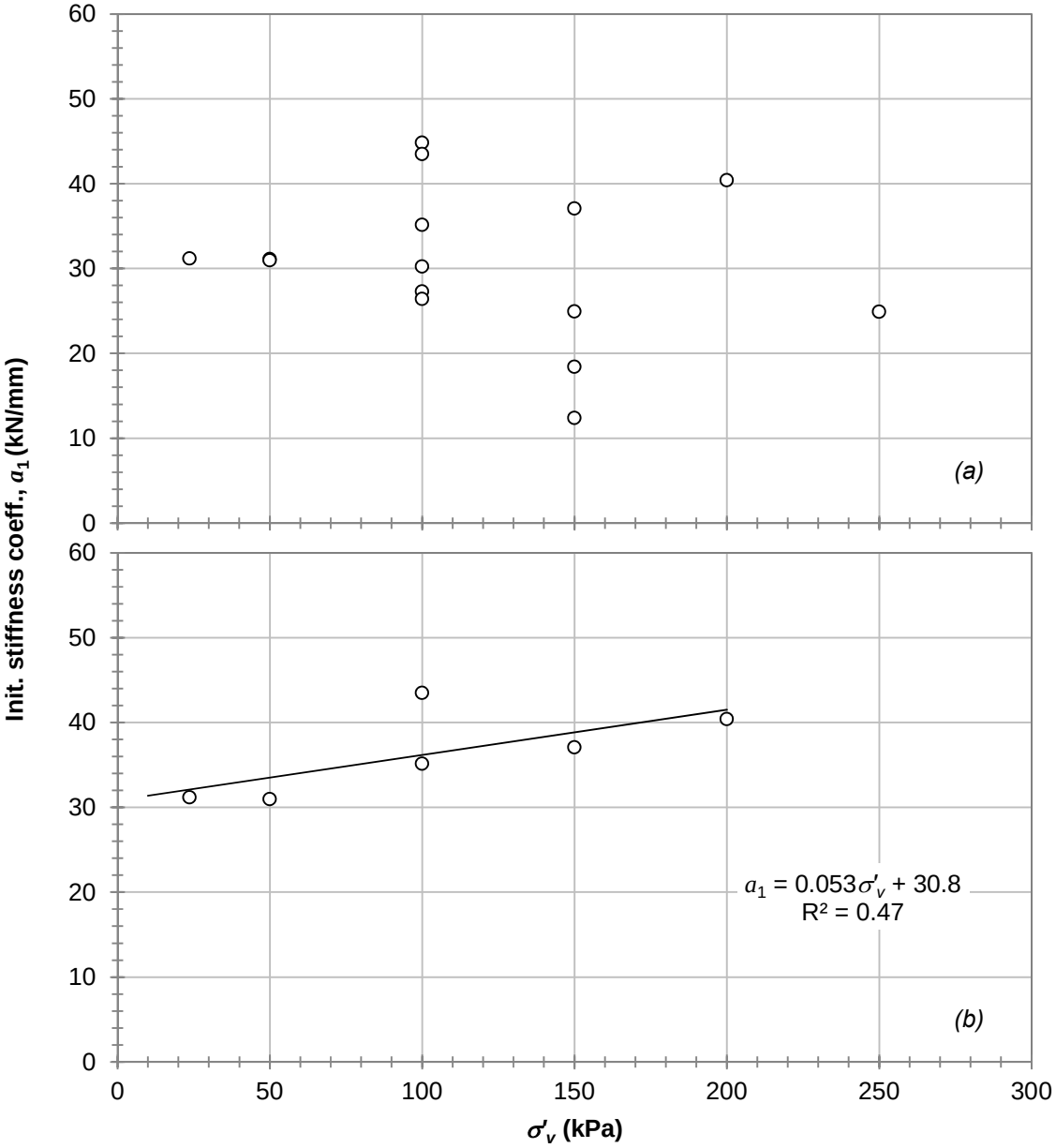

Figure 5.22. Variation of the initial stiffness coefficient, a_1, with effective vertical stress for (a) all test data, and (b) data meeting density requirements.

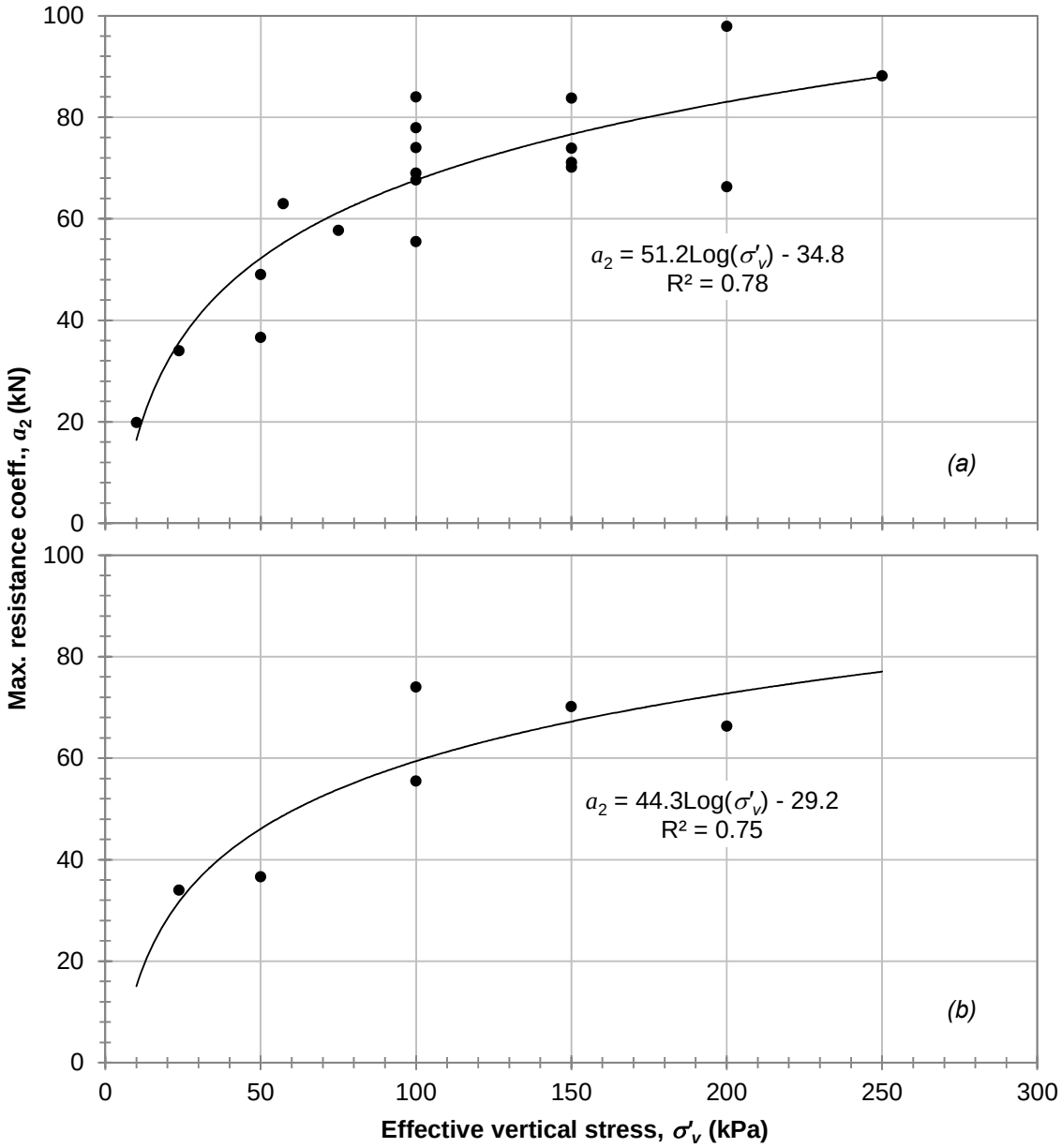

Figure 5.23. Variation of the maximum pullout resistance coefficient, a_2, with effective vertical stress for (a) all test data, and (b) data meeting density requirements..

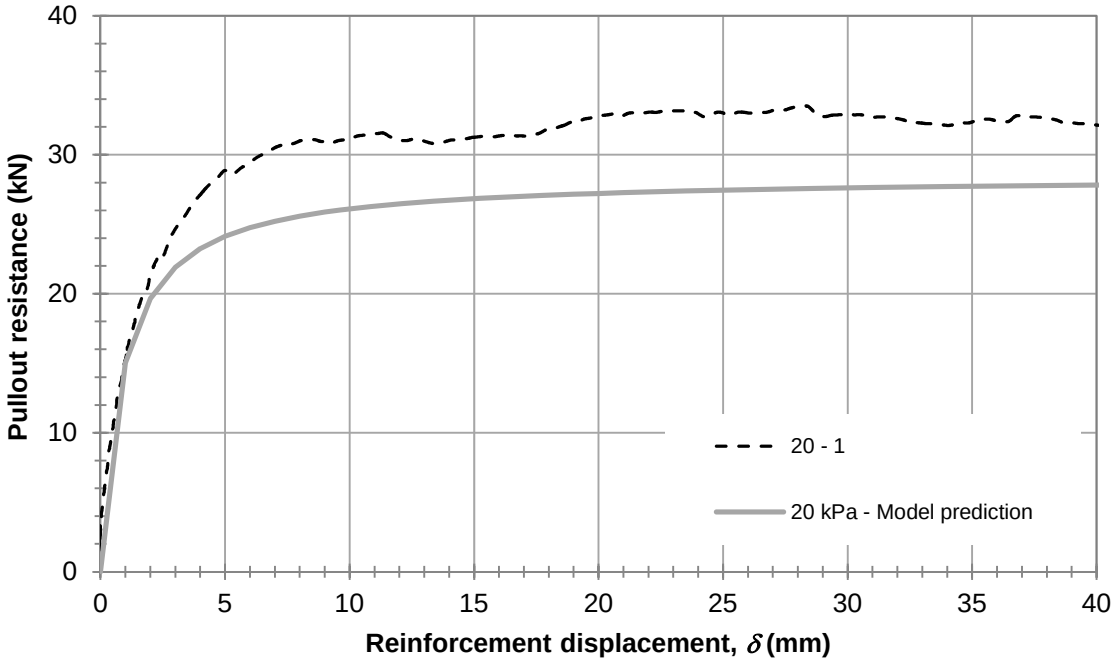

Figure 5.24. Comparison of measured pullout load-displacement behavior and the hyperbolic model prediction for σ'_v = 20 kPa.

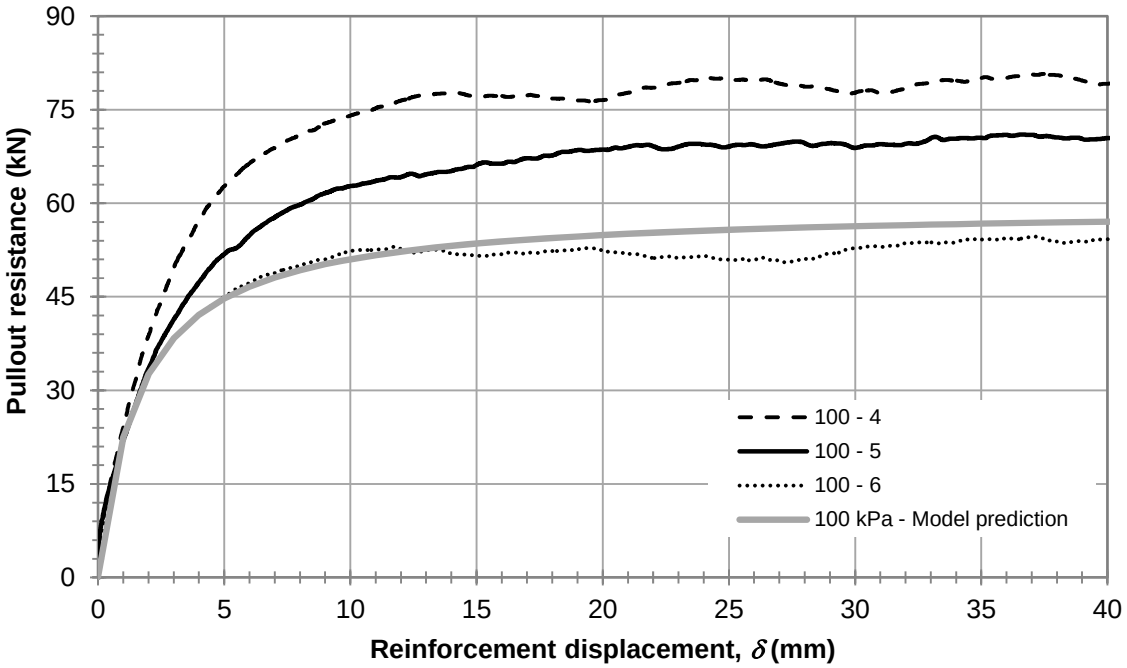

Figure 5.25. Comparison of measured pullout load-displacement behavior and the hyperbolic model prediction for tests conducted at σ'_v = 100 kPa.

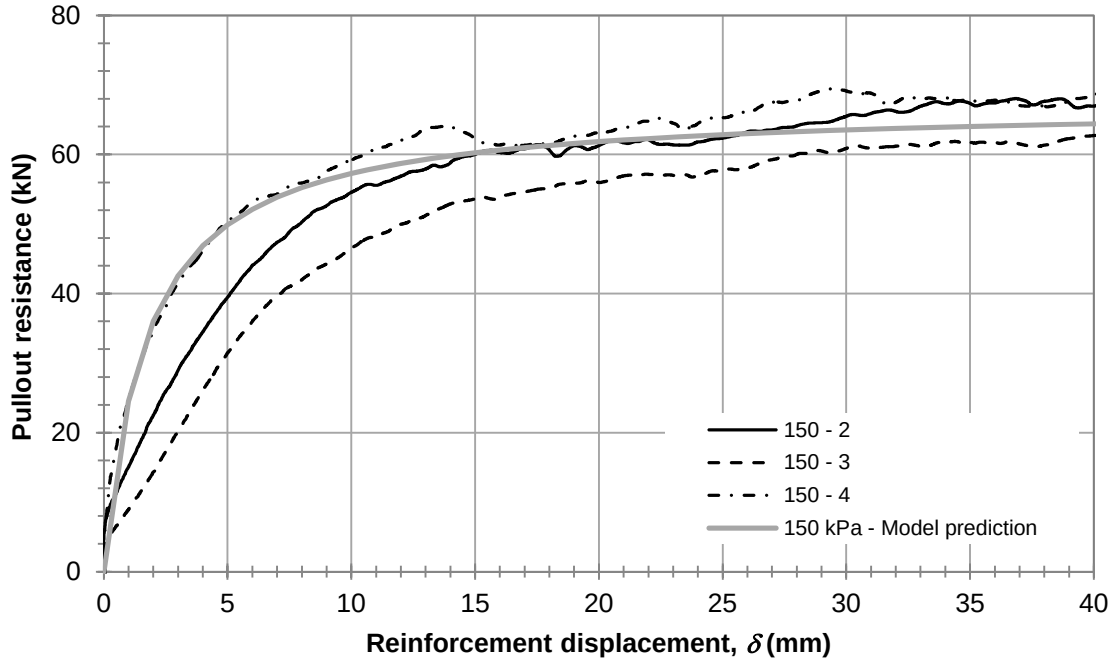

Figure 5.26. Comparison of measured pullout load-displacement behavior and the hyperbolic model prediction for tests conducted at σ'_v = 150 kPa.

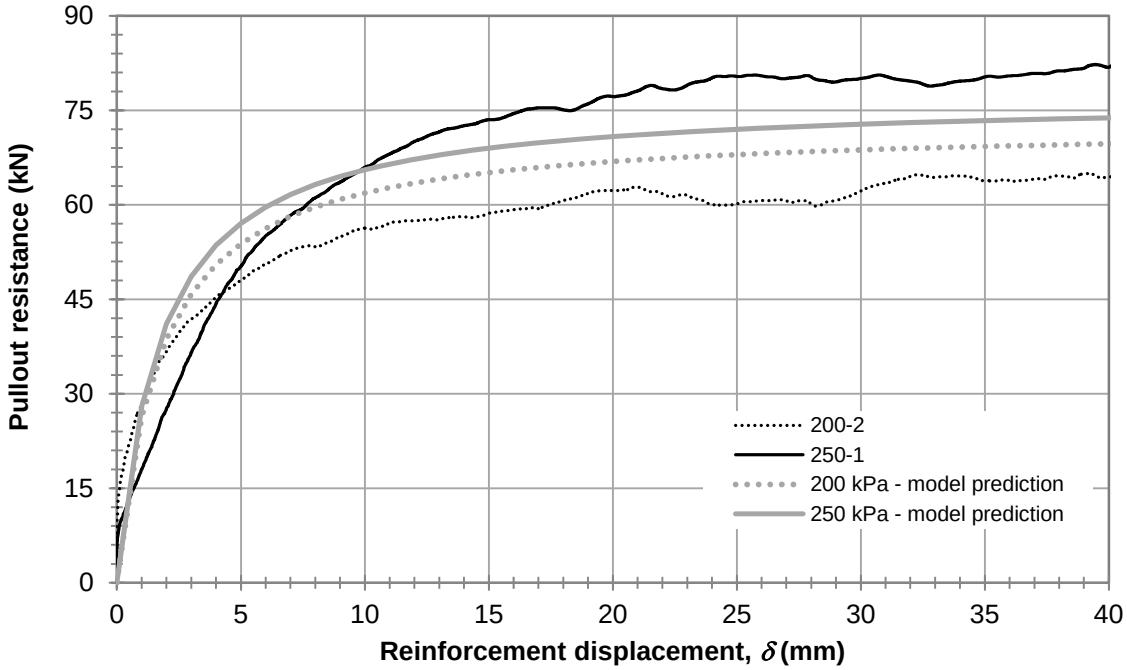

Figure 5.27. Comparison of measured pullout load-displacement behavior and the hyperbolic model prediction for tests conducted at σ'_v = 200 and 250 kPa.

5.5 Pullout Resistance Design Models for Gravel and Sand-Gravel Mixtures

The apparent friction coefficient, f^*, is an empirical design parameter used in determining the pullout resistance of MSE wall reinforcements as discussed in Section 2.2.1.2. Since the introduction of the apparent friction coefficient into accepted MSE wall design procedures, the same design model has been used to determine f^* as a function of depth. As specified by AASHTO (2010), values of f^* are not permitted to be taken as larger than 2. This limit applies to all soils types, even highly dilative soils such as gravels and sand-gravel mixtures. As shown in Figure 2.26, values of f^* well above the current design model have been measured for gravels and sand-gravel mixtures.

In order to better represent the relationship between the apparent friction coefficient and vertical effective stress for gravels and sand-gravel mixtures, a new gravel-specific design model was developed. Apparent friction coefficients of five soils were used in the calibration of the new model and are presented in Figure 5.28. The soils reported by McKittrick (1978) consisted of two gravels (G-1 and G-2) and a sand-gravel mixture (SG-1). Specific gradation information for each of these soils were not provided, however, the friction angles were reported equal to 47, 46, and 37 degrees, respectively. The soil taken from Boyd (1993) is a poorly graded gravel with the gradation presented in Figure 5.29. Though a friction angle of 35 degrees was assumed for the design of the wall, the results of strength tests were not reported by Boyd (1993).

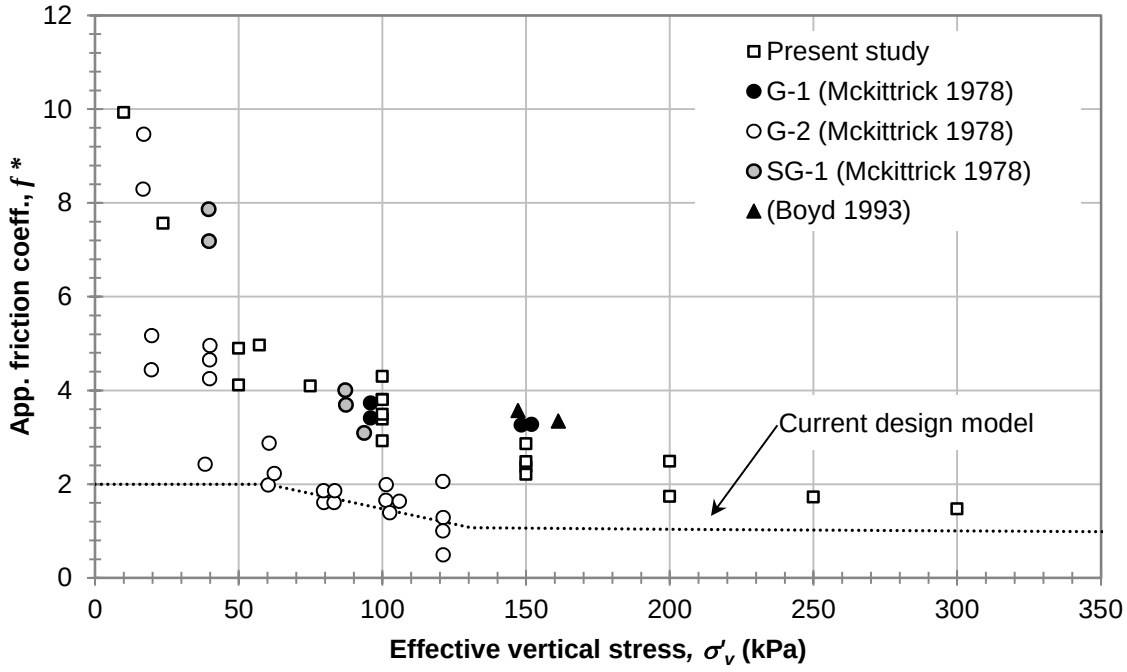

Figure 5.28. Apparent friction coefficient versus effective vertical stress for pullout tests with gravel and sand-gravel mixtures.

A new gravel-specific *f** model was calibrated using the pullout resistance data reported for the five different soils. An ordinary least squares regression with the form of an assumed function was used in the calibration. The model is presented in Figure 5.30(a) which indicates that at $\sigma'_v = 0$, $f^* = 17$, and then f^* decreases with increases in σ'_v to eventually converge to an asymptote of $f^* = 1$. The proposed general gravel model is expressed as:

$$f^* = \frac{194}{12 + \sigma'_v} + \tan\phi' \qquad (5.5)$$

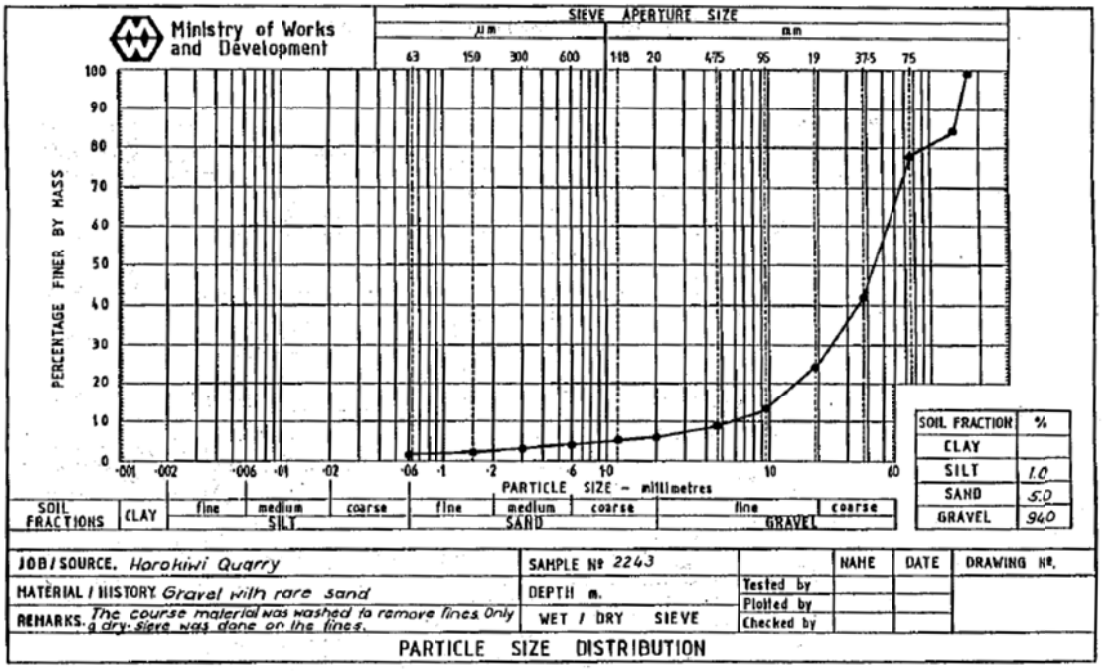

Figure 5.29. Particle size distribution of poorly graded gravel (after Boyd 1993).

Though the conservative design model discussed in Section 2.2.1.4 is typically used in design, AASHTO allows more aggressive *f** distributions if adequate pullout testing is completed. Using the same calibration procedure as was used for the general gravel model, a new backfill-specific model was calibrated for use with single strips. The backfill-specific model is presented in Figure 5.30(b), in which similar behavior to the general model was observed. The main difference between the two models is the rate of reduction in *f** which is greater for the general model than for the backfill-specific model. The proposed backfill-specific design model is proposed as:

$$f^* = \frac{286}{21 + \sigma'_v} + \tan\phi' \qquad (5.6)$$

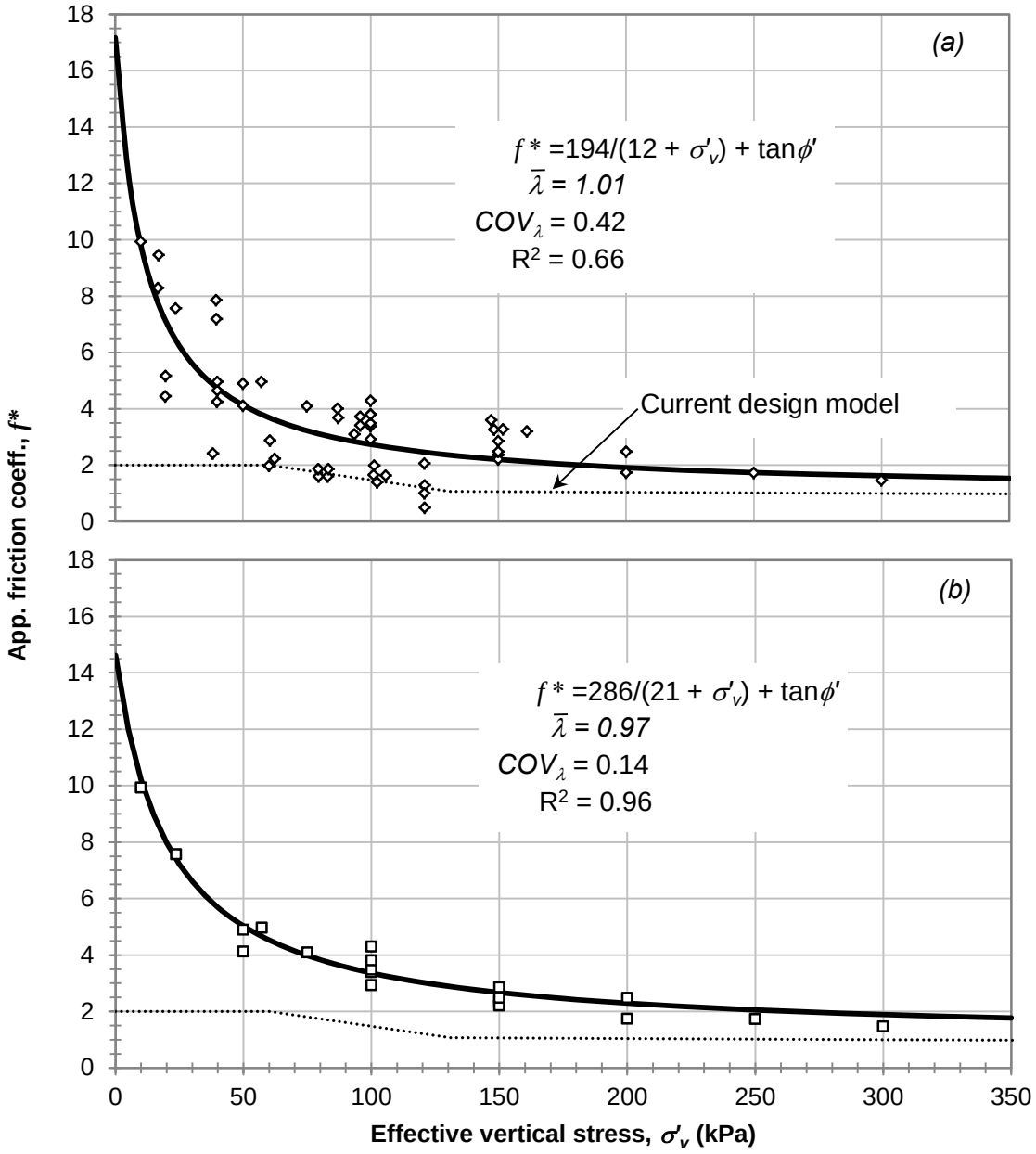

Figure 5.30. *f design models for (a) general gravel and sand-gravel backfills, and (b) specific design model for backfill tested during the present study.**

Table 5.4 presents the results of a statistical analysis performed to analyze the quality of fit of the AASHTO and general gravel *f** models to the general gravel pullout dataset (Dataset A), and the quality of fit of the AASHTO, general gravel, and backfill -specific *f** design models to the dataset of pullout results from the present study (Dataset B).

Overall, the sample biases ranged from 0.20 to 4.96 with an average sample bias between 0.97, and 2.45. The AASHTO design model produced the highest average biases for both datasets, indicating the under-prediction of *f** values and thus a more conservative model. For Dataset B, the global gravel and backfill-specific models produced similar *f** predictions, though the backfill-specific model produced a smaller average bias. For Dataset A, the global gravel model produced biases ranging from 0.20 to 1.65 with an average bias of 1.01, whereas AASHTO model bias values ranged from 0.45 to 4.96 with an average of 2.23, indicating more conservative and less accurate predictions of *f**. For the global gravel model and Dataset A, a coefficient of variation (COV) of 36 percent and coefficient of determination, R^2, of 0.66 were computed, indicating a better fit to the data when compared to the AASHTO model, which produced a COV and R^2 of 44 percent and 0.40, respectively. The use of the AASHTO model in predicting the *f** values for Dataset B resulted in biases ranging from a minimum of 1.37 to a maximum of 4.96, a COV of 32 percent, and a R^2 value of 0.65. In comparison, the global gravel and backfill-specific models produced biases ranging from 0.97 to 1.57, coefficients of variation of approximately 15 percent, and coefficients of variation of 0.94 and 0.96, respectively, indicating much more accurate and precise predictions of *f** when compared to the AASHTO model.

Table 5.4. Summary statistics on the performance of different *f design models considered in the present study.**

Dataset/Design Model	Mean bias	Range in bias		COV (%)	R^2
A: General gravel data base					
AASHTO	2.23	4.96	0.45	44	0.40
Global gravel	1.01	1.65	0.20	36	0.66
B: Present study (all tests)					
AASHTO	2.45	4.96	1.37	32	0.64
Global gravel	1.17	1.57	0.90	15	0.94
Backfill Specific	0.97	1.28	0.75	14	0.96

5.6 Summary

This chapter presented the results of twenty pullout tests on MSE wall ribbed steel strip reinforcements embedded in the sand-gravel backfill analyzed in Chapter 4. The primary conclusions and contributions of this chapter include:

1. A new apparatus was design and constructed for performing full scale laboratory pullout tests on ribbed steel strip reinforcements;
2. Twenty pullout tests were performed on the steel ribbed strips and backfill discussed in Chapter 4;
3. The effects of compaction and vertical effective stress on maximum pullout resistance was quantified statistically;
4. Hyperbolic coefficients were fit to the load-displacement data from pullout test results for future possible use in a working stress displacement prediction model.
5. A database of ribbed steel strip pullout tests in gravels and sandy gravels was developed by combining available data in literature with the pullout results from the present study;
6. Two new pullout resistance design models for use with gravels were calibrated:
    a. using all of the available pullout tests data for gravels in the literature; and
    b. using the pullout test results from the present study exclusively to form a backfill-specific design model.
7. The performance of the two new pullout resistance models were compared to the current AASHTO design model and found to produce much more accurate and precise predictions of the apparent friction coefficient.

6.0 ANALYSIS OF INTERNAL STABILITY OF VERY TALL MSE WALLS

In order to construct the 3rd Runway at the Seattle-Tacoma International Airport (SeaTac) two very tall MSE walls were erected, including the North MSE Wall (Figure 6.1) and the West MSE Wall (Figures 6.1, 6.2). The design and performance of these walls have been documented in literature by Stuedlein et al. (2007), Lindquist (2008), and Stuedlein et al. (2010a, 2010b, 2012). However, previous studies have been limited to the use of material properties originally assumed for design, or, in some cases, measured by the contractor as part of the submittal process. The main focus of this Chapter is to reevaluate the internal stability of the North and West MSE walls using the results from the extensive laboratory testing program presented in the previous chapters.

Figure 6.1. Aerial photo of the SeaTac 3rd Runway showing the location of the North and West MSE walls (looking southeast) (after Stuedlein et al. 2010b).

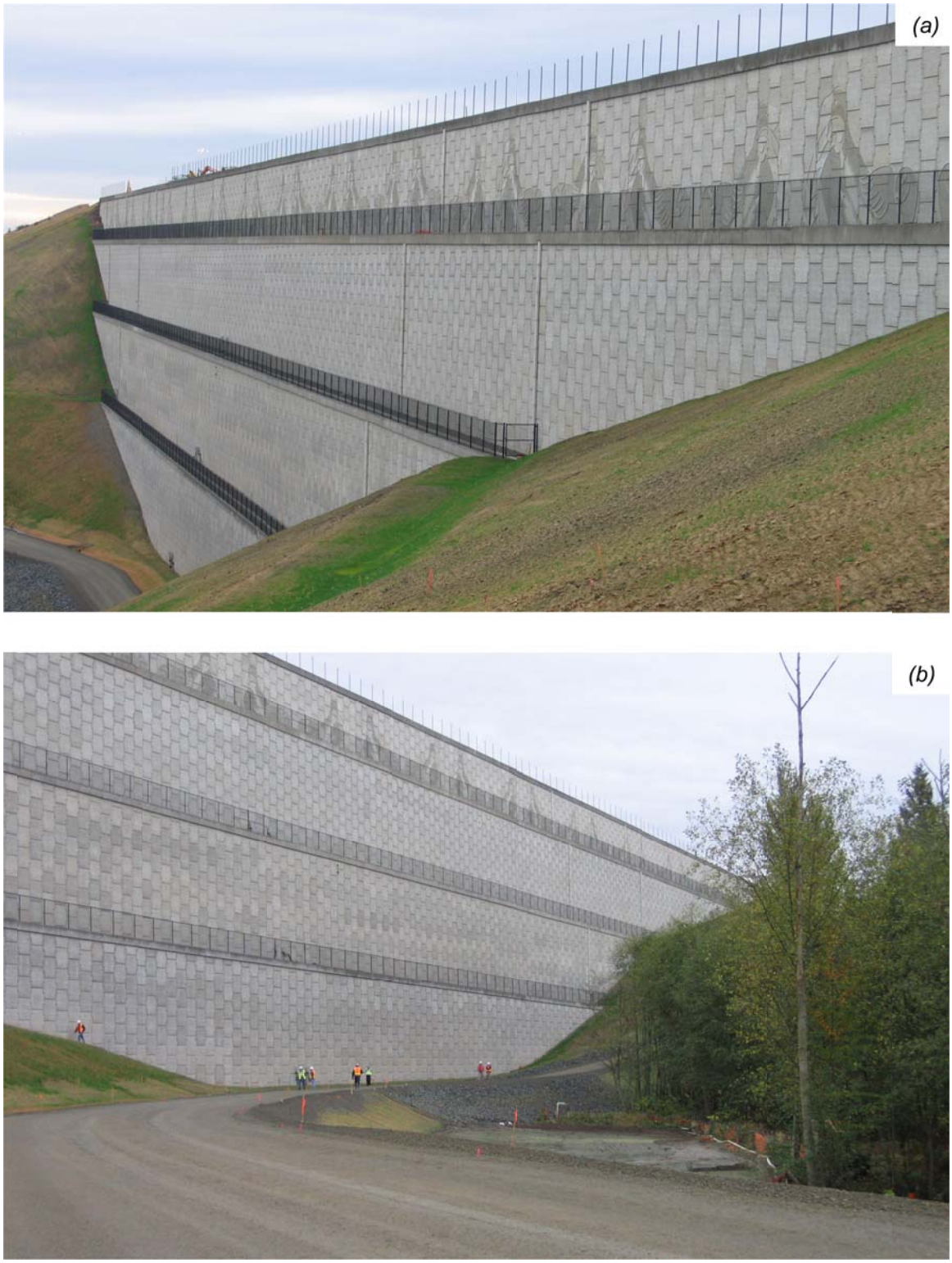

Figure 6.2. Close up view of West wall looking (a) north east, and (b) south east (Photo Credit: Tony M. Allen).

6.1 North and West MSE Wall Design Geometry

Details of the design geometry and instrumentation program, as they apply to internal stability, were taken from Stuedlein et al. (2007), Lindquist (2008), and Stuedlein et al. (2010b, 2012), and are summarized here. The interested reader is directed to these papers for a more comprehensive overview of the design and instrumentation program. The reinforced zone of the North MSE wall is 25.9 m (85 ft.) high at its tallest section with an exposed height of 23.6 m (77 ft.). The top half of the North wall is set back 2.4 m (8 ft.) from the bottom creating two separate tiers. The North wall has a level back surface. The West MSE wall has a 45.7 m (150 ft.) tall reinforced zone with a maximum exposed face height of 41.9 m (137 ft.). The West wall is separated into four tiers, each set back 2.4 m (8 ft.) from the previous tier. The West MSE wall has a sloped surcharge of structural fill with an average height of 3.8 m.

In order to account for the horizontal offsets of these tiers in design calculations (e.g., earth pressures), both walls were assigned an equivalent face batter. The equivalent face batter was determined using the total tier spacing and the total wall height (including the unexposed section) resulting in wall inclinations of 9.1 and 5.4 degrees for the West and North MSE walls, respectively. As shown in Figure 6.3, the reinforcement layers terminated at the same horizontal distance from the toe of the wall. The reinforcement lengths in each tier ranged from 18.9 (62 ft.) for the top tier of the North wall to 35.4 m (to 116 ft.) for the bottom tier of the West wall. All reinforcing layers were greater or equal to 70 percent of the overlying height as required by AASHTO. Table 6.1 presents the reinforcement geometry for both walls including the reinforcement lengths and average vertical and horizontal spacing for each tier. The values of reinforcement spacing reported in Table 6.1 are averaged over large wall areas, when in reality the west wall had local vertical reinforcement spacing as small as 0.24 m (0.79 ft.) with as many as 28 reinforcing strips per 2.25 m^2 panel.

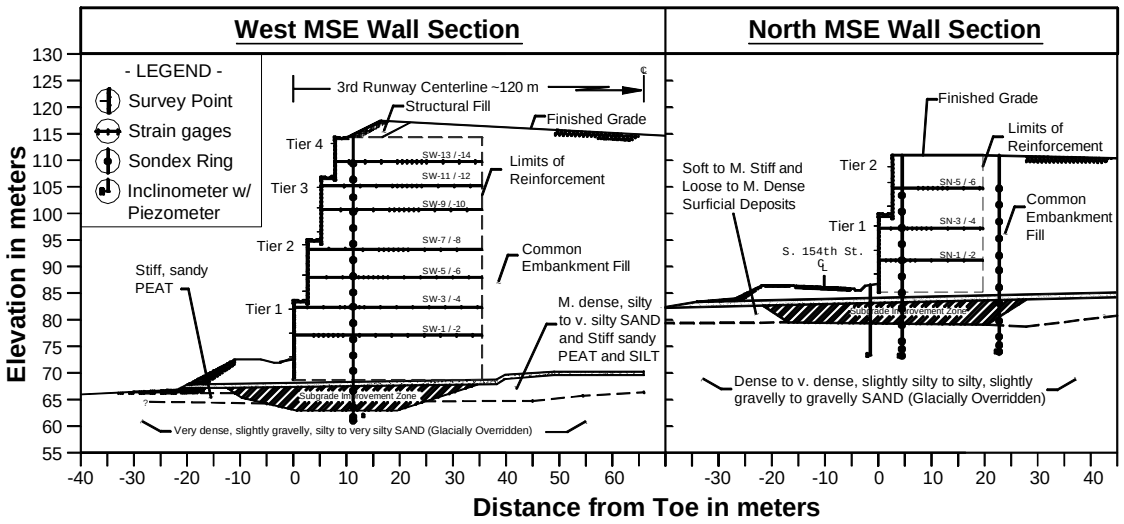

Figure 6.3. Sections of the (a) West and (b) North MSE walls showing the location of instrumentation (after Stuedlein et al. 2012).

Table 6.1. Reinforcement geometry for the North and West MSE walls (after Stuedlein et al. 2012).

	Length of strip (m)	Mean vertical spacing (m)	Mean horizontal spacing (m)
West MSE wall			
Tier 4	28.0	0.74	0.74
Tier 3	30.5	0.74	0.63
Tier 2	32.9	0.70	0.39
Tier 1	35.4	0.42	0.18
North MSE wall			
Tier 2	18.9	0.75	0.71
Tier 1	21.3	0.66	0.43

6.2 Instrumentation of Steel Strip Reinforcements

An extensive instrumentation program was implemented for the North and the West MSE walls to monitor wall performance during following construction. These instrumentation programs included two identical sections of instrumented reinforcing strips installed approximately 4 m (13 ft.) apart in each wall. Each instrumented reinforcement strip was given a designation that consisted of a wall identifier (SN for the North wall, and SW for the West wall), and an identification number that increased with

elevation (odd numbered reinforcements were in section one, and evens numbered reinforcements in section two). The number of strain gauge pairs used along the length of each instrumented reinforcement strip ranged from 13 to 16. In order to increase the resolution, strain gauges were more densely situated where the wall manufacturer (i.e., Reinforced Earth Co.) expected the maximum reinforcement strains to occur. Both the elevation of each instrumented reinforcement, as well as the distribution of strain gauge pairs for the North and West MSE walls are shown in Figure 6.3.

6.3 Reevaluation of Inferred Loads Using Measured Reinforcement Properties

The measured peak reinforcement strains reported in Stuedlein et al. (2012) were used to reevaluate the maximum reinforcement loads and stresses in the North and West MSE walls. As reported in Section 4.2, a representative value of the Young's modulus was equal to 208 GPa for the actual reinforcement strips used in the SeaTac MSE wall and corresponds to a four percent increase over the assumed nominal design value of 200 GPa. Because Young's modulus and load are directly proportional, a four percent increase in the Young's modulus corresponded to a four percent increase in computed reinforcement load for all reinforcement layers. In the present study, the maximum reinforcement loads were divided by the horizontal reinforcement spacing to show the increase in unit reinforcement load with depth, which allows easier visual comparison of loads for such tall MSE walls. The reinforcement loads reported in Stuedlein et al. (2012), which used an assumed Young's modulus of 200 GPa, as well as those computed using the measured Young's modulus of 208 GPa are provided in Table 6.2 and Table 6.3 for the North and West MSE walls respectively. The maximum reinforcement loads computed using the measured reinforcement Young's modulus will be the basis for all further comparisons.

Owing to the larger value of measured yield strength (taken as the representative value from Section 4.1) than the nominal value originally used, apparent net reductions in stress as a percent of the non-factored yield strength of 2.3 and 3.3 percent was observed for the North and West walls respectively.

Table 6.2. Comparison of maximum reinforcement loads and stresses for the North MSE wall computed using the measured material properties and those assumed for wall design (strain measurements taken August 2009).

Designation	Load per reinforcement strip (kN)		Load per unit width of wall (kN/m)		Stress as a percent of yield strength	
	Assumed	Measured	Assumed	Measured	Assumed	Measured
SN-1	34.7	36.1	81.9	85.2	25.8	22.9
SN-2	31.4	32.6	73.9	76.9	23.3	20.7
SN-3	30.5	31.7	51.3	53.4	22.7	20.1
SN-4	35.4	36.8	59.6	62	26.3	23.3
SN-5	29	30.1	39	40.6	21.6	19.1
SN-6	23.6	24.5	31.7	33	17.5	15.5
Avg. percent change	4.0		4.0		-2.6	

[a] Assumed material properties: E = 200 GPa, f_y = 448 MPa
[b] Measured material properties: E = 208 GPa, f_y = 526 MPa

Table 6.3. Comparison of maximum reinforcement loads and stresses for the West MSE wall computed using the measured material properties and those assumed for wall design (strain measurements taken August 2009).

Designation	Load per reinforcement strip (kN)		Load per unit width of wall (kN/m)		Stress as a percent of yield strength	
	Assumed	Measured	Assumed	Measured	Assumed	Measured
SW-1	44.3	46.1	238.3	247.9	33	29.2
SW-2	47.7	49.6	256.5	266.8	35.5	31.5
SW-3	40.8	42.4	164.3	170.9	30.3	26.9
SW-4	41.3	42.9	166.4	173.1	30.7	27.2
SW-5	42.5	44.2	114.5	119.1	31.6	28
SW-6	38.5	40	103.6	107.8	28.6	25.3
SW-7	40.6	42.2	81.9	85.2	30.2	26.7
SW-8	39.8	41.4	80.3	83.6	29.6	26.2
SW-9	31.7	33	53.4	55.6	23.6	20.9
SW-10	34.2	35.6	57.6	59.9	25.4	22.5
SW-11	48.7	50.6	65.8	68.4	36.2	32.1
SW-12	36.8	38.3	49.7	51.7	27.4	24.3
SW-13	30.4	31.6	41.1	42.8	22.6	20.1
SW-14	26.9	28	36.4	37.9	20	17.8
Avg. percent change	4.0		4.0		-3.3	

[a] Assumed material properties: E = 200 GPa, f_y = 448 MPa
[b] Measured material properties: E = 208 GPa, f_y = 526 MPa

6.4 Selection of Parameters for Use with Reinforcement Load Prediction Methods

As discussed in Section 2.2.1, research performed by Allen et al. (2001) observed that the Coherent Gravity and Simplified Methods significantly under predict reinforcement loads when friction angles greater than 40 degrees were used on walls with steel reinforcements. The research performed by Allen et al. (2001) was the basis for the current stipulation by AASHTO that the use of friction angles greater than 40 degrees is not permitted when steel reinforcements are used (Berg et al. 2009; Stuedlein et al. 2012). Additionally, Allen et al. (2004) limited plane strain friction angles to ϕ_{PS} = 44 degrees for the calibration of the K-Stiffness method in order to be consistent with the empiricism in the Coherent Gravity and Simplified methods as well as AASHTO guidelines.

The distribution of maximum reinforcement load with depth as predicted by the Coherent Gravity, Simplified, Ehrlich and Mitchell (1994), and K-Stiffness methods were compared to the measured maximum reinforcement loads. For each of these methods, four different Mohr-Coulomb failure envelopes were used to determine a total of 16 load distributions for each wall; these included:

- Case 1: the failure envelope assumed for wall design;
- Case 2: the failure envelope capped to the appropriate value of ϕ' per AASHTO;
- Case 3: the curved failure envelope as measured in triaxial compression; and,
- Case 4: the curved failure envelope transformed to plane strain.

The motivation for considering Case 1 was to assess the sensitivity of each method to more conservative input parameters as well as to provide a baseline for further comparisons. A constant “direct shear” friction angle of 37 degrees was used for design as this was a minimum requirement for the reinforced backfill to be used in constructing the wall (Stuedlein et al. 2010b). Contractors were required to perform strength testing prior to and periodically throughout construction in order to ensure the strength requirements of the backfill were being met. Because the Ehrlich and Mitchell (1994) method was not considered during design, the Duncan and Chang (1970) hyperbolic

fitting parameters were chosen based on "conservative" recommendations by Duncan et al. (1980). For sands and gravels at a relative compaction of 95 percent, Duncan et al. (1980) recommends values of modulus number, modulus exponent, and failure ratio of K = 300, n = 0.4, and R_f = 0.7, respectively. However, in order to reduce the number of parameters being varied, the modulus exponent and failure ratio were set equal to those values reported in Chapter 4 for all four failure envelopes.

The results from the CD triaxial strength test program and the Duncan and Chang (1970) calibration reported in Chapter 4 were used in Case 3 (without modification) to calculate reinforcement loads using the Ehrlich and Mitchell (1994) method. However, because the Ehrlich and Mitchell (1994) method calls for plane strain soil parameters, both the friction angles and modulus numbers were increased from their measured or assumed value to an equivalent plane strain value for all other cases. The following empirical relationship was used to transform friction angles measured in triaxial compression to plane strain (Lade and Lee 1976):

$$\phi_{PS} = 1.5\phi_{TX} - 17° \qquad (6.1)$$

To determine an equivalent plane strain modulus number, the modulus number determined using triaxial strength test data was multiplied by a factor of 2.25 as suggested by Hatami and Bathurst (2005) based on their experimental evidence on a granular soil. Consequently, the modulus number reported in Section 4.4 for a relative density of D_r = 65 percent (K = 1200), was transformed to an equivalent plane strain value of 2700. In order to assess the appropriateness of this assumption, plane strain friction angles were determined using the Duncan Chang (1970) hyperbolic stress-strain model using the equivalent plane strain modulus number, and compared to those computed using Equation 6.1. Figure 6.4 shows the plane strain and triaxial hyperbolic curves for effective confining stresses of 100, 200 and 300 kPa as well as the stress-strain behavior measured for the corresponding CD triaxial strength test specimen. Unlike the stress-strain behavior of the CD triaxial strength test specimens, the hyperbolic curves do

not show an obvious point of "failure" (e.g., peak principal stress ratio or peak principal stress difference) for determining the friction angle. For simplicity, failure was assumed to coincide with the equivalent triaxial test specimen's peak principal stress ratio (i.e., failure of the triaxial specimen as defined in Section 4.2.4). As shown in Figure 6.5, friction angles determined from the modified hyperbolic model are in agreement with the values of plane strain friction angles estimated using Equation 6.1 with an average bias, defined as the ratio of measured and predicted values, of 1.06 and a coefficient of variation of 4.2 percent. Regrettably, plane strain data is neither available for this specific backfill nor for a similar backfill material with which a more in-depth comparison could be made at this time.

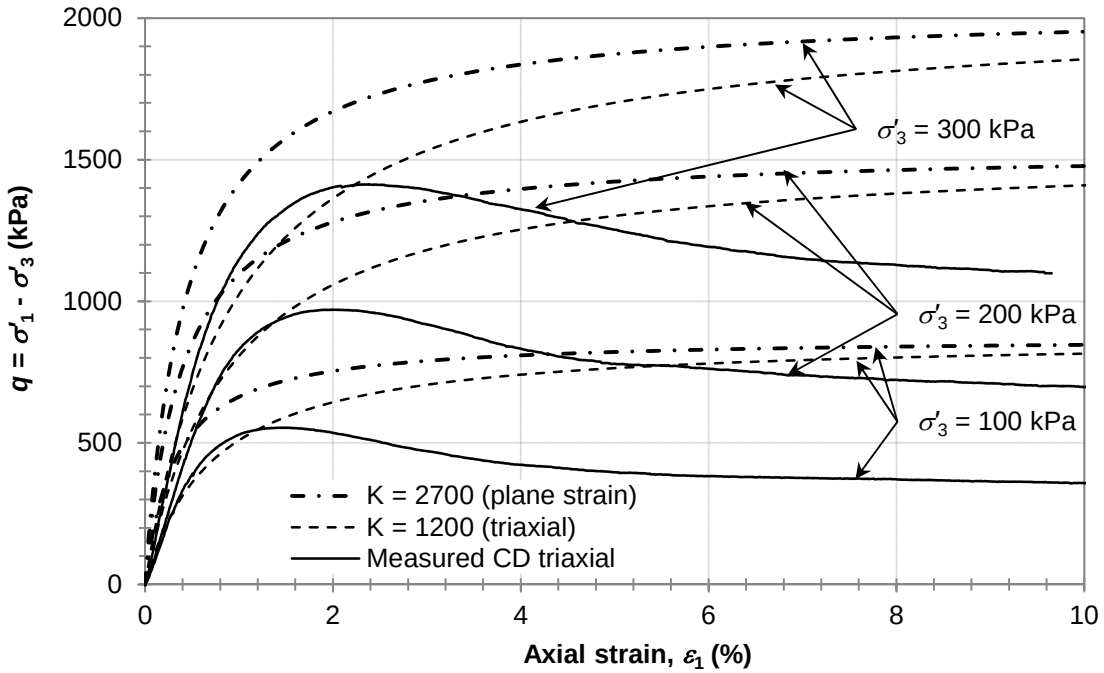

Figure 6.4. Comparison of stress-strain curves generated using the Duncan and Chang (1970) hyperbolic model with plane strain and triaxial modulus numbers.

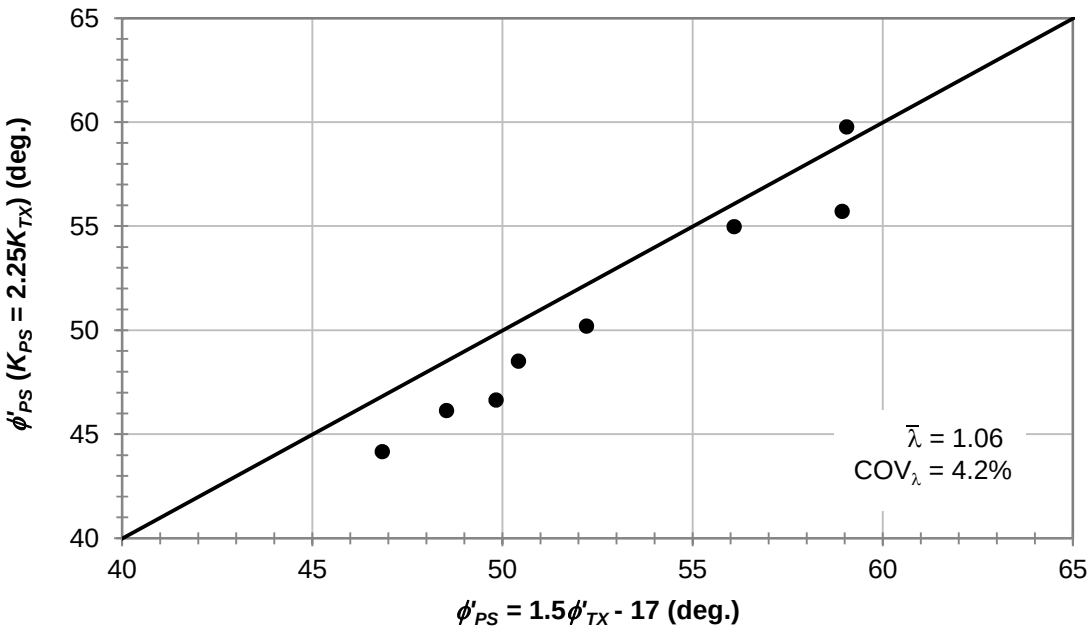

Figure 6.5. Comparison of plane strain friction angles determined using the empirical correlation recommended by Lade and Lee (1976) and those determined from the Duncan and Chang (1970) hyperbolic model with the modulus number increased by a factor of 2.25.

In addition to the hyperbolic parameters, the energy and dimensional specification of the compaction equipment were needed to perform the Ehrlich and Mitchell (1994) method. For both the North and West MSE walls, a Caterpillar model CS-563D vibratory roller with a smooth 10,875 kg (24 kip) drum was used to compact the reinforced backfill. The drum had a diameter of 1.55 m (61 in.), a width of 2.13 m (84 in.), and delivered static and dynamic compaction forces of 26.4 and 127.5 kg/cm (148 and 714 lb/in.), respectively (Stuedlein et al. 2010b).

When using a curved Mohr-Coulomb failure envelope in earth pressure calculations, the variation of friction angle with depth must be determined iteratively due to the friction angles interdependence with effective confining pressure and the lateral earth pressure coefficient. For the case of no surcharge load and Rankine active earth pressure theory, the iterative process to determine the friction angle at a given depth below the top of the wall, *Z*, can be summarized by:

$$\phi_n = \phi_{1atm} - \Delta\phi \log\left(\frac{\gamma Z \tan^2\left(45 - \frac{\phi_{n-1}}{2}\right)}{P_{atm}}\right) \qquad (6.2)$$

where ϕ_n is an improved guess of the friction angle to be used in the following iteration, $\phi_{1\text{atm}}$ is the friction angle measured at a confining pressure of one atmosphere (gauge pressure), and $\Delta\phi$ is the change in friction angle over one log cycle of effective confining pressure. Typically seven iterations were sufficient to achieve convergence of the friction angle for any given depth.

Table 6.4. Constitutive parameters used with each design case investigated.

Case No.	$\phi_{TX,\,DS}$ at 1 atm (deg.)	ϕ_{PS} at 1 atm (deg.)	$\Delta\phi$ per Log_{10} (σ'_3/P_{atm}) cycle (deg.)	Modulus number, *K*
Coherent Gravity and Simplified methods				
Case 1	37	N/A	0	N/A
Case 2	40	N/A	0	N/A
Case 3	47.9	N/A	6.4	N/A
Case 4	N/A	54.9	6.4	N/A
Ehrlich & Mitchell (1994)				
Case 1	N/A	38.5	0	675
Case 2	N/A	44	0	2700
Case 3	47.9	N/A	6.4	1200
Case 4	N/A	54.9	6.4	2700
K-Stiffness method				
Case 1	N/A	38.5	0	N/A
Case 2	N/A	44	0	N/A
Case 3	47.9	N/A	6.4	N/A
Case 4	N/A	54.9	6.4	N/A

6.5 Comparison of Predicted and Measured Reinforcement Loads

The accuracy of the reinforcement load distributions for the North and West MSE walls were analyzed using two approaches. First, the measured maximum reinforcement loads were plotted alongside the predicted maximum load distribution from each case and visual comparisons made. Second, a statistical analysis of the accuracy of the predicted reinforcement loads was performed by computing the bias and their variation.

6.5.1 North MSE Wall

Large variations in the predicted loads were observed between the prediction methods and the cases investigated. As shown in Figure 6.6(a), the Simplified method produced the most accurate predictions of reinforcement loads for Case 1. However, for the Coherent Gravity and Simplified methods, reinforcement loads were under-predicted near the top of the wall with an increase in accuracy with decreases in elevation. The Ehrlich and Mitchell (1994) method agreed with the measured reinforcement loads closest to the top of the wall, but over-predicted the loads in the lower elevations. The K-Stiffness method produced overly conservative estimates at all three comparison depths.

For Case 2 (Figure 6.6b), the Coherent Gravity and Simplified methods both under-predicted the reinforcement loads at all elevations, whereas the Ehrlich and Mitchell (1994) method produced accurate predictions at the top, but slightly under-predicted the loads in the bottom two thirds of the wall. In the upper-most reinforcement layers, the K-Stiffness method predicted smaller loads than the Ehrlich and Mitchell (1994) method. However, at the elevation of the top instrumented reinforcement strip, the K-Stiffness predicted load distribution became conservative and remains conservative for all remaining elevations.

The K-Stiffness method best predicted the reinforcement loads with Case 3 near the top of the wall, although the predictions were slightly non-conservative. Near the top of the wall, the Ehrlich and Mitchell (1994) distribution produced the best reinforcement load estimates, but became non-conservative at lower elevations. Both the Coherent Gravity and Simplified methods produced highly non-conservative load distributions for

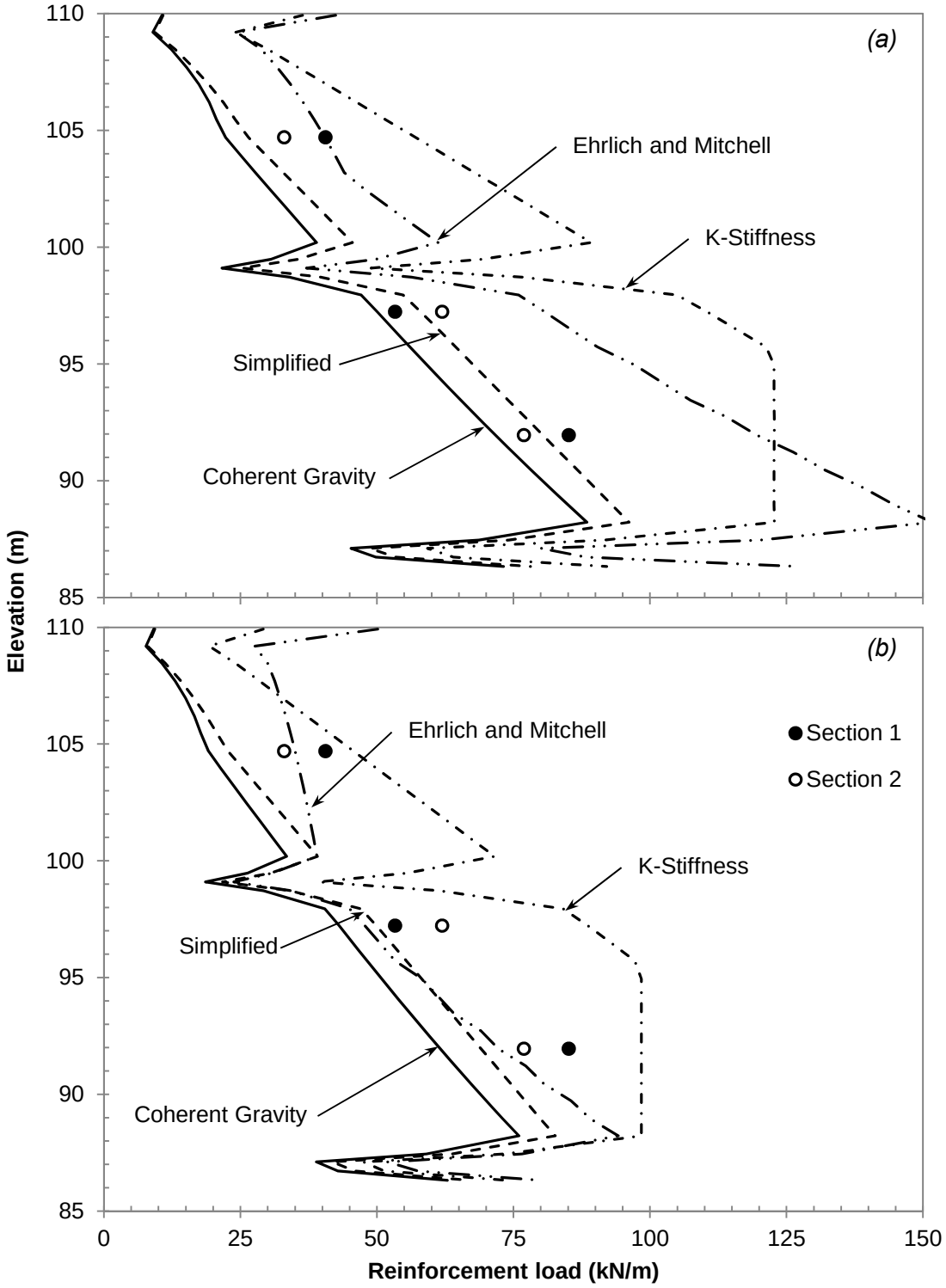

Figure 6.6. Observed and predicted peak reinforcement loads for the North MSE wall using (a) the soil properties assumed during design (Case 1) , and (b) the actual soil properties capped per AASHTO (Case 2).

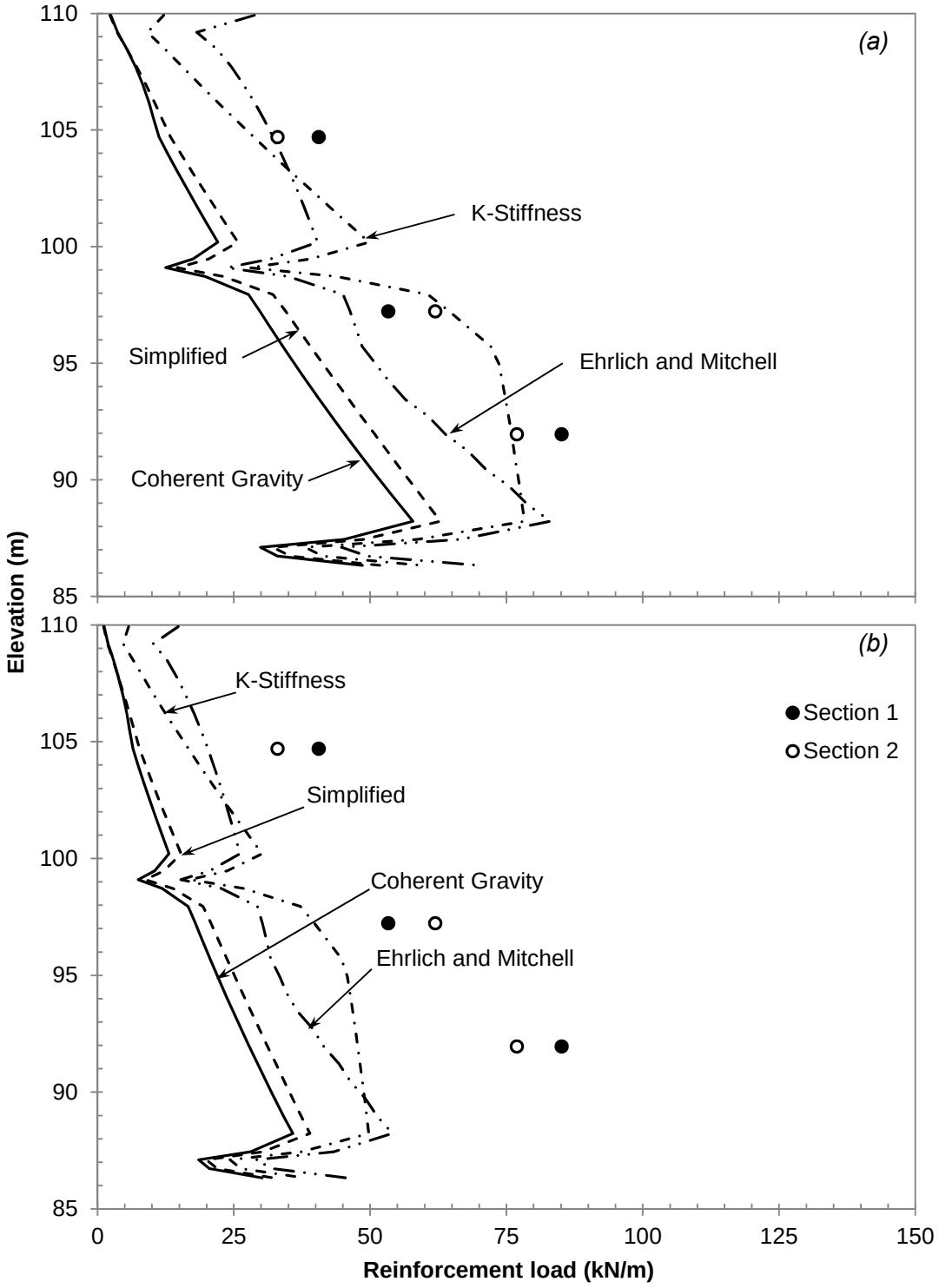

Figure 6.7. Observed and predicted peak reinforcement loads for the North MSE wall using (a) triaxial properties with a curved failure envelope (Case 3), and (b) plane strain properties with a curved failure envelope (Case 4).

Case 3. As shown in Figure 6.7(b), all of the load prediction methods produced non-conservative estimates of reinforcement load at all wall elevations for Case 4.

Figure 6.8 and Figure 6.9 show the effect of using different Mohr-Coulomb failure envelopes on the accuracy of each reinforcement load prediction method. As shown in Figure 6.8a, the Coherent Gravity method under predicts the reinforcement loads for each of the four failure envelopes considered with the "design" failure envelope producing the least amount of error. The Simplified method performs fairly well when utilizing conservative strength parameters as shown in Figure 6.8(b) consistent with Bathurst et al. (2009). However, when using the plane strain and triaxial curved failure envelopes, the Coherent Gravity and Simplified methods produce large, non-conservative errors. In contrast, the K-Stiffness method generally produced conservative predictions of reinforcement load, as shown in Figure 6.9(a), especially when more conservative strength parameters were used.

The Ehrlich and Mitchell (1994) method (Figure 6.9b) produced the most variation in shape between each failure envelope, demonstrating its flexibility and analytical power. With visual inspection of Figure 6.9(b) it is apparent that none of the selected combinations of input parameters (K and ϕ) provided the best possible fit when using the Ehrlich and Mitchell (1994) method; however, this method still produced the best "overall" prediction of maximum reinforcement load for the North MSE wall despite its lack of optimization.

In order to quantify the visual fit in Figures 6.6 through 6.9, the average bias for each case was computed; the statistics are presented in Table 6.5. Due to the low number of data points, the COV was calculated using the small sample standard deviation method (Lacasse and Nadim 1996). The minimum average bias, corresponding to the most conservative distribution, of 0.61 was computed for the K-Stiffness method using a constant friction angle of ϕ'_{PS} = 38.5 degrees. The maximum average bias, corresponding to the least conservative distribution, of 3.94 was computed for the Coherent Gravity method using the plane strain curved failure envelope. This was expected as the Coherent Gravity method is an empirically based method calibrated using triaxial and direct shear

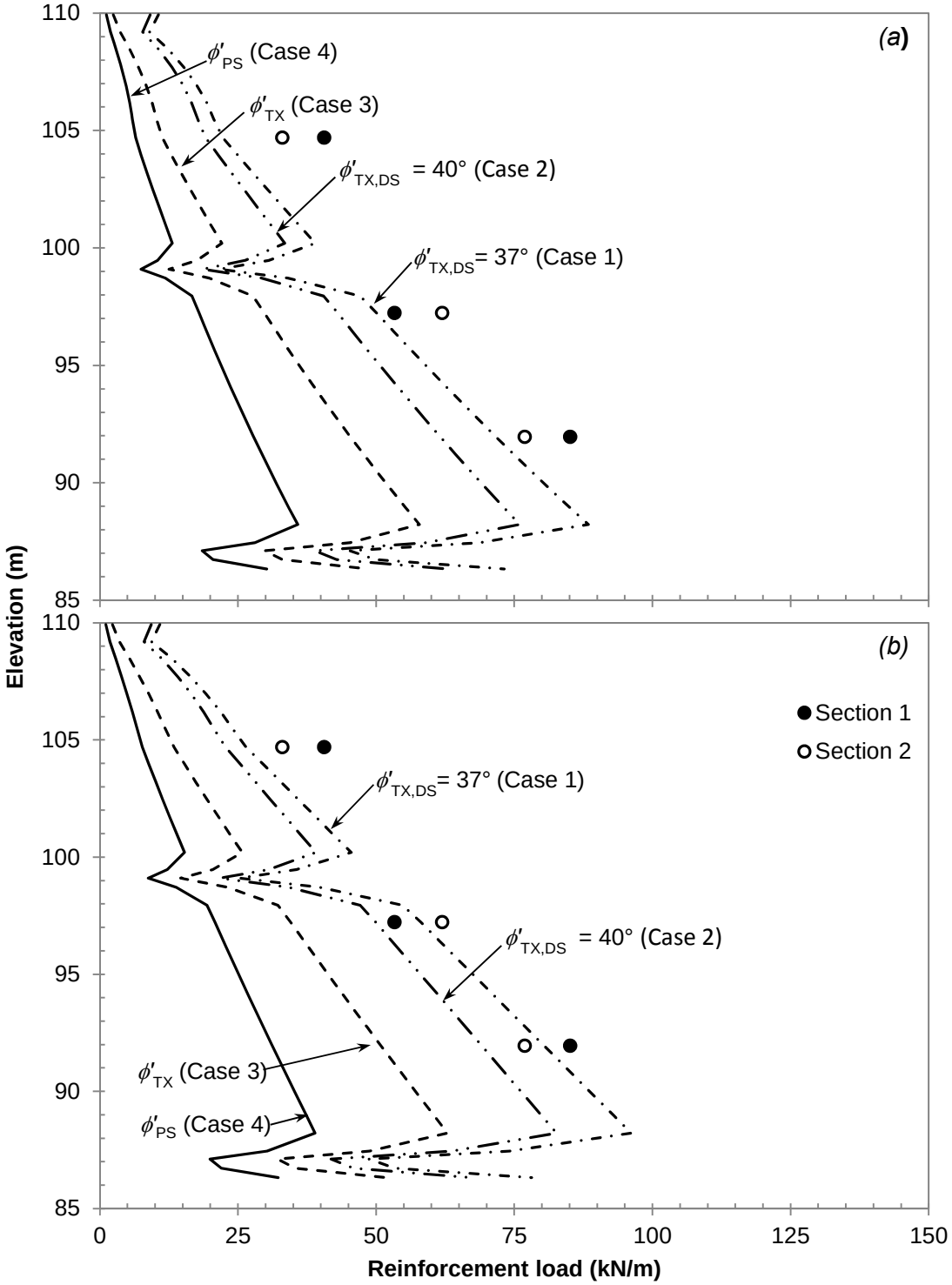

Figure 6.8. Observed and predicted peak reinforcement loads for the North MSE wall using (a) Coherent Gravity method, and (b) the AASHTO Simplified method.

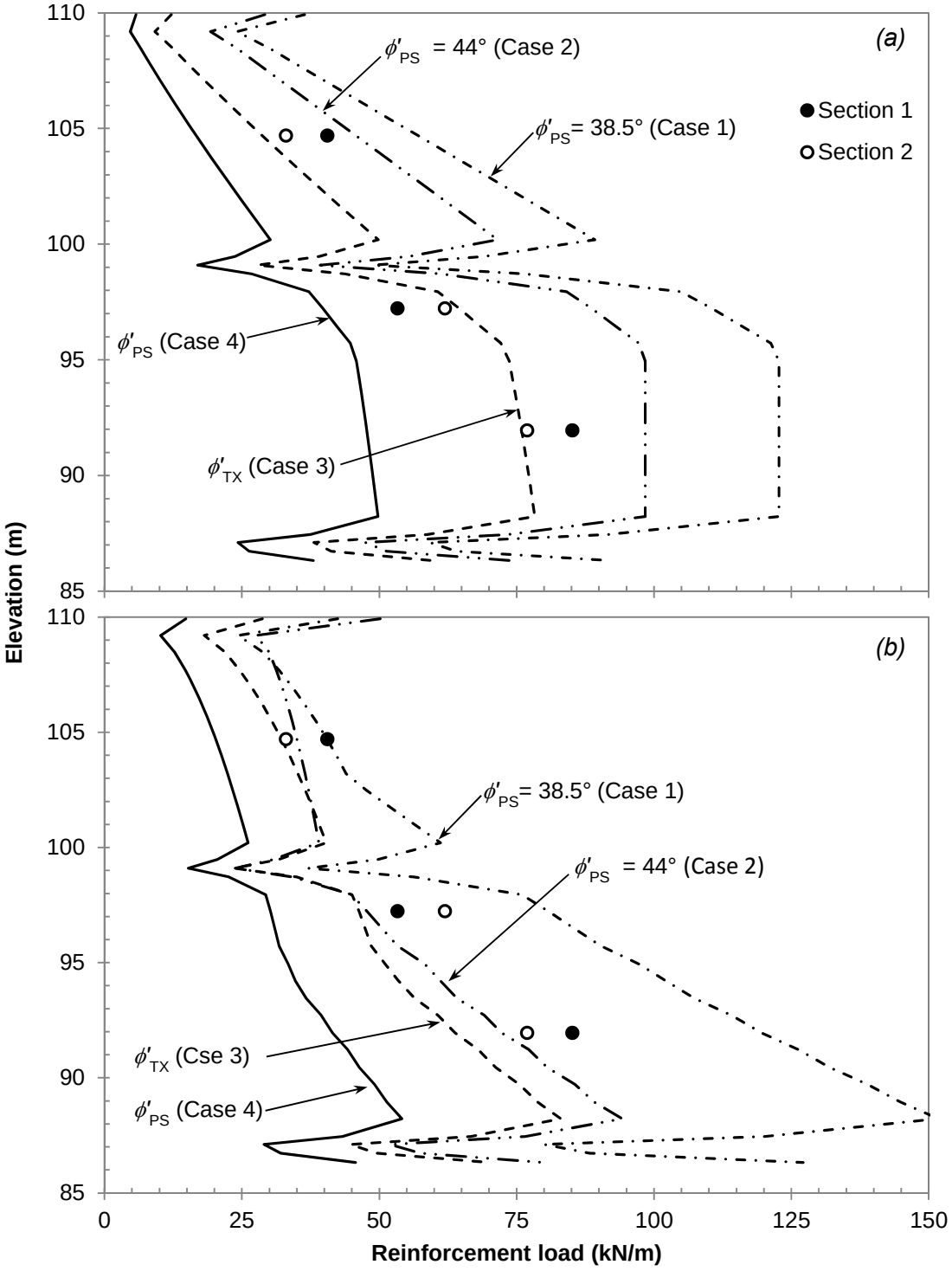

Figure 6.9. Observed and predicted peak reinforcement loads for the North MSE wall using (a) Ehrlich and Mitchell (1994), and (b) the K-Stiffness method.

friction angles which are typically 10 to 15 percent smaller than plane strain friction angles. The K-Stiffness method with the triaxial curved failure envelope produced an average bias of 1.08, corresponding to the most accurate method. However, with a COV = 21 percent, this was not the most precise distribution produced. When considering both precision and accuracy, the best overall prediction was made by the Ehrlich and Mitchell (1994) method with the friction angle capped at 44 degrees with an average bias of 1.13 and COV = 12 percent.

Table 6.5. Summary statistics of the bias in reinforcement loads calculated for the North MSE wall.

Case No.	Mean bias	Range in bias		COV[a] (%)
Coherent Gravity method				
Case 1	1.31	1.82	1.06	23
Case 2	1.53	2.12	1.24	23
Case 3	2.33	3.60	1.70	32
Case 4	3.94	6.27	2.76	35
AASHTO Simplified method				
Case 1	1.13	1.53	0.92	21
Case 2	1.32	1.78	1.07	21
Case 3	2.00	3.03	1.51	30
Case 4	3.38	5.27	2.47	33
Ehrlich & Mitchell (1994)				
Case 1	0.77	1.00	0.64	19
Case 2	1.13	1.30	0.94	12
Case 3	1.22	1.34	1.03	10
Case 4	1.89	2.05	1.63	9
K-Stiffness method				
Case 1	0.61	0.71	0.48	15
Case 2	0.76	0.89	0.60	15
Case 3	1.08	1.42	0.83	21
Case 4	1.79	2.43	1.34	24

[a] Estimated using small-sample standard deviation method (Lacasse and Nadim 1996).

6.5.2 West MSE Wall

Many of the trends observed for the North MSE wall were also observed in the West MSE wall. As shown in Figure 6.10(a) and Figure 6.10(b), the Coherent Gravity and Simplified methods produced good estimates of reinforcement load at the top of the West

MSE wall for Cases 1 and 2; however, at lower elevations large non-conservative errors were observed. In contrast, the K-Stiffness method greatly over-predicted the loads except at the very lowest elevations for both Cases 1 and 2.

For Case 1, the Ehrlich and Mitchell (1994) method produced large conservative errors at all but the lowest reinforcement levels. For Case 2, the Ehrlich and Mitchell (1994) method agreed with the measured reinforcement loads throughout most of the wall height, but under-predicted the reinforcement loads near the base of the wall. The Coherent Gravity and Simplified methods both under-predicted the reinforcement loads at all evaluations for the triaxial curved failure envelope, whereas the Ehrlich and Mitchell (1994) method produced precise and accurate predictions in the top and middle sections of the wall, but under-predicted the loads in the bottom third. Once again, the K-Stiffness method produced conservative estimates for load except at the very lowest reinforcement layers.

For the curved plane strain failure envelope (Figure 6.11a), the K-Stiffness method best predicted the reinforcement loads overall, but under-predicted the load both near the top and in the lower half of the wall. Near the top of the wall, the Ehrlich and Mitchell (1994) distribution produced fairly good, but non-conservative reinforcement load estimates; however, it became non-conservative at lower elevations. The Coherent Gravity and Simplified methods produced highly non-conservative load distributions for Case 1.

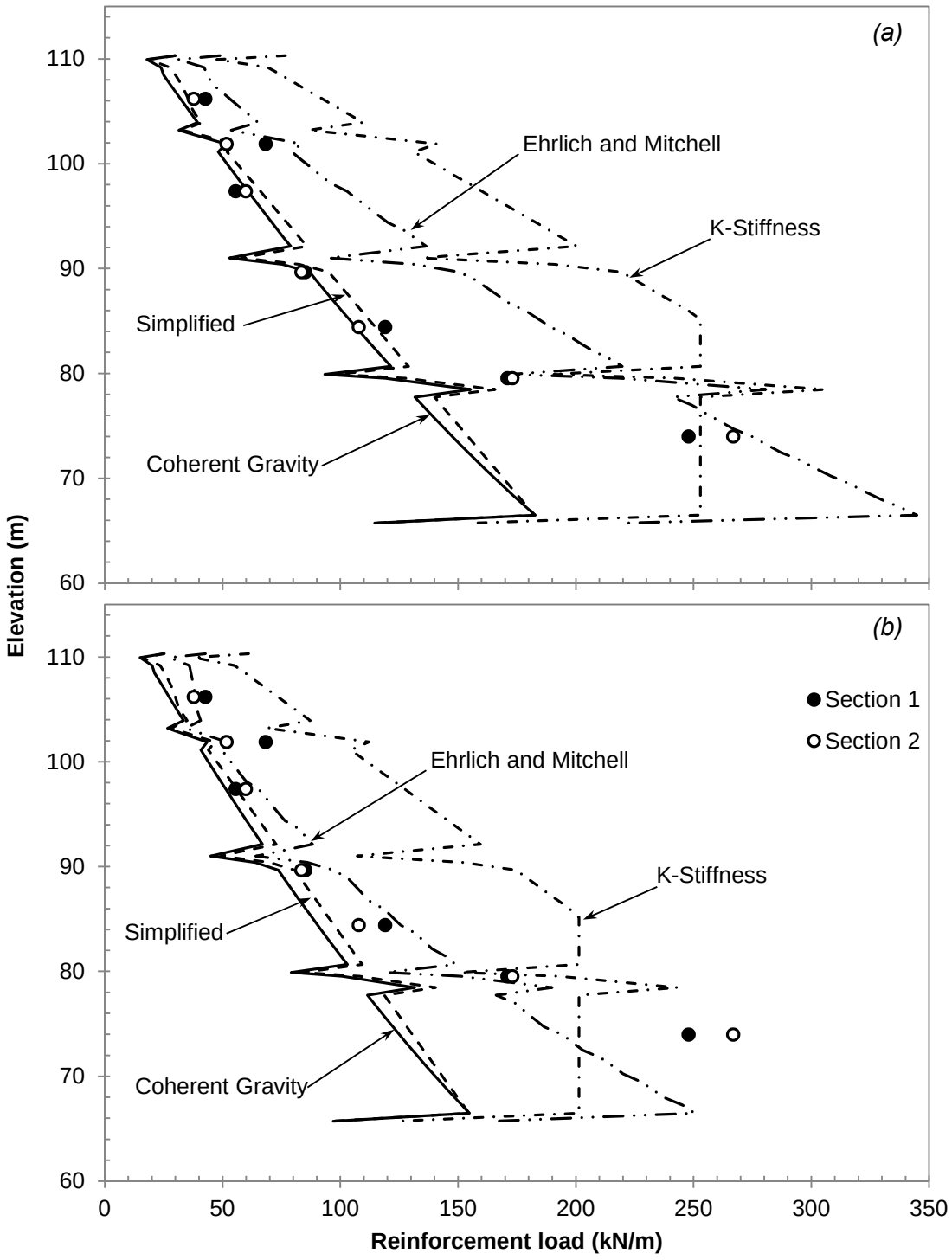

Figure 6.10. Observed and predicted peak reinforcement loads for the West MSE wall using (a) the soil properties assumed during design, and (b) The actual soil properties capped per AASHTO.

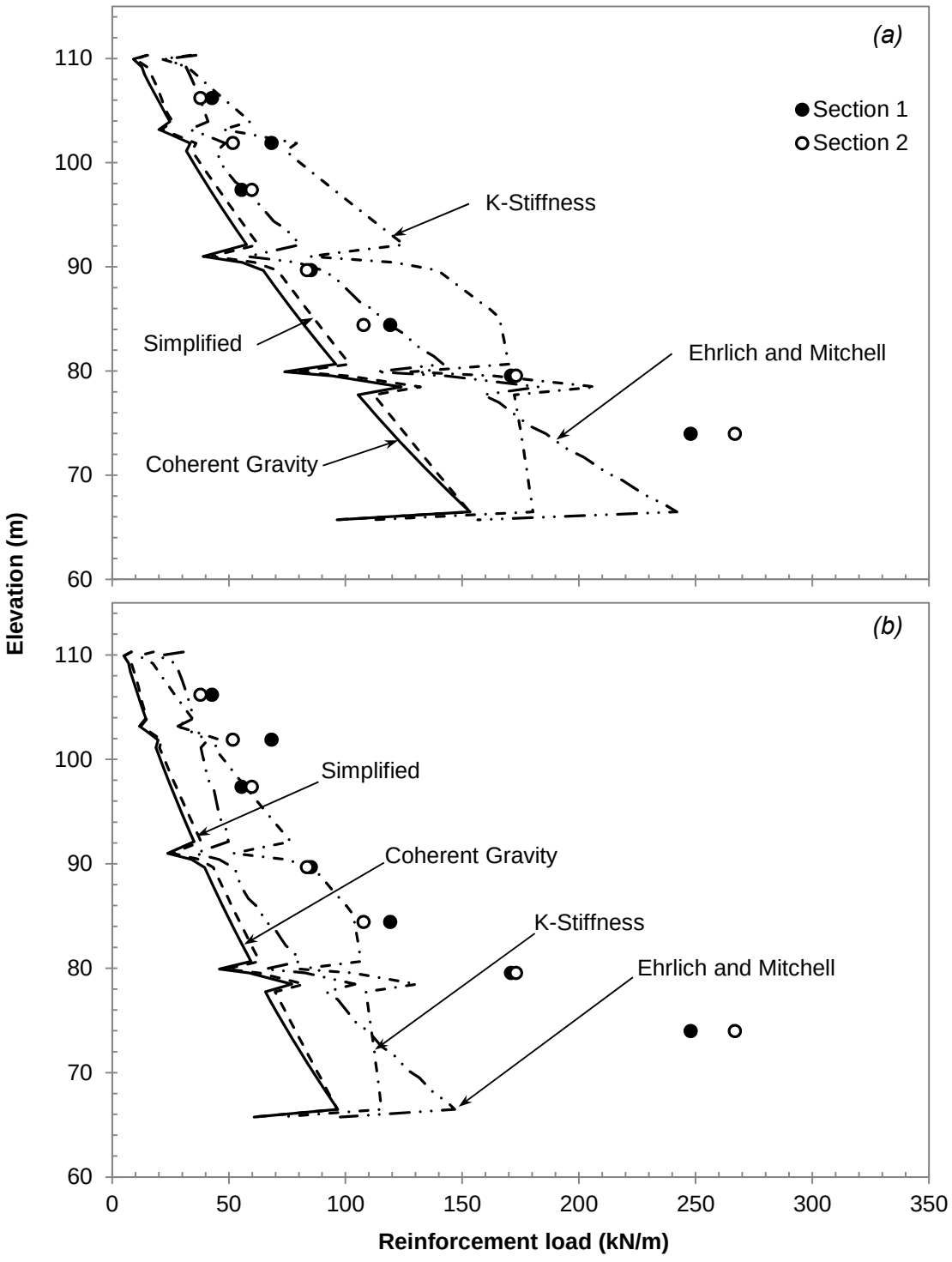

Figure 6.11. Observed and predicted peak reinforcement loads for the West MSE wall using (a) triaxial properties with a curved failure envelope, and (b) plane strain properties with a curved failure envelope.

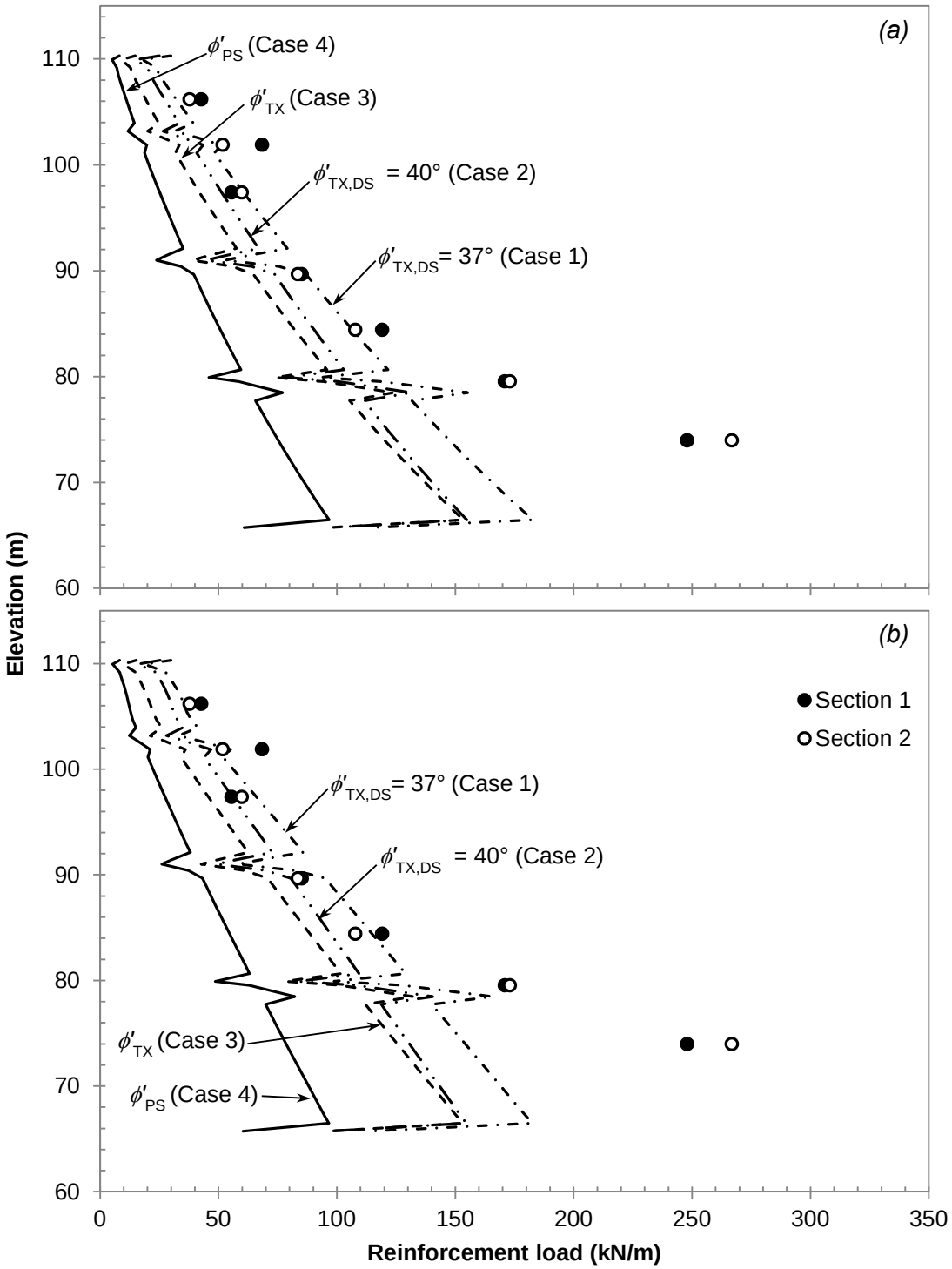

Figure 6.12. Observed and predicted peak reinforcement loads for the West MSE wall using (a) Coherent Gravity method, and (b) the AASHTO Simplified method.

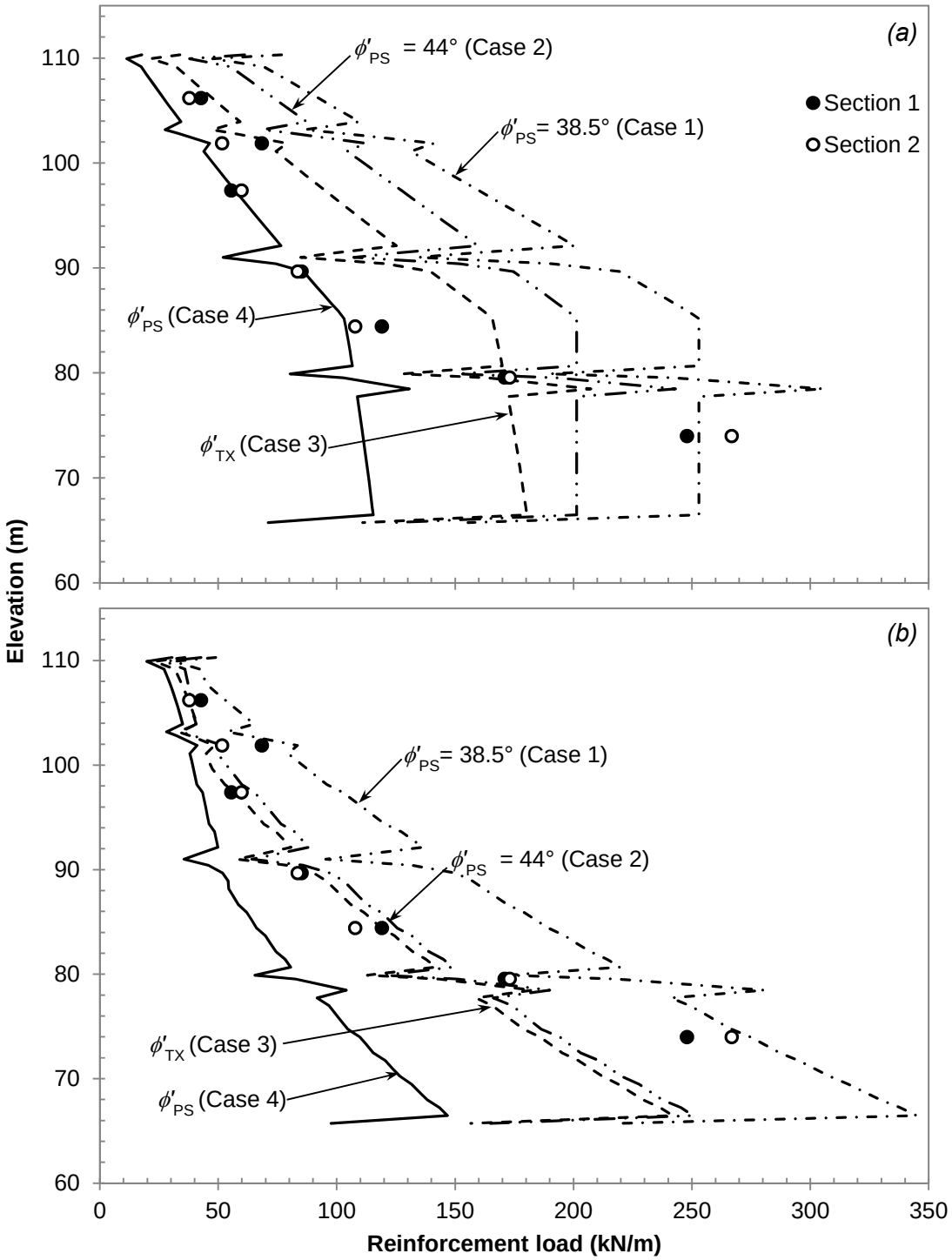

Figure 6.13. Observed and predicted peak reinforcement loads for the West MSE wall using (a) Ehrlich and Mitchell (1994), and (b) the K-Stiffness method.

Biases in reinforcement load estimates were also computed for the West MSE wall, similar to the North wall. The statistics summarizing the prediction method accuracy for the West wall are presented in Table 6.6. Similar to the North wall, the load prediction methods that produced the largest average bias, corresponding to the least conservative methods, were the Coherent Gravity and Simplified methods. The K-Stiffness method produced the lowest mean bias, suggesting that it is the most conservative method evaluated, with average bias values ranging from 0.54 for Case 1 to 1.41 for Case 4. Once again, the Ehrlich and Mitchell (1994) method performed the best overall, however, for the West wall, Case 3 performed comparably to Case 2 shown with average biases of 1.11 and 1.05, respectively.

On average, the coefficient of variation for the West wall was much higher than for the North wall. This is largely attributed to the large loads measured in the lowest set of instrumented reinforcement strips. The cause of this load is not well understood, though it is suspected to be due to the extremely large local soil-reinforcement stiffness caused by the close reinforcement spacing (Stuedlein et al. 2012). However, the investigation of this effect is outside the scope of this thesis.

Table 6.6. Summary statistics of the bias in reinforcement loads calculated for the West MSE wall.

Case No.	Mean bias	Range in bias		COV[a] (%)
Coherent Gravity Method				
Case 1	1.23	1.81	0.92	21
Case 2	1.45	2.13	1.08	21
Case 3	1.70	2.22	1.29	16
Case 4	2.82	3.89	2.11	19
AASHTO Simplified method				
Case 1	1.14	1.73	0.84	23
Case 2	1.35	2.04	0.99	23
Case 3	1.58	2.12	1.18	18
Case 4	2.62	3.54	1.93	18
Ehrlich & Mitchell (1994)				
Case 1	0.70	0.97	0.54	18
Case 2	1.05	1.37	0.85	15
Case 3	1.11	1.44	0.91	14
Case 4	1.69	2.43	1.18	22
K-Stiffness Method				
Case 1	0.54	1.05	0.35	38
Case 2	0.68	1.33	0.44	38
Case 3	0.86	1.52	0.58	32
Case 4	1.41	2.40	0.97	30

[a] Estimated using small-sample standard deviation method (Snedecor and Cochran 1964; Lacasse and Nadim 1996).

6.6 Sensitivity of the Ehrlich and Mitchell (1994) Method to Modulus Number and Friction Angle

As discussed in Section 6.3.1, the Ehrlich and Mitchell (1994) method produced the most variation in shape between each failure envelope assumed and showed the sensitivity of the method to the friction angle and modulus number. However, because both ϕ and K were being varied simultaneously, it was difficult to assess the effect of each variable on the predicted load distribution. In order to visualize the effect of friction angle and modulus number on the predicted load distribution, a parametric analysis was performed where the friction angle was varied between 37 and 48 degrees while holding the modulus number constant at values of 1200 and 2700.

Figure 6.14(a) shows the sets of load prediction distributions computed for modulus numbers of 1200 and 2700. For two soil with the same friction angle, the use of the

smaller modulus number resulted in increases in load. These increases were smaller near the top then becoming larger with decreases in elevation with maximum a maximum observed increase of 14.8 kN/m.

The effect of friction angle on computed load prediction distribution is shown in Figure 6.14(b). Similar to the modulus number, the use of lower fiction angles caused large increases in predicted load (up to 20.6 kN/m) at lower wall elevations, however, for lower vertical effective stresses (near the top of the wall), the use of lower friction angles resulted in a reduction in the predicted load. This is a result of the Ehrlich and Mitchell (1994) method employing the Duncan and Seed (1986) hysteretic compaction induced stress model which accounts for the "locking-in" of compaction stresses at shallow wall depths and which is typically greater for soils with larger friction angles.

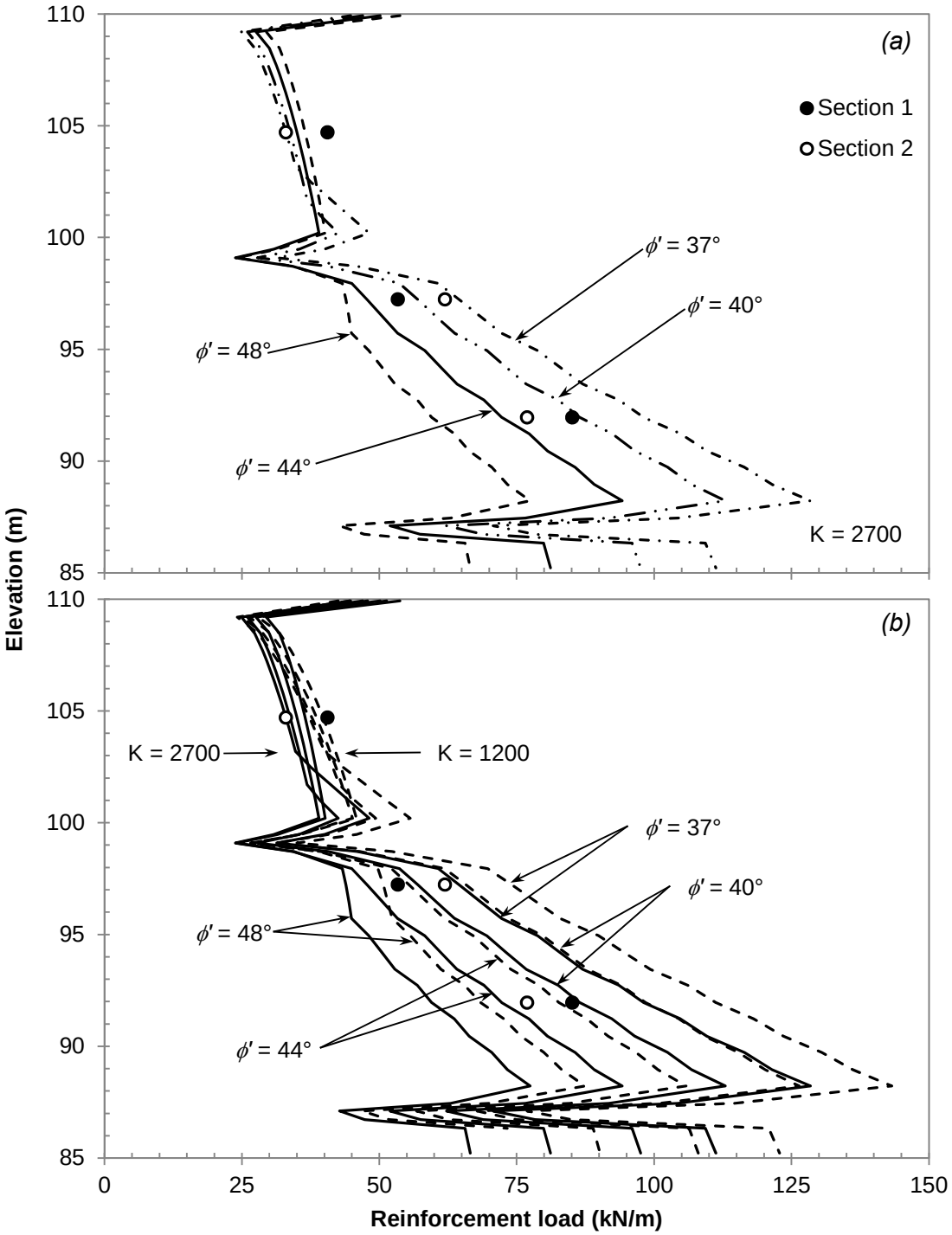

Figure 6.14. Parametric analysis of the Ehrlich and Mitchell (1994) method varying (a) friction angle only with the modulus number at held constant at *K* = 2700 and (b) the friction angle with the modulus number held constant at K = 1200 and K = 2700 (North MSE wall).

6.7 Pullout Performance

The internal stability of a MSE wall is determined by comparing the maximum predicted reinforcement load to the allowable reinforcement tension with respect to rupture, and pullout resistance at each reinforcement level as discussed in Section 2.2.1. The allowable reinforcement pullout resistance in steel strip reinforced MSE walls is a function of vertical effective stress, embedded reinforcement length and apparent friction coefficient:

$$P_r = \sigma'_v \; 2L_e b \, f^* \tag{2.46}$$

In this Section, the required embedment lengths with respect to pullout are determined by setting the pullout resistance from Equation 2.46 equal to maximum reinforcement load multiplied by the factor of safety against pullout, FS_{PO} (note: T_{max} is on a per-strip basis rather than a per unit width of wall as used in previous sections). The equation for required embedment length, $L_{e,req'd}$, can be expressed as:

$$L_{e,req'd} = \frac{T_{max}}{\sigma_v \; 2 \, f^* b} FS_{PO} \tag{6.3}$$

where the factor of safety with respect to pullout is taken as 1.5.

Figure 6.15 and 6.16 show the variation in required embedment lengths when using the four different load prediction methods for the North and West MSE walls, respectively, with Case 2 as described in Table 6.4 and the backfill-specific f^* design model presented in Section 5.5. For both walls, the largest embedment lengths were required when considering the K-Stiffness method with maximum required embedment lengths of approximately 4 m corresponding to a 230 percent increase over the other methods. The Coherent Gravity, Simplified and Ehrlich and Mitchell (1994) methods produced maximum required embedment lengths of approximately 1 m. For the West MSE wall, the same general shape is maintained for each distribution, however, for the

North wall, the distribution of required embedment lengths produced by using the Ehrlich and Mitchell (1994) method is more conservative at the top of the wall than the distributions produced by the other methods, and can be attributed to the hysteretic compaction stress model used by Ehrlich and Mitchell (1994). For the West wall, the influence of the compaction induced stresses is not as prominent due to the presence of the 3.8 m high surcharge load which causes a vertical effective stress at the upper-most reinforcement layer of approximately 100 kPa. Appendix F provides similar plots with the AASHTO and global gravel f^* models.

Figure 6.17 and Figure 6.18 show the variation in required embedment lengths for the North and West MSE walls when using the current AASHTO f^* design model discussed in Section 2.2.1.4, and the global gravel and backfill specific design models developed in Chapter 5. Near the top of the wall, the embedment lengths computed using the different f^* design models had the largest variation were the backfill specific model required the smallest embedment lengths and the AASHTO model required the largest lengths (as much as 200 percent greater than those computed using the backfill-specific model). The difference in required embedment lengths decreased with increases in effective vertical stress.

Typically in MSE wall design pullout resistance controls near the top of the wall where vertical effective stresses are low. However, the pullout resistance in tall walls is not likely to control due to the AASHTO requirement that the total reinforcement length be at least 70 percent of the design height, $L_r \geq 0.7H$. With such large embedment lengths, the allowable yield strength is reached well before pullout can occurs. Although the use of the global gravel and backfill-specific f^* models would not affect the design of the North or West MSE walls using the current AASHTO design procedure, their use in smaller walls would provide significant reductions in the amount of reinforcement material required.

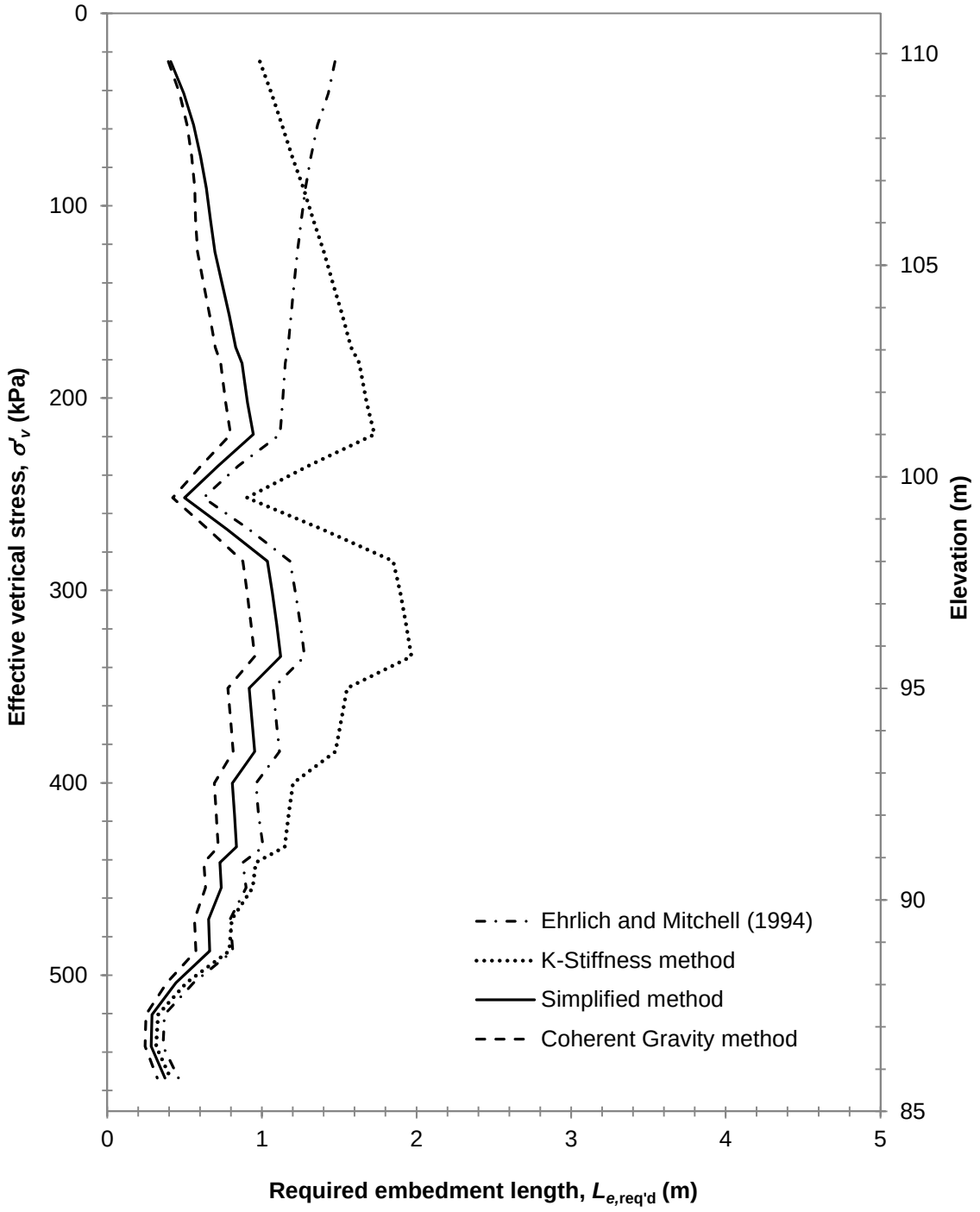

Figure 6.15. North MSE wall required embedment lengths for pullout using different load prediction methods and the proposed backfill specific *f design model.**

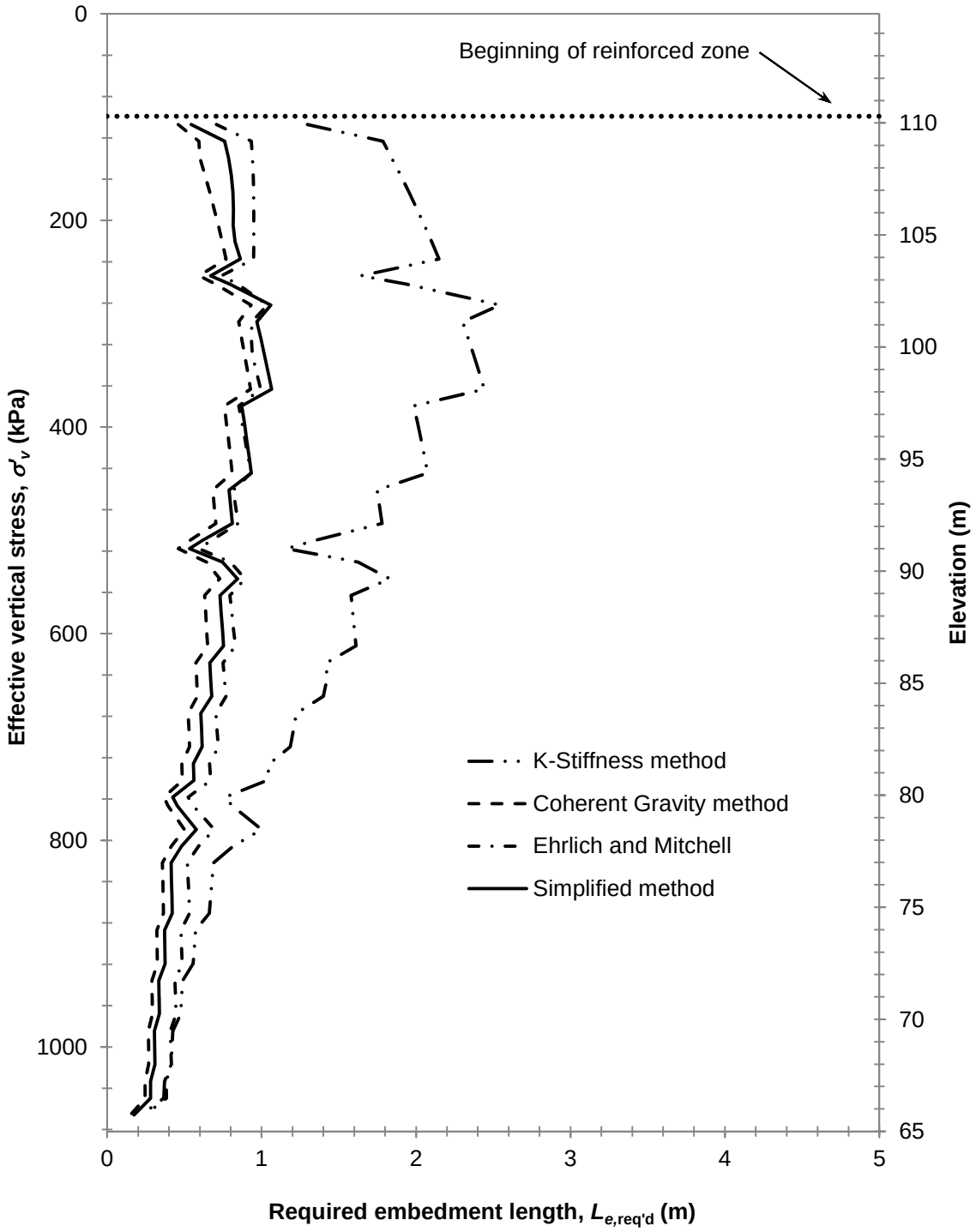

Figure 6.16. Embedment lengths required for pullout using different load prediction methods and the proposed backfill specific *f design model.**

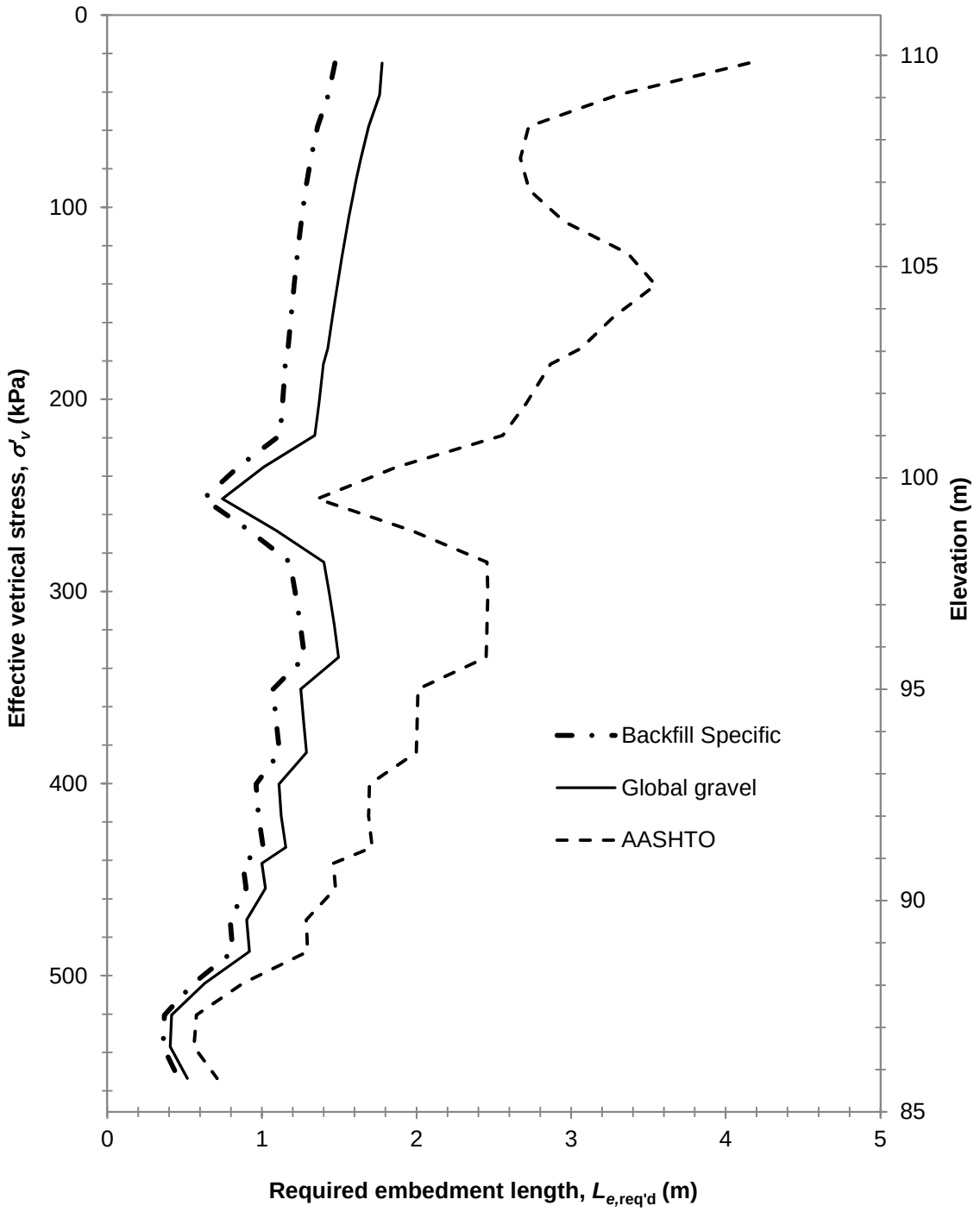

Figure 6.17. Embedment lengths required for pullout resistance in the North MSE wall computed using the two proposed *f design models and the AASTO standard model with reinforcement loads calculated using the Ehrlich and Mitchell (1994) method.**

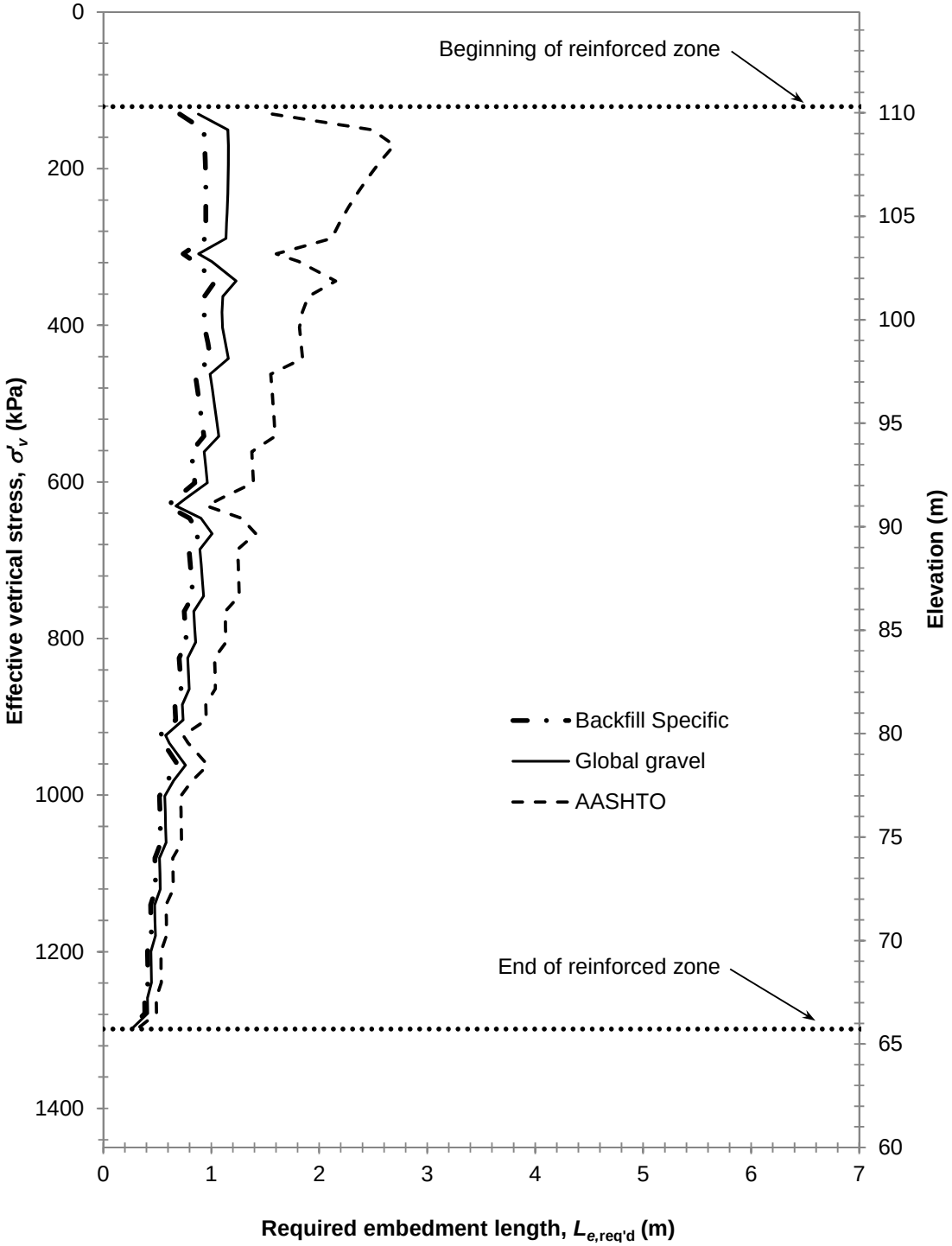

Figure 6.18. Embedment lengths required for pullout resistance in the West MSE wall computed using the two proposed *f design models and the AASTO standard model with reinforcement loads calculated using the Ehrlich and Mitchell (1994) method.**

6.8 Summary

The internal stability of an MSE wall design is determined by predicting reinforcement loads, then comparing the predicted loads to an estimated allowable pullout resistance and reinforcement yield strength. In this Chapter, the internal stability of two very tall MSE walls was analyzed and the following contributions and conclusions were made:

1. The reinforcement loads previously inferred from reinforcement strain measurements were reevaluated using the representative Young's modulus reported in Chapter 2; an apparent increase in load of 4 percent was observed.
2. The reinforcement stresses as a percent of yield strength inferred from reinforcement strain measurements and nominal values of yield strength were revised using the yield strength measured in Chapter 2; an apparent reduction of 2.6 and 3.3 percent were observed for the North and West MSE walls, respectively.
3. Using four different reinforcement load prediction methods and four sets of constitutive parameters, 32 reinforcement load distributions were generated and compared to the measured reinforcement loads by computing bias values; the Ehrlich and Mitchell (1994) method used with the constitutive parameters determined for the backfill in Chapter 4 produced the most precise and accurate predictions for both the North and West MSE walls.
4. Required pullout embedment length distributions were determined using the different load distributions from the four prediction methods analyzed above; the K-Stiffness method was found to be the most conservative, producing required embedment lengths of up to 230 percent greater than other prediction methods.
5. Required pullout embedment length distributions were determined using the global gravel and backfill-specific f^* design models developed in Chapter 5 as well as the AASHTO standard f^* design model discussed in Chapter 2; visual comparisons of the resulting distributions showed the AASHTO model to be

much more conservative, producing required embedment lengths up to 200 percent greater than the global gravel and backfill-specific design models.

7.0 SUMMARY AND CONCLUSIONS

7.1 Summary of Research Investigation

The main objectives of this thesis were to characterize the constitutive behavior of a sandy gravel backfill material used in two very tall MSE walls, to develop a better understanding of the soil-reinforcement interaction between the sandy gravel backfill and the ribbed steel strip reinforcements used in two very tall MSE walls, and to assess the effect of the backfill and the soil-reinforcement interaction on internal stability of these two walls. Laboratory tests were performed on the backfill and reinforcement materials separately to determine their constitutive properties. Full-scale laboratory pullout tests were performed and the results used to produce a backfill-specific design models that can be used to predict peak reinforcement pullout resistance.

7.2 Conclusions

7.2.1 Laboratory Test Program

The following summarizes the findings of the laboratory testing program:

1. Tension testing was performed on coupons cut from the ribbed steel strip reinforcements and the following representative constitutive properties determined: yield strength, f_y = 526 MPa; and, Young's modulus, E = 208 GPa
2. Consolidated drained axisymmetric triaxial strength tests were performed on the reinforced backfill material compacted to 35, 55 and 65 percent relative density. The friction angles of the material at a confining pressure of one atmosphere were found equal to 47.9, 45.3 and 40.0 degrees, respectively. The reduction in peak friction angle with a log-cycle increase in confining pressure was equal to 2.1, 4.7, and 6.8 degrees for relative densities of 35, 55, and 65 percent, respectively.
3. Duncan and Chang (1970) Hyperbolic stress-strain models were calibrated for the material at relative densities of 35, 55, and 65 percent. The modulus number ranged from 725 to 1200, whereas the modulus exponent ranged from 0.385 to 0.525.

4. A large, single strip pullout test apparatus was designed and constructed in order to evaluate the soil-reinforcement interaction of ribbed steel strip reinforcements.
5. Twenty pullout tests were performed at effective vertical stresses ranging from 10 to 300 kPa resulting in peak reinforcement loads ranging from 18.6 to 93.8 kN.
6. Multi-linear regression was used to quantify the combined effect of vertical effective stress and compaction on the maximum pullout resistance. Although both variables control the peak pullout resistance, the effect of dry unit weight was found to be statistically insignificant, likely due to the small range in dry unit weight evaluated and experimental error. A regression model requiring the use of the vertical effective stress as the single independent variable was recommended for use until further tests could be obtained.
7. New backfill-specific and gravel models for the prediction of the apparent friction coefficient with normal effective stress were developed for use with ribbed steel strip reinforcements.
8. The performance of the proposed f^* design models were compared to the current AASHTO design model and found to produce significantly more accurate predictions of the apparent friction coefficient

7.2.2 Analysis of Internal Stability

The internal stability of the 25.9 m tall North MSE wall and 45.7 m tall West MSE walls were analyzed using various combinations of design models and constitutive properties and the following conclusions were obtained:

1. The reinforcement loads previously inferred from reinforcement strain measurements were reevaluated using the representative Young's modulus reported in Chapter 2; an apparent increase in load of 4 percent was observed.
2. The reinforcement stresses as a percent of yield strength inferred from reinforcement strain measurements and nominal values of yield strength were revised using the results from the tension testing; an apparent reduction of 2.6 and 3.3 percent were observed for the North and West MSE walls, respectively.

3. The accuracy and uncertainty of four different reinforcement load prediction methods with four sets of constitutive parameters was evaluated. The Ehrlich and Mitchell (1994) method used with the constitutive parameters determined for the backfill in Chapter 4 with the fiction angle capped at 40 degrees produced the most precise and accurate predictions for both the North and West MSE walls.
4. Required pullout embedment length distributions were determined using the different load distributions from the four prediction methods analyzed above; the K-Stiffness method was found to be the most conservative, producing required embedment lengths of up to 230 percent greater than other prediction methods.
5. Required pullout embedment length distributions were determined using the global gravel and backfill-specific f^* design models developed in Chapter 5 as well as the AASHTO standard f^* design model discussed in Chapter 2. Visual comparisons of the resulting distributions showed the AASHTO model to be much more conservative, producing required embedment lengths up to 200 percent greater than the global gravel and backfill-specific design models.

REFERENCES

AASHTO. (2010). *AASHTO LRFD bridge design specifications*. American Association of State and Highway Transportation Officials, Washington, DC.

AISC. (2010). *Steel Construction Manual*. American Institute of Steel Construction.

Alimi, I., Bacot, J., Lareal, P., Long, N. T., and Schlosser, F. (1978). "In-situ and laboratory study of the adhesion between soil and reinforcement." *Bull Liaison Lab Ponts Chauss*, (SPEC VI-E).

Allen, T. M., Bathurst, R. J., Holtz, R. D., Lee, W. F., and Walters, D. (2004). "New Method for Prediction of Loads in Steel Reinforced Soil Walls." *Journal of Geotechnical and Geoenvironmental Engineering*, 130(11), 1109–1120.

Allen, T. M., Christopher, B. R., Elias, V., and DeMaggio, J. (2001). *Development of the simplified method for internal stability design of mechanically stabilized earth walls*. Research report, Washington State Department of Transportation.

ASTM. (2006a). *Test Methods for Minimum Index Density and Unit Weight of Soils and Calculation of Relative Density*. ASTM International.

ASTM. (2006b). *Test Methods for Maximum Index Density and Unit Weight of Soils Using a Vibratory Table*. ASTM International.

ASTM. (2009). *Test Methods for Laboratory Compaction Characteristics of Soil Using Modified Effort (56,000 ft-lbf/ft3 (2,700 kN-m/m3))*. ASTM International.

ASTM. (2011a). *Test Methods for Tension Testing of Metallic Materials*. Standard, ASTM International.

ASTM. (2011b). *Test Method for Consolidated Drained Triaxial Compression Test for Soils*. ASTM International, 11.

ASTM. (2012). *Test Methods and Definitions for Mechanical Testing of Steel Products*. Standard, ASTM International.

Baquelin, F. (1978). "Construction and Instrumentation of Reinforced Earth Walls in French Highway Administration." ASCE, Pittsburgh, 186–201.

Bareither, C., Edil, T., Benson, C., and Mickelson, D. (2008). "Geological and Physical Factors Affecting the Friction Angle of Compacted Sands." *Journal of Geotechnical and Geoenvironmental Engineering*, 134(10), 1476–1489.

Bathurst, R. J., Allen, T. M., and Nowak, A. S. (2008a). "Calibration concepts for load and resistance factor design (LRFD) of reinforced soil walls." *Canadian Geotechnical Journal*, 45(10), 1377–1392.

Bathurst, R. J., Nernheim, A., and Allen, T. M. (2008b). "Predicted and measured loads using the coherent gravity method." *Proceedings of the Institution of Civil Engineers: Ground Improvement*, 161(3), 113–120.

Bathurst, R. J., Nernheim, A., and Allen, T. M. (2009). "Predicted Loads in Steel Reinforced Soil Walls Using the AASHTO Simplified Method." *Journal of Geotechnical and Geoenvironmental Engineering*, 135(2), 177–184.

Bell, J. R., Barrett, R. K., and Ruckman, A. C. (1983). "Geotextile earth-reinforced retaining wall tests: Glenwood Canyon, Colorado." *Transportation Research Record*, (916), 59–69.

Bell, J. R., Stilley, A., and Vandre, B. (1975). "Fabric retained earth walls." *Engineering Geology & Soils Engineering Symp Proc*, 13, 271–287.

Berg, R. R., Christopher, B. R., and Samtani, N. C. (2009). *Design and Construction of Mechanically Stabilized Earth Walls and Reinforced Soil Slopes*. Federal Highway Administration.

Bishop, A. W. (1954). "correspondence on 'Characteristics of saturated silt, measured in triaxial compression'." *Géotechnique*, 4, 43–45.

Bishop, A. W., and Henkel, D. J. (1962). *The Measurement of Soil Properties in the Triaxial Test*. E. Arnold.

Black, D. K., and Lee, K. L. (1973). "Saturating laboratory samples by back pressure." *Journal of the Soil Mechanics and Foundations Division, ASCE*, 99(1), 75–93.

Bolton, M. D. (1986). "The strength and dilatancy of sands." *Geotechnique*, 36(1), 65–78.

Boyd, M. S. (1993). "Behaviour of a reinforced earth wall at Ngauranga, New Zealand." *Reinforcement Des Sols: Experimentations en Vraie Grandeur des Annees*, Paris, 229–257.

Casagrande, A. (1938). "The shearing resistance of soils and its relation to the stability of earth dams." *Proceedings of the Soils and Foundation Conference of the US Engineer Department*.

Casagrande, A. (1940). "Characteristics of cohesionless soils affecting the stability of slopes and earth fills." *Contributions to Soils Mechanics, 1925-1940, Boston Society of Civil Engineers*.

Chang, J. C., and Forsyth, R. A. (1977). "Design and field behavior of reinforced earth wall." *Journal of Geotechnical and Geoenvironmental Engineering*, 103(ASCE 13034).

Christopher, B. R. (1993). "Deformation response and wall stiffness in relation to reinforced soil wall design." Ph.D., Purdue University, United States -- Indiana.

Christopher, B. R., Gill, S. A., Giroud, J. P., Juran, I., Mitchell, J. K., Schlosser, F., and Dunnicliff, J. (1990a). *Reinforced soil structures Volume I. Design and construction guidelines*. Federal Highway Administration, Washington, DC.

Christopher, B. R., Gill, S. A., Giroud, J. P., Juran, I., Schlosser, F., and Dunnicliff, J. (1990b). *Reinforced soil structures Volume II. Summary of resuarch and systems information*. FHWA.

Cornforth, D. H. (1973). "Prediction of drained strength of sands from relative density measurements." *American Society for Testing and Materials*, Evaluation of relative density and its role in geotechnical projects involving cohesionless soils, 523, 281–303.

D18 Committee. (2006). *Test Methods for Minimum Index Density and Unit Weight of Soils and Calculation of Relative Density*. Standard, ASTM International.

Duncan, J. M., Brandon, T., Jian, W., Smith, G., Park, Y., Griffith, T., Corton, J., and Ryan, E. (2007). *Densities and Friction Angles of Granular Materials with Standard Gradations 21b and #57*. Virginia Tech.

Duncan, J. M., and Chang, C. (1970). "Nonlinear Analysis of Stress and Strain in Soils." *Journal of the Soil Mechanics and Foundations Division*, 96(5), 1629–1653.

Duncan, J. M., Wong, K. S., and Mabry, P. (1980). *Strength, stress-strain and bulk modulus parameters for finite element analyses of stresses and movements in soil masses*. University of California - Berkeley, 70.

Ehrlich, M., and Mitchell, J. K. (1994). "Working Stress Design Method for Reinforced Soil Walls." *Journal of Geotechnical Engineering*, 120(4), 625–645.

Elias, V., Christopher, B. R., and Berg, R. R. (2001). *Mechanically Stabilized Earth Walls and Reinforced Soil Slopes Design and Construction Guidelines*. National Highway Institute Federal Highway Administration U.S. Department of Transportation, Washington, DC, 394.

FEI. (2011). *Modified - C proctor tests on Sea-Tac MSE wall backfill*. FEI Testing & Inspection, Corvallis, OR.

FEI. (2012a). *Pullout test compaction verification (09/10/2012)*. Test Results - ASTM D 2922, FEI Testing & Inspection, Corvallis, OR, 1.

FEI. (2012b). *Pullout test compaction verification (09/24/2012)*. Test Results - ASTM D 2922, FEI Testing & Inspection, Corvallis, OR, 1.

FEI. (2012c). *Pullout test compaction verification (09/27/2012)*. Test Results - ASTM D 2922, FEI Testing & Inspection, Corvallis, OR, 1.

Golder, H. Q., and Akroyd, T. N. W. (1954). "An Apparatus for Triaxial-Compression Tests at High Pressures." *Géotechnique*, 4(4), 131–136.

Hall, E. B., and Gordon, B. B. (1963). "Triaxial testing with large scale high pressure equipment." *Special Technical Publication*, 361, 315–328.

Hashash, Y. M. A., Fu, Q., Ghaboussi, J., Lade, P. V., and Saucier, C. (2009). "Inverse analysis–based interpretation of sand behavior from triaxial compression tests subjected to full end restraint." *Canadian Geotechnical Journal*, 46(7), 768–791.

Hatami, K., and Bathurst, R. J. (2005). "Development and verification of a numerical model for the analysis of geosynthetic-reinforced soil segmental walls under working stress conditions." *Canadian Geotechnical Journal*, 42(4), 1066–1085.

Hirschfeld, R. C., and Poulos, S. J. (1963). "High-pressure triaxial tests on a compacted sand and an undisturbed silt." *ASTM Laboratory Shear Testing of Soils Technical Publication No*, 361, 329–339.

Holtz, R. D., and Kovacs, W. D. (1981). *An Introduction to Geotechnical Engineering*. Prentice Hall.

Holtz, R. D., Kovacs, W. D., and Sheahan, T. C. (2011). *An Introduction to Geotechnical Engineering*. Prentice Hall.

Huang, B., Bathurst, R. J., and Allen, T. M. (2012). "LRFD Calibration for Steel Strip Reinforced Soil Walls." *Journal of Geotechnical and Geoenvironmental Engineering*, 138(8), 922–933.

Jaky, J. (1948). "Pressure in silos." *Proceedings of the 2nd International Conference on Soil Mechanics and Foundation Engineering*, 103–107.

Jewell, R. A., and Wroth, C. P. (1987). "Direct shear tests on reinforced sand." *Géotechnique*, 37(1), 53–68.

Juran, I. (1977). “Dimensionment interne des ouvrages en terre armee.” Laboratoire Central des Pons et Chaussees, Paris.

Juran, I., and Schlosser, F. (1978). “Theoretical analysis of failure in reinforced earth structures.” ASCE, Pittsburgh, 528–555.

Kline, S. J., and McClintock, F. A. (1953). “Describing uncertainties in single-sample experiments.” *Mechanical engineering*, 75(1), 3–8.

Lacasse, S., and Nadim, F. (1996). “Uncertainties in characterising soil properties.” *Uncertainty in the geologic environment: From theory to practice*, ASCE, Reston, VA, 49–75.

Lade, P. V., and Lee, K. L. (1976). *Engineering properties of soils*. University of California, Los Angeles, 145.

Larson, D. G. (1992). “A laboratory investigation of load transfer in reinforced soil.” Ph.D., Massachusetts Institute of Technology.

Lee, K. L. (1978). “Mechanisms, analysis and design of reinforced earth.” ASCE, Pittsburgh, 62–76.

Lee, K. L., Adams, B. D., and Vagneron, J. M. J. (1973). “Reinforced Earth Retaining Walls.” *Journal of the Soil Mechanics and Foundations Division*, 99(10), 745–764.

Lee, K. L., and Seed, H. B. (1967). “Drained Strength Characteristics of Sands.” *Journal of Soil Mechanics & Foundations Division*, 93(6), 117–141.

Liang, R. (2004). *MSE Wall and Reinforcement Testing at MUS-16-7.16 Bridge Site*. University of Akron, Department of Civil Engineering.

Lindquist, D. D. (2008). “Seismic modeling of a 135-foot-tall MSE wall.” *Geotechnical Earthquake Engineering and Soil Dynamics IV Congress 2008 - Geotechnical Earthquake Engineering and Soil Dynamics, May 18, 2008 - May 22, 2008*, Geotechnical Special Publication, American Society of Civil Engineers.

McKittrick, D. P. (1978). “Design, Construction, Technology and Performance of Reinforced Earth Structures.” ASCE, Pittsburgh, 596–617.

Mitchell, J. K., and Christopher, B. R. (1990). “North American Practice in Reinforced Soil Systems.” ASCE, 322–346.

Miyata, Y., and Bathurst, R. J. (2012). “Analysis and calibration of default steel strip pullout models used in Japan.” *Soils and Foundations*, 52(3), 481–497.

Neely, W. (1995). "Working Stress Design Method for Reinforced Soil Walls - Discussion." *Journal of Geotechnical Engineering*, 121(11), 818–821.

Palmeira, E. M., and Milligan, G. W. E. (1989). "Scale and other factors affecting the results of pull-out tests of grids buried in sand." *Geotechnique*, 39(3), 511–542.

Potyondy, J. G. (1961). "Skin Friction between Various Soils and Construction Materials." *Géotechnique*, 11(4), 339–353.

Rankine, W. J. M. (1857). "On the stability of loose earth." *Philosophical Transactions of the Royal Society of London*, 147, 9–27.

Reynolds, O. (1885). "On the dilatancy of media composed of rigid particles in contact." *Philosophical Magazine Series 5*, 20(127), 469–481.

Roscoe, K. H. (1970). "The influence of strains in soil mechanics." *Geotechnique*, 20(2), 129–170.

Rowe, P. W. (1962). "The Stress-Dilatancy Relation for Static Equilibrium of an Assembly of Particles in Contact." *Proceedings of the Royal Society of London. Series A, Mathematical and Physical Sciences*, 269(1339), 500–527.

Schlosser, F. (1978). "History, current development, and future developments of reinforced earth." *Symp. on Soil Reinforcing and Stabilizing Techniques*, Sydney, 5–28.

Schlosser, F. (1990). "Mechanically Stabilized Earth Retaining Structures." ASCE, 347–378.

Schlosser, F., and Elias, V. (1978). "Friction in reinforced earth." *Symp on Earth Reinf, Proc of a Symp at the ASCE Annu Conv, April 27, 1978 - April 27, 1978*, 735–776.

Schlosser, F., and Segrestin, P. (1979). "Dimensionnement des ouvrages en terre armee par la methode de l'equilibre local (Local stability analysis method of design of reinforced earth structures)." *Int. Conf. on Soil Reinforcement: Reinforced Earth and Other Techniques*, 157–162.

Snedecor, G. W., and Cochran, W. G. (1964). *Statistical methods*. University of Iowa Press, Iowa City, IA.

Steward, J., Williamson, R., and Mohney, J. (1977). *Guidelines for use of fabrics in construction and maintenance of low-volume roads*. Federal Highway Administration, 171.

Stuedlein, A. W., Allen, T. M., Holtz, R. D., and Christopher, B. R. (2010a). "Factors Affecting the Development of MSE Wall Reinforcement Strain." *Earth Retention Conference 3*, American Society of Civil Engineers, 502–511.

Stuedlein, A. W., Allen, T. M., Holtz, R. D., and Christopher, B. R. (2012). "Assessment of Reinforcement Strains in Very Tall Mechanically Stabilized Earth Walls." *Journal of Geotechnical and Geoenvironmental Engineering*, 138(3), 345–356.

Stuedlein, A. W., Bailey, M. J., Lindquist, D. D., Sankey, J., and Neely, W. (2010b). "Design and Performance of a 46-m-High MSE Wall." *Journal of Geotechnical and Geoenvironmental Engineering*, 136(6), 786–796.

Stuedlein, A. W., Mikkelsen, P. E., and Bailey, M. J. (2007). "Instrumentation and performance of the third runway north MSE wall at seattle-tacoma international airport." *7th International Symposium on Field Measurements in Geomechanics, FMGM 2007, September 24, 2007 - September 27, 2007*, Geotechnical Special Publication, American Society of Civil Engineers, 26.

Taylor, D. W. (1948). *Fundamentals of Soil Mechanics*. John Wiley, New York.

Verdugo, R., and Hoz, K. de la. (2007). "Strength and Stiffness of Coarse Granular Soils." *Soil Stress-Strain Behavior: Measurement, Modeling and Analysis*, Solid Mechanics and Its Applications, H. I. Ling, L. Callisto, D. Leshchinsky, and J. Koseki, eds., Springer Netherlands, 243–252.

Vesiĉ, A. S., and Barksdale, L. D. (1963). *On the Shear Strength of Sands at Very High Confining Pressures*. Soil Mechanics Laboratory, Georgia Institute of Technology.

Vesiĉ, A. S., and Clough, G. W. (1968). "Behavior of granular materials under high stresses." *Journal of Soil Mechanics & Foundations Division*, 94(5), 661–687.

Vidal, H. (1969). "The principle of reinforced earth." *Highway Research Record*.

Wong, K. S., and Duncan, J. M. (1974). *Hyperbolic Stress-Strain Parameters for Nonlinear Finite Element Analyses of Stresses and Movements in Soil Masses*. University of California, Berkeley.

APPENDICES

APPENDIX A

CD Triaxial Testing Manual

Testing Procedure:
Consolidated-Drained Axisymmetric Triaxial Tests

6" Diameter, Remolded Granular Soil Specimens
ASTM D7181

A. Specimen Preparation

1. Prepare a sample of material at the specified gradation to be tested.

2. Record the dry mass of the prepared sample.

3. Compute the mass of water that must be added to the prepared sample to facilitate compaction to the specified density (i.e., the target void ratio). The optimum water content derived from a modified Proctor test (ASTM D 1557) may typically be used for preparing dense specimens; the water content to be used will depend on specific project requirements. Be sure to obtain the advisor's approval of the selected water content *prior to testing*.

4. Add the mass of water required to achieve the desired water content and mix thoroughly. The specimen should be covered prior to and during compaction to prevent moisture loss.

5. Assemble the compaction mold and place it on a level surface. Compact lifts using a modified proctor hammer (for preparing dense specimens; loose specimens may require different approaches). Evenly distribute each lift of soil prior to compaction.

6. Mix the remaining sample in the pan before each lift to maintain even grain size distribution and water content.

7. Continue compacting lifts of equal height until the top of the compacted specimen is level with the top of the mold.

8. Smooth and level the specimen surface to ensuring the top of the specimen is level with the top of the compaction mold (use a # 4 sieve to obtain sand to use in leveling the sample).

9. Measure and record the mass of the mold and sample ($m_{mold\ +\ soil}$) with the bottom plate still attached to the mold.

10. Compute the estimated initial void ratio and check it against the target range. If estimated initial void ratio is within the target range, continue to the mounting procedure, if not, start over with new soil (do not reuse previously compacted soil).

B. Mounting Specimen in Triaxial Chamber

NOTE: In the following images, the cell base was placed on the floor for illustrative purposes. All steps of the mounting procedure should take place with the cell base on the load frame platform as seen in Figure 0.3below.

1. Check the membrane for leaks. Place four O-rings on the membrane applicator (two on each end), then place the membrane on the membrane applicator and roll the O-rings over the membrane to create a seal. Evacuate using ~ 4 inches of Hg (15 kPa) with a vacuum regulator attached to a bubble bottle. If bubbling does not stop, the membrane likely has a hole and should be discarded. **Caution**: Be very careful with membranes as they are easily punctured. If the bubbles stop, close the intake valve on the applicator and remove the applicator from the bubble bottle.

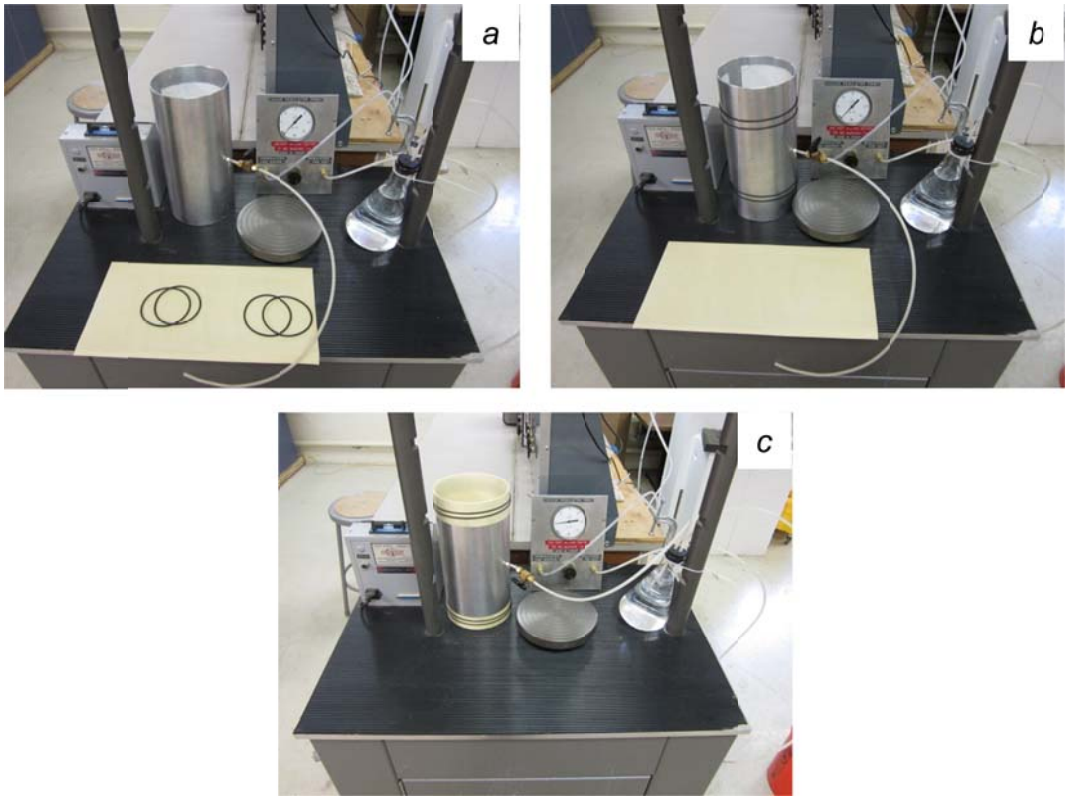

Figure 0.1: View of (a) membrane aplicator, membrane, O-rings, bubble botle, and vacume regulator; (b) O-rings on membrane aplicator; (c) membrane aplicator with vacume regulator and bubble bottle during step B-1.

2. Porous stones should be boiled for 10 minutes and allowed to cool to room temperature prior to mounting the specimen. Filter paper should be soaked in water prior to mounting the specimen. Place the bottom porous stone, two filter papers, the top porous stone, the top platen and the measuring plate on top of the bottom

platen respectively, then record the average of 3 measurements from the top of the measuring plate to the bottom of the bottom platen using the calipers depth probe as shown in Figure 0.14 below. Then remove the measuring plate, top platen, top porous stone, and top filter paper.

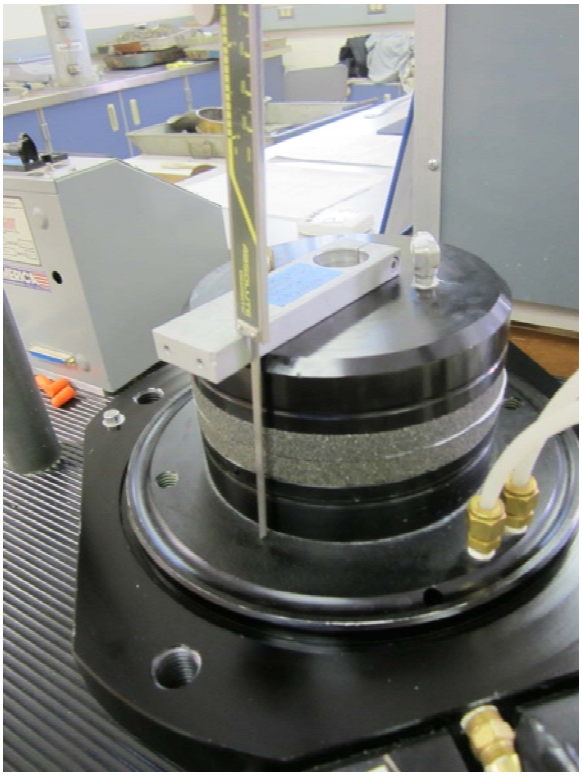

Figure 0.2: Combined measurement of platens, porous stones and filter paper during step B-2.

3. Ensure that porous stone and filter paper are aligned with the bottom platen and that the stone sits flat on the platen and does not wobble. Stones can become warped and should not be used if they no longer lie flat on the platen.

4. Plug the holes in the bottom of the triaxial chamber base plate with ear plugs prior to mounting the sample. This is to prevent material from becoming trapped in the holes.

5. Loosen the wing nuts on the bottom of the compaction mold and carefully remove the mold from the bottom plate by sliding the two top pieces of the mold (which contain the specimen) off of the bottom plate. **Caution:** do not lift the specimen strait up off the bottom plate.

6. Place the compaction mold, with the specimen, on top of the bottom platen with the porous stone and filter paper in place. Ensure that the specimen and stone are aligned with the bottom platen.

7. Loosen the wing nuts on the side of the compaction mold taking care not to disturb the compacted sample contained within the mold. It may be helpful to have someone hold the sides of the split mold together while loosening the wing nuts to prevent the sides from coming loose and disturbing the specimen.

8. Carefully remove bolts from the sides of the split mold and remove the sides of the mold from the compacted sample. Record the mass of the mold (before cleaning it) along with any soil which has fallen off of the sample on to the bottom platen; **make sure not to forget any washers, wing nuts, or bolts**. Subtract the mass of the excess soil and water from the initial "in-mold" soil mass.

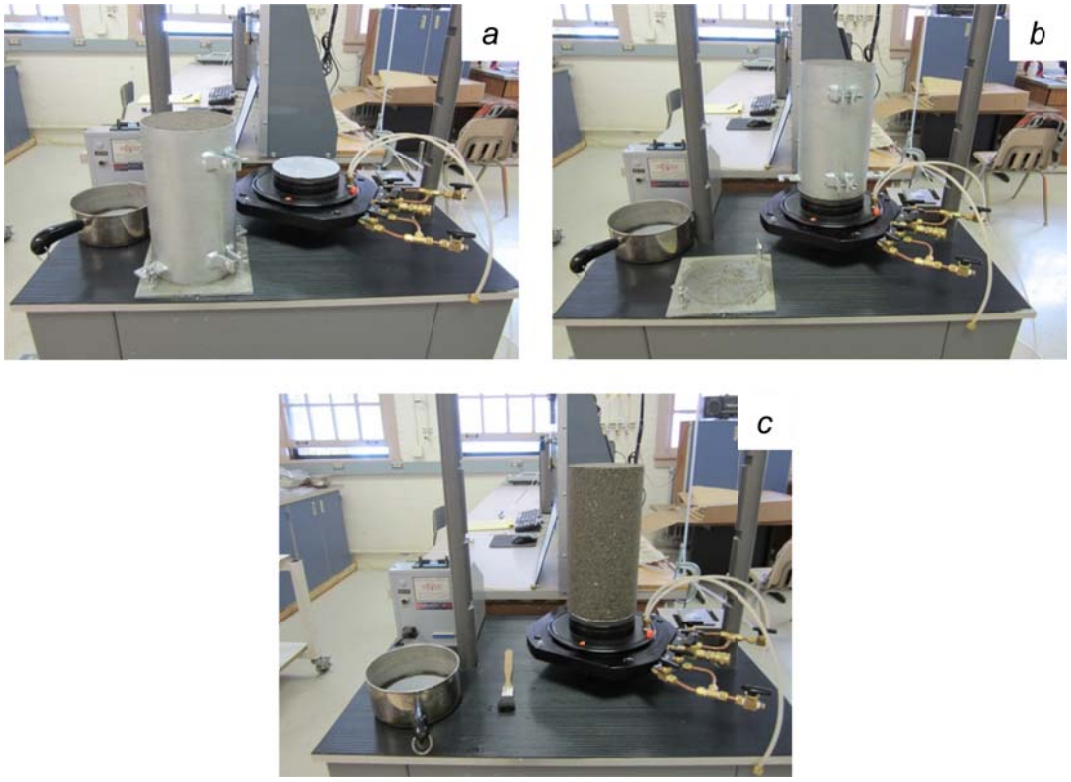

Figure 0.3: View of (a) specimen and compaction mold still attached to mold base prior to step B-5; (b) specimen and compaction mold mounted on the cell base after step B-6; (c) prepared specimen mounted on cell base after Step B-8.

9. Place the evacuated membrane applicator, with the membrane, over the specimen. Open the valve on the applicator and blow air into the applicator tube to secure the membrane to the sides of the specimen.

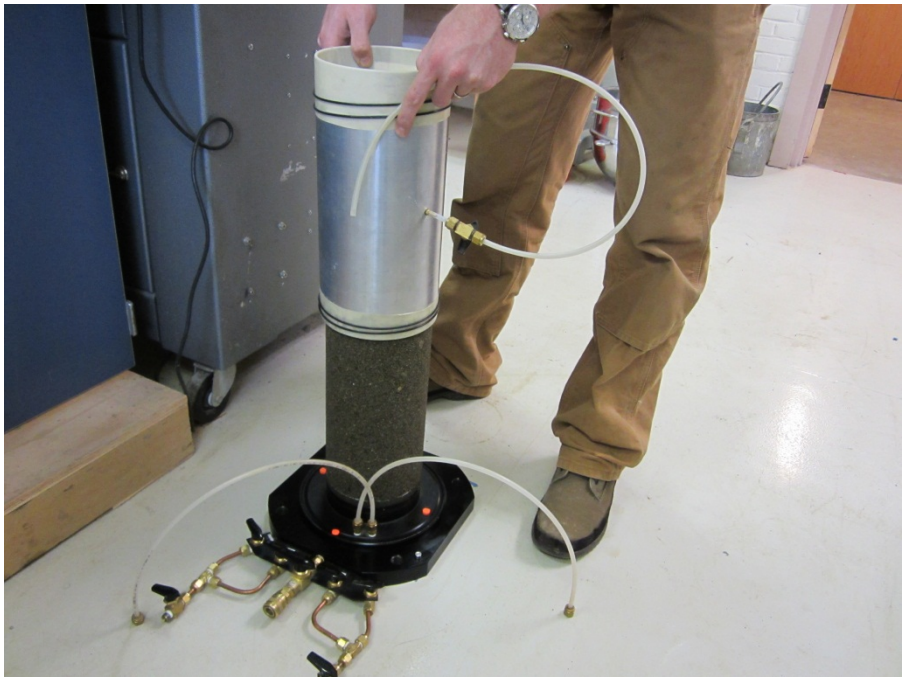

Figure 0.4: Placing the membrane and membrane applicator over the specimen during step B-9.

Figure 0.5: Blowing air into the applicator tube to secure the membrane to the sides of the specimen during step B-9.

10. Make sure the surface is level using a bubble level. Place the saturated filter paper, porous stone and top platen on the top of the surface of the specimen respectively. Ensure that the stone and cap are in direct contact with the top of the specimen.

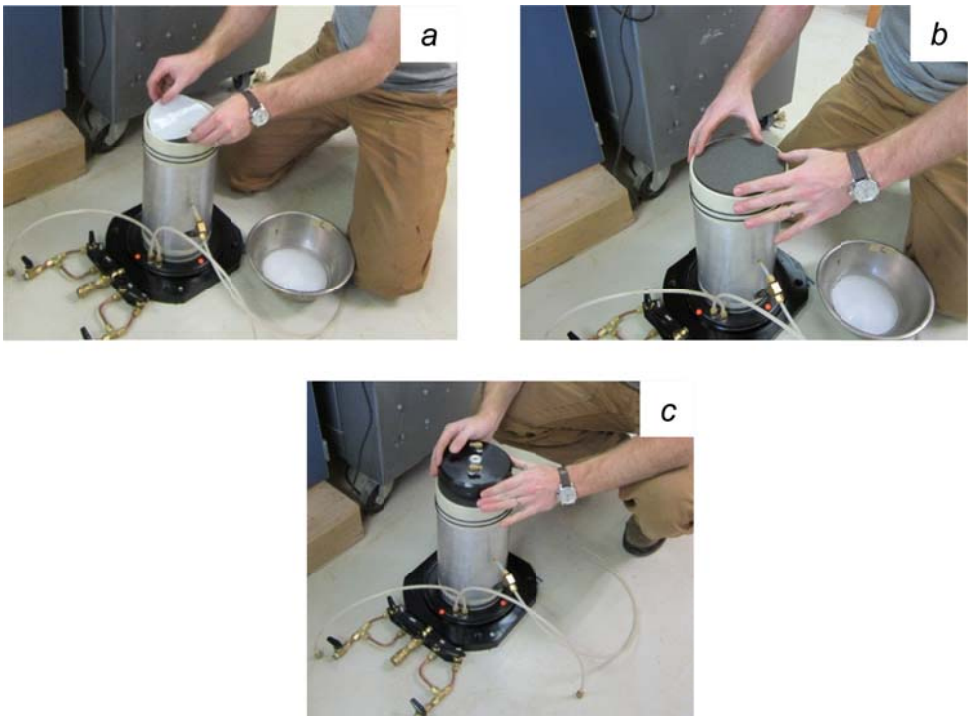

Figure 0.6: Placement of (a) filter paper on specimen; (b) porous stone on filter paper; and (c) top platen on porous stone during step B-10.

11. Slide the O-rings off of the membrane and onto the metal surface of the membrane applicator. Roll the membrane onto the bottom and top platens. Remove slack in the membrane and adjust to remove any wrinkles.

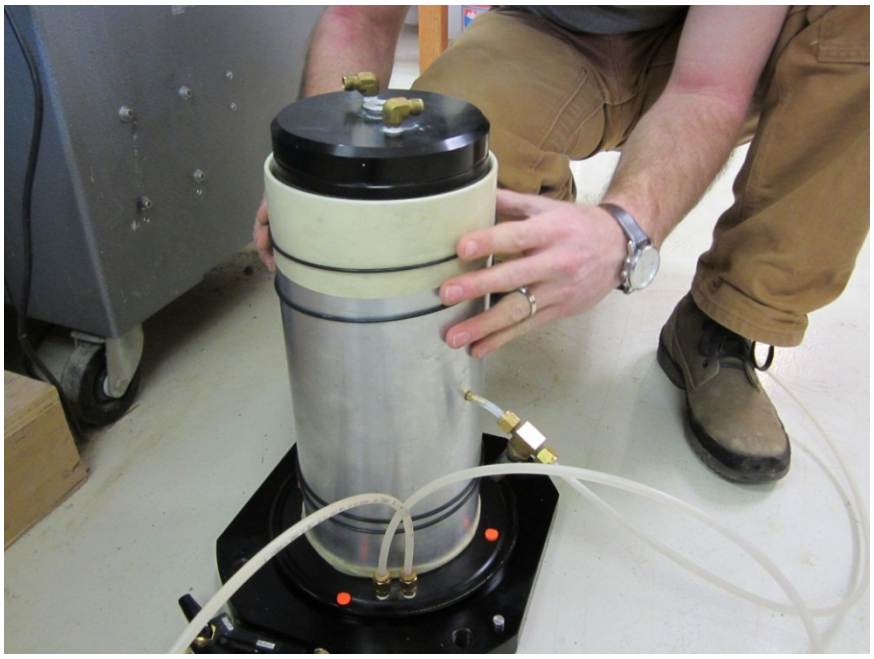

Figure 0.7: Sliding the O-rings off the membrane and on to the membrane applicator during step B-11.

12. Carefully roll the bottom O-ring off the membrane applicator and onto the specimen base. Ensure that the O-ring is seated in the groove on the bottom platen.

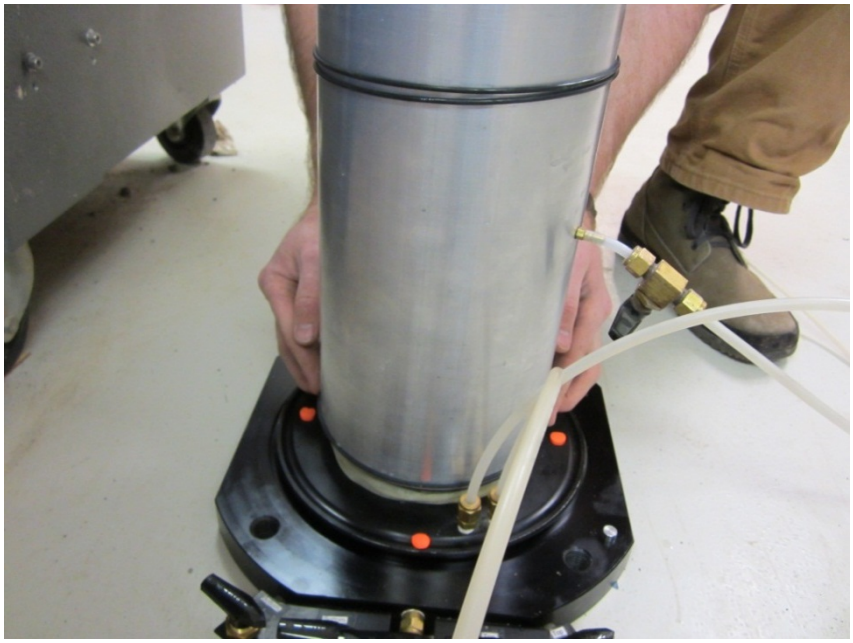

Figure 0.8: Rolling the bottom O-rings of the applicator and on to the membrane and bottom platen during step B-12.

13. Pull the applicator up and off of the specimen, flip the applicator over, and roll top O-ring(s) down onto the top platen. Ensure that the O-ring is properly seated in the groove on the top platen.

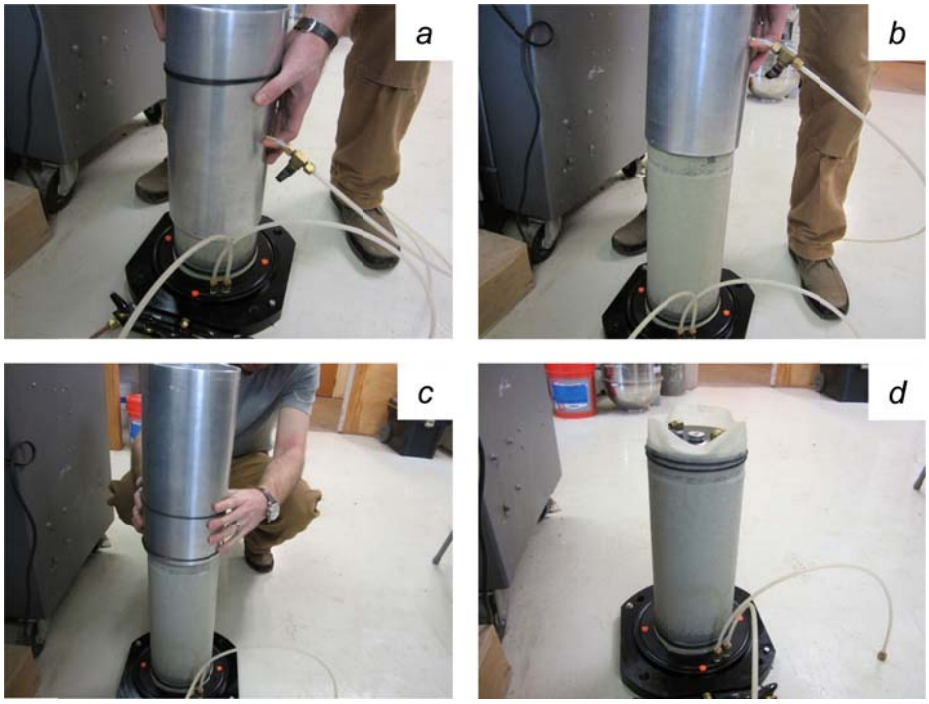

Figure 0.9: Views of (a) the removal of the membrane applicator after placing the bottom O-rings; (c) the membrane applicator after it has been rotated, but before the top O-rings have been placed; (d) the specimen after the top O-rings have been placed during step B-13.

14. Connect the top drainage hoses to the top platen and carefully tighten without disturbing the sample.

Figure 0.10: View of specimen after the membrane has been applied and the top drainage hoses connected after step B-14.

15. Connect the vacuum regulator to a bubble bottle, and connect the bubble bottle intake to top drainage valves on the cell base. Apply ~ 3 in Hg (10 kPa) vacuum and slowly evacuate air from the specimen until the bottle stops bubbling (Figures 11 and 12). Do not exceed 15 kPa of confining pressure at any time prior to the first B-value check (described below).

Figure 0.11: View of specimen, vacuum regulator and bubble bottle prior to evacuation of the specimen during step B-15.

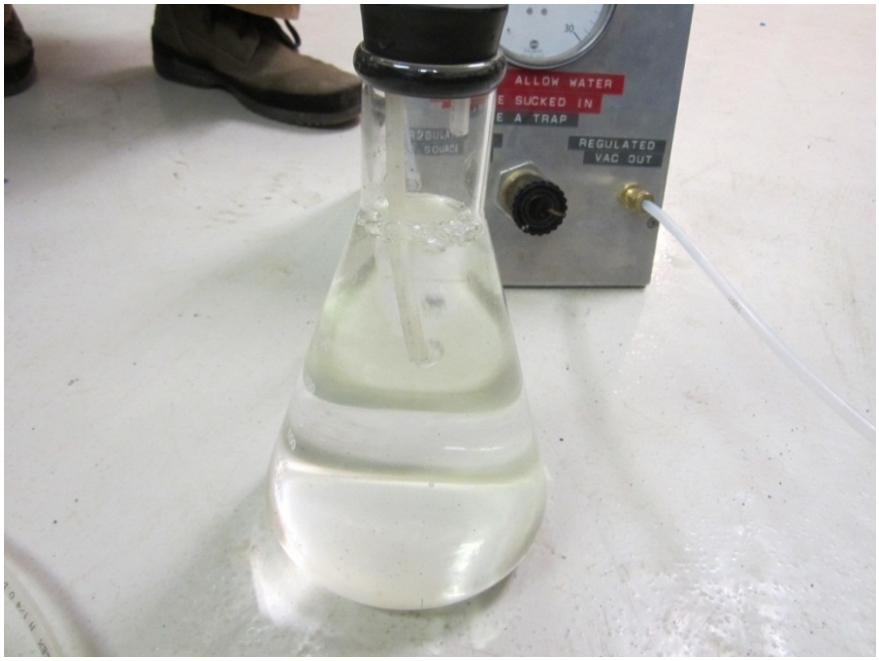

Figure 0.12: View of the bubble bottle during the evacuation of the specimen in step B-15.

16. Measure and record three equally spaced diameters on the specimen using pi tape, and record three equally spaced (120° apart) heights around the periphery of the specimen. Height measurements should be taken using the Mitutoyo digital caliper (MN: CD-8”CS, SN: 0025921) with the top outside jaw resting on the measuring plate and depth probe at the bottom of the bottom platen as shown in Figure 0.13c. Adding 10.6940 inches to the reading on the LCD screen will return the distance from the outside jaw to the end of the depth probe (see Figure 0.14).

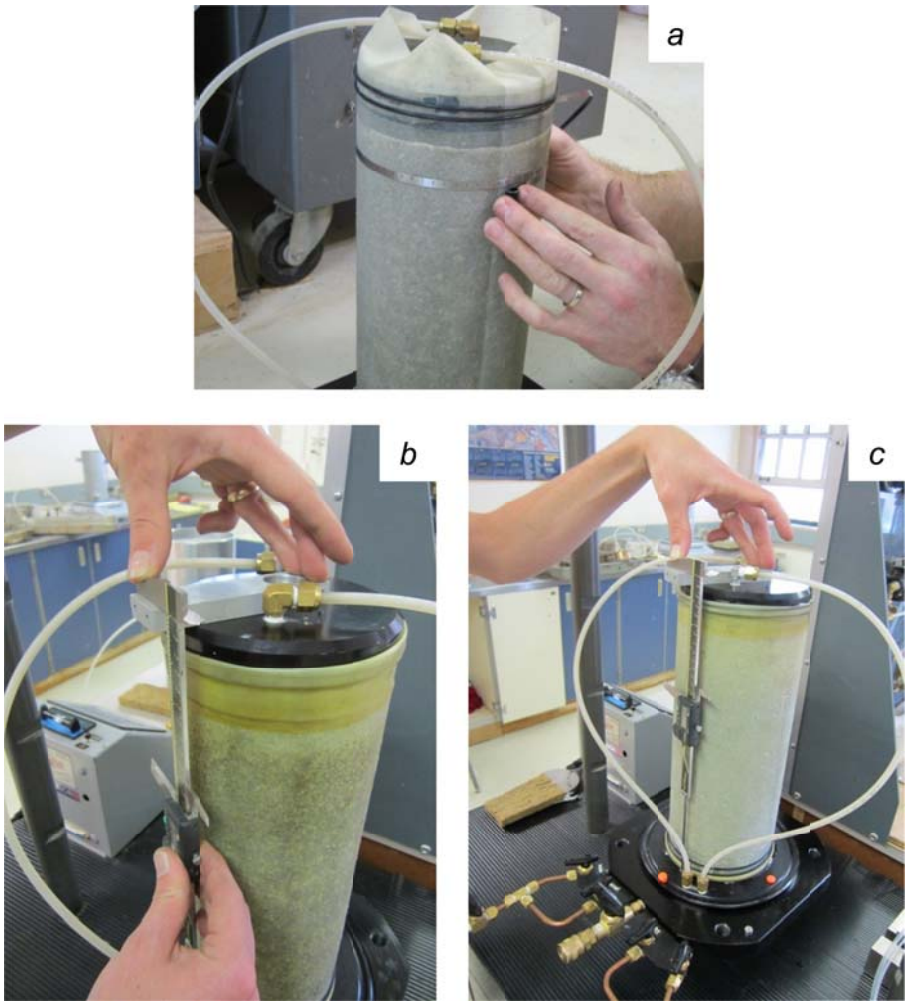

Figure 0.13: (a) Diameter measurement of specimen using a PI tape; (b & c) height measurement using a caliper and measuring platen during step B-16.

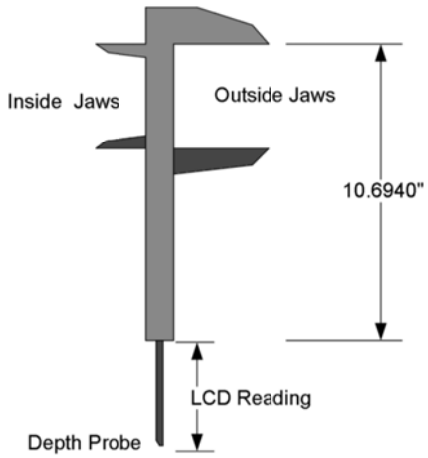

Figure 0.14: Simplified caliper diagram of Mitutoyo digital caliper (MN: CD-8”CS, SN: 0025921) for use with height measurements during step B-16.

17. Using the average of the three height and diameter measurements from Step 16, and the weight of the soil calculated in Step B-8; calculate the void ratio of the sample (make sure to subtract two membrane thicknesses from the average of the diameter measurements). If the void ratio is within the target range move on to Step 18, if not, tear down the sample and start over.

18. Close top drainage valves, pull hose from bubble bottle, drop the vacuum pressure, then disconnect and remove vacuum.

19. Clean off the chamber base and remove plugs from holes in the base. Ensure that o-rings and seals along the triaxial chamber and base are free of debris. Grease large O-rings and seals around the triaxial chamber using vacuum grease. Flip top of membrane up around the specimen cap so that it forms a collar.

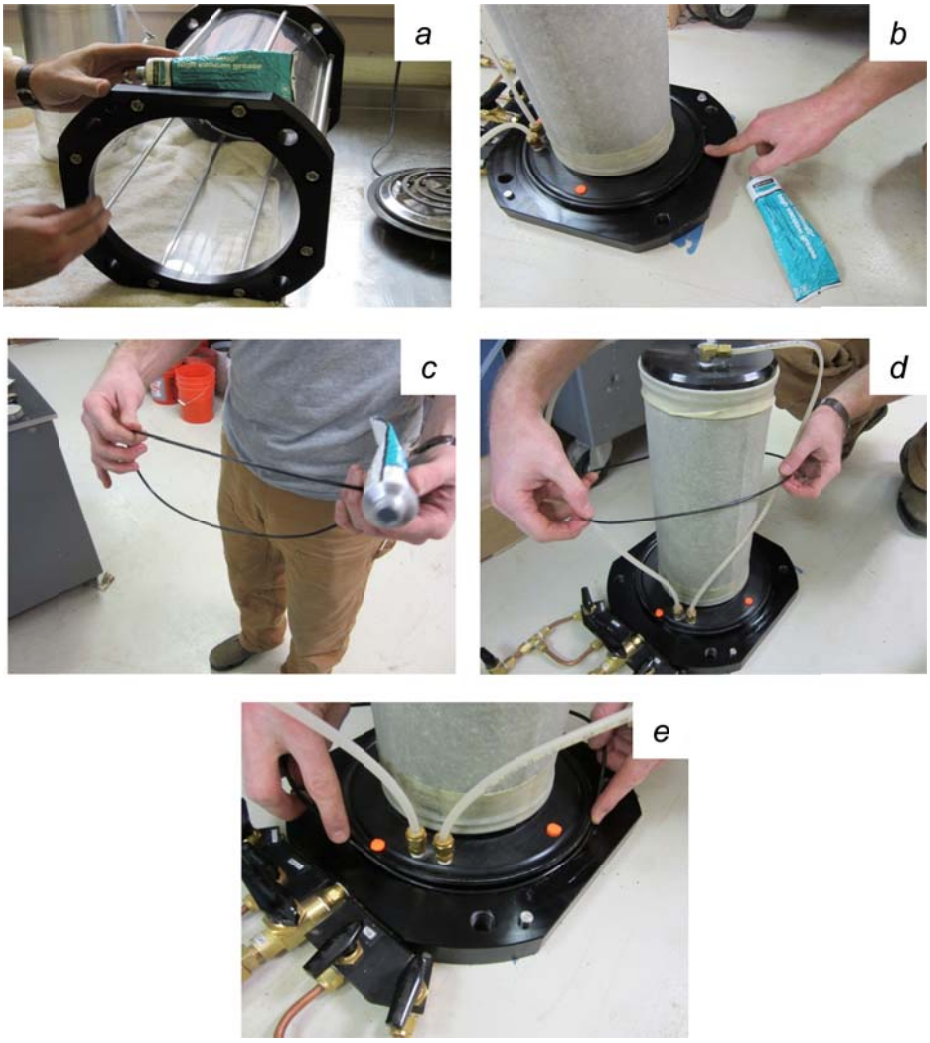

Figure 0.15: (a) Applying grease to the O-ring seal on the bottom of the cell; (b) applying grease to the O-ring seal on the triaxial base; (c) applying grease to the O-ring; (d) placing the O-ring around the specimen; (e) placing the O-ring in the O-ring seal on the cell base during step B-19.

20. Carefully install triaxial chamber on base with greased O-rings in place and ensure the base and chamber are seated properly.

21. Insert the top piston though the hole in the top of the triaxial chamber and carefully thread the bolt on the end of the piston into the top platen.

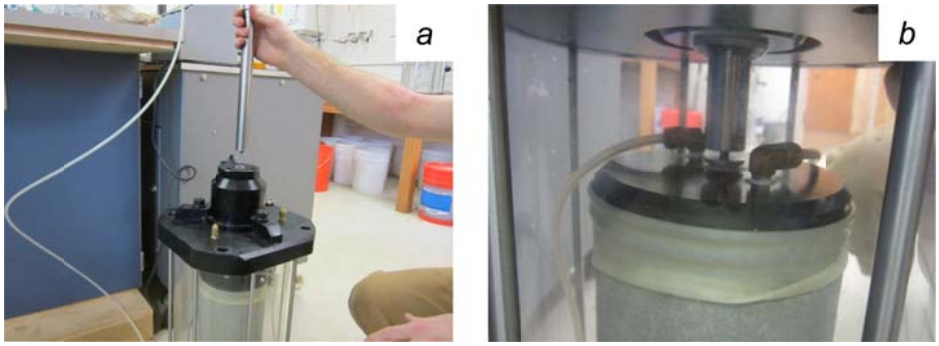

Figure 0.16: (a) Inserting the loading piston into the top of the cell; (b) aliening the loading piston and the top platen during step B-21.

22. Secure the triaxial chamber to the base using the long steel bolts by tightening with a wrench. Ensure that the piston and platen are seated firmly against the sample and lock the piston into place.

23. Fill the triaxial chamber with de-aired water by connecting the de-aired water line to the "Cell" quick connector.

    - Connect chamber vent hose to quick connector on top of triaxial chamber to allow air to escape during filling.

    - Remove brass caps from top of chamber and continue filling until water comes out of top holes. Remove remaining air pockets in the top of the chamber using the cane shaped hollow metal tube.

    - Fill brass caps with water and replace on the top of the chamber.

    - Bleed remaining air from top vent quick connector and ensure that all large air pockets have been removed from triaxial chamber.

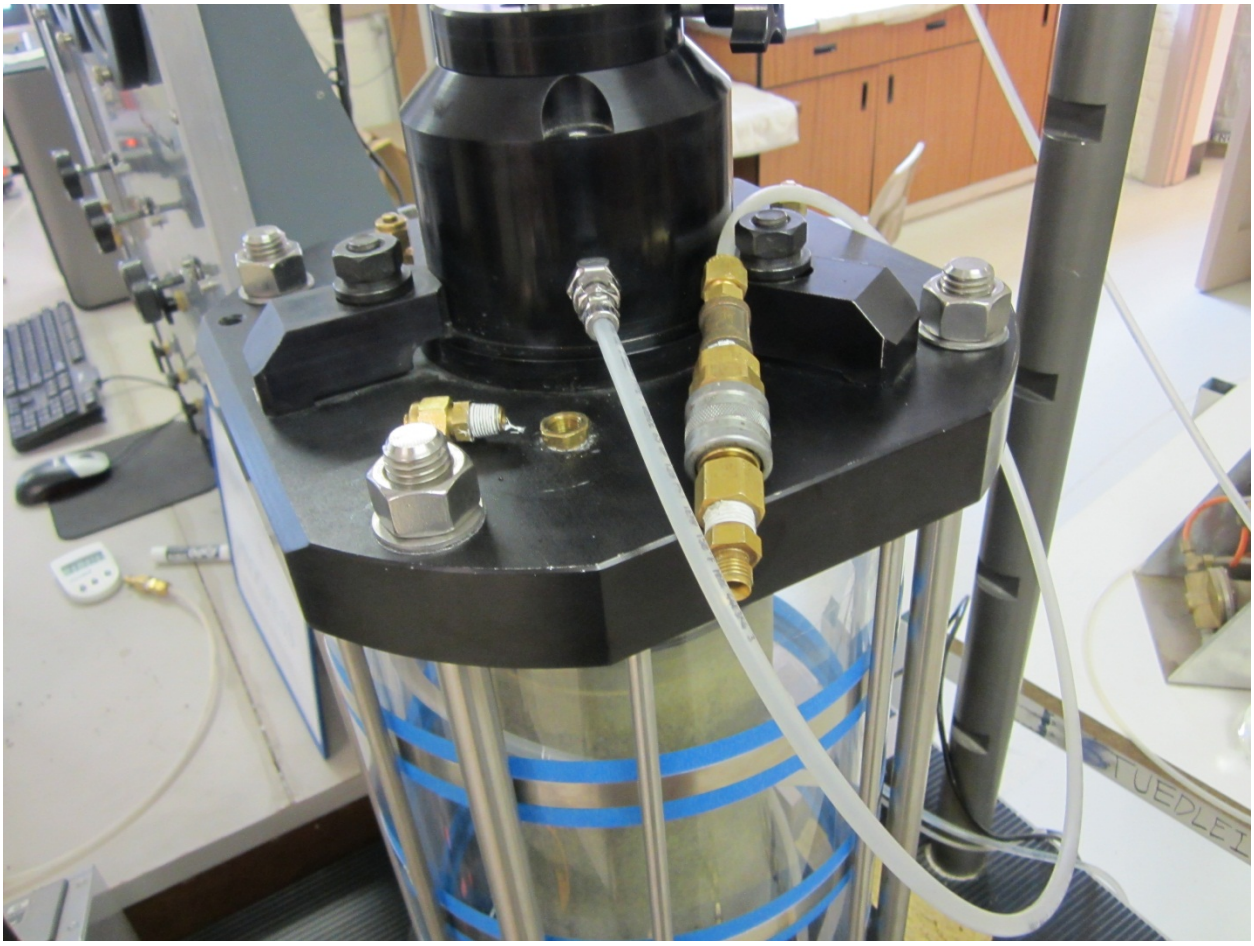

Figure 0.17: View of the cell prepared to be filled with water during step B-23.

24. Ensure that the cell pressure oil-water interface has sufficient water (see Figure 0.18 below). Make sure the cell pressure control valve is set to manual and the manual cell pressure regulator is set to zero. Connect the cell pressure hose from the back of the panel to the triaxial cell.

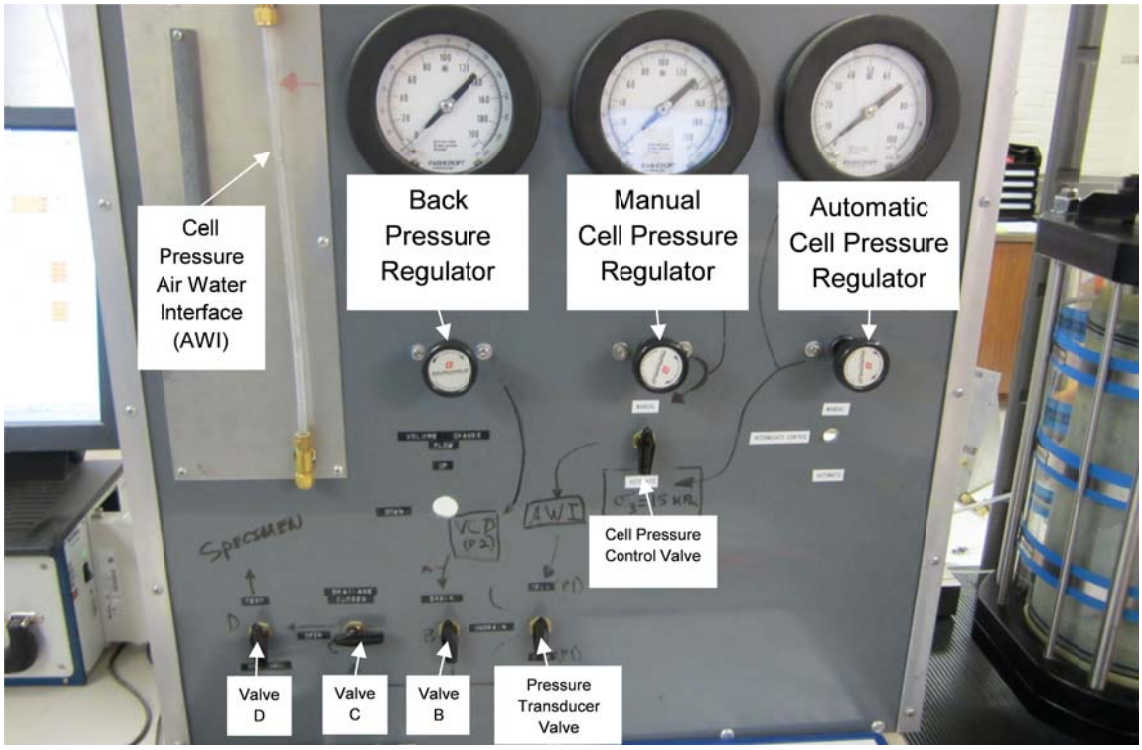

Figure 0.18: Control Panel (front)

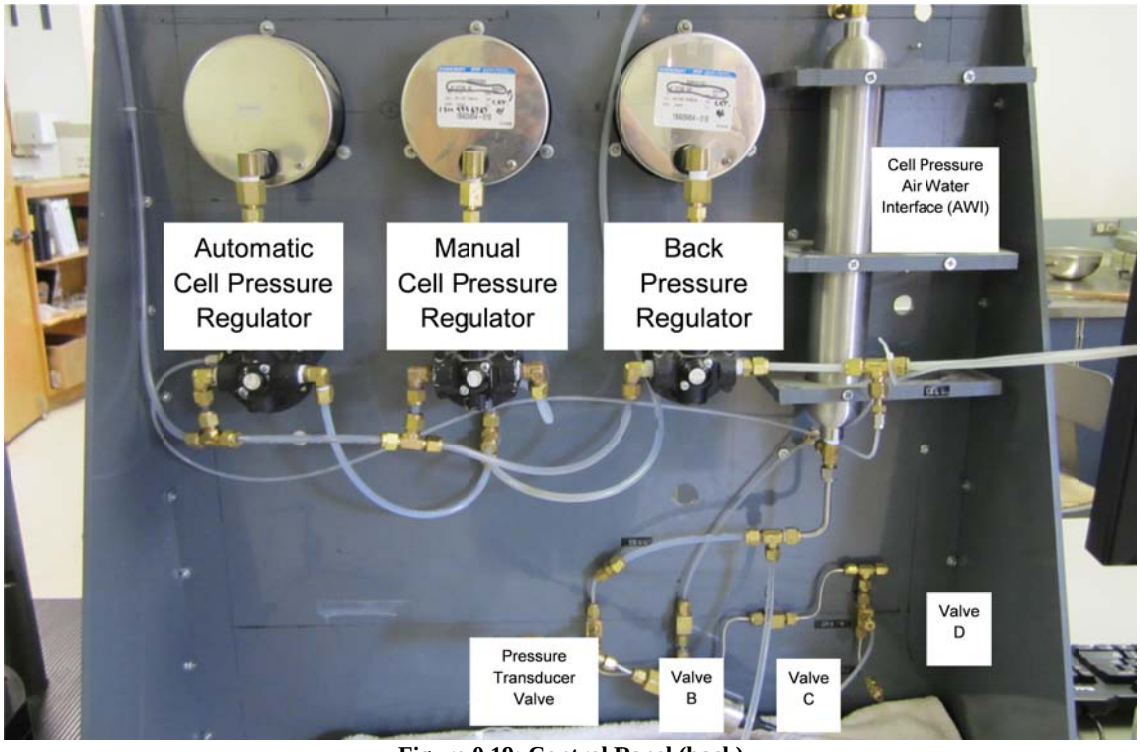

Figure 0.19: Control Panel (back)

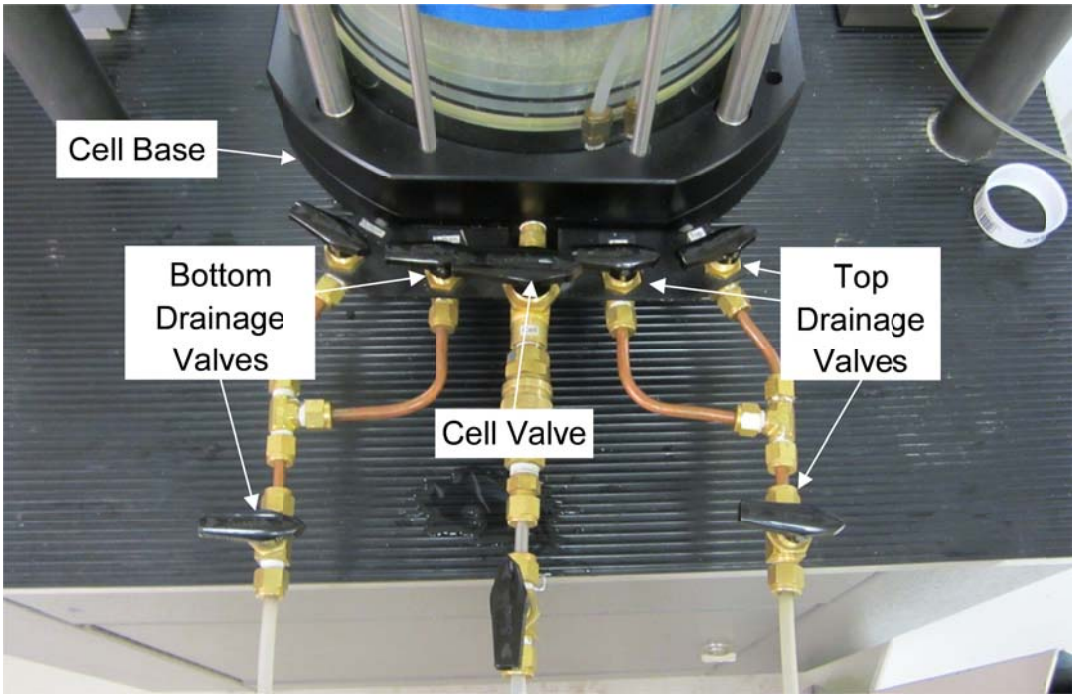

Figure 0.20: Cell Base

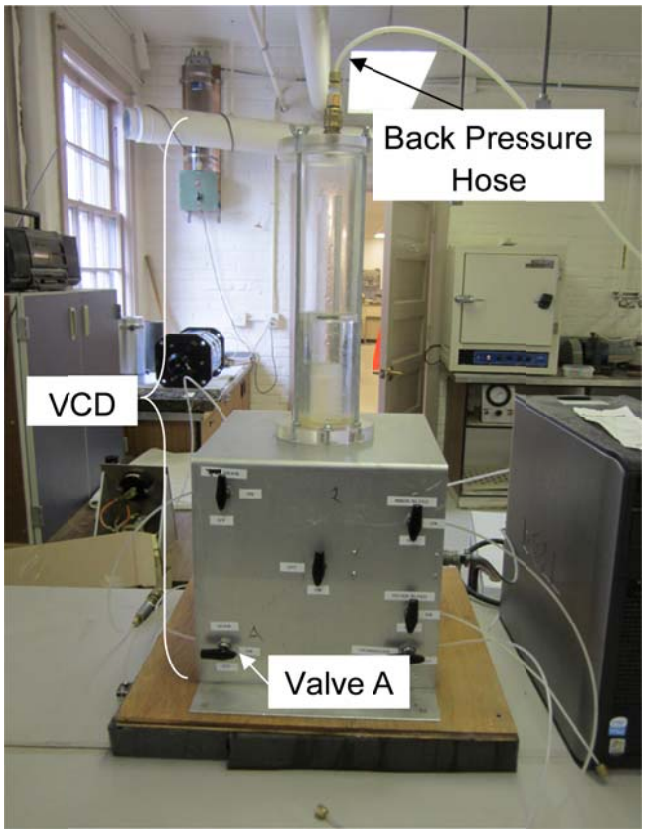

Figure 0.21: Volume Change Device (VCD)

C. Saturating the Specimen

1. Release the vacuum on the specimen by opening the top drainage valves (3) on the cell base.

2. Make sure the back pressure regulator is set to zero, and then close the cell valve on the cell base.

3. Rotate the cell pressure control valve to automatic.

4. Check that the bias is set to an appropriate value (typically 15 kPa).

5. Open the cell valve on the cell base.

6. Connect CO_2 tank and regulator to bottom drainage valve. Open top drainage and run CO_2 through the specimen so that is flows through the specimen, out the top drainage, and into the bubble bottle at a rate of ~ three bubbles per second for approximately 20 minutes.

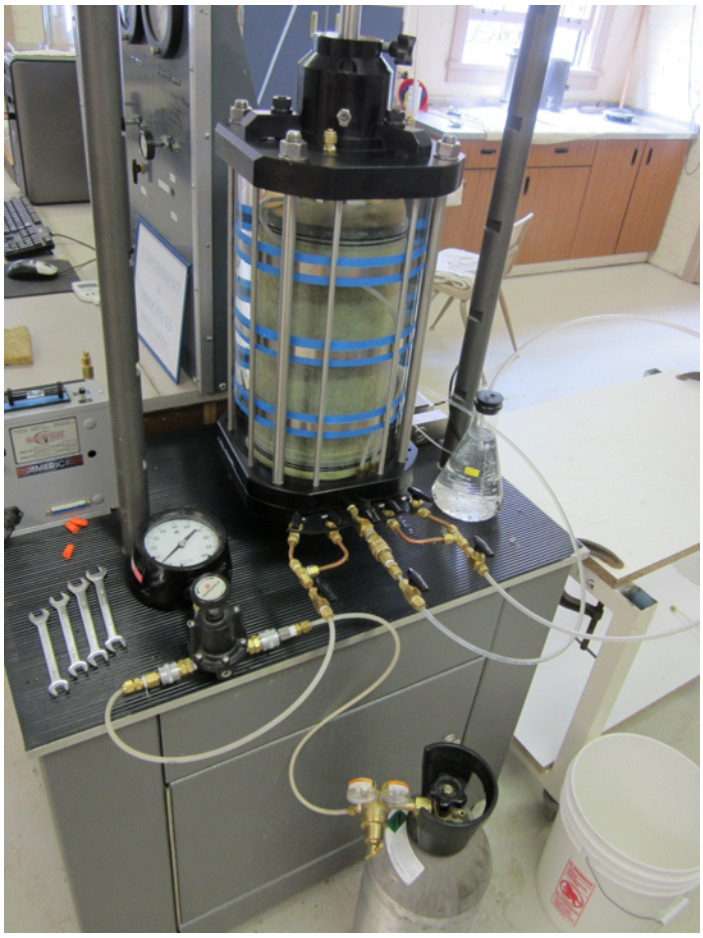

Figure 0.22: View of the specimen during CO2 saturation (step C-6).

7. Turn off flow of CO_2 to the cell (close tank valve), then close bottom valve, then top valve to the specimen and remove CO_2 tank and regulator. Leave the bubble bottle connected to the top drainage valve.

8. Connect de-aired water hose to bottom drainage valve (Note: Always control flow through the specimen from the bottom drainage valve). Turn knob on de-aired water tank to "Draw" and slowly open the valve on the de-aired water hose to allow water to saturate the specimen from the bottom up. Monitor the rate that air is pushed out of the specimen by watching the bubble bottle. Once bubbles no longer form in the bubble jar, close bottom drainage, then top drainage, remove the bubble bottle, and open top, then bottom drainage valves to allow water to drip slowly from the top drainage valve into 5 gallon bucket. Run water through the specimen for at least 20 minutes. Once desired amount of water has passed through the specimen, close bottom, then top drainage valves and disconnect de-aired water hose.

9. Ensure that the volume change device (VCD) has sufficient water to run the test (~ 500 cc). Use only de-aired water in the VCD. Remove caps from back pressure hose and saturate the line prior to connecting to both top and bottom drainage valves. Connect ends of the T-hose one at a time with the drainage valves closed and water running through the back pressure line from the VCD.

D. B-value check

1. Check that the loading piston is locked off.

2. Place the load cell. The load cell should be carefully centered above the loading piston, then lower the cell so that it is touching the piston but not resting on it. Make sure the threaded rod is securely clamped to the load frames cross head by rotating the circular nuts.

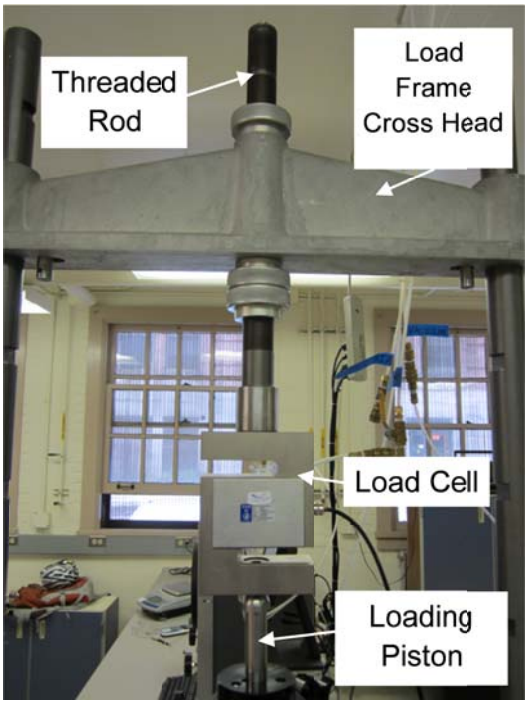

Figure 0.23: Load frame with load cell in place after step D-2

3. Connect the drainage hose to the top and bottom drains.

4. Open drainage to sample (check that all 10 valves are open, A, B, C, D, and 6 on cell base).

5. Record the initial back pressure (zero) reading.

6. Check that the cell pressure is being controlled with the positive bias relay ("Automatic").

7. Slowly increase the back pressure {500 kPa} (watch the cell and back pressure in LabView to make sure the back pressure is keeping up with the cell pressure).

8. Wait 4 min.

9. Take Initial B-value back pressure and cell pressure readings.

10. Close the cell valve on cell base.

11. Rotate the cell pressure control valve to "manual".

12. Increase the manual cell pressure regulator to 30 kPa greater than that of the back pressure {530 kPa}.

13. Close drainage valve B (note that you are still able to measure pore pressure).

14. Open the cell valve on cell base.

15. Take final B-value back pressure and cell pressure readings, and calculate the B-value.

16. Close off the cell valve on cell base.

17. Rotate the cell pressure control valve to "automatic".

18. Open the cell valve on the cell base.

19. Open drainage valve B.

20. If the B-value is greater than or equal to 0.90, then move to consolidation, If not, repeat steps 7 through 20 at a higher pressure.

E. Consolidation

1. Place the LVDT.

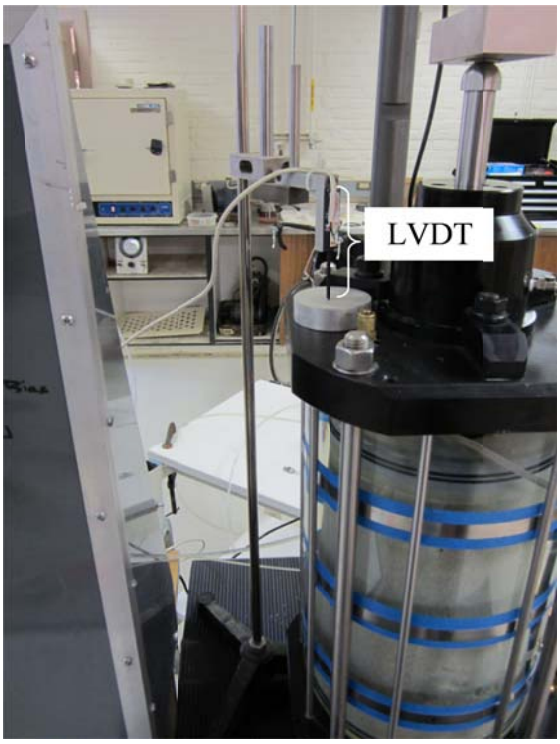

Figure 0.24: View of the load cell and old LVDT during Step E-1

2. Unlock the loading piston.
3. Begin recording on the DAQ system.
4. Close the chamber valve on the cell base.
5. Rotate the chamber pressure control valve to "manual"
6. Decrease the manual pressure to match the automatic cell pressure
7. Open the cell valve on the cell base.
8. Increase the manual cell pressure regulator to the consolidation effective pressure (back pressure + OCR x σ'3), then wait 5 minutes (If OCR = 1, skip step 9).

9. Decrease the manual cell pressure regulator to the test-effective pressure (back pressure + σ'3) and wait 5 minutes.

F. Shear

1. Check that LabView is still recording data.

2. Turn on the load frame controller
   - Press Enter
   - Select English
   - Verify displacement rate (ASTM D7181 section 8.4.2, typically 0.02 in/min for cohesionless soil) and push Enter
   - Push Test => Now ready to start

3. Record the back pressure for 10 seconds, and then rotate the pressure transducer valve to cell.

4. Push Start on load frame controller. Shearing will commence immediately. **Note: The VCD is very sensitive.** *Avoid touching the table that the VCD rests on during testing*.

5. Monitor progress of shear by observing plots in LabView and the specimen in the cell.

6. Once displacement has reached 2.4 inches (20 percent axial strain), stop recording, and then push stop on load frame controller.

G. Disassembly

1. Lock the piston into place

2. Close the top and bottom drainage, and cell valves on the base of the cell.

3. Rotate the cell pressure control valve to automatic.

4. Decrease the back pressure regulator to zero.

5. Decrease the manual cell pressure regulator to zero.

6. Unhook the cell pressure line from the cell valve on the cell base.

7. Unhook and re-plug the top and bottom drainage lines one at a time.

8. Slowly open the bottom drainage valve on the cell base until a stable drip develops.

9. Allow the specimen to drain for 5 minutes, and then close the bottom drainage valve.

10. Connect a drainage hose to the cell valve on the cell base to drain the cell into a 5 gallon bucket.

11. Disconnect the back pressure hose from quick connect on the top of the VCD and connect it to the vent on top of the chamber with the quick release extension.

12. Pressurize the chamber lightly by increasing the back pressure regulator.

13. Once the chamber has drained completely, disconnect hoses from the cell.

14. Place cart and metal pan to collect the sample next to the load frame.

15. Transfer the entire triaxial apparatus to the cart.

16. Unbolt the chamber. Loosen and remove the piston, and carefully remove the chamber from the base plate.

17. Disconnect top drainage lines from top platen and carefully the sample and membrane into the pan. Save all material. Be careful when removing specimen from the membrane.

18. Wash the membrane with water and store the used membrane in water for reuse.

19. Oven-dry the sample.

20. Determine the actual initial void ratio of the sample by measuring the dry mass of the specimen after testing.

APPENDIX B

Principal Stress Difference-Axial Strain Curves

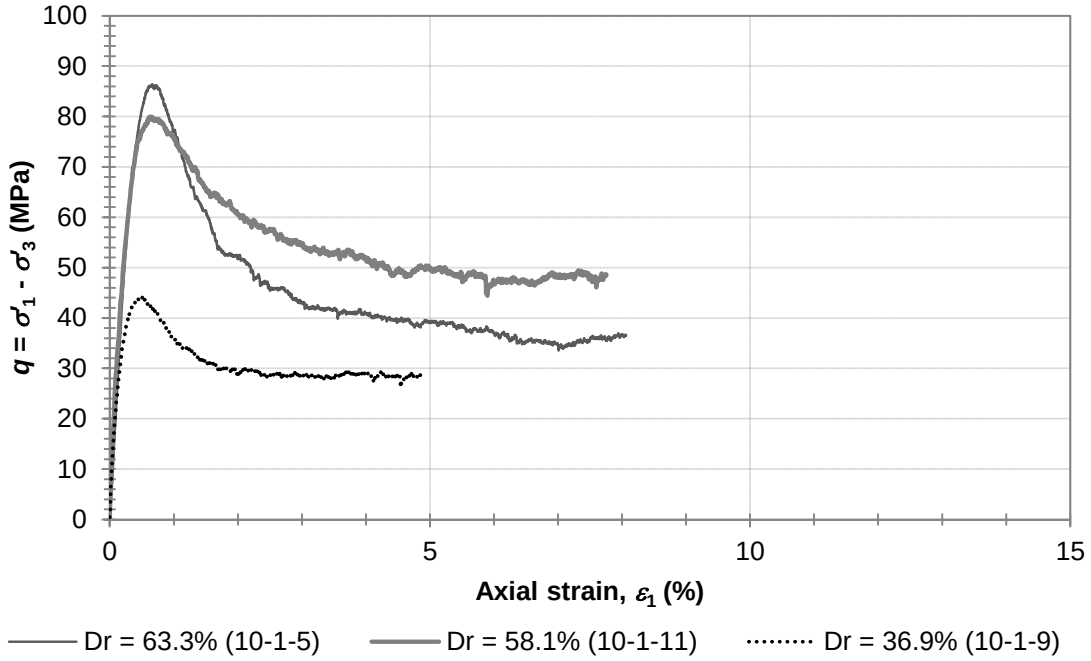

Figure 0.1. Effective principal stress difference versus axial strain for tests at an effective confining pressure of 10 kPa.

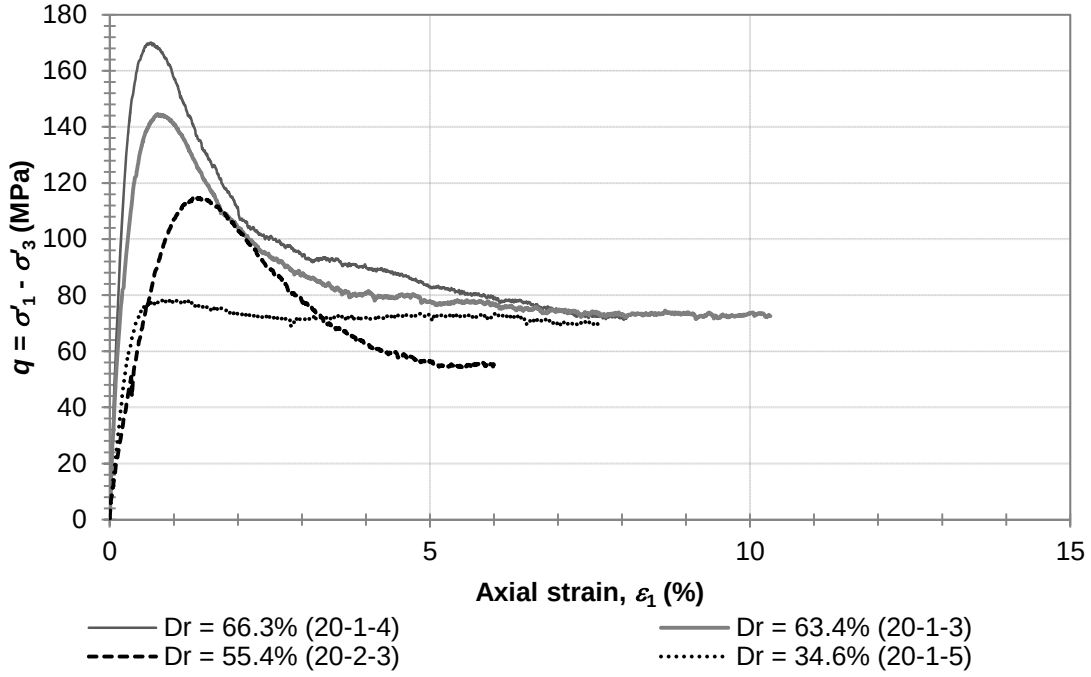

Figure 0.2. Effective principal stress difference versus axial strain for tests at an effective confining pressure of 20 kPa.

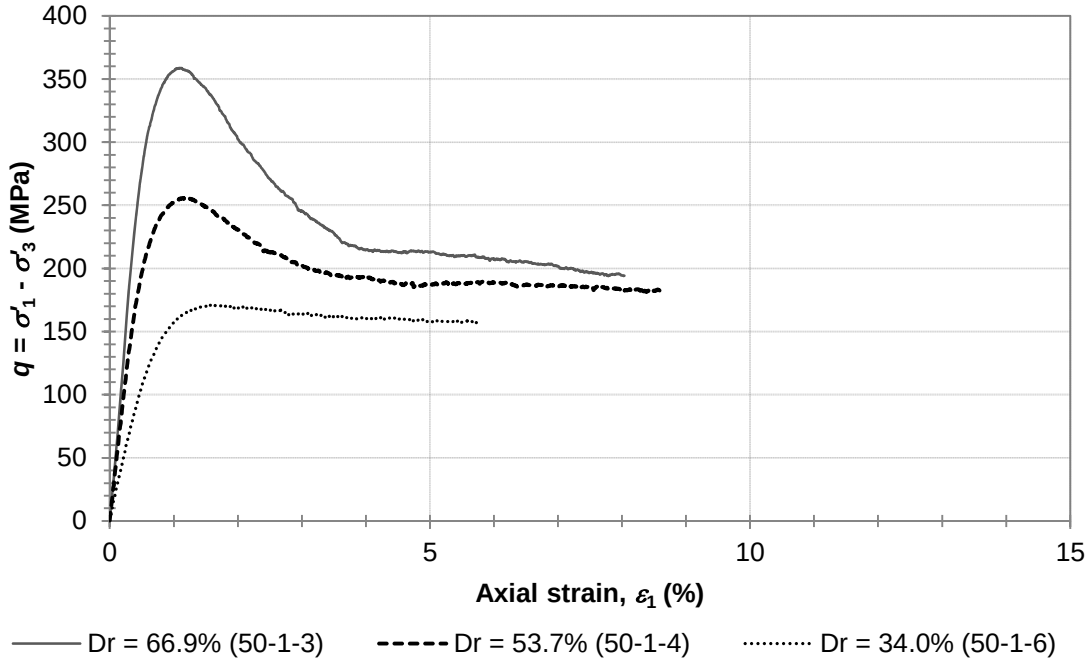

Figure 0.3. Effective principal stress difference versus axial strain for tests at an effective confining pressure of 50 kPa.

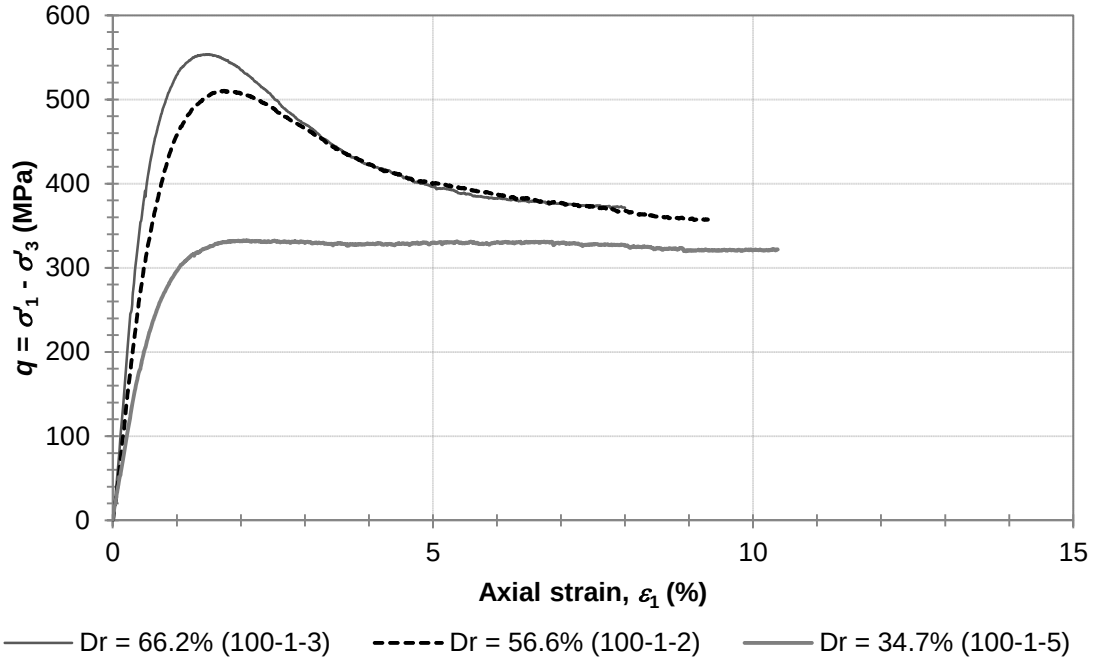

Figure 0.4. Effective principal stress difference versus axial strain for tests at an effective confining pressure of 100 kPa.

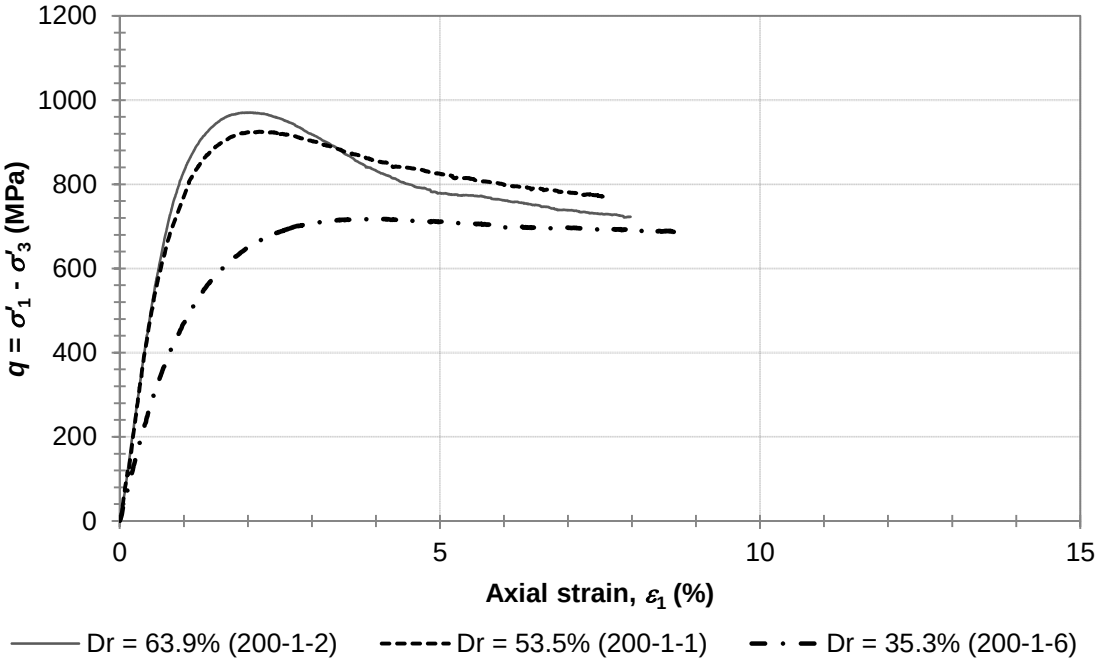

Figure 0.5. Effective principal stress difference versus axial strain for tests at an effective confining pressure of 200 kPa.

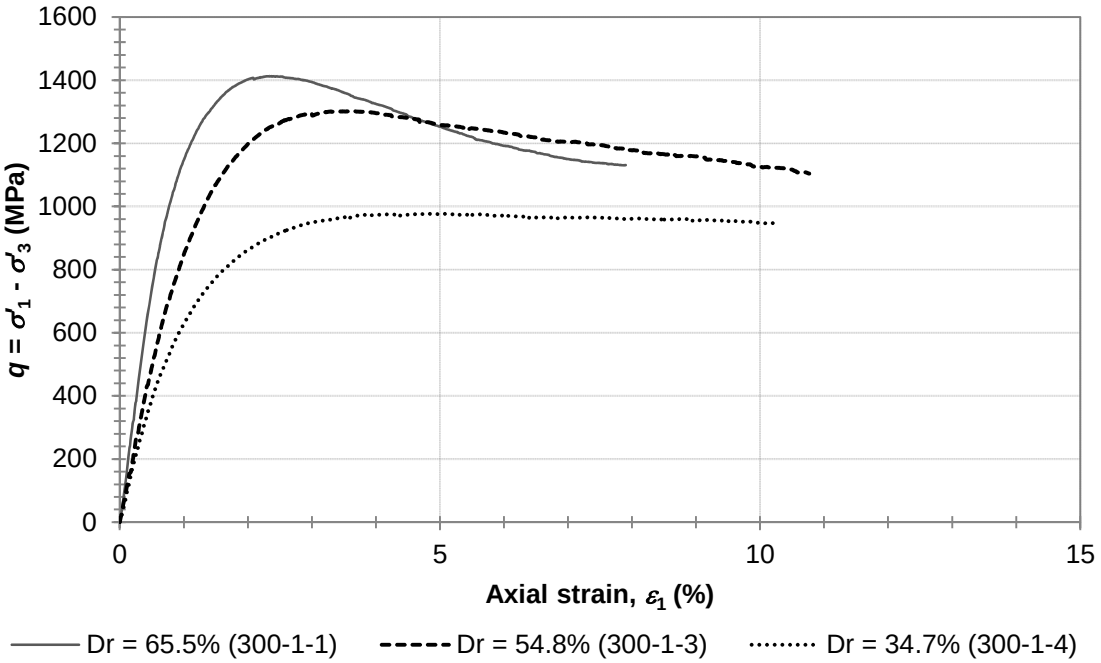

Figure 0.6. Effective principal stress difference versus axial strain for tests at an effective confining pressure of 300 kPa.

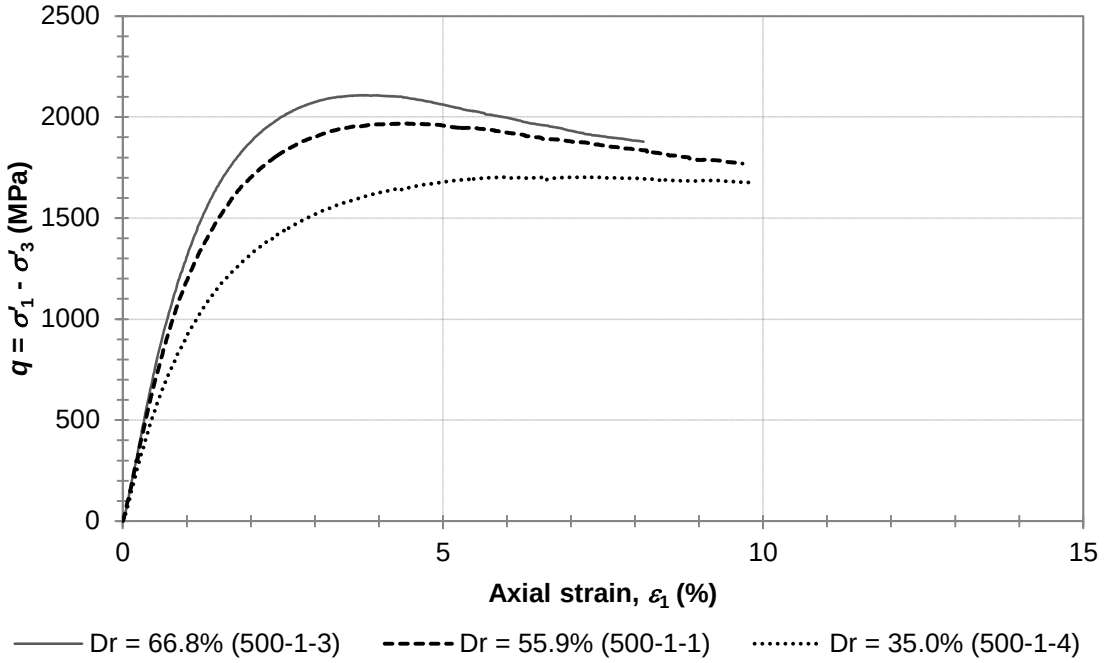

Figure 0.7. Effective principal stress difference versus axial strain for tests at an effective confining pressure of 500 kPa.

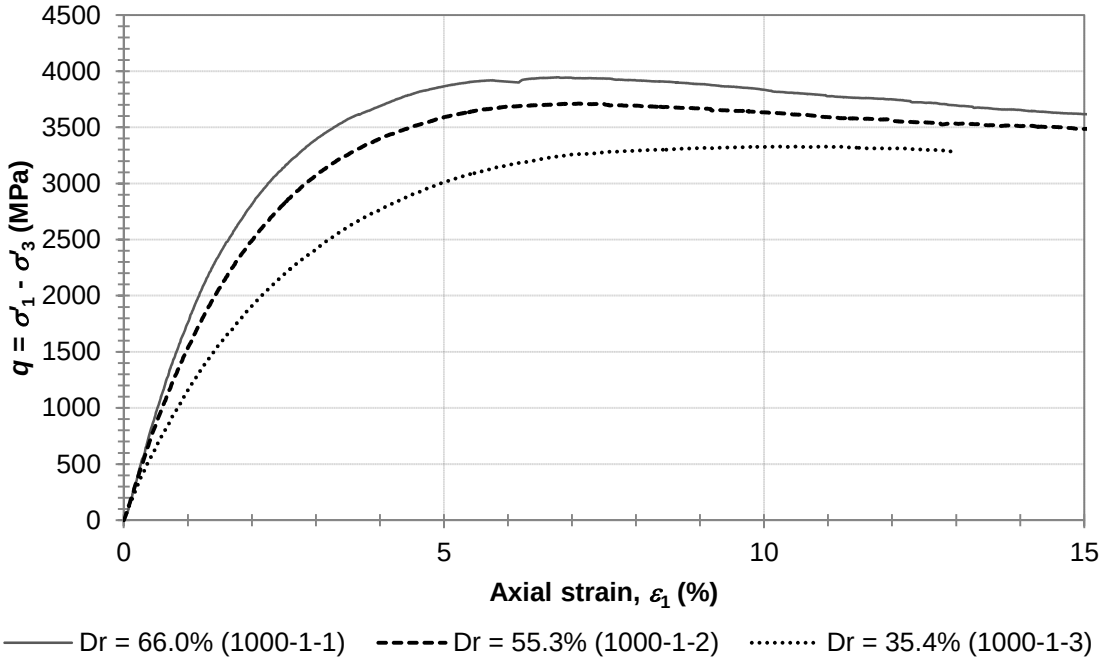

Figure 0.8. Effective principal stress difference versus axial strain for tests at an effective confining pressure of 1000 kPa.

APPENDIX C

Volumetric Strain-Axial Strain Curves

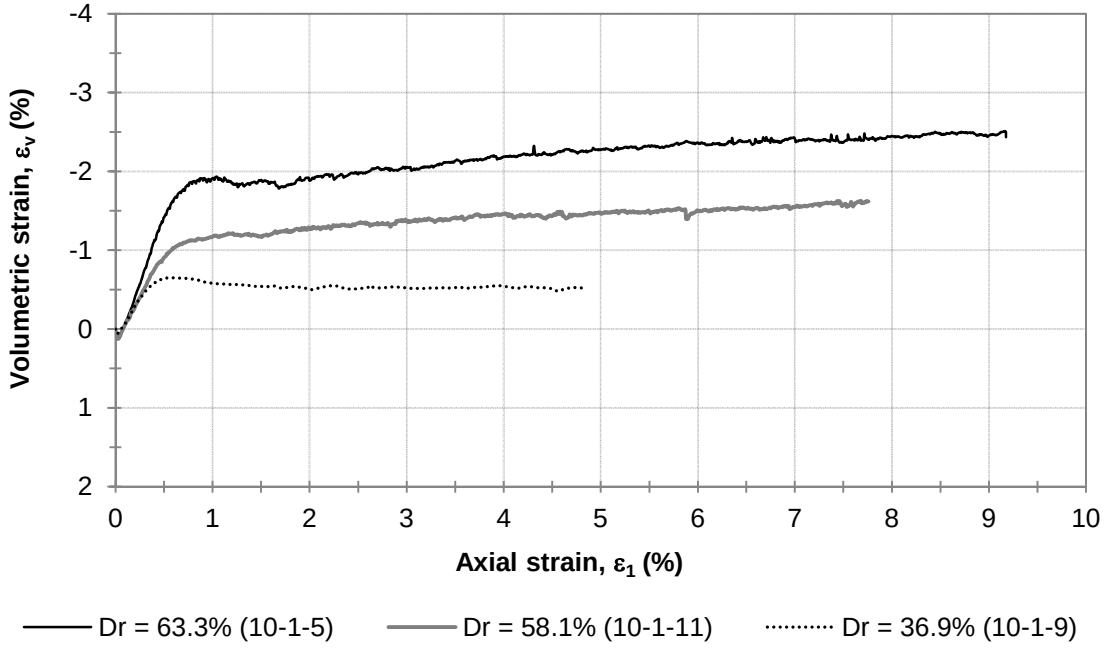

Figure 0.1. Effective principal stress difference verses axial strain for tests at an effective confining pressure of 10 kPa.

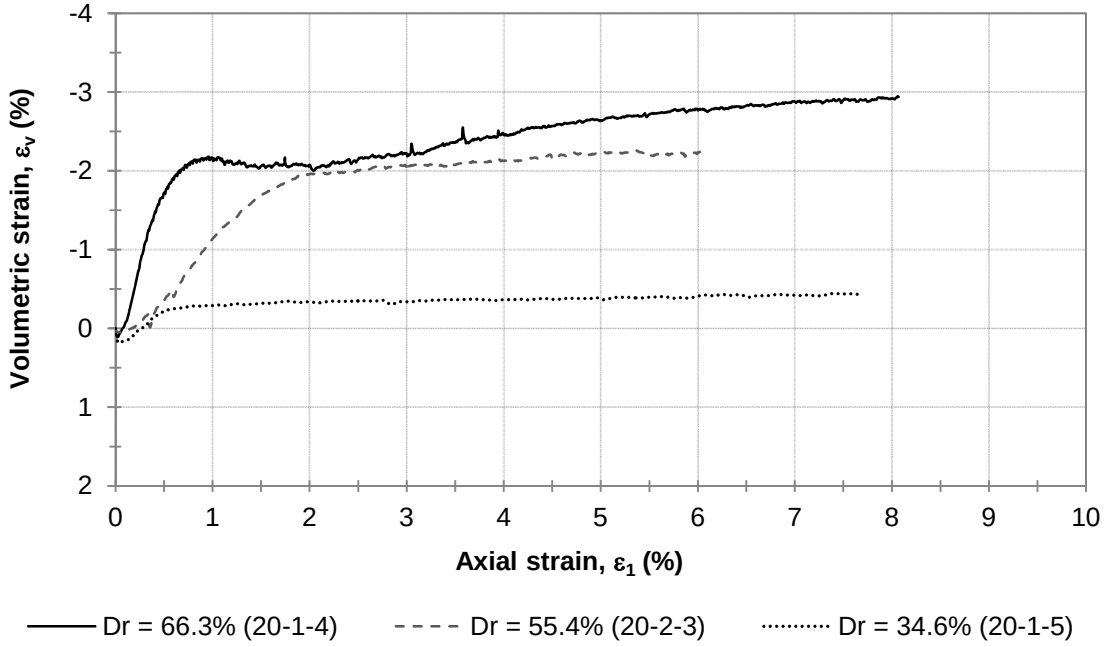

Figure 0.2. Effective principal stress difference verses axial strain for tests at an effective confining pressure of 20 kPa.

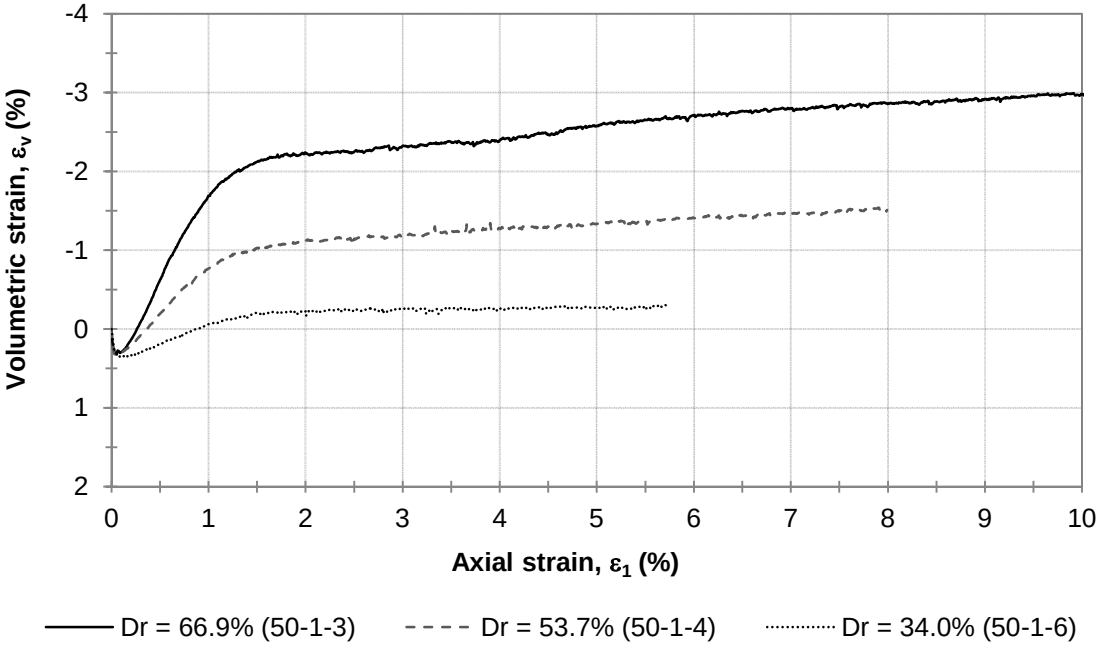

Figure 0.3. Effective principal stress difference verses axial strain for tests at an effective confining pressure of 50 kPa.

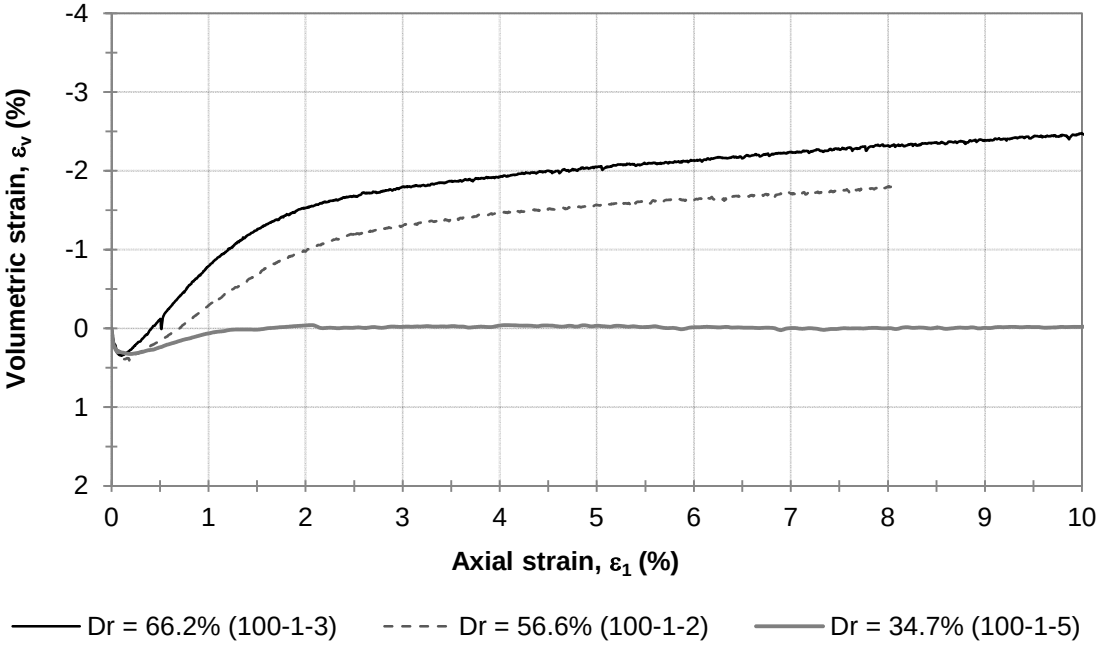

Figure 0.4. Effective principal stress difference verses axial strain for tests at an effective confining pressure of 100 kPa.

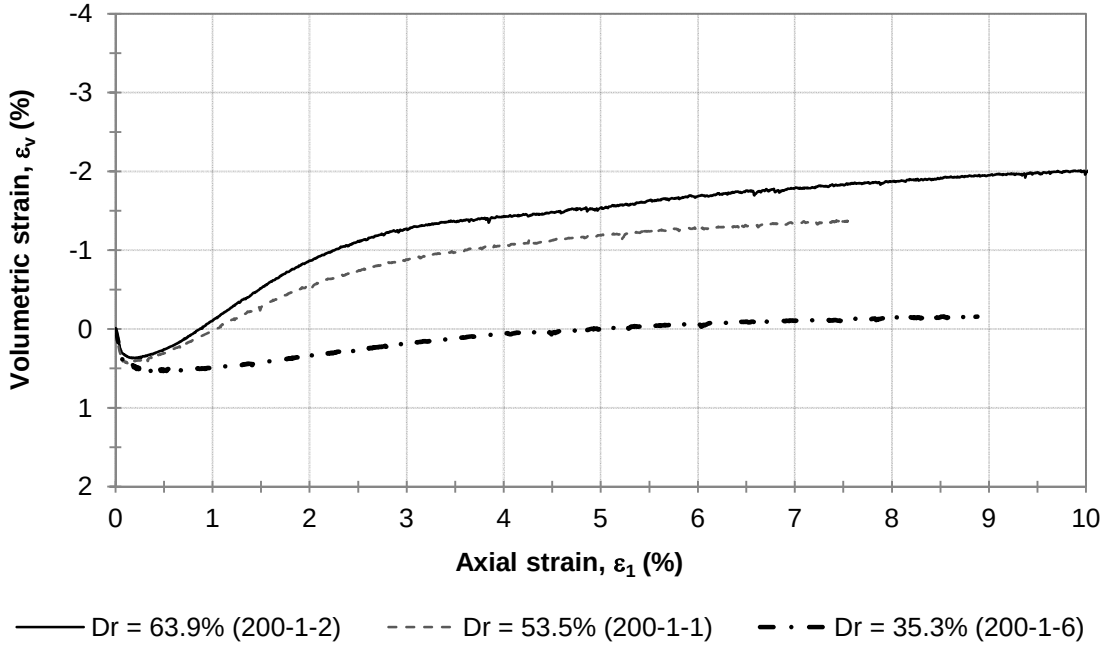

Figure 0.5. Effective principal stress difference verses axial strain for tests at an effective confining pressure of 200 kPa.

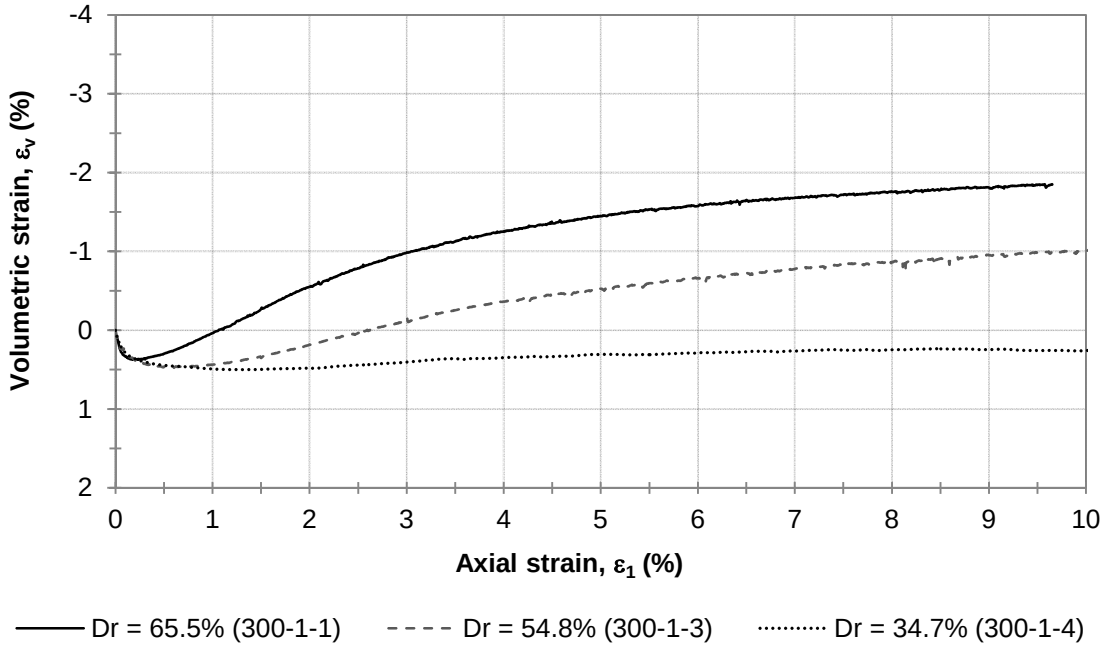

Figure 0.6. Effective principal stress difference verses axial strain for tests at an effective confining pressure of 300 kPa.

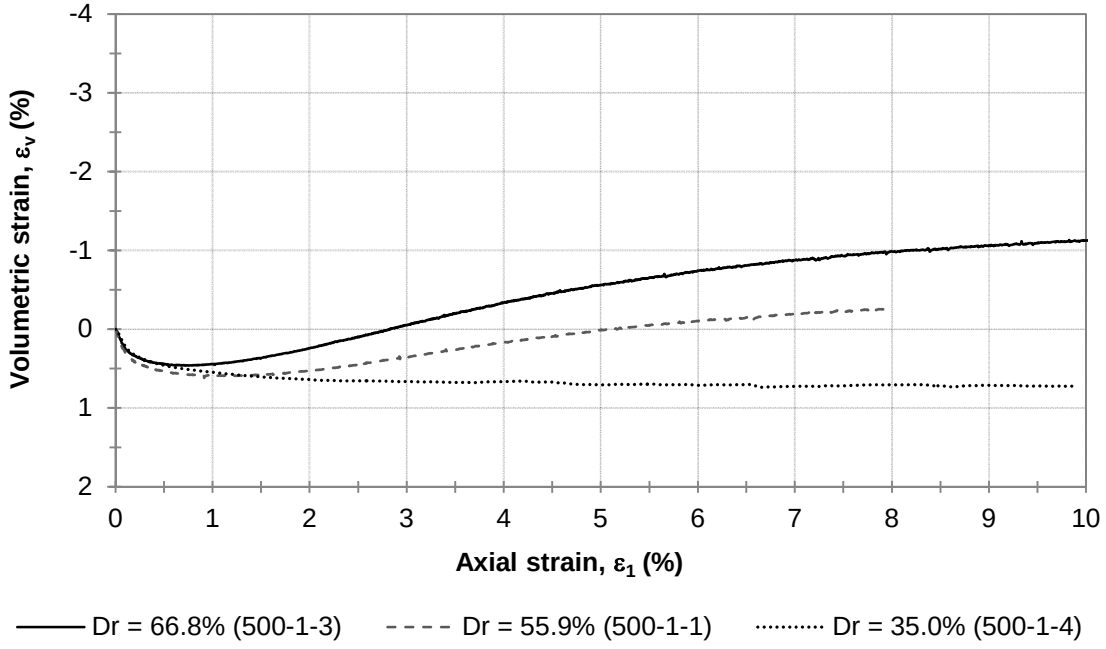

Figure 0.7. Effective principal stress difference verses axial strain for tests at an effective confining pressure of 500 kPa.

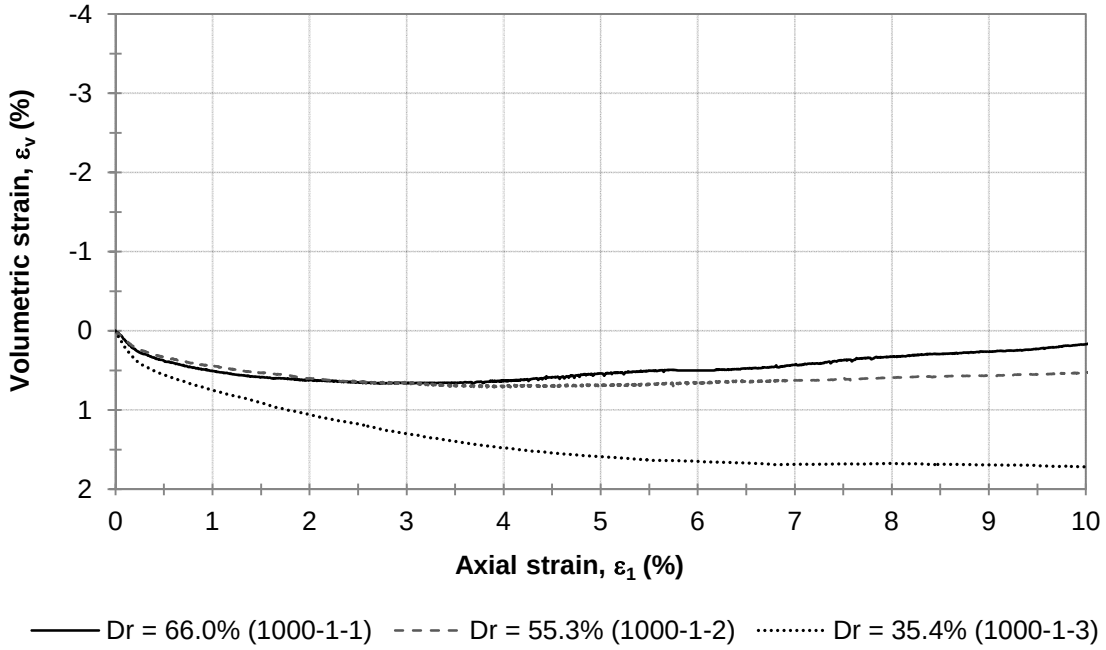

Figure 0.8. Effective principal stress difference verses axial strain for tests at an effective confining pressure of 1000 kPa.

APPENDIX D

Pullout Box Design Schematics

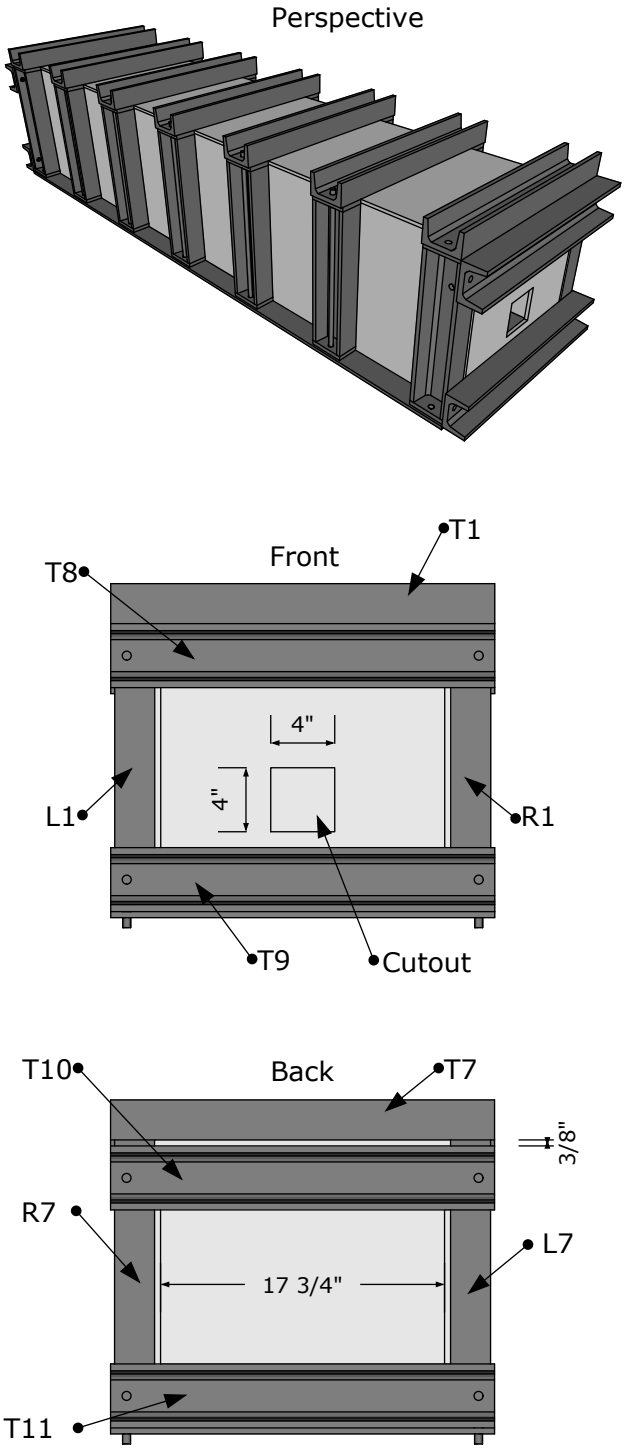

Figure D-1. Front, back, and perspective views of assembled pullout box.

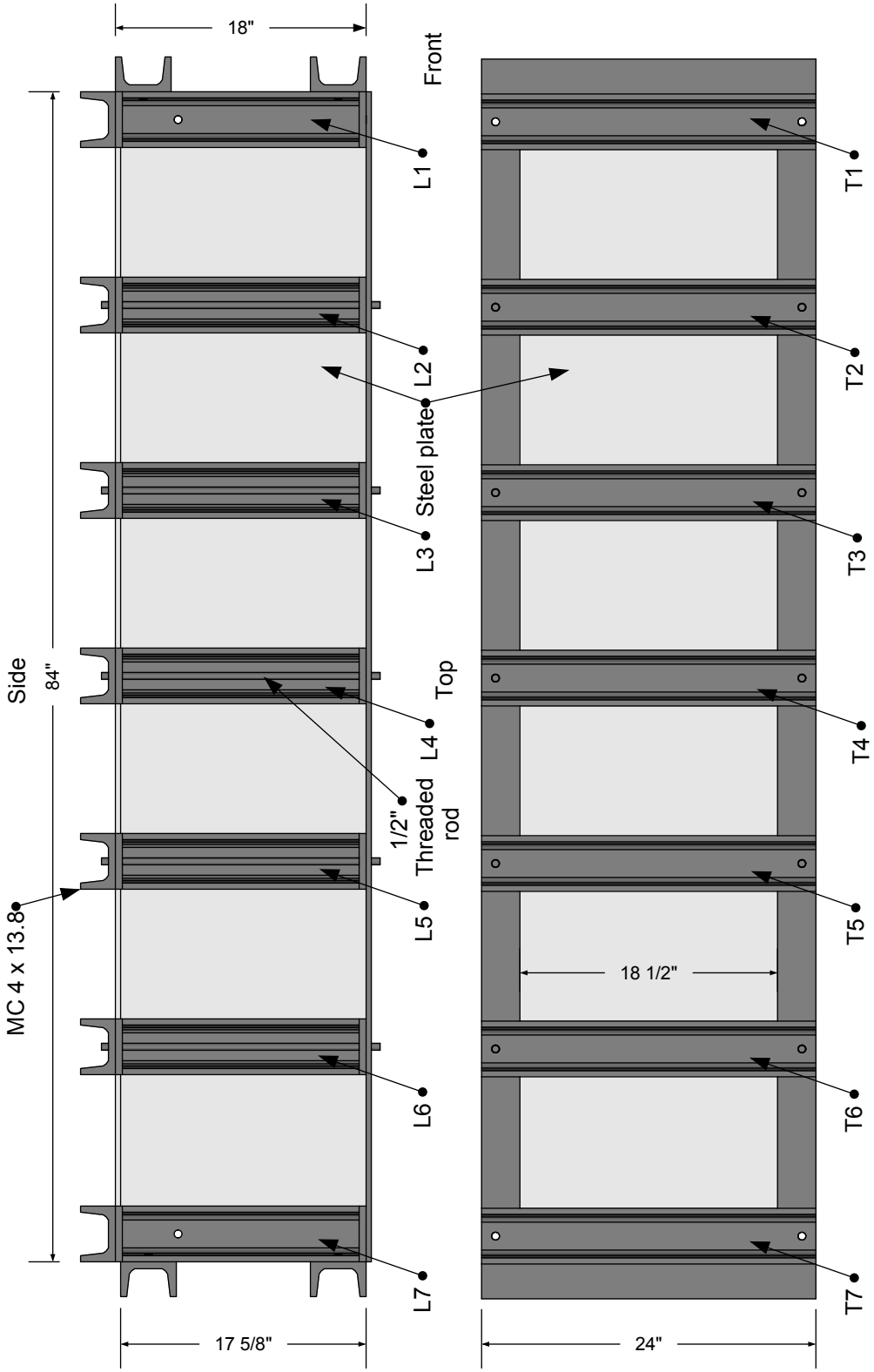

Figure D-2. Side and top view of assembled pullout box.

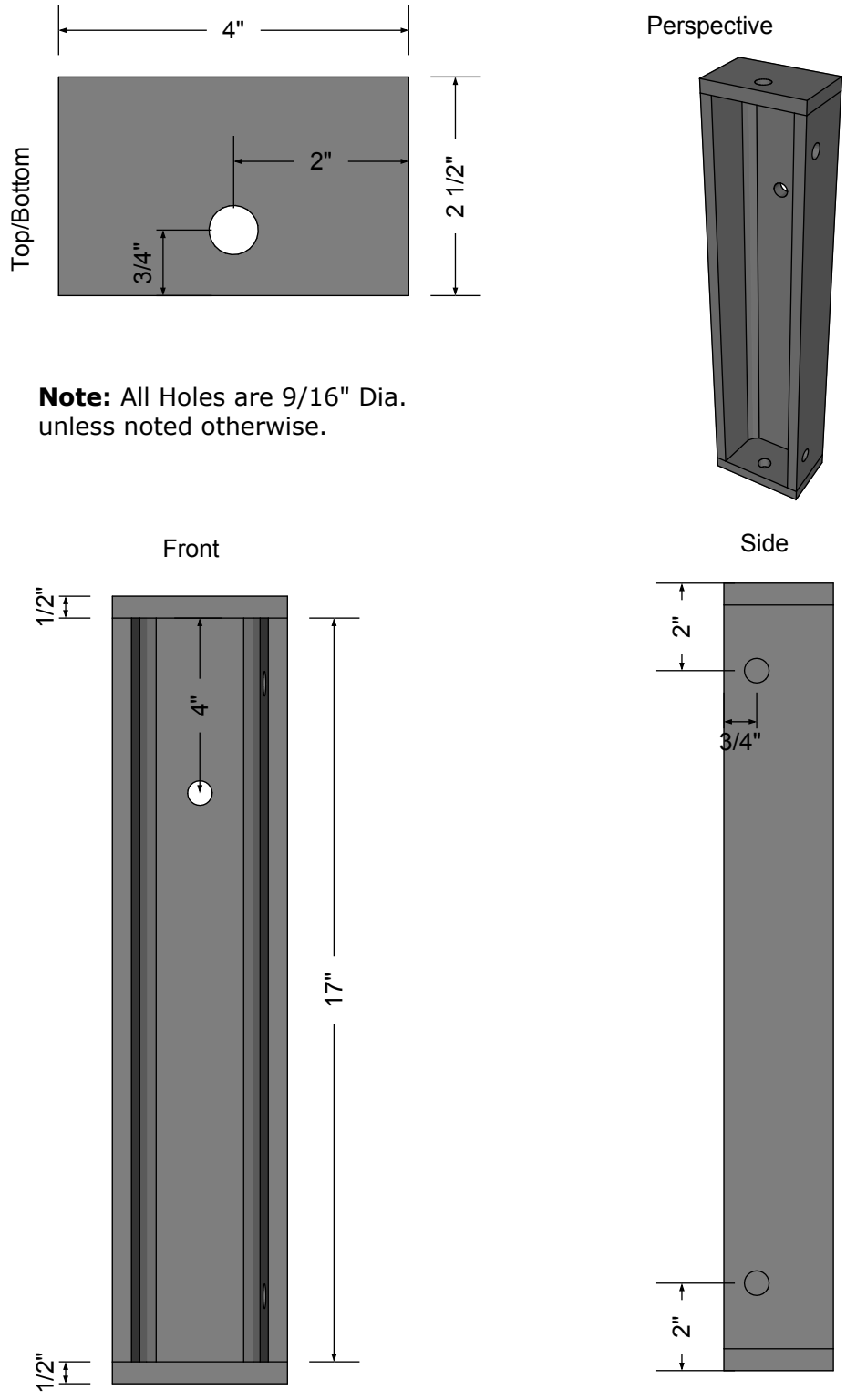

Figure D-3. Schematic of pullout box part L1, quantity = 1.

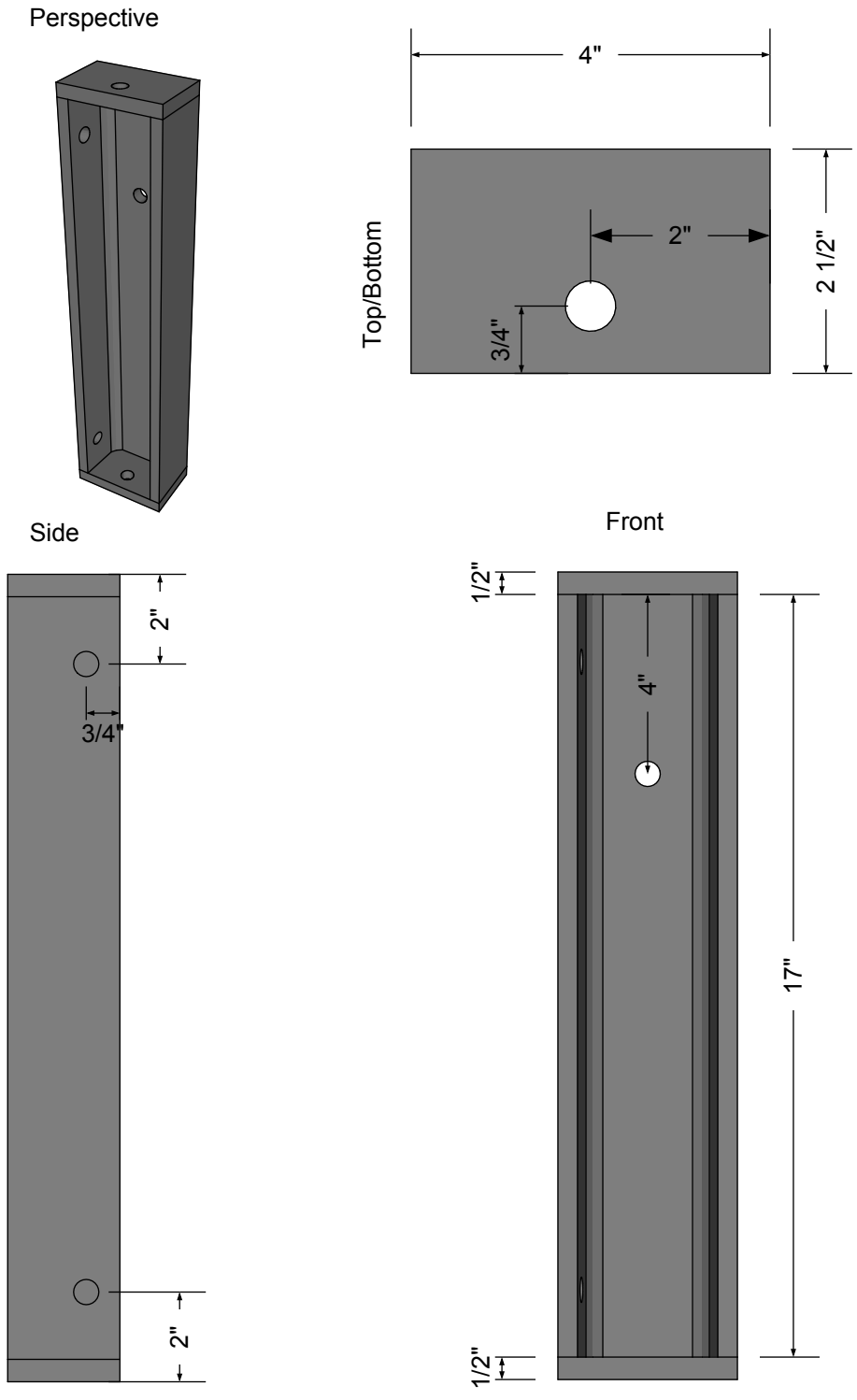

Figure D-4. Schematic of pullout box part R1, quantity = 1.

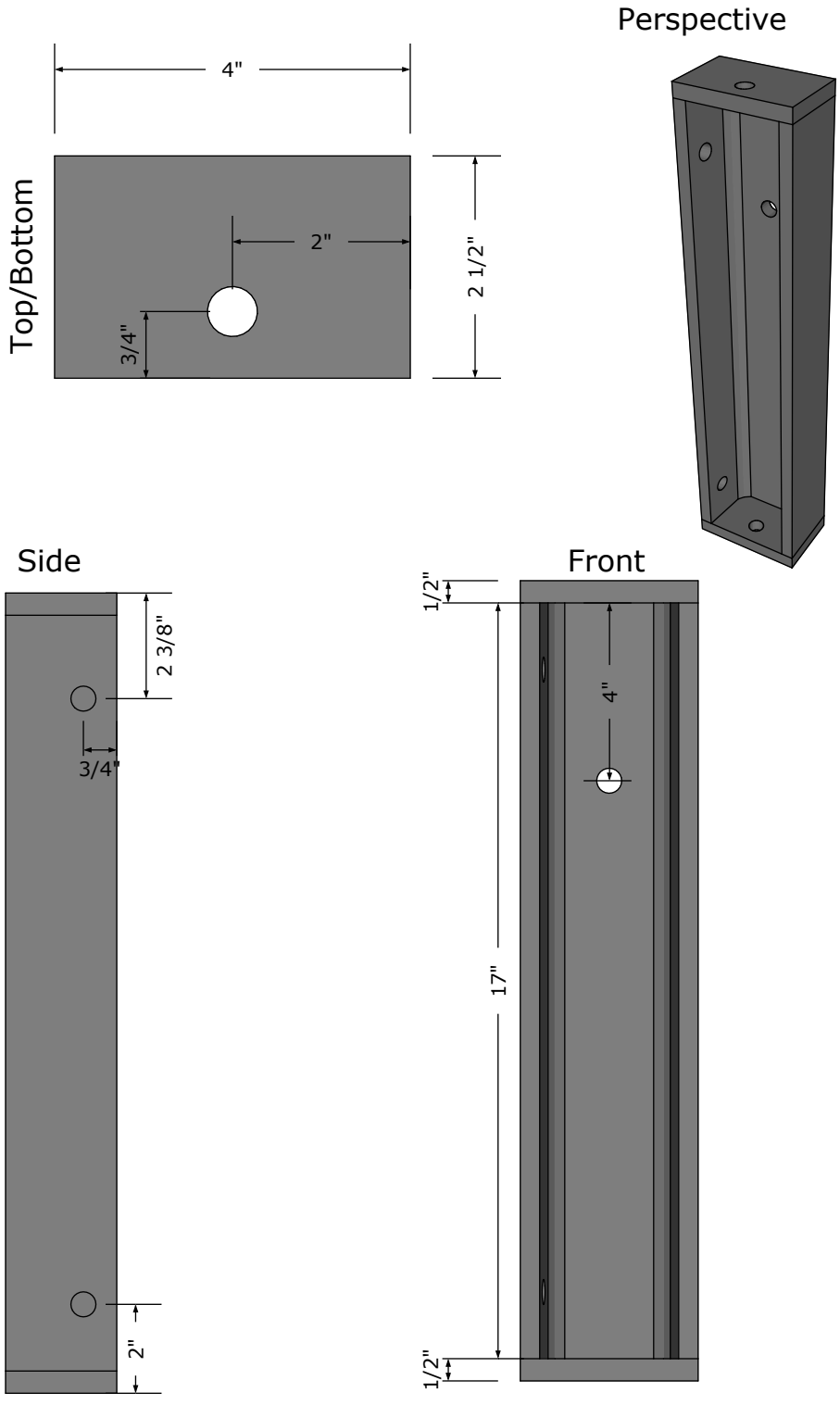

Figure D-5. Schematic of pullout box part L7, quantity = 1.

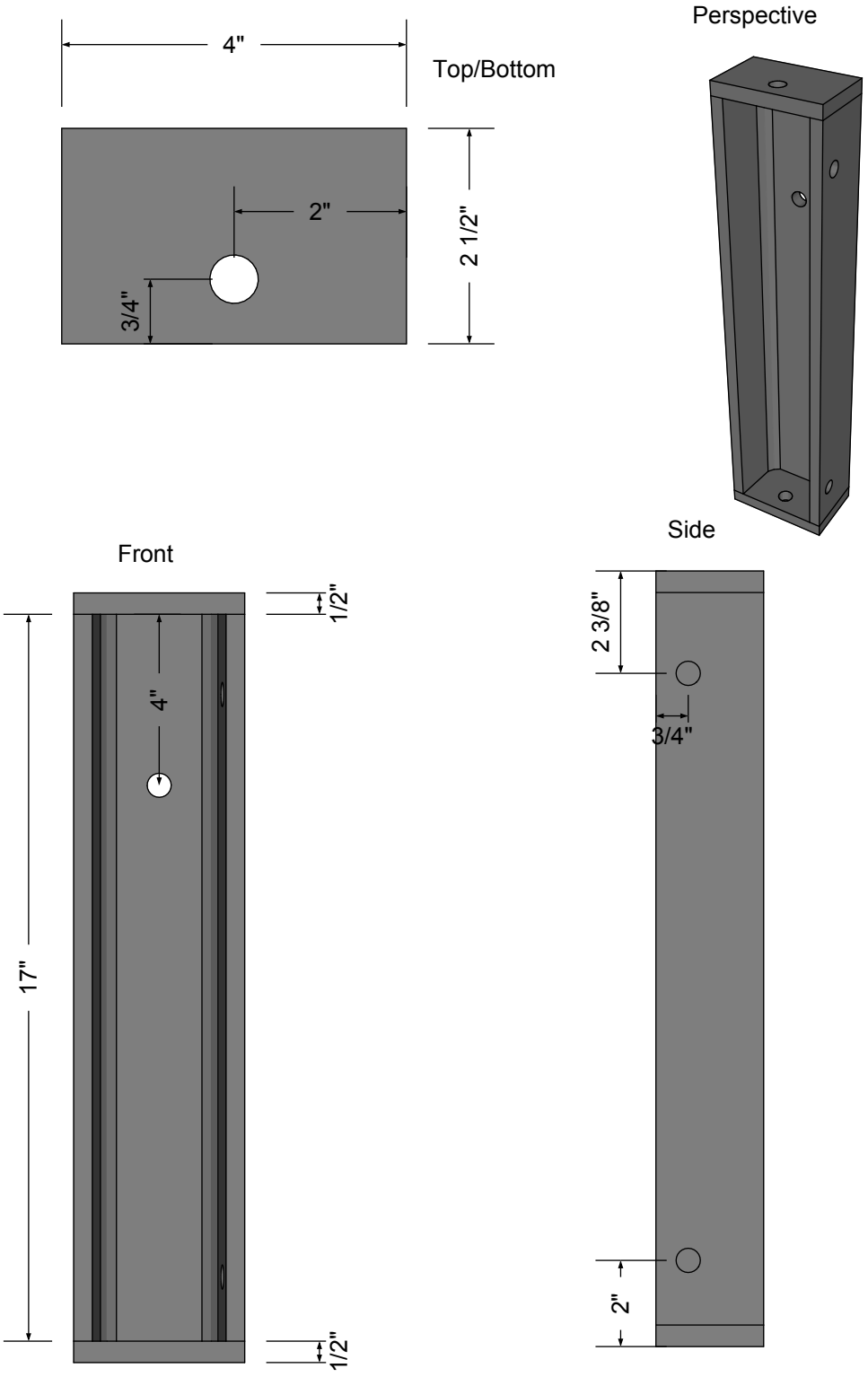

Figure D-6. Schematic of pullout box part R7, quantity = 1.

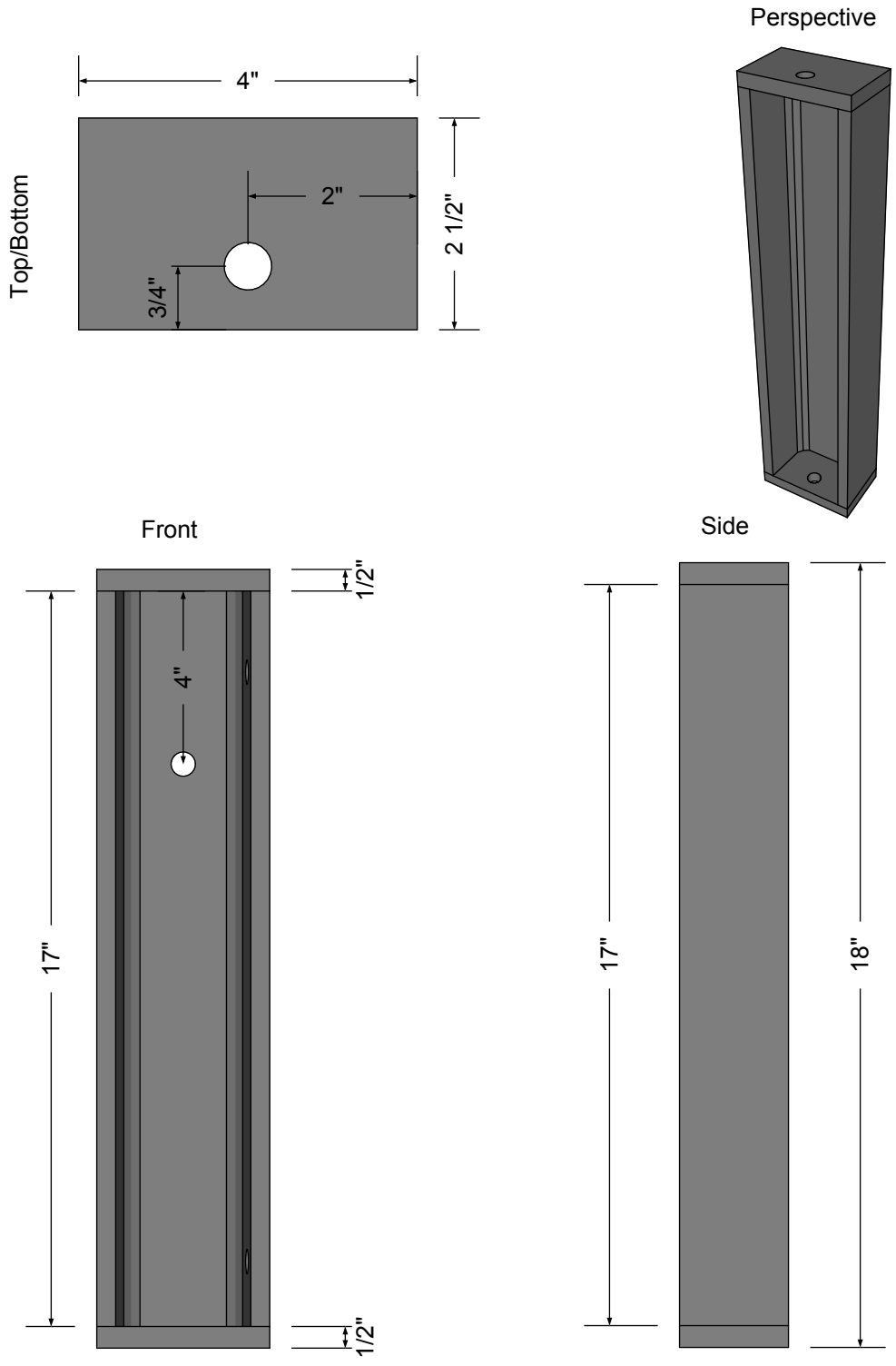

Figure D-7. Schematic of pullout box part R2-R6 and L2-L6, quantity = 10.

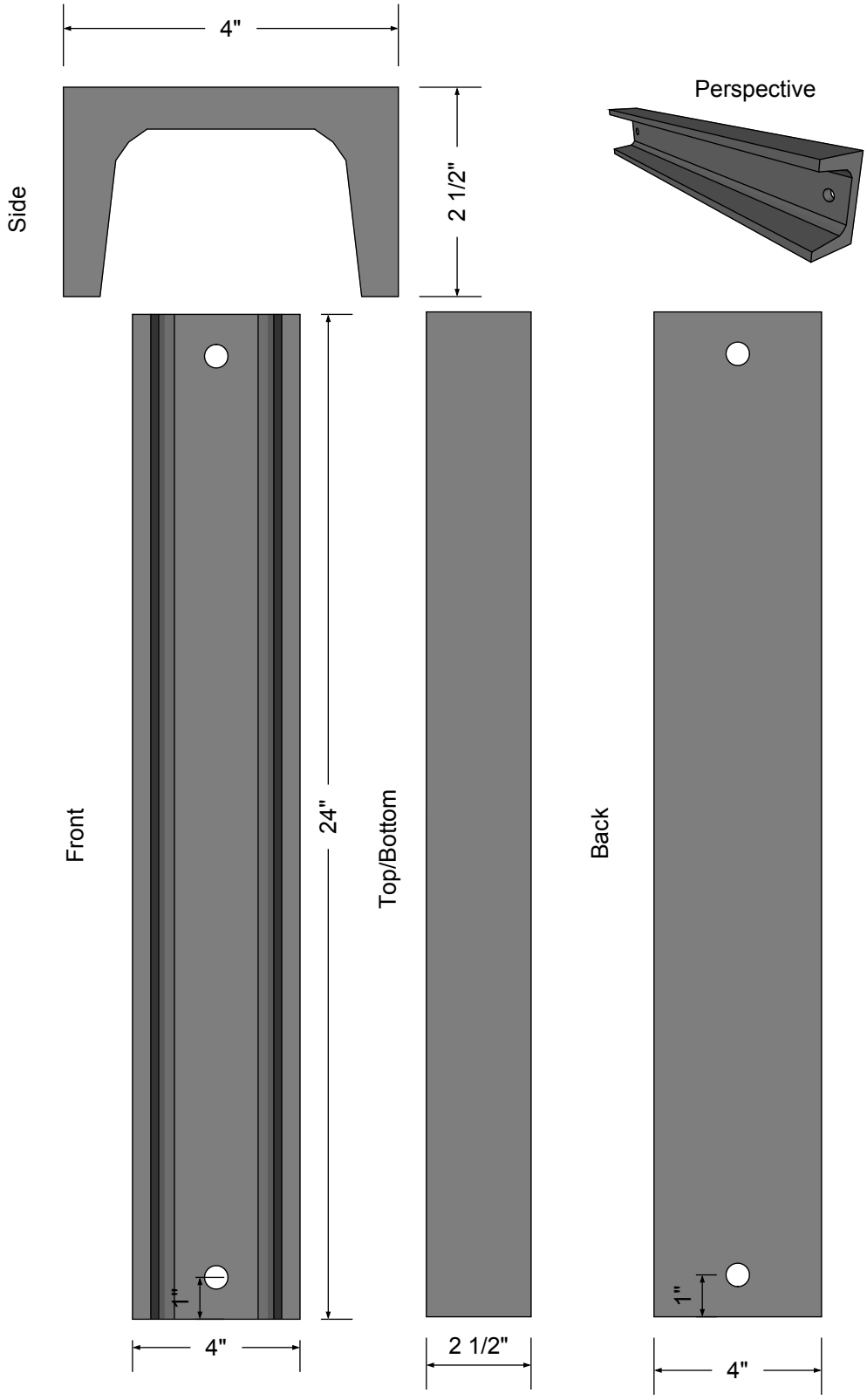

Figure D-8. Schematic of pullout box part T1 - T11, quantity = 11.

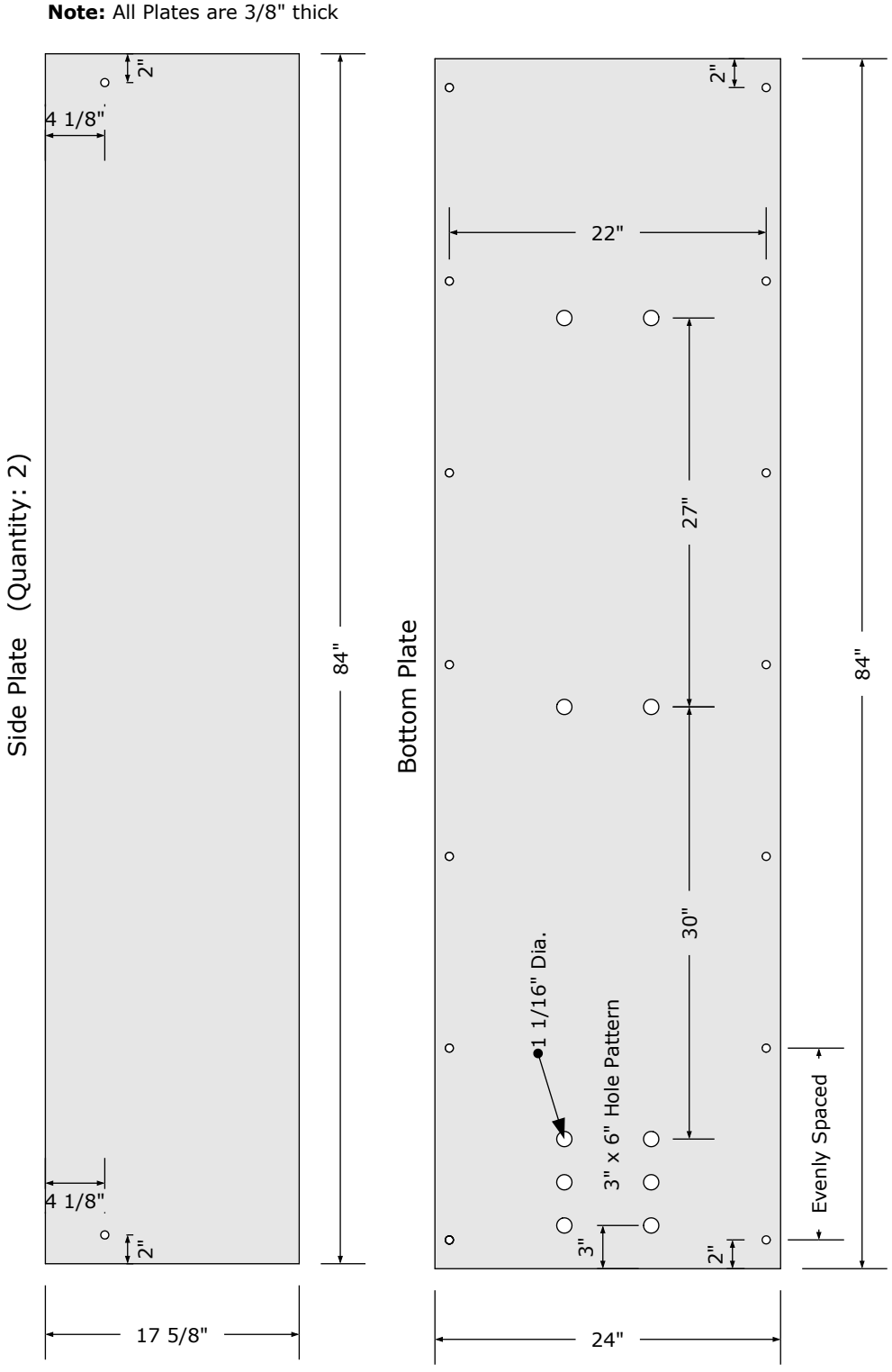

Figure D-9. Schematic of side plate and bottom plate.

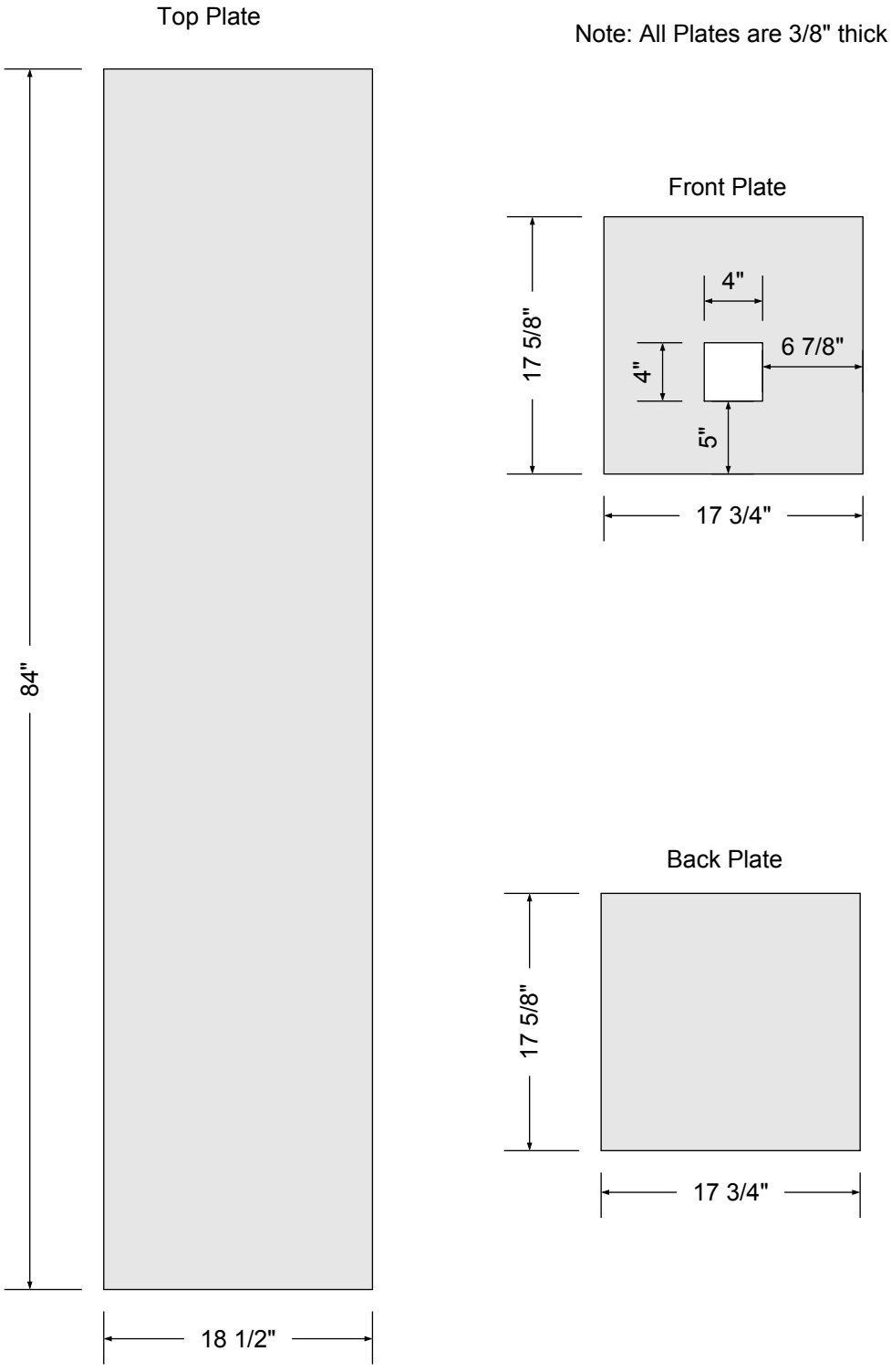

Figure D-10. Schematic of pullout box top, front, and back plates.

APPENDIX E

Pullout Box Design Calculations

Tensile strength of threaded rod:

Required tensile strength of threaded rod:

$P := 300kPa = 43.511 \cdot psi$ Pressure

$A_t := 9in \cdot 13.25in = 119.25 \cdot in^2$ Tributary area

$P_r := P \cdot A_t = 5.2 \cdot kip$ Tensile Load

Allowable tensile strength in threaded rod: 1/2 in

$F_u := 150ksi$

$d := 0.5in$

$$P_n := \frac{\left(0.75 \cdot F_u \cdot \frac{\pi d^2}{4}\right)}{2} = 11 \cdot kip$$

Since: $P_n > P_r$, **1/2 in, high strength threaded rod will work (Fu > 150 ksi).**

Shear strength of threaded rod:

Required shear strength of Threaded Rod:

$R_r := P_r = 5.2 \cdot kip$

Allowable shear strength in threaded rod: 1/2 in

$F_n := 0.4F_u = 60 \cdot ksi$

$d := 0.5in$

$$A_b := \frac{d^2 \cdot \pi}{4} = 0.196 in^2$$

$R_n := F_n \cdot A_b = 11.8 \cdot kip$

Since: $R_n > R_r$, **1/2 in, high strength threaded rod will work (Fu > 150 ksi).**

Bearing strength at bolt holes:

Required Strength: $P_r = 5.2 \cdot kip$

Allowable Bearing Strength: 3/8 in thick Plate with 3/4 in hole clearance

$F_u := 58ksi$ $L_c := 0.75in$

$t := 0.375in$

$d = 0.5 \cdot in$ $\Omega_{to} := 2$ ..... (J3.10)

$$R_n := \begin{cases} \left(1.2 L_c \cdot t \cdot F_u\right) & \text{if } 1.2 L_c \cdot t \cdot F_u \le 2.4 \cdot d \cdot t \cdot F_u \\ \left(2.4 \cdot d \cdot t \cdot F_u\right) & \text{otherwise} \end{cases}$$ ..... Equation J3-6a (AISC 13)

$R_n = 19.575 \cdot kip$ $\frac{R_n}{\Omega_{to}} = 9.8 \cdot kip$

Since $\frac{R_n}{\Omega_{to}} > P_r$, **3/8 in thick Plate with 3/4 in hole clearance will work.**

Shear strength in top channel:

Required Shear Strength of top channel:

$w := 13.25in \cdot 43.5psi$

$L_1 := 22in$

$V_r := \frac{w \cdot L_1}{2} = 6.34 \cdot kip$

Where L_1 is the center to center channel spacing, w is the expected shear force, and V_r is the Required shear strength.

Allowable shear strength in the top channel: MC 4 x 13.8

$b_f := 2.5in = 0.064 \cdot m$

$t_f := 0.5in = 0.013\,m$

$t_w := t_f$

$E := 2900ksi$

$F_y := 36ksi$

$\Omega_v := 1.67$

$k_v := 1.2$ 16.1 Chapter (G 7)

$A_w := 2b_f \cdot t_f = 2.5 \cdot in^2$ (use 2 because there are two shear resisting members)

$b := b_f$

$h := b$

$h = 0.064\,m$

Since : $\frac{h}{t_w} \le 1.10\sqrt{\frac{k_v \cdot E}{F_y}}$, $C_v := 1.0$ (G2 - 3)

$V_n := 0.6F_y \cdot A_w \cdot C_v = 54 \cdot kip$ (G2 - 1)

$\frac{V_n}{\Omega_v} = 32.335 \cdot kip$

Since $\frac{V_n}{\Omega_v} > V_r$, **MC 4 x 13.8 will work**.

Flexure in top channel:

Required Flexural Strength:

$$M_r := \frac{\left(w \cdot L_1^{\,2}\right)}{8} = 34.871 \cdot kip \cdot in$$

w and L_1 from Required shear strength calculations.

Allowable Flexural strength in top channel: MC 4 x 13.8

$F_y := 36ksi$

$Z_y := 2.40in^3$

$S_y := 1.29in^3$

$\Omega_b := 1.67$

$$M_n := \begin{cases} \left(F_y \cdot Z_y\right) & \text{if } F_y \cdot Z_y \le 1.6 \cdot F_y \cdot S_y \\ \left(1.6 \cdot F_y \cdot S_y\right) & \text{otherwise} \end{cases}$$

$M_n = 74.304 \cdot kip \cdot in$

$\frac{M_n}{\Omega_b} = 44.493 \cdot kip \cdot in$ Since $\frac{M_n}{\Omega_b} > M_r$, **MC 4 x 13.8 will work.**

Tension in top channel

Required Tensile Strength:

$P_r = 5.189 \cdot kip$

Allowable flexural strength in top Channel:

$U := 1 \qquad \Omega_t := 1.67$

$A_g := 4.03in^2$

$A_n := A_g - \left[d + \left(\frac{1}{16}\right)in\right] \cdot 0.5in = 3.749 \cdot in^2$

$A_e := A_n \cdot U = 3.749 \cdot in^2$

$$P_n := \begin{cases} \left(F_u \cdot A_e\right) & \text{if } F_u \cdot A_e \le F_y \cdot A_g \quad \text{.....Rupture} \\ \left(F_y \cdot A_g\right) & \text{otherwise} \quad \text{.....Yielding} \end{cases}$$

$P_n = 145.08 \cdot kip$ (Yielding Controls)

$\frac{P_n}{\Omega_t} = 86.874 \cdot kip$

Since $\frac{P_n}{\Omega_t} > P_r$, **MC 4 x 13.8 will work.**

Weld Strength at side channel ends:

Required Weld Strength: (J2 - 3)

$R_{req} := P_r = 5.189 \cdot kip$

Weld area

$l := 2in + 2in + 2in + 2in = 8 \cdot in$ .....weld length in inches

$D := 4$ .....weld size in sixteenths of an inch

$F_{EXX} := 70ksi$ ..... F_u of welding material

Available Strength: $\Omega := 2.0$

$$R_n := 0.6 \cdot F_{EXX} \cdot \left(\frac{\sqrt{2}}{2}\right) \cdot \left(\frac{D}{16}\right) in \cdot l = 59.397 \cdot kip$$ Pg. 8-8 (AISC - 12)

$$\frac{R_n}{\Omega} = 29.698 \cdot kip$$

Since $\frac{R_n}{\Omega} > R_{req}$, **8 in of 4/16in welds will work.**

Support spacing for top plate flexure:

Plate thickness:

$\Omega_b := 1.67$

$b := 17in$

$w := P \cdot b = 739.7 \cdot \frac{lbf}{in}$ $I_{plate} := \frac{b \cdot t^3}{12} = 0.075 \cdot in^4$ $y := \frac{t}{2}$

$M_n := \frac{F_y \cdot I_{plate}}{y} = 14.344 \cdot kip \cdot in$ $\frac{M_n}{\Omega_b} = 8.59 \cdot kip \cdot in$

Try:

$s_{fl} := 9.5in$ $M_{app} := \frac{w \cdot s_{fl}^2}{8} = 8.34 \cdot kip \cdot in$ $M_{app} \le \frac{M_n}{\Omega_b} = 1$

Flange to flange distance must be limited to 9.5".

APPENDIX F

Required Reinforcement Embedment Lengths

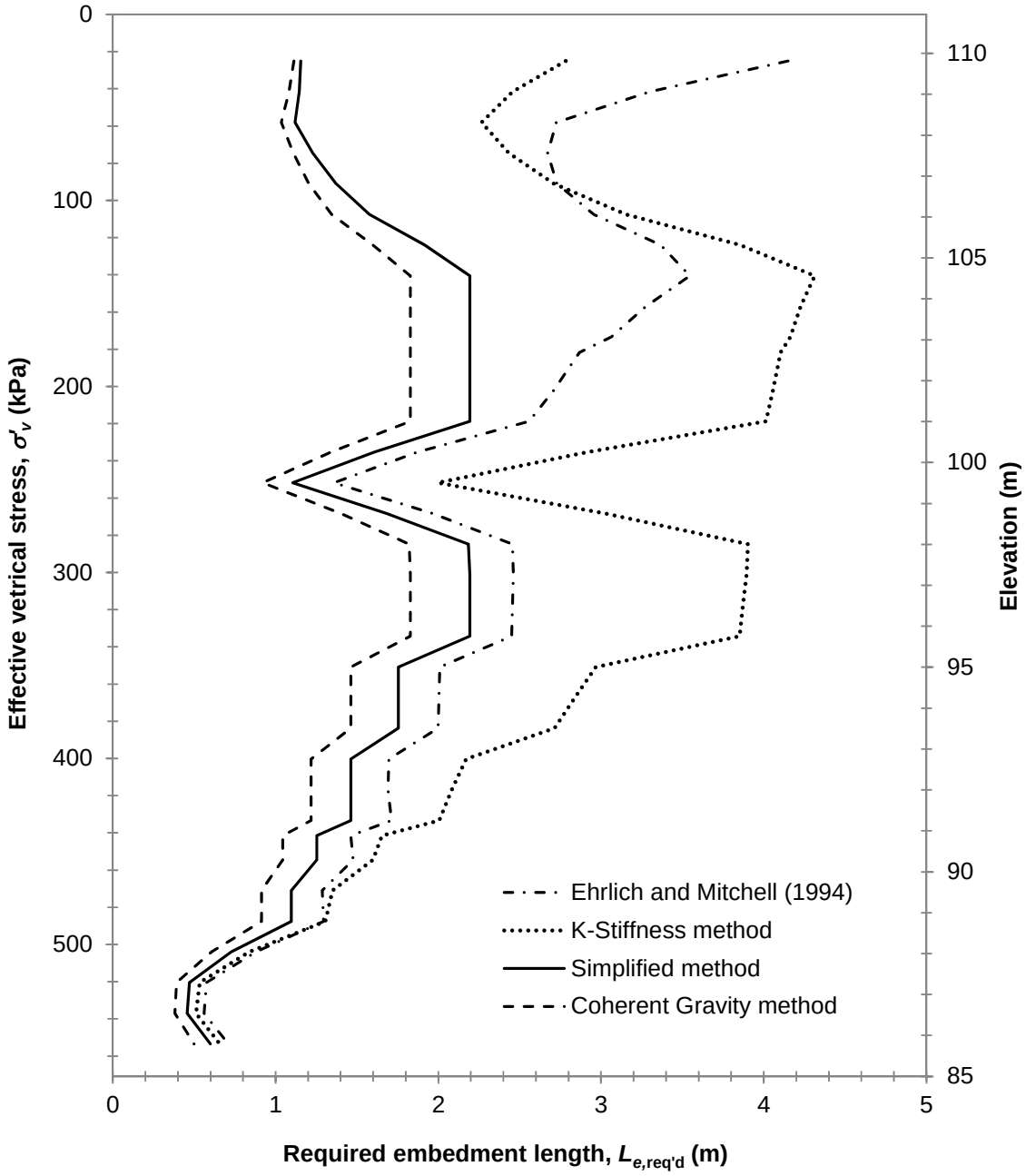

Figure 0.1. North MSE wall required embedment lengths for pullout using different load prediction methods and the current AASHTO *f design model.**

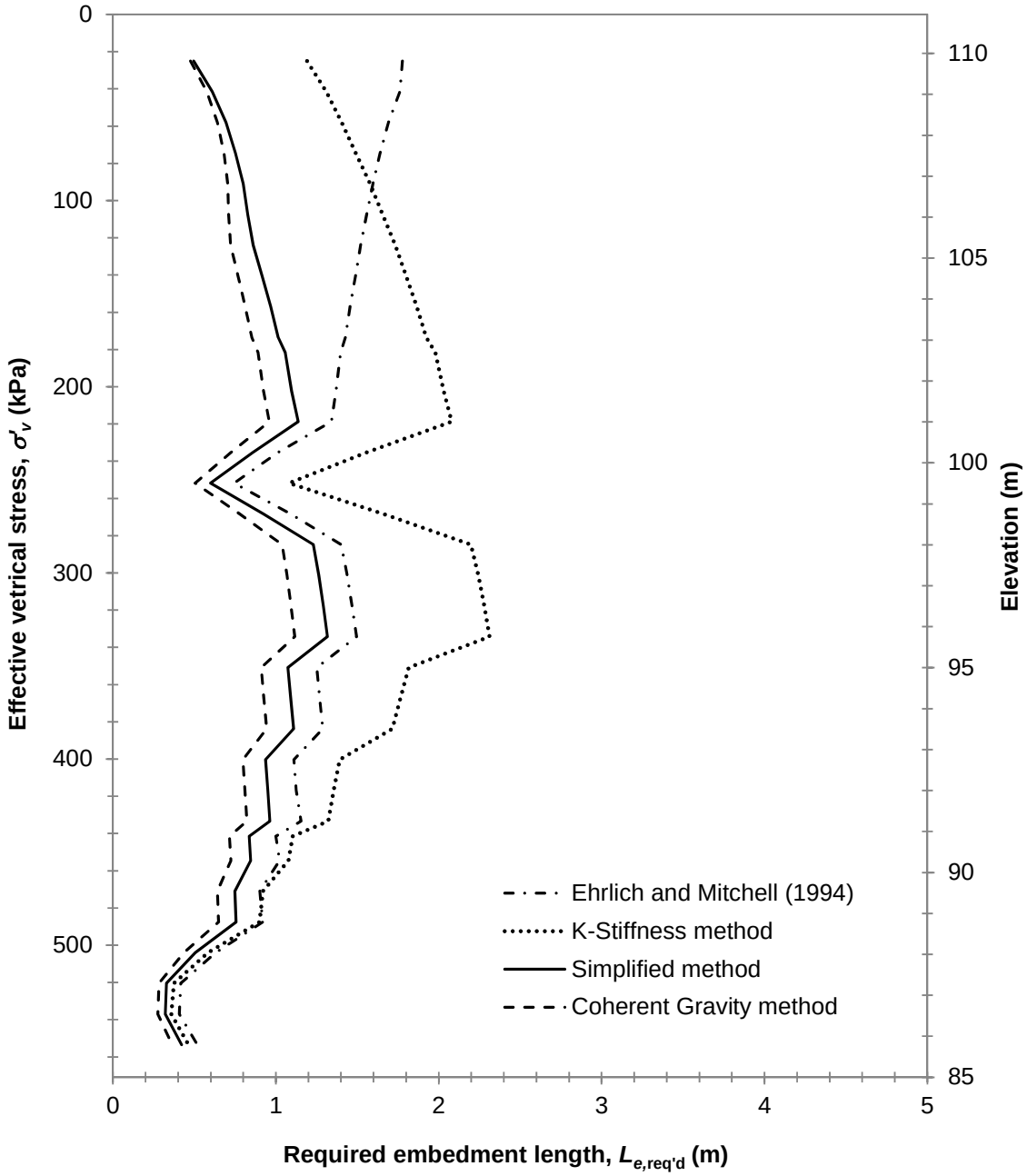

Figure 0.2. North MSE wall required embedment lengths for pullout using different load prediction methods and the proposed global gravel *f design model.**

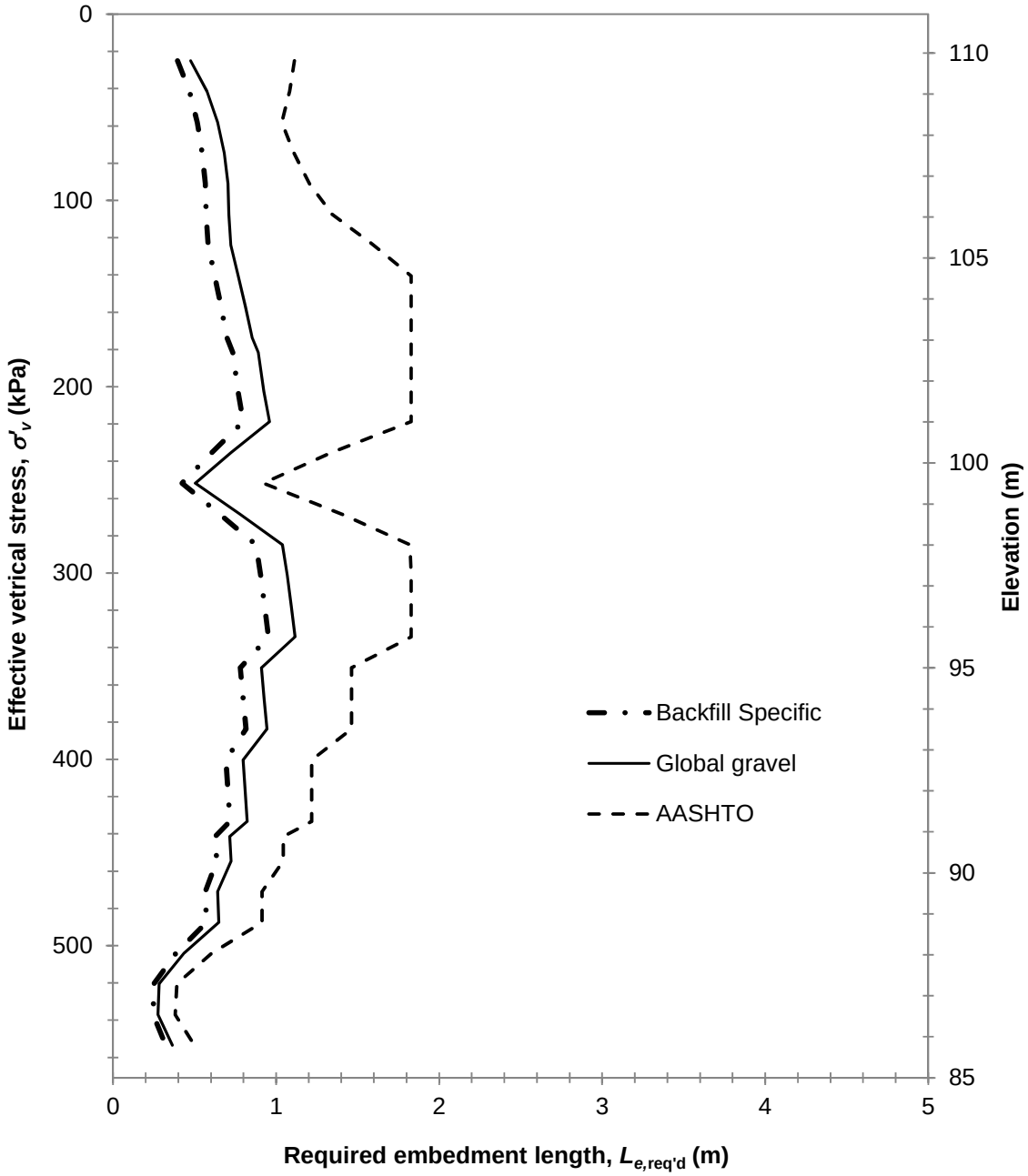

Figure 0.3. Embedment lengths required for pullout resistance in the North MSE wall computed using the two proposed f* design models and the AASTO standard model with reinforcement loads calculated using the Coherent Gravity method

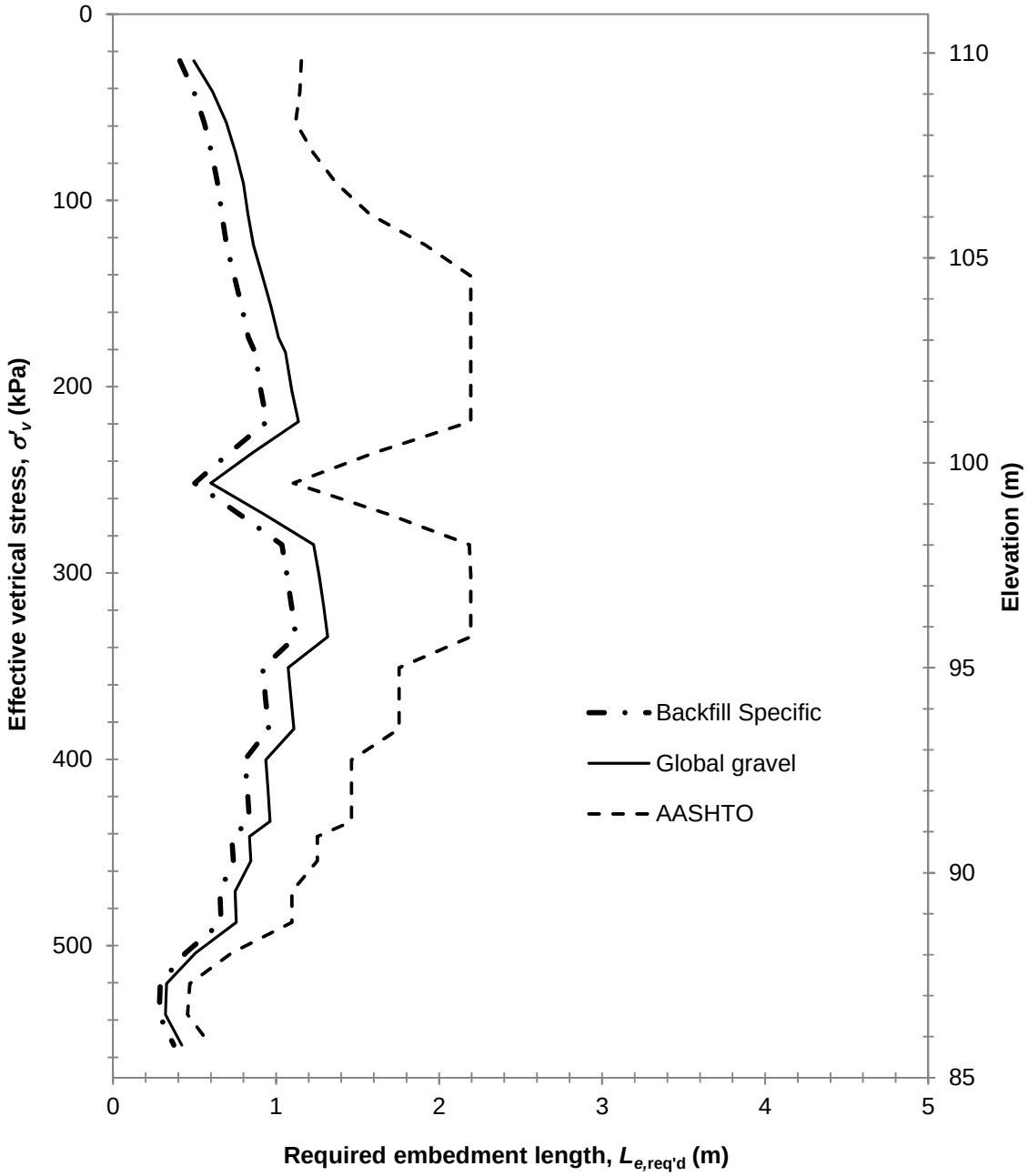

Figure 0.4. Embedment lengths required for pullout resistance in the North MSE wall computed using the two proposed *f design models and the AASTO standard model with reinforcement loads calculated using the Simplified method.**

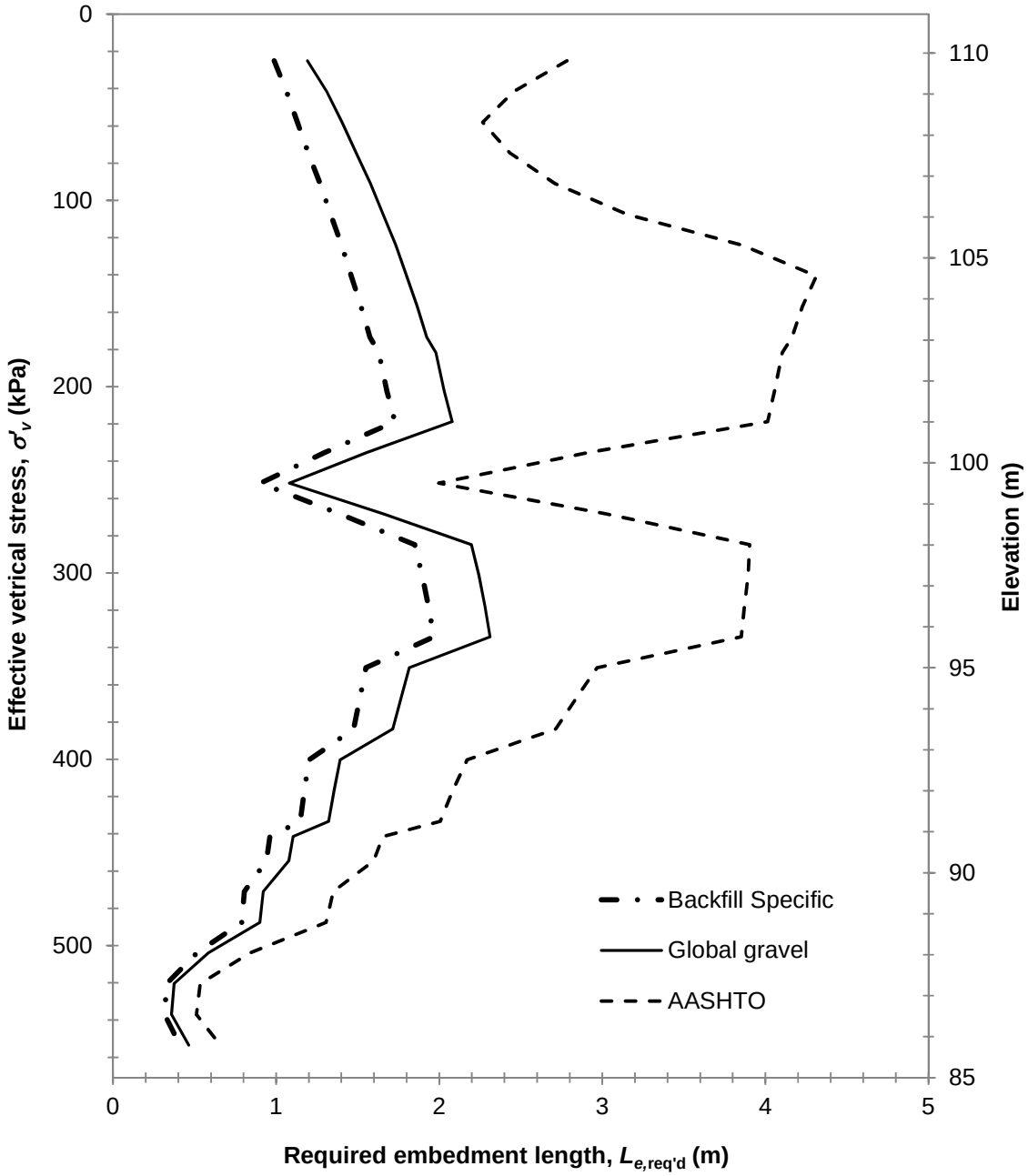

Figure 0.5. Embedment lengths required for pullout resistance in the North MSE wall computed using the two proposed *f design models and the AASTO standard model with reinforcement loads calculated using the K-Stiffness method.**

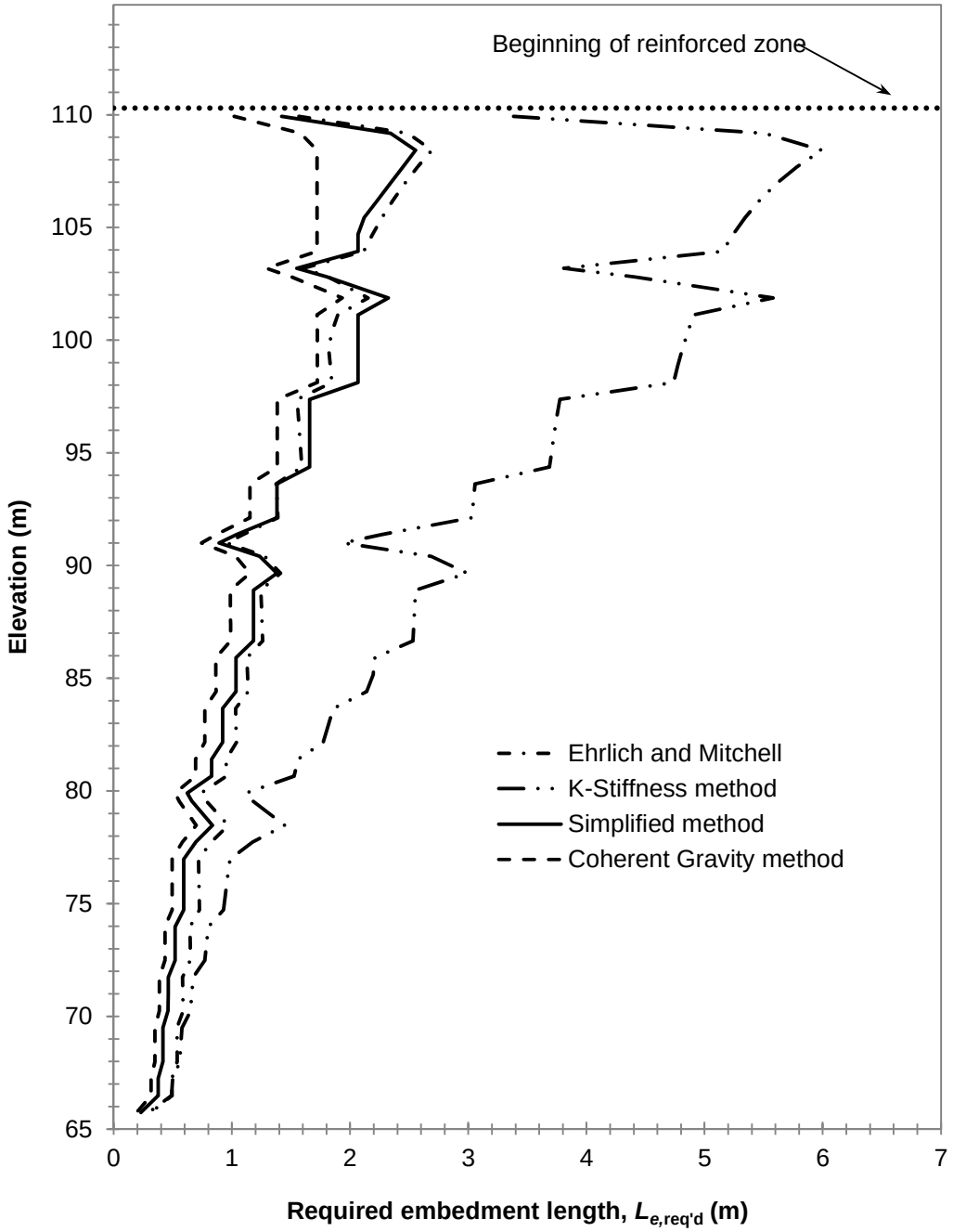

Figure 0.6. West MSE wall required embedment lengths for pullout using different load prediction methods and the current AASHTO *f design model.**

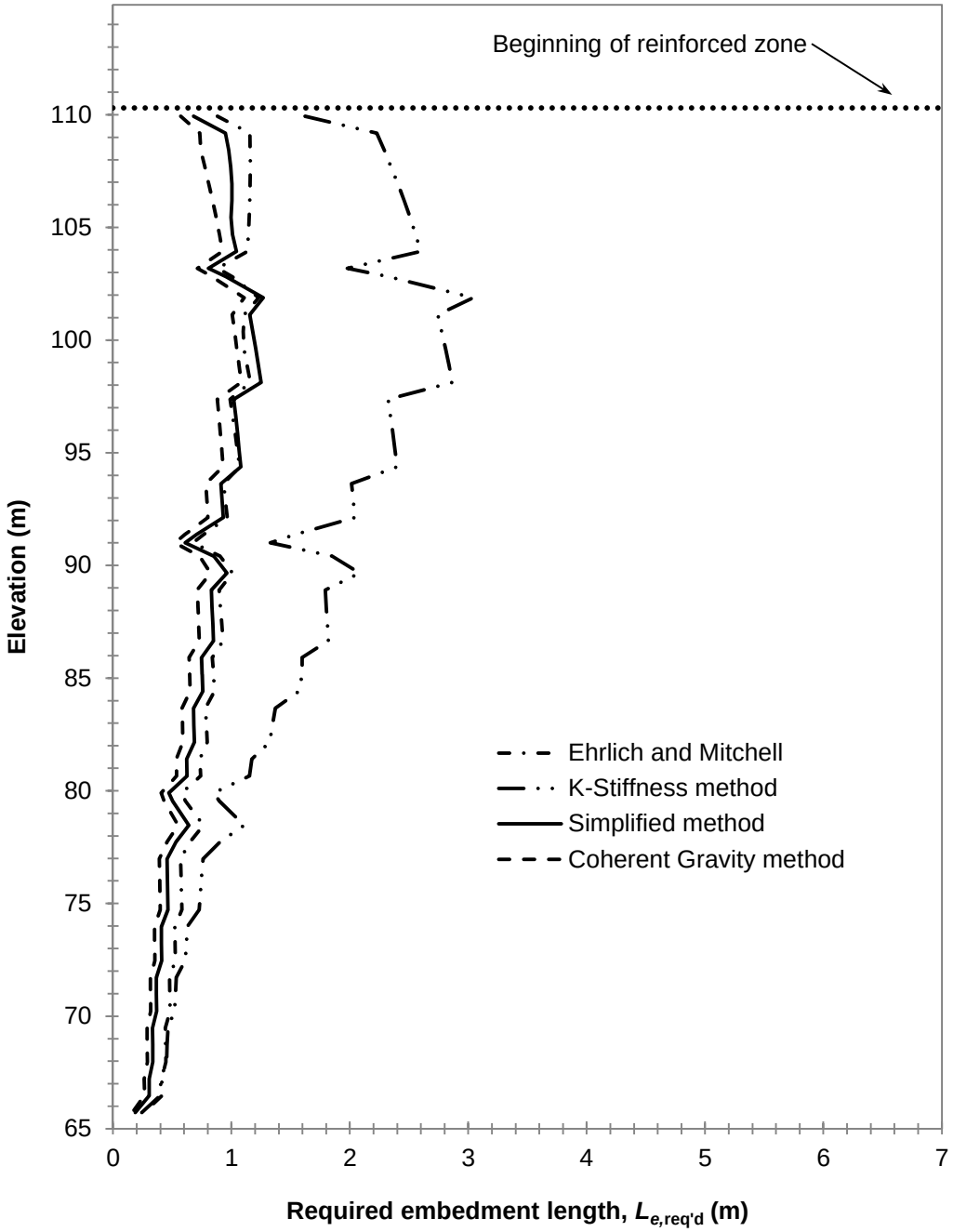

Figure 0.7. West MSE wall required embedment lengths for pullout using different load prediction methods and the proposed global gravel *f design model.**

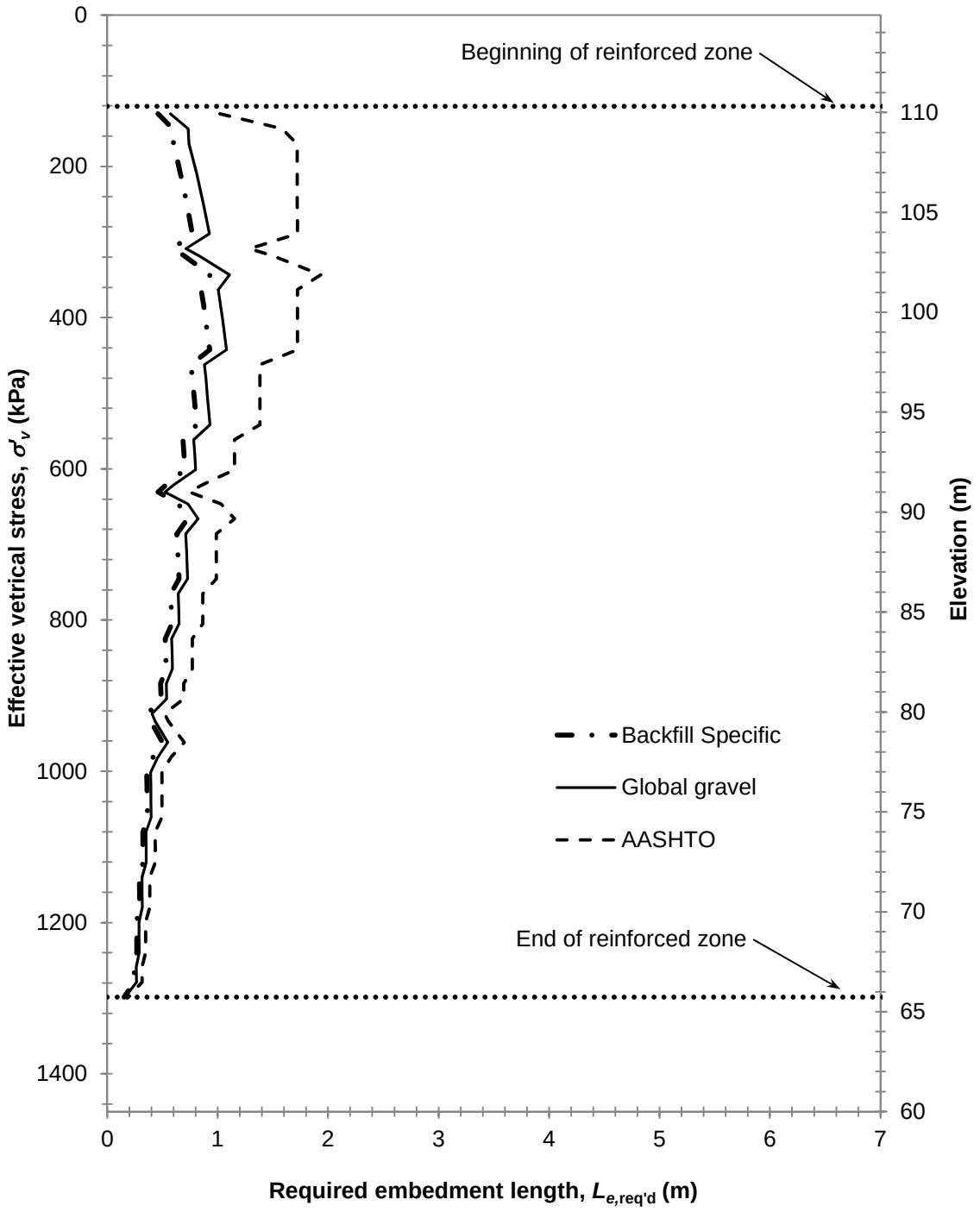

Figure 0.8. Embedment lengths required for pullout resistance in the West MSE wall computed using the two proposed *f design models and the AASTO standard model with reinforcement loads calculated using the Coherent Gravity method**

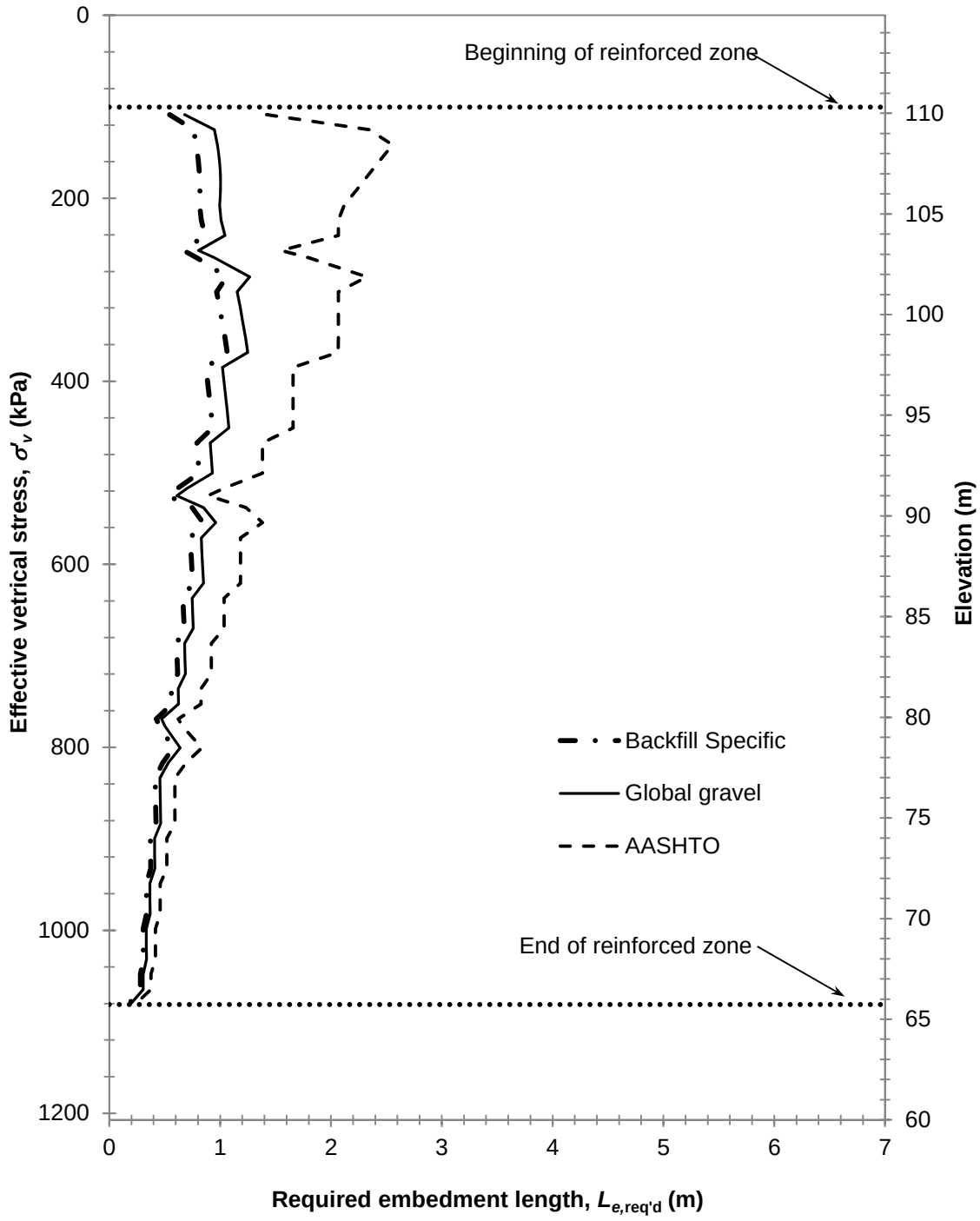

Figure 0.9. Embedment lengths required for pullout resistance in the West MSE wall computed using the two proposed *f design models and the AASTO standard model with reinforcement loads calculated using the Simplified method.**

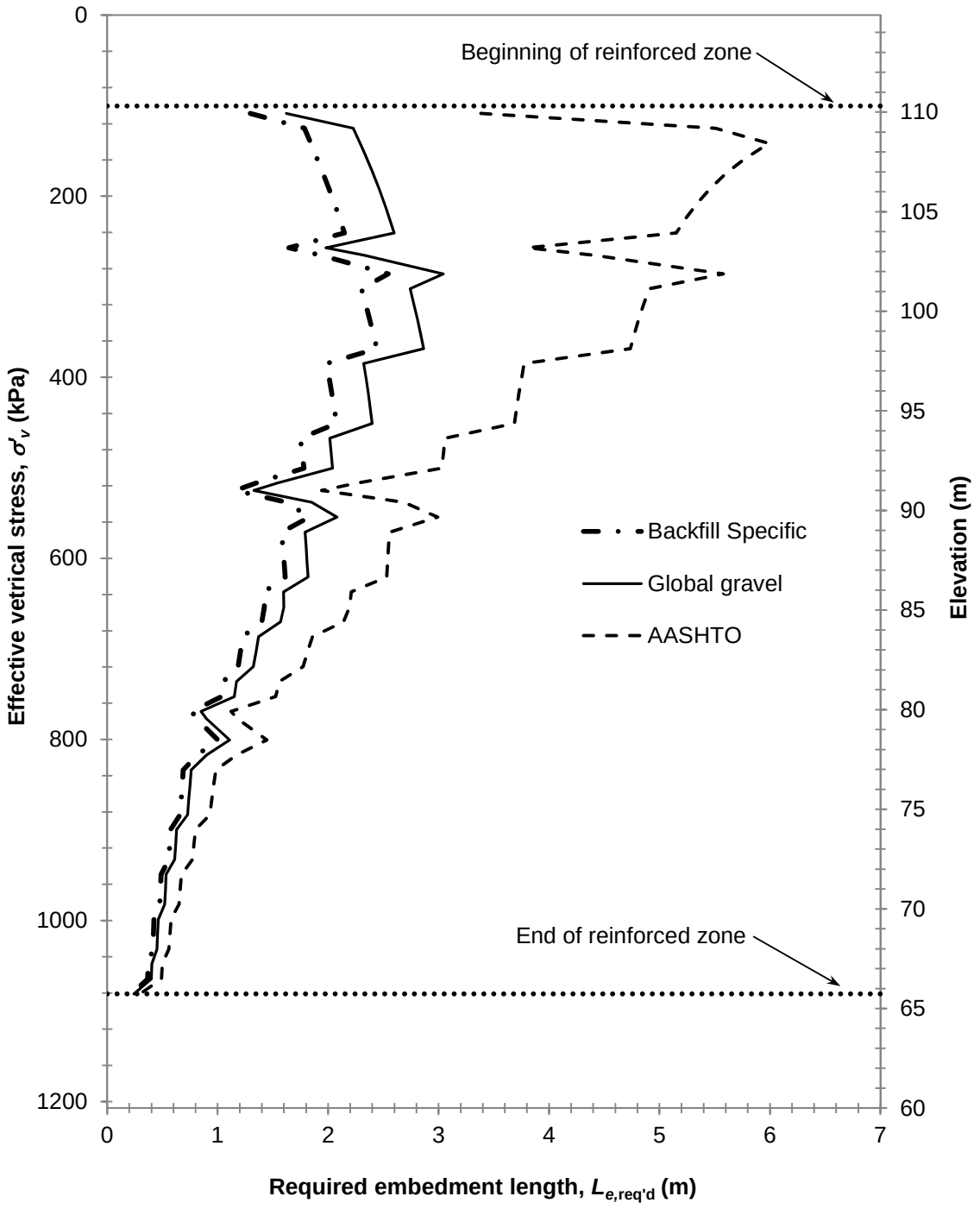

Figure 0.10. Embedment lengths required for pullout resistance in the West MSE wall computed using the two proposed *f design models and the AASTO standard model with reinforcement loads calculated using the K-Stiffness method.**